BARYONS FROM LATTICE QCD

A thesis submitted to
Tata Institute of Fundamental Research, Mumbai, India
for the degree of
Doctor of Philosophy
in
Physics

By

M. Padmanath
Department of Theoretical Physics
Tata Institute of Fundamental Research
Mumbai - 400 005, India

May, 2014

Declaration

This thesis is a presentation of my original research work. Wherever contributions of others are involved, every effort is made to indicate this clearly, with due reference to the literature, and acknowledgement of collaborative research and discussions.

The work was done under the guidance of Professor Nilmani Mathur, at the Tata Institute of Fundamental Research, Mumbai.

(M. Padmanath)

In my capacity as the supervisor of the candidate's thesis, I certify that the above statements are true to the best of my knowledge.

(Nilmani Mathur)

Acknowledgement

First and foremost, I would like to express my gratitude to my thesis advisor Prof. Nilmani Mathur for all that I have learned from him during my Ph. D work. It has been a wonderful experience working with him. I believe I have been able to better myself over the years through his constant guidance, support and encouragement. I gratefully acknowledge Prof. Saumen Datta for all the excellent discussions, which helped me learn many aspects about QCD and lattice, with him. I am equally grateful to Prof. Mike Peardon for all the help and suggestions and giving me opportunity to spend time at Trinity College, Dublin. I would also like to thank Prof. Sourendu Gupta, Prof. Robert Edwards and Dr. Christopher Thomas for all the fruitful discussions that resulted in many of the contents discussed in this thesis. For making the time spent in the office really fun and for numerous physics discussions, I am grateful to all my DTP colleagues, many of whom are elsewhere at present. Special thanks to Dr. Debasish Banerjee, Nikhil Karthik, Dr. Jyotirmoy Maiti and Dr. Sayantan Sharma for all their help during my Ph. D. I would like to acknowledge all the help from the DTP office staff : Girish Ogale, Mohan Shinde, Rajan Pawar and Raju Bathija. Special thanks also are due to the system administrators Kapil Ghadiali and Ajay Salve for being extremely helpful all the times. Thanks are also due to the ILGTI (Indian Lattice Gauge Theory Initiative) for making available the computing resources of Blue gene, CRAY and three clusters of the Department of Theoretical Physics - GAGGLE, HIVE and BROOD, on which most of the computations reported in the thesis were done. I would like to acknowledge the support during the course of my Ph. D. from the Council of Scientific and Industrial Research(CSIR), Government of India through the SPM fellowship and the support from the Trinity College Dublin Indian Research Collaboration Initiative.

I have to thank a lot of friends whose help and support made my life in TIFR enjoyable. Specially I would like to appreciate and acknowledge the constant company from Carina, Debjyoti, Mathimalar, Rajeev, Rishad, Sasidevan, Shyama and Thomas among others whom I have not named explicitly : my stay at TIFR would not have been so much enjoyable without their presence. I would also like to thank all my friends in the Malayali community in TIFR for a wonderful time I had with them. It was a joy to have your company and because of you, I didn't feel like missing my home. Finally, I would like to thank my parents, Madanagopalan and Kalavathy, and my brother, Premnath, for always being extremely supportive and for all their love and care they have for me.

Collaborators

This thesis is based on the work done in collaboration with Subhasish Basak, Saumen Datta, Robert G. Edwards, Sourendu Gupta, Andrew Lytle, Jyotirmoy Maiti, Pushan Majumdar, Nilmani Mathur and Mike Peardon. In particular, Chapter 3 and 4 was done in collaboration with Robert G. Edwards, Nilmani Mathur and Mike Peardon (2013-); Chapter 5 with Subhasish Basak, Saumen Datta, Andrew Lytle, Pushan Majumdar and Nilmani Mathur (2012-); Chapter 5 with Saumen Datta, Sourendu Gupta, Jyotirmoy Maiti and Nilmani Mathur (2013).

To my family

Contents

Synopsis

Abstract

In this synopsis, I report on non-perturbative studies of various aspects of baryon physics using lattice QCD. The first part of the thesis consists of spectroscopy of baryons with one or more charm quarks using two complementary non-perturbative approaches. The first approach enables us to extract highly excited states, which are very difficult to extract using the previously existing lattice QCD techniques, of charm baryons and the second allows us to extract the ground states of various charm and strange hadrons with improved control over cut-off effects. The second part of the synopsis deals with a study of baryon screening masses at finite temperature.

In the work on excited state charm baryon spectroscopy, which constitutes the major part of this thesis, we use anisotropic lattices having $N_f = 2 + 1$ dynamical quark fields with very fine temporal lattice spacing, which is crucial for minimizing the discretization errors. After constructing the correlation functions with a large basis of interpolating operators employing a recently developed technique, called distillation, we extract the highly excited states using a variational fitting method. The spectra of excitations of charm baryons thus computed have baryonic states with well-defined total spin up to $\frac{7}{2}$ for both the parities and the low lying states closely resemble the pattern expected from non-relativistic potential models. We also study various energy splittings between the extracted states, which can provide insights on the interactions within heavy baryons.

Complementary to the above work, we perform lattice calculations of charm hadrons adopting a mixed action approach with the overlap action for the valence quarks on a background of 2+1+1 flavors highly improved staggered quarks. We calculate the low lying hadron spectra as well as energy splittings at various lattice spacings with improved control over cut-off effects and compare with results from the above work.

In the second part, we perform a finite temperature study of screening masses of hadrons, particularly for baryons, where we analyze the temperature dependence of the hadronic screening correlators above and immediately below the deconfinement transition temperature (T_c).

Above T_c, both mesonic and baryonic screening correlators show clear evidence for weakly interacting quarks, while below T_c, unlike mesonic channels, baryonic screening correlators show precursor effects for chiral symmetry restoration.

0.1 Introduction

Most of the mass of the visible universe - about 99% - constitute of baryons. Though the recently discovered Higgs boson [1] is believed to provide mass to the fundamental particles like leptons and quarks, it does not explain the total mass of the baryons that are made of these quarks. Baryons are relatively simple systems in which quintessentially confining character of multiple quarks is manifest and are sufficiently complex to shed light on physics hidden from us in the mesons. Understanding the baryon spectra is thus expected to answer a large series of questions on baryons and the interactions that exist within them. Particularly, with the recent excitement in heavy hadron physics and fore-seeing the observations from large statistical samples that will be collected in many future and ongoing experiments, a detailed understanding of the heavy baryon spectra is expected to provide insights into various aspects of the strong force that cannot be probed with light baryons.

The physical properties of baryons are believed to be governed by the theory of Quantum ChromoDynamics (QCD), an asymptotically free local non-Abelian quantum gauge field theory. As one of four recognized fundamental forces of nature, the theory of QCD, also known as the strong force, is one of the most important areas of research in modern particle physics. In high energy domain, where the coupling constant is small enough for pursuing a perturbative study, analytical calculations based on QCD have been proved to be highly accurate in explaining numerous experimental data, such as in deep inelastic scattering. However, at low energies, the coupling constant becomes very large, rendering perturbation theory in the coupling inapplicable.

A comprehensive understanding of the theory of QCD in the strong coupling regime implies a rigorous determination and understanding of its bound states. If QCD is the correct theory, then one should be able to reproduce the physical hadron spectra from a high precision first principles non-perturbative calculation. Much like the role of atomic spectroscopy in the development of quantum mechanics, hadron spectroscopy, both theoretically and experimentally, has played a crucial role in understanding the nature of the fundamental strong force and its degrees of freedom. The rich spectra of physical hadrons for light quarks provided us with a framework for constructing the theory of strong interaction starting from eightfold way to quarks-partons as the fundamental degrees of freedom. The discovery of the heavier hadron, J/ψ meson, and the subsequent discoveries of other charmonia put this framework on solid footing. The discovery of J/ψ meson triggered so huge scientific interest that it was termed as the *November revolution*.

From a mere mathematical construct, the concept of quarks became reality. The charm quark being heavier in mass, the approximation that the charm quark and anti-quark are non-relativistic were found to be good for many predictions. Studies on various energy splittings provided crucial information on heavy quark-antiquark potential, hyperfine and spin-orbit interactions, etc. The ground state charmonia, J/Ψ and η_c, gave an excellent example of a kind of hydrogen atom of strong interactions, which revealed the quark layer of substructure for hadrons. Potential models, consisting of non-relativistic quark kinetic energy, a central confining potential, and spin-dependent interaction terms were found to be very successful in explaining various observed states. Recently, a tower of heavy hadron states, including the X's, Y's and Z's, have been discovered with unusual properties [2]. These discoveries have rejuvenated the heavy hadron spectroscopy tremendously and offer a bright promise in detailed understanding of various interesting aspects of the theory of strong interaction.

While the heavy quarkonia and other heavy flavored mesons have been studied quite extensively, the heavy baryon physics has received substantially less attention, even though they can provide similar insight in understanding the strong interaction. Just as the quark-antiquark interactions are examined in charmonia, these studies can probe the interactions between multiple heavy quarks and heavy quarks with one or more lighter quarks. Various spin dependent splittings between baryons can provide information to constrain spin dependent potential terms which are crucial to build successful Non-Relativistic QCD (NRQCD), pNRQCD and similar models. Experimentally only a handful of charm baryons have been discovered and a reliable determination of the quantum number of most of the observed states has not been made [2]. Only very recently have a few excited singly charm baryons been observed and the discovery status of the doubly charm baryons remains unsettled. While the SELEX experiment observed doubly charm $\Xi_{cc}(ccu)$ baryons [3], these have not been confirmed either by BABAR [4] or Belle [5]. Along with the well-established triply flavored $\Delta(uuu)$ and strange $\Omega(sss)$ baryons, QCD predicts similar states built from charm quarks, the triply charm baryon, Ω_{ccc}. Such a state is yet to be observed. This could be because of the large energy threshold required for their production via either resonant or continuum production mechanisms, their very short lifetime and the very low reconstruction efficiency for the highly excited heavy hadron resonances, which follows cascade decays into multi-particle final states. The extremely low production rate hinders the identification of the spin-parity quantum numbers, even though the partial wave analysis is relatively simpler in heavy hadrons in comparison with the light hadron spectra. However, it is expected that the large sta-

tistical sample collected at the LHCb experiment, the PANDA experiment at the FAIR facility, Belle II at KEK and BES III may be able to provide some information on charm baryons.

On the theoretical side, one expects that potential models will be able to describe, charm baryons [6, 7, 8], in particular the triply charm baryons, to a similar level of precision as their success in charmonia. The triply charm baryons may provide a new window for understanding the structure of baryons, as pointed out by Bjorken several years ago [9]. The spectra of charm baryons have been studied theoretically [6, 7, 8] using non-relativistic potential models and various improvised versions of that.

QCD, like other quantum field theories, needs to be regularized. Regularization using a lattice discretization of space-time (known as lattice QCD) has the advantage that one can use numerical techniques to access the non-perturbative aspects of QCD. A quantitative description of the spectra of the charm baryons using rigorous ab-initio computations like lattice QCD are important for a number of reasons. Firstly, all the estimates of physical states from these calculations will be predictions and thus can naturally provide crucial inputs to the future experimental discovery. Secondly, lattice results can provide a guide in identifying unknown quantum numbers (spin-parity) of the discovered states, based on what one expects from QCD. Moreover, it will be interesting to compare the low lying spectra of charm baryons computed from a first principles method to those obtained from potential models which have been very successful for charmonia. It is expected that more information about interactions between multiple charm quarks and, charm quark and light quarks can be obtained by computing the excited state spectra of charm baryons, including in particular the spin-dependent energy splittings.

The success of lattice QCD calculations in light hadron spectroscopy is well documented, e.g. Ref. [10, 11, 12, 13, 14]. There were quite a few successful heavy hadron spectroscopic studies, for mesons, e.g. [15, 16, 17, 18, 19, 20, 21], and for baryons, e.g. [22, 23, 24, 25, 26, 27, 28, 29], but they were limited only to the ground state determinations. In spite of all these motivating results from lattice QCD, estimation of excited state spectrum remained a major challenge till last 7-8 years. Invention of novel smearing techniques called distillation [30] and the proper utilization of fitting techniques, such as the generalized eigenvalue method [31, 32], along with the derivative based operator construction formalism [33, 34], boosted the hadron spectroscopic studies, facilitating the determination of the excited state spectra [34, 35, 36, 37, 38].

The major part of this synopsis consists of spectroscopy of charm baryons using two complementary non-perturbative approaches. The first, which constitutes the major part,

employs these novel techniques mentioned above, enabling us to extract a tower of spin identified excited states for all charm baryons. Using an anisotropic lattice with very fine temporal resolution and a large set of carefully constructed interpolating operators, we study the ground as well as the excited states of charm baryons with one or more valence charm quark content for each spin-parity channel up to spin 7/2. We also computed several energy splittings, for example, hyperfine as well as spin-orbit splittings between various states. The results on these studies were reported in Ref. [39].

In the above mentioned work, we used the tree level tadpole improved clover action with no $\mathcal{O}(ma_t)$ and $\mathcal{O}(ma_s)$ errors. We have not addressed other higher order terms, as the temporal lattice spacing is quite small. We also do not make a quantitative study of $\mathcal{O}(m^2a_s^2)$ errors. However, to study the charm physics, it is essential to have an action with discretization errors as small as possible. Another caveat in the above study is that the clover action does not have chiral symmetry at finite lattice spacing, *i.e.*, we have not addressed the effects of chiral symmetry on observables. Keeping these caveats in mind, confronting this study with a totally different non-perturbative approach, having better control over the systematics, will be a good check to validate the smallness of systematic corrections in the above results.

Hence to complement the above work, we performed another non-perturbative calculation of the low lying spectra using overlap valence quarks in the background of a large set of 2+1+1 flavors dynamical configurations generated with the one-loop, tadpole improved Symanzik gauge action and the highly improved staggered quark (HISQ) fermion action [40, 41]. By adopting such a mixed action approach, one can get advantage of the chiral symmetry and low quark mass limit of overlap fermions, and the advantage of having a large set of configurations with small discretization errors as well as small taste breaking effects. One also gets the advantage of simulating both light, strange as well as heavy fermions on the same lattice formalism with chiral fermions having no $\mathcal{O}(a)$ errors. With the above formulation we have calculated the ground state spectra of various charm hadrons and have made a comparative study between these two projects along with other results from literature where available. Agreement between these results from different approaches gives confidence in our estimates. The results from these studies were reported in Ref. [27].

In the third work, we performed a finite temperature analysis of hadronic screening correlators [42], with main focus on the baryon sector. The question is what are the degrees of freedom that exist in a QCD medium at finite temperature and how they are modified across the crossover / transition temperature. These can be answered by study-

ing the static correlation lengths in a QCD medium in thermal equilibrium. In this work, we focused on the static spatial correlations in the equilibrium thermodynamic system for probes with mesonic and baryonic quantum numbers. We performed simulations of pure gauge theory for three different temperatures across the transition temperature and studied screening correlators for mesonic and nucleonic resonances with clover fermions.

0.2 Lattice methodology in excited state spectroscopy

Lattice QCD is the first principles non-perturbative numerical technique widely used in determining the QCD observables. Introduced by Kenneth Wilson in 1974 [43], it regularizes the theory by discretizing the Euclidean space-time and representing QCD Lagrangian on a finite size lattice. Expectation values of the QCD observables can be expressed as path integrals which can be directly evaluated with controlled systematics using Monte Carlo methods.

Lattice computations of hadron masses proceed through the calculations of the Euclidean two point correlation functions, C_{ji}, between creation operators, $\bar{O}_i$, at time t_i and annihilation operators, O_j, at time t_f.

$$C_{ji}(t_f - t_i) = \langle 0|O_j(t_f)\bar{O}_i(t_i)|0\rangle = \sum_n \frac{Z_i^{n*} Z_j^n}{2m_n} e^{-m_n(t_f - t_i)} \tag{1}$$

The RHS is the spectral decomposition of such two point functions, where the sum is over a discrete set of states, n, with energies, m_n. $Z^n = \langle 0|O_i|n\rangle$ is the vacuum state matrix element, also called an overlap factor. In general, the calculation of hadronic masses by lattice QCD methods takes place by performing non-linear exponential fits to the long distance tail of these two point correlators, where only the ground state contribution dominates.

The goal of this work is to calculate the ground as well as the higher excited state spectra of charm baryons. However, one encounters several problems while extracting the masses of these states by using the naïve method as mentioned. The first major hurdle in charm hadron spectroscopy is attributed to the heavyness of the charm quark. One needs to use a very fine lattice so that the $m_c a << 1$ to keep discretization error as small as possible. Moreover, the physical states comprised of valence charm quarks are quite heavy and their temporal correlation functions decay increasingly rapidly in the Euclidean time with increase in the energy of the resonances, while the noise behaves in the same

manner as in the ground state. Hence the signal-to-noise ratio in the correlators of these states exhibits increasingly rapid degradation in Euclidean time with increasing energy. A remedy of these problems is to use an anisotropic lattice, as discussed in Section 0.2.1. Another difficulty is in the extraction of multiple excited states from a single correlator using a reliable non-linear fitting method. One way to get away with this issue is to use correlation functions for multiple interpolators as well as to use a better analysis method to extract excited states from them reliably. A careful construction of large basis of interpolating operators that could overlap strongly with the desired excited states is crucial for this purpose. In Section 0.2.2, we discuss the construction of a large basis of interpolating operators and the novel smearing technique that provides an efficient method to compute the two point correlation functions. In addition to the operator construction, the extraction of the physical states with correct quantum numbers from correlation functions of such large basis of operators, relies on a good analysis procedure. In Section 0.2.2, we discuss the variational fitting method that we have used to extract the spectrum of baryon states from matrix of correlation functions using such large basis of operators. A reliable identification of the spin-parity quantum numbers of a state is highly non-trivial on a finite lattice. However, it is possible to identify these quantum numbers on lattices with even single lattice spacing using the overlap factors as described in Section 0.2.2 [32].

0.2.1 Anisotropic lattice

A possible solution for the issues related to discretization error as well as the rapid decay of the temporal correlations is to increase the temporal resolution by adopting a finer lattice spacing along the Euclidean time direction while keeping the spatial lattice constants same, so that one can avoid the computational cost that would come from reducing the spacing in all directions[44, 45]. In this work, we adopt such an anisotropic dynamical lattice formulation to extract the highly excited charm baryon spectra.

We used the anisotropic $N_f = 2 + 1$ flavor dynamical gauge configurations generated by the Hadron Spectrum Collaboration (HSC) with clover improved Wilson fermions for both sea and valence quarks. The gauge field sector utilized the tree-level Symanzik-improved gauge action, while the fermion sector used an anisotropic Shekholeslami-Wohlert fermion action with tree-level tadpole improvement and three-dimensional stout-link smearing of gauge fields. More details of the formulation of actions as well as the techniques used to determine the anisotropy parameters can be found in Refs. [45, 46].

Lattice size	$a_t m_\ell$	$a_t m_s$	N_{cfgs}	m_K/m_π	m_π/MeV	$a_t m_\Omega$
$16^3 \times 128$	-0.0840	-0.0743	96	1.39	391	0.2951(22)

Table 1: Properties of the gauge-field ensembles used. N_{cfgs} is the number of gauge-field configurations.

The lattice action parameters of the gauge-field ensembles used in this work are given in Table 3.1. The temporal lattice spacing a_t was determined using the Ω-baryon mass measured on these ensembles [46]. This leads to $a_t^{-1} = 5.67(4)$ GeV. On this lattices we find $m_c a_t << 1$, which assures the use of these lattice to study the charm physics. With an anisotropy close to 3.5, $a_s = 0.12$ fm. This gives a spatial extent of about 1.9 fm, which would be sufficient to study charm baryons, in particular doubly and triply charm baryons.

The details of the charm quark action used in this study are given in Ref. [37]. The action parameters for the charm quark are obtained by ensuring that the mass of the η_c meson takes its physical value and its dispersion relation at low momentum is relativistic. It is expected that the effects due to the absence of dynamical charm quark fields in this calculation will be small, as the disconnected diagrams are OZI suppressed.

0.2.2 Construction of baryon operators

In this section, we briefly discuss the construction of baryon interpolating operators using up to two derivatives, such that they project up to $J = \frac{7}{2}$ states with both even and odd parities. The construction has been detailed in [34]. Hence in this synopsis, we discuss only the basics and the essentially different part from that in Ref. [34], which are the flavor structures. The details about the construction of the operators used for the study also provides insight into the results obtained from the numerical studies.

The methodology involves first constructing a basis of baryon interpolating operators in the continuum with well-defined continuum spin-parity quantum numbers. These continuum operators are then subduced/reduced to the irreducible representations (irrep) of the octahedral group on the lattice. The correlation functions, constructed out of these octahedral operators, are expected to show rotational symmetry breaking artefacts in these calculations due to the reduced symmetry on a lattice. However, we see an effective rotational symmetry from the primary spin identification tests and that the symmetry breaking effects are very small.

Continuum baryon interpolating operators

All hadrons are color singlet objects and thus they form totally anti-symmetric combinations in the color indices of its constituents. Since baryons are fermions made of three quarks, their interpolating operators excluding the color part should be totally symmetric combinations of all the quark labels representing flavor, spin and the spatial structure. The overall flavor-spin-spatial structure of a continuum baryon interpolating operator with quantum numbers, J^P, can be decomposed into a combination as

$$O^{[J^P]} = [\mathcal{F}_{\Sigma_F} \otimes \mathcal{S}_{\Sigma_S} \otimes \mathcal{D}_{\Sigma_D}]^{J^P}, \tag{2}$$

where $\mathcal{F}$, $\mathcal{S}$ and $\mathcal{D}$ are flavor, Dirac spin and spatial projection operators respectively and the subscripts stands for the symmetry in the respective subspaces. For every baryon operator, we must combine the symmetry projection operators such that the resulting baryon operator, excluding the color part, is overall symmetric.

Flavor symmetry structures

With only three different flavors simultaneously possible, the flavor wave functions of the charm baryon operators can be constructed to be members of $SU(3)_F$ multiplets as $3 \otimes 3 \otimes 3 = 10_S \oplus 8_{MS} \oplus 8_{MA} \oplus 1_A$, where S, MS, MA and A stands for Symmetric, Mixed-Symmetric, Mixed-Antisymmetric and Antisymmetric constructions. These represent a subset of states from the larger group of $SU(4)_F$ which has a decomposition based on symmetry considerations as $4 \otimes 4 \otimes 4 = 20_S \oplus 20_{MS} \oplus 20_{MA} \oplus 4_A$. Table 3.2 contains the details of the flavor symmetry constructions possible for various charm baryons.

For the spin and spatial parts also, we construct similar symmetry structures.[1] For the spatial symmetry structures we considered operators that include up to two derivatives. Totally symmetric constructions in flavor-spin-spatial indices from combinations of these flavor symmetry structures and the symmetry structures in the spin and the spatial parts forms the desired local and non-local charm baryon interpolating operators [34].

Only a subset of operators that are formed purely from the upper two components of the Dirac spinor, in Dirac-Pauli representation, appear at a leading order velocity expansion and hence are referred to as "non-relativistic". All other operators other than this subset is referred to as "relativistic". Using non-relativistic components alone, it is not possible to construct a negative parity state with a spin higher than 5/2, even

[1] The details about the spin-spatial symmetry structures are omitted for the sake of space.

20_M					
	I	I_z	S	$\mathcal{F}_{MS}$	$\mathcal{F}_{MA}$
Λ_c^+	0	0	0	$\frac{1}{\sqrt{2}}(\lvert cud\rangle_{MS} - \lvert udc\rangle_{MS})$	$\frac{1}{\sqrt{2}}(\lvert cud\rangle_{MA} - \lvert udc\rangle_{MA})$
Σ_c^{++}	1	+1	0	$\lvert uuc\rangle_{MS}$	$\lvert uuc\rangle_{MA}$
Σ_c^{+}	1	0	0	$\lvert ucd\rangle_{MS}$	$\lvert ucd\rangle_{MA}$
Σ_c^{0}	1	−1	0	$\lvert ddc\rangle_{MS}$	$\lvert ddc\rangle_{MA}$
$\Xi_c^{\prime +}$	$\frac{1}{2}$	$+\frac{1}{2}$	−1	$\lvert ucs\rangle_{MS}$	$\lvert ucs\rangle_{MA}$
$\Xi_c^{\prime 0}$	$\frac{1}{2}$	$-\frac{1}{2}$	−1	$\lvert dcs\rangle_{MS}$	$\lvert dcs\rangle_{MA}$
Ξ_c^{+}	$\frac{1}{2}$	$+\frac{1}{2}$	−1	$\frac{1}{\sqrt{2}}(\lvert cus\rangle_{MS} - \lvert usc\rangle_{MS})$	$\frac{1}{\sqrt{2}}(\lvert cus\rangle_{MA} - \lvert usc\rangle_{MA})$
Ξ_c^{0}	$\frac{1}{2}$	$-\frac{1}{2}$	−1	$\frac{1}{\sqrt{2}}(\lvert cds\rangle_{MS} - \lvert dsc\rangle_{MS})$	$\frac{1}{\sqrt{2}}(\lvert cds\rangle_{MA} - \lvert dsc\rangle_{MA})$
Ω_c^{0}	0	0	−2	$\lvert scs\rangle_{MS}$	$\lvert scs\rangle_{MA}$
Ξ_{cc}^{++}	$\frac{1}{2}$	$+\frac{1}{2}$	0	$\lvert ccu\rangle_{MS}$	$\lvert ccu\rangle_{MA}$
Ξ_{cc}^{+}	$\frac{1}{2}$	$-\frac{1}{2}$	0	$\lvert ccd\rangle_{MS}$	$\lvert ccd\rangle_{MA}$
Ω_{cc}^{+}	0	0	−1	$\lvert ccs\rangle_{MS}$	$\lvert ccs\rangle_{MA}$

20_S				
	I	I_z	S	$\mathcal{F}_S$
Σ_c^{++}	1	+1	0	$\lvert uuc\rangle_S$
Σ_c^{+}	1	0	0	$\lvert ucd\rangle_S$
Σ_c^{0}	1	−1	0	$\lvert ddc\rangle_S$
Ξ_c^{+}	$\frac{1}{2}$	$+\frac{1}{2}$	−1	$\lvert ucs\rangle_S$
Ξ_c^{0}	$\frac{1}{2}$	$-\frac{1}{2}$	−1	$\lvert dcs\rangle_S$
Ω_c^{0}	0	0	−2	$\lvert ssc\rangle_S$
Ξ_{cc}^{++}	$\frac{1}{2}$	$+\frac{1}{2}$	0	$\lvert ccu\rangle_S$
Ξ_{cc}^{+}	$\frac{1}{2}$	$-\frac{1}{2}$	0	$\lvert ccd\rangle_S$
Ω_{cc}^{+}	0	0	−1	$\lvert ccs\rangle_S$
Ω_{ccc}^{++}	0	0	0	$\lvert ccc\rangle_S$

4_A				
	I	I_z	S	ϕ_A
Λ_c^{+}	0	0	0	$\lvert udc\rangle_A$
Ξ_c^{+}	$\frac{1}{2}$	$+\frac{1}{2}$	−1	$\lvert ucs\rangle_A$
Ξ_c^{0}	$\frac{1}{2}$	$-\frac{1}{2}$	−1	$\lvert dcs\rangle_A$

Table 2: Flavor symmetry structures for charm baryons. I in the first column stands for the isospin, I_z in the second column is for the third component of isospin and S in the third column is for the strangeness.

with operators that include two derivatives. Use of relativistic operators along with non-relativistic ones enables us to extract states with spin up to 7/2 for both the parities. A subset of operators constructed using two derivatives and projected onto $L = 1$ orbital angular momentum with MS/MA, are proportional to the field strength tensor and are zero in a theory without gauge fields. These operators are identified as hybrid operators. Account of the orbital motion classifies the total symmetry in a non-relativistic approach with 3 flavors to be $SU(6) \otimes O(3)$ super-multiplets with the $O(3)$ describing the orbital motion. With four component Dirac spinors, the actual construction of the operators corresponds to $SU(12) \otimes O(3)$.

Subduction into lattice irreps

Ω_{ccc}	G_1		H		G_2	
S_F	g	u	g	u	g	u
Total	20	20	33	33	12	12
Hybrid	4	4	5	5	1	1
NR	4	1	8	1	3	0

(b)

Ξ_{cc}, Ω_{cc}	G_1		H		G_2	
$(S_F + M_F)$	g	u	g	u	g	u
Total	55	55	90	90	35	35
Hybrid	12	12	16	16	4	4
NR	11	3	19	4	8	1

(a)

	Σ_c, Ω_c $(S_F + M_F)$						Λ_c $(M_F + A_F)$						Ξ_c $(S_F + M_F + A_F)$					
	G_1		H		G_2		G_1		H		G_2		G_1		H		G_2	
	g	u	g	u	g	u	g	u	g	u	g	u	g	u	g	u	g	u
Total	55	55	90	90	35	35	53	53	86	86	33	33	116	116	180	180	68	68
Hybrid	12	12	16	16	4	4	12	12	16	16	4	4	24	24	32	32	8	8
NR	11	3	19	4	8	1	10	3	17	4	7	1	23	6	37	8	15	2

(c)

Table 3: The number of lattice operators for different charm baryons obtained after subduction to various irreps from continuum operators with up to two covariant derivatives. The number of non-relativistic (NR) and hybrid operators for each irreps and for both even (g) and odd (u) parities are given.

In lattice QCD computations, one considers the theory in a discretized four dimensional Euclidean hyper-cubic box. The hyper-cubic lattice does not possess the full symmetry of the continuum. Thus, in a lattice calculation, the states at rest are classified not according to the continuum spin (J,J_z), but rather according to the irreps of a cube. There are eight irreps of the double-valued representations of the octahedral group (O_h), named as A_1, A_2, E, T_1 and T_2 for the integer spins, and G_1, G_2 and H representing the half-integer spins. For baryons, there are four two-dimensional irreps corresponding to G_1, G_2 (two for each parity) and two four dimensional representations for H. The G_1 irrep contains $J = \frac{1}{2}, \frac{7}{2}, \frac{9}{2}, \frac{11}{2}, ...$ states, the G_2 irrep contains $J = \frac{5}{2}, \frac{7}{2}, \frac{11}{2}, ...$ states while H irrep has $J = \frac{3}{2}, \frac{5}{2}, \frac{7}{2}, \frac{9}{2}, ...$ states. One needs to examine the degeneracy patterns across the different O_h irreps to reliably deduce continuum-limit spins J of these states which will be discussed later. Mathematically this subduction of continuum spin to lattice irreps can be expressed as,

$$\Omega^J{}_{n\Lambda,r} = \sum_m \mathcal{S}^{J,m}_{\ n\Lambda,r}\ \Omega^J_m, \tag{3}$$

where $\Omega^{J}{}_{{}^{n}\Lambda,r}$ is the lattice operator representing the r^{th} row of the n^{th} embedding of the irrep Λ on the continuum spin J, subduced from a continuum spin operator Ω^{J}_{m}. The $\mathcal{S}^{J,m}_{{}^{n}\Lambda,r}$ are called the subduction coefficients. Table 3 shows the total number of relativistic and non-relativistic operators constructed based on eq. (3.15) for various charm baryons. It also contains the number of non-relativistic and hybrid operators constructed for various charm baryons.

The complexity of these operators is evident from this example. A continuum Ω_{ccc} operator with spin and parity of the three quarks as $\frac{3}{2}^{-}$ in the first embedding of mixed-symmetry Dirac spin constructions and with two derivatives coupled into $L = 2$ with a mixed-symmetric spatial part and total spin and parity $J^P = \frac{7}{2}^{-}$, is denoted as $\left(\Omega_{ccc,S} \otimes (H_{u,1,M}) \otimes D^{[2]}_{L=2,M}\right)^{J^P=\frac{7}{2}^{-}}$. On the lattice this operator gets subduced once over G_{1u}, G_{2u} and H_u.

Distillation

Having constructed a large set of operators it is possible to calculate their diagonal and off-diagonal correlation functions to extract excited states by using variational methods. However, construction of correlation functions with so many operators, particularly for the operators with one or more derivatives, is very computationally intensive as it needs one inversion for each non-local source. The total time needed for the construction of correlation function could be as intensive as gauge field generations. To avoid this we use a recently developed novel technique, called the "*distillation method*" [30]. Using this method, one can efficiently construct a large number of correlation functions with multiple operators. Moreover, this method automatically includes a smearing process, a requirement for suppressing the high frequency modes that do not contribute significantly to the low energy regime in the spectrum and thus increases the relative contributions from the low lying states in the correlation functions.

In the distillation method one uses a smearing operator which is a projection operator constructed by outer product over the low lying eigenmodes of the discretized gauge-covariant Laplacian, ∇^2, as

$$\Box_{xy}(t) = V_{xz}(t)V^{\dagger}_{zy}(t) = \sum_{k=1}^{N_{vecs}} \xi^{(k)}_{x}(t)\xi^{(k)\dagger}_{x}(t), \tag{4}$$

where $\xi^{(k)}_{x}$ are N_{vecs} number of eigenvectors, sorted by the eigenvalues, of ∇^2 evaluated

on the background of spatial gauge fields of the time slice t. The number of these modes, N_{vecs} (volume dependent), should be sufficient to sample the required angular structure of the low lying hadronic states, but is small compared to the number of sites on a time slice. When N_{vecs} is the same as the number of sites on a time-slice, then the distillation operator becomes identity, and the fields acted upon are unsmeared. The computational cost is highly reduced because inversions need to be performed in a smaller space of Dirac spin and distillation vectors, with dimensionality $4 \times N_{vecs}$. A factorization of the correlation function in terms of the eigenvectors of the Laplacian allows efficient computation of correlation functions with a large basis of interpolating operators at both the source and the sink time slices. Furthermore, this factorization also enables a momentum projection at both the source and the sink time slices, in contrast with what is possible in conventional spectroscopy. In this work, we used $N_{vecs} = 64$. It can be shown that the correlation functions constructed using the distilled fields have same symmetry properties on the lattice as those constructed using the Laplacian methods.

Variational fitting technique

Once we construct the matrix of two point correlation functions, $C_{ij}(t)$, for each lattice irrep, we extract the energies and overlaps of the physical states over the interpolating operators by solving a generalized eigenvalue problem of the form,

$$C_{ij}(t)v_j^n = \lambda^n(t, t_0)C_{ij}(t_0)v_j^n, \tag{5}$$

where an appropriate reference time-slice t_0 is selected following the description as in Ref. [31]. The energies of the physical states are extracted by fitting the $t - t_0$ dependence of the eigenvalues, λ^n, called the principal correlators and the overlaps being determined from the eigenvectors, v_j^n. The principal correlators are fit using a double exponential form

$$\lambda_\alpha(t) = e^{-m_\alpha(t-t_0)}(1 + \mathcal{O}(e^{-|\delta m|(t-t_0)})), \tag{6}$$

where m_α is the mass of a state labeled by α and δm is the energy splitting from the nearest excited state to α.

One main goal, which is a highly non-trivial task, in these lattice calculations is to ensure that any state identified can be assigned continuum quantum numbers in a reliable way. To identify the spin of a state we followed the same method detailed in Ref. [32] and used in the calculations of light baryons [34, 35], light mesons [36], charm mesons

as well as heavy-light mesons [37]. The main ingredient is the overlap factor, Z_i^n, as defined in eq. (1). However, spin-$\frac{5}{2}$ and spin-$\frac{7}{2}$ states appear in multiple lattice irreps. In these cases, the continuum operator is subduced to multiple lattice irreps. In the continuum limit, for a given physical state, the overlap factors obtained from different operators, which are subduced from the same continuum operators should become equal. They should nearly be equal even on a finite lattice, if the rotational symmetry breaking effects are small. Hence in order to confirm the reliability of the identification of a state with a given spin $> 3/2$, one has to compare the magnitudes of overlap factors of those operators which are subduced into different irreps. After identification of the spin of states with matching overlap factors, it is also necessary to check whether the energy of this state also matches over the irreps. Once this is made, one needs to do simultaneous fitting of its masses over the irreps to get the final mass.

0.3 RESULTS : Excited state spectroscopy of charm baryons

In this section, we present our results on spectra of charm baryons with spins up to $\frac{7}{2}$ and for both parities. Various spin dependent energy splittings between the extracted states are also considered and compared with the similar splittings at light, strange as well as bottom quark masses. We present our results in terms of energy splittings relative to a reference hadron rather than their absolute energies. This reduces the systematic uncertainties associated with charm quark mass determination as well as the with the discretization errors.

0.3.1 Triply charm baryons

In Figure 1(a), we present relativistic spectra of the triply charm baryons in terms of the energy splittings from the mass of the pseudoscalar charmonium, η_c, which is made of a charm and an anti-charm quarks. A factor of $\frac{3}{2}$ is multiplied with η_c mass to balance the different number of valence charm quarks in triply charm baryon and η_c. Boxes with the thick borders correspond to those states with a greater overlap onto operators proportional to the field strength tensor as discussed in the previous section, which might consequently be hybrid states. The states inside the magenta ellipses have relatively large overlap with the non-relativistic operators. The number of states inside

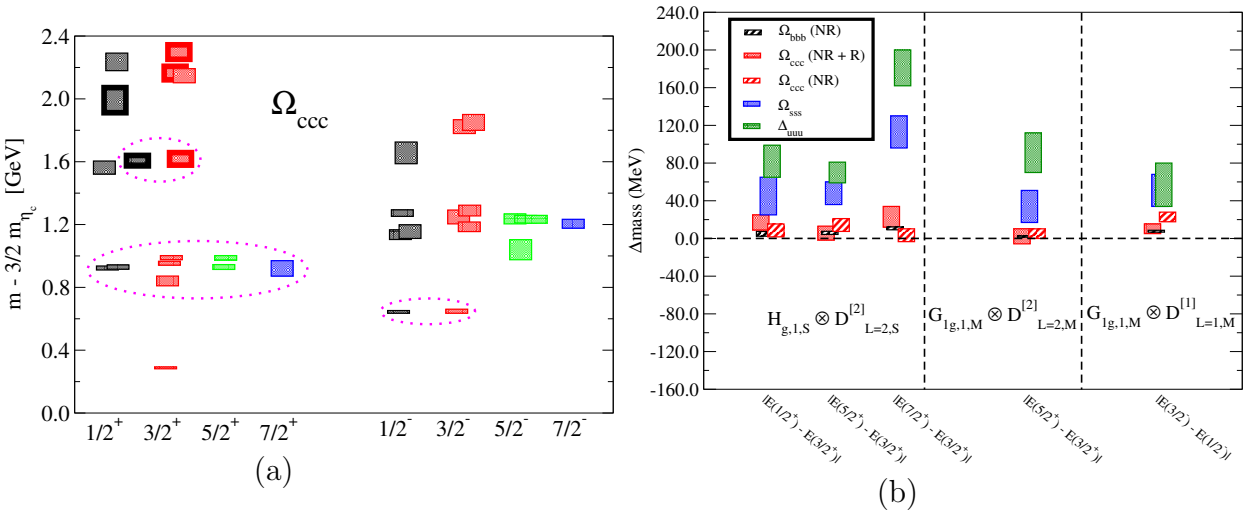

Figure 1: (a) Spin identified spectra of triply charm baryons with respect to $\frac{3}{2}m_{\eta_c}$. The boxes with thick borders corresponds to the states with strong overlap with hybrid operators. The states inside the magenta ellipses are those with relatively large overlap to non-relativistic operators. (b) Energy splittings between states with same L and S values, starting from light to heavy baryons. The details are described in the Section 0.3.1.

these ellipses are also the number of states expected based on a quark model with only non-relativistic quark spins. This agreement of the pattern of low lying states between the lattice spectra obtained in this work and from non-relativistic quark model implies a clear signature of $SU(6) \times O(3)$ symmetry in the low-lying spectra. It is to be noted that though we used non-relativistic as well as relativistic operators, the low-lying spectra resembles with the non-relativistic spectra. Such $SU(6) \times O(3)$ symmetric nature of spectra was also observed for light baryons in Ref. [35]. However, it is not meaningful to interpret the higher excited states in terms of $SU(6) \times O(3)$ symmetry [35] since we did not include non-relativistic operators with three derivatives. For negative parity, it is not possible even to identify a state with strong hybrid content because it is unclear how the relative importance of all the relevant operators overlapping to that state will change in the presence of non-relativistic operators having three or more derivatives.

Energy splittings

Spin-dependent splittings, such as the hyperfine and spin-orbit splittings between hadrons, can provide important information about the interquark interaction which are necessary to build a successful model. Here we also calculated those splittings of triply charm

baryons and compare those with such splittings of similar baryons at other quark masses. Among the states that we extract in our calculations, several of them have the same L and S values, but with different J values. For example, we construct flavor (F) decuplet states with $D = 2, S = \frac{3}{2}$ and $L = 2$ with the combination $\{10F_S \otimes (S)_S \otimes (D)_S\}$, where S in the subscript stands for symmetric combinations. In this construction, we get four operators with $J^P = \frac{1}{2}^+, \frac{3}{2}^+, \frac{5}{2}^+$ and $\frac{7}{2}^+$. In the heavy quark limit, the spin-orbit interaction vanishes since the interaction term is inversely proportional to the square of the quark mass. States corresponding to quantum numbers ($|L, S, J^P\rangle \equiv |2, \frac{3}{2}, \frac{1}{2}^+\rangle, |2, \frac{3}{2}, \frac{3}{2}^+\rangle, |2, \frac{3}{2}, \frac{5}{2}^+\rangle$ and $|2, \frac{3}{2}, \frac{7}{2}^+\rangle$) will thus be degenerate in the heavy quark limit. Similarly, two states with quantum numbers $J^P = \frac{1}{2}^-$ and $\frac{3}{2}^-$ with $L = 1$ and $S = \frac{1}{2}$ will also be degenerate in the heavy quark limit. In Figure 1(b), we plot absolute values of energy differences between energy levels which originate from the spin-orbit interaction of the following $(L\,, S)$ pairs : $(2,\frac{3}{2}$ –in the left column), $(2,\frac{1}{2}$ –in the middle column) and $(1,\frac{1}{2}$ –in the right column). We plot these spin-orbit energy splittings at various quark masses corresponding to following triply flavored baryons : Δ_{uuu}, Ω_{sss}, Ω_{ccc} and Ω_{bbb}. We identify the states with these (L, S) pairs by finding the operators which incorporate these pairs and have major overlaps to these states. These energy differences are obtained from the ratio of jackknifed correlators, which in general, reduce error bars by canceling correlation between these correlators. For bottom baryons, we use data from Ref. [47] and for light and strange baryons, results from Ref. [35] are used. One can observe that the degeneracy between these states is more or less satisfied both for bottom and charm quarks, justifying a heavy quark status for charm and bottom quarks. However, data with higher statistics are necessary to identify the breaking of this degeneracy at charm quark mass.

We also made similar comparisons for some other energy splittings using our results and similar results at other quark masses. Some of these, such as the hyperfine splitting, vanish in the heavy quark limit while others become constant. However, as expected, most splittings tend to be higher at lighter quark masses where relativistic effects are prominent. As an example, we consider following splittings: $m_{\Delta_{uuu}} - \frac{3}{2}\, m_{\omega_{\bar{u}u}}\,, m_{\Omega_{sss}} - \frac{3}{2}\, m_{\phi_{\bar{s}s}}\,, m_{\Omega_{ccc}} - \frac{3}{2}\, m_{J/\psi_{\bar{c}c}}$ and $m_{\Omega_{bbb}} - \frac{3}{2}\, m_{\Upsilon_{\bar{b}b}}$. For $\Delta^{++}(uuu)$ and Ω_{sss} baryons, results are from Ref. [35], while for Ω_{bbb}, we use results from Ref. [47]. These splittings mimic the binding energies of triply flavored states and thus it is interesting to compare these as a function of quark masses. One can expect that, in the heavy quark limit, the quark mass dependence of these splittings can be expressed is a form $a + b/m_{PS}$. We observe such quark mass dependence starting from strange to bottom quarks. This validates the

heavy quark expansion for these splittings, particularly for charm and bottom quarks.[2]

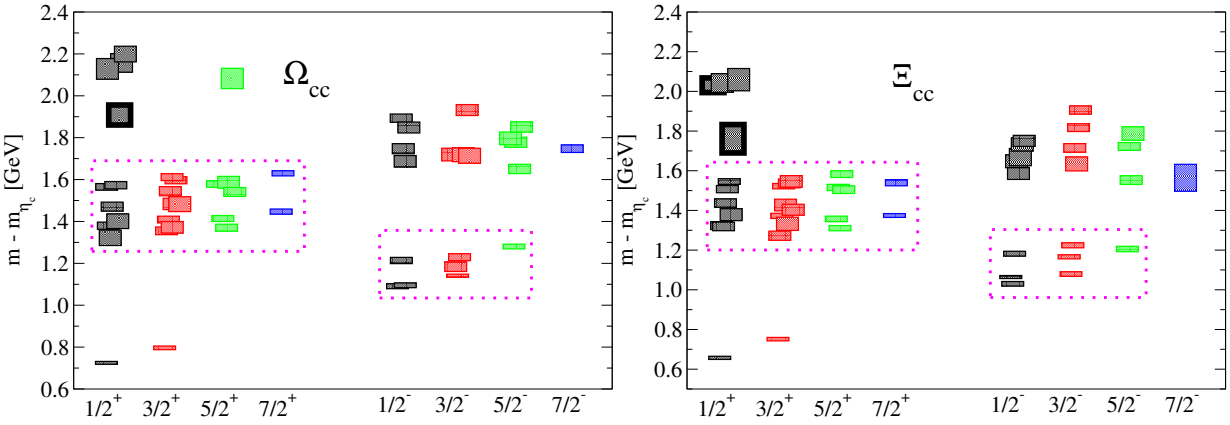

Figure 2: Spin identified spectra of doubly charm baryons, a) Ω_{cc} and b) Ξ_{cc}, with respect to m_{η_c}. States with strong overlap with operators that are proportional to field strength tensor are painted with thick borders. While the low lying bands showing the pattern of states as expected from an $SU(6) \otimes O(3)$ potential model are highlighted by enclosing them within magenta closed curves.

0.3.2 Doubly charm baryons

The study of doubly charm baryons is important as these systems provide a unique opportunity to get insight into the nature of strong force in the presence of slow relative motion of the heavy quarks along with the relativistic motion of a light quark. The excited spectra and the splittings between different energy levels will help to understand how the collective degrees of freedom give rise excitations of these systems. A comparison of their excitations with the corresponding spectra of singly and triply charm baryons, where the number of charm quark is one less and more respectively, will be helpful to get information about quark-quark interactions. Doubly charm baryons are characterized by two widely separated scales: the low momentum scale, of order Λ_{QCD}, of the light quark and the relatively heavy charm quark mass. A doubly heavy baryon can be treated as a bound state of a heavy antiquark and a light quark in the limit when the typical momentum transfer between the two heavy quarks is larger than Λ_{QCD} [48]. In this limit of quark-diquark symmetry, $QQq \leftrightarrow \bar{Q}q$, one can get definite prediction of spin dependent energy splittings [49]. It is thus interesting to study those spin splittings to check whether charm quark is heavy enough to respect this quark-diquark symmetry.

[2]The details have been skipped to save space.

All previous lattice calculations involve only the ground state spectrum of Ξ_{cc}, Ξ^*_{cc}, Ω_{cc} and Ω^*_{cc}. However, it is expected that much more information about the interactions between two charm quarks and between charm and light quarks can be obtained by computing the excited state spectra of these baryons, including in particular the spin-dependent energy splittings, as well as by studying similar spectra for other spin-parity channels. Towards this goal, in this work, we make the first attempt to compute the excited state spectra of doubly charm baryons by using dynamical lattice QCD. The ground states for each spin-parity channel as well as their excited states up to spin 7/2 are computed and a few spin-dependent energy splittings are studied.

In Figure 2 we present the relativistic spectra of the doubly charm baryons, $\Omega_{cc}(ccs)$ and $\Xi_{cc}(ccu)$, in terms of the energy splittings from the mass of η_c meson, which has the same valence charm quark content. Even here, the number and the pattern of states in the lowest negative parity band and the first excitation band in the positive parity (magenta boxes in Figure 2) can be seen to be well in agreement with the expectations based on $SU(6) \otimes O(3)$ symmetry, which assumes non-relativistic nature for quarks. As before, the states with significant overlap with the operators proportional to the field strength tensor are shown with thick borders, and are identified to be strongly hybrid in nature.

Similar to the case of triply charm baryons, we estimate spin-dependent energy splittings, including hyperfine splittings, for doubly charm baryons, and then study the quark mass dependence of some of those energy splittings. For some cases, we observe that the quark mass dependence can also be fitted with a heavy quark inspired form $a + b/m_{PS}$. From such quark mass dependencies we are able to make the following predictions : $m_{B_c*} - m_{B_c} = 80 \pm 8$ MeV, and $m_{\Omega_{ccb}} = 8050 \pm 10$ MeV.

0.3.3 Singly charm baryons

After triply and doubly charm baryons, we studied singly charm baryons with the same details. However, for singly charm baryons the number of channels are many more, namely, $\Lambda_c(cud)$, $\Sigma_c(cuu)$, $\Xi_c(cus)$, and $\Omega_c(css)$. In the presence of one or two light quarks, the dynamics of these particles become much more complicated and these particles provide a unique opportunity to study the interaction between one or more light quarks in the presence of a heavy quark. The number of possible interpolating operators are also more as was shown in Table 3.

We show our results for the spectra of singly charm baryons in Figure 3 (name of each

particle channel are shown inside). As before, we plot spectra in terms of mass splittings instead of absolute masses. In our calculation, the pion mass is $m_\pi \sim 391$ MeV. Due to this unphysical light quark mass, we plot the $\Lambda_c(cud)$ and $\Sigma_c(cuu)$ spectra in terms of their splitting from the vector meson mass $m_\rho(\bar{u}d)$ calculated on these lattices. For $\Xi_c(cus)$, and $\Omega_c(css)$, we show the spectra in terms of their splittings from the mass of vector mesons $K^*(\bar{u}s)$ and $\phi(\bar{s}s)$, respectively. This set of splittings for singly charm baryons is considered, since the leading order all the singly charm baryon spectrum have the same discretization errors and the same effect of the light quark dynamics, making a comparative study between the singly charm baryon spectra possible. It is to be noted that with physical quark masses one may also opt to subtract D and D_s meson masses instead, to reduce discretization error due to heavier charm quark.

As in the previous cases, we observed that the pattern of the extracted low-lying states are remarkably similar to the expectation from a model with broken $SU(6) \times O(3)$ symmetry. As previously, the low lying bands that have relatively large overlap with the non-relativistic operators are shown with magenta boxes. Similarly the states with significant overlap with the operators proportional to the field strength tensor are painted with thick borders, and are identified as strongly hybrid in nature. Known physical states are shown by violet stars (question marks are shown where quantum numbers are not known). The mismatch between the experimental value and our calculated energies is believed to be due to the unphysical quark masses and the finite volume effects.

The Σ_c^{++} and Ω_c baryons have the same flavor structure : pqq. The allowed flavor symmetries are similar to that of the doubly charm baryons, where one can have a symmetric flavor structure and a MS/MA flavor structure. Thus the spectrum of these two baryons should resemble the spectrum obtained for the doubly charm baryons. This is quite evident from the two plots on the right in Figure 3.

The Λ_c baryons are those with quark content udc and can have an antisymmetric or MS/MA flavor structure, which corresponds to Λ_c-singlet and Λ_c-octet respectively. The difference between the Λ_c-octet and the Σ_c^+ is that the latter is a part of the isospin triplet, while the former forms an isospin singlet. The details of the flavor structure is shown in Table 3.2. Since there is no totally antisymmetric spin combination that can be constructed from a purely non-relativistic formalism, one requires angular momentum structure through non-local behavior to construct a flavor-singlet Λ_c interpolating operator. Figure 3(a) shows the spectrum of Λ_c, where one can see only one state in the low lying band. This state has significant overlap with the flavors MS/MA with non-relativistic spin 1/2. As observed for the other channels, the number and the pattern of

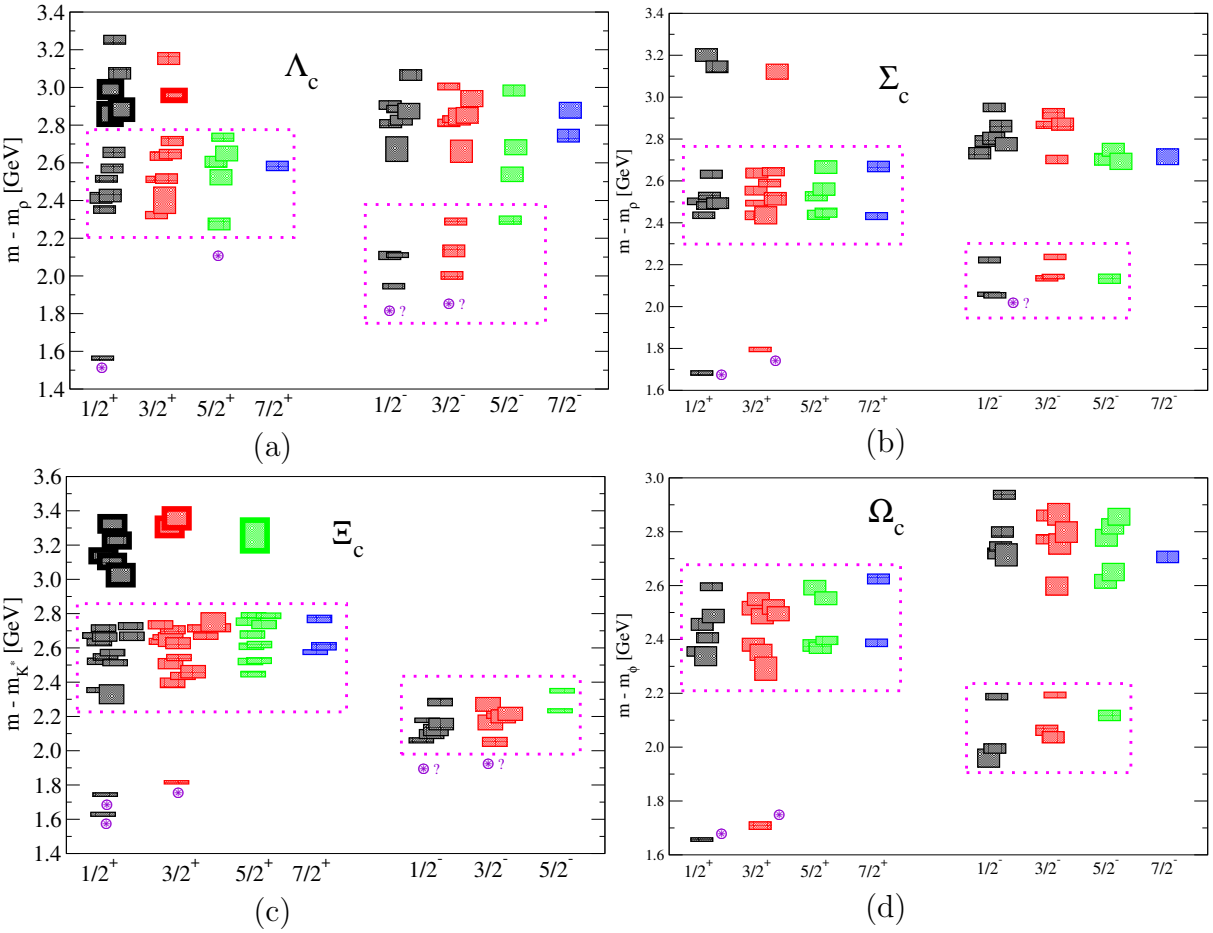

Figure 3: Results on the spin identified spectra of (a) Λ_c, (b) Σ_c, (c) Ξ_c and (d) Ω_c baryons for both parities *w.r.t.* vector mesons, ρ (upper two) and K^*, ϕ (lower two). The keys are same as in Figure 1(a). Known physical states are shown by violet star (question marks are shown where quantum numbers are not known).

the first negative parity band and the first excited positive parity band agrees with the non-relativistic predictions. It is to be noted that the ordering of the first two states, particularly the lowest lying first excited positive parity state, is observed to have spin 5/2 which is similar to the pattern supported by experiments.

The Ξ_c baryons, with quark content usc, can have S, A or MS/MA flavor structure, which correspond to Ξ_c-decuplet, Ξ_c-singlet and Ξ_c-octet respectively. Within Ξ_c-octet flavor structure, one has two possibilities. If we assume an us-spin symmetry, similar to the isospin that describes the symmetry between u and d quarks, there are two possible MS/MA combinations : the Ξ_c-octet and the $\Xi_c^{'}$-octet. The latter is a part of the us-spin triplet, of which Ω_c and Σ_c^{++} are included, while the former is a us-spin singlet. As in

the case of Λ_c, due to the absence of a totally antisymmetric spin combination that can be constructed from a purely non-relativistic formalism, one requires angular momentum structure through non-local behavior to construct a flavor-singlet Ξ_c interpolating operator. Hence the low lying spectrum for Ξ_c baryon will have two spin 1/2 states from the Ξ_c-octet and $\Xi_c^{'}$-octet operators and a spin 3/2 state with the Ξ_c-decuplet flavor structure. This can clearly be seen in Figure 3(c). The full set of operators for Ξ_c baryon forms a very large set that fails to converge and produce a reliable spectrum from the variational fitting. In this analysis, hence we use purely non-relativistic operators for fitting, and the Ξ_c spectrum shown in Figure 3(c) is non-relativistic.

0.4 Mixed action approach : Charm and strange hadron spectroscopy

The main aim of this study is to explore heavy hadron spectra using the chiral overlap fermions on the background of a set of improved gauge configurations generated with highly improved staggered quarks. By using such an approach, we get an advantage to use a chiral action as well as a large set of highly improved configurations with multiple lattice spacings. Below I mention results obtained from my contribution in this project. As mentioned in the introduction, this is a calculation complementary to the previous study of excited charm baryon spectra, particularly to improve the control over the discretization errors.

We use two sets of dynamical 2+1+1 flavors HISQ lattice ensemble generated by the MILC collaboration : a set of $32^3 \times 96$ lattices with a =0.0877(10) fm and another set of $48^3 \times 144$ lattices a =0.0582(5) fm. For valence quarks we use overlap action [50]. The strange and charm masses are set at their physical values while $m_l/m_s = 1/5$ for both lattices. The details of these configurations are summarized in Ref. [41]. The above lattice spacings are determined using the Ω baryon mass measured on these ensembles. The results reported here are obtained from 110 configurations on the coarser lattice, and 65 configurations on the finer lattice. Using both point and wall sources, we calculate various point-point, wall-point as well as wall-wall quark propagators to study the low lying hadron spectra.

Our extracted pseudoscalar meson masses are within the range $400 - 5130$ MeV and $230 - 4000$ MeV for the coarser and finer lattices, respectively. In following two subsections, we will discuss our estimates for mesons and baryons mostly in terms of

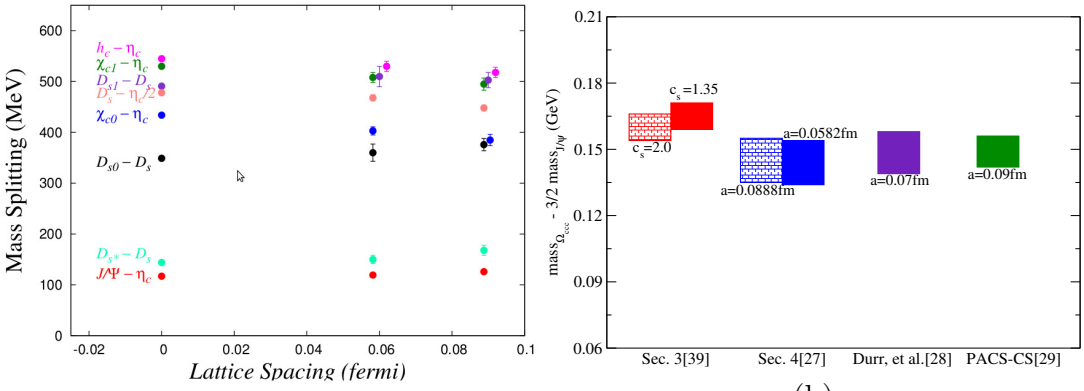

(a) (b)

Figure 4: (a) Meson mass splitting for charmonia and charm-strange mesons at two lattice spacings. Experimental values are shown in the left side. (b) Mass splitting of the ground state of $J^P = \frac{3}{2}^+$ Ω_{ccc} from $3/2m_{J/\psi}$. Results of this mass splitting from this work (blue) are compared with those obtained from the excited charm baryon studies in the previous sections (red), Ref. [28] (violet) and Ref. [29] (green).

energy splittings as those have less systematics compared to extracted energies.

0.4.1 Energy splittings in charmonia and charm-strange mesons

In Figure 4(a) we present the energy splittings between axial, scalar and tensor charmonia from pseudoscalar charmonia. In addition to this, we also calculate charm-strange mesons with various quantum numbers. The energy splittings between these mesons are as shown in Figure 4(b). We find that tuning of charm mass using kinetic mass brings these splittings closer to their experimental values than when performed with the pole mass [27]. Our results for the hyperfine splitting in 1S charmonia are 125(6) MeV and 119(3) MeV corresponding to coarser and finer lattices respectively. It is to be noted that the this hyperfine splitting is one of the most well studied physical quantities in lattice charmonium calculations over the year, and until very recently [15, 16], lattice results were found to be smaller than the experimental value ($\sim$ 116 MeV). Our results are closer to the experimental value.

Charm baryons

We also study the ground state spectra of charm baryons with one or more charm quark content, e.g., with quark content *css*, *ccs*, and *ccc* on these lattices. The mass splittings $\Omega_{ccc} - \frac{3}{2}J/\Psi$ are shown in Figure 4(b). The blue rectangles represent the results from this

work for the two different lattice spacings, while the rectangles in red are results from the work discussed in the previous section. The two red points are with the tree-level clover coefficient $c_s = 1.35$ and at a boosted value of $c_s = 2$, which gives correct charmonium hyperfine splitting, $J/\psi - \eta_c$. The red and blue squares showed the consistency between our two independent calculations. These results are also consistent with other independent lattice results [28, 29]. We also calculate various spin splittings for doubly charm baryons and find similar consistency between our two results and results from other lattice calculations.

0.5 Baryon screening masses at finite temperature

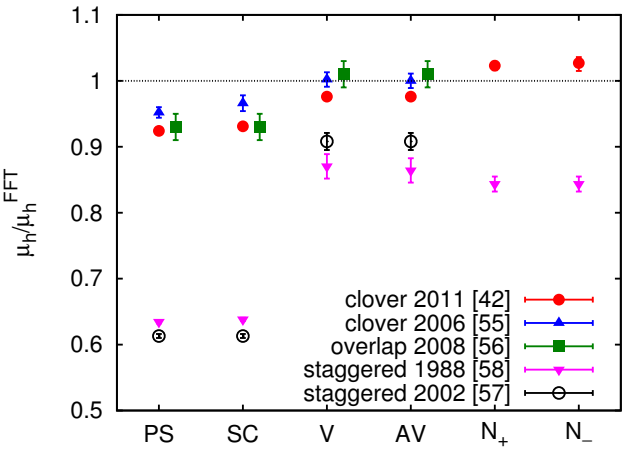

Figure 5: The ratio of screening masses measured at $T = 1.5T_c$ in quenched QCD with those in FFT. Although all the results are not taken for exactly the same quark mass, the effects of the quark mass are very small (less than 1% in this study).

$\frac{m_\pi}{T_c}$	$\frac{\mu_{N_+}}{m_{N_+}}$	$\frac{\mu_{N_-}-\mu_{N_+}}{m_{N_-}-m_{N_+}}$
2.20	1.05 ± 0.05	0.75 ± 0.10
1.99	1.07 ± 0.04	0.68 ± 0.12

Table 4: Thermal shifts in nucleon masses and mass splittings at $T = 0.95T_c$; μ_{N_+/N_-} denotes the inverse screening length in the positive/negative parity nucleonic channel, and m_{N_+/N_-} the respective mass at $T = 0$.

The long term experimental programs on finite temperature QCD are beginning to probe the finer details of the non-perturbative predictions of QCD [51], at various collider experiments, including Relativistic Heavy Ion Collider (RHIC) at BNL and Large Hadron Collider (LHC) at CERN. This is possible because fireballs produced in these collisions come close to thermal equilibrium [52] and the data from such experiments need to be confronted with first principles calculations such as Lattice QCD techniques that can make useful theoretical predictions on the expectation value of observables.

Using lattice QCD, the phases and properties of the medium can be studied by analyzing the static correlation lengths (which is inverse of the screening mass, μ) [53]. These correlations are measured by introducing static probes into the equilibrium plasma and measuring the response of the medium. The response depends on the quantum numbers carried by the probes; so one can classify static correlators as glueball-like, meson-like and baryon-like probes with the usual quantum numbers of these quantities corrected for the fact that the static spatial symmetries are different from the Poincare group. In this work, we study the meson-like and baryon-like static correlation lengths above ($1.5\ T_c$) and immediately below ($0.95\ T_c$) the deconfinement transition temperature. It is expected that these studies provide important inputs to the study of baryon-number fluctuations, which is of much interest in the experimental search for the critical point of QCD. We reboot the study of these correlators in the high temperature phase.

At $1.5\ T_c$, we find that the scalar/psuedoscalar (S/PS) and the (vector/axialvector) V/AV correlators become pairwise degenerate. We find strong signals of approximate chiral symmetry restoration from the near degeneracy of the screening masses of the mesonic parity partners. Figure 5 shows the ratio of screening masses of various hadrons in an interacting theory to the respective screening masses in free field theory. In addition we found, as before [54, 55, 56], that the screening masses are not far from those obtained in Free Field Theory (FFT), which is a model of non-interacting quarks. Along with our estimates for the ratio of screening masses in interacting theory to the free theory, Figure 5 also contains a survey of the literature. This work uses the smallest lattice spacing used in a quenched study to date, and agrees with previous work using clover quarks [55]. It also agrees with results from studies using overlap quarks at smaller lattice spacing [56]. However, it seems that studies with naïve staggered quarks always indicate stronger deviations from FFT than any of these above studies [57, 58]. Immediately below T_c, we find that the mass of the mesons is hardly affected by the temperature below the deconfinement transition temperature.

As in the mesonic correlations, the nucleonic screening lengths at $T = 1.5\ T_c$, show strong signals of approximate chiral symmetry restoration through the near degeneracy of their screening masses. It is also evident from Figure 5 that above T_c the baryonic screening lengths also support the evidence for weakly interacting quarks. However, below T_c some interesting observations can be seen from Table 4. We find that $\mu_{N_+} = m_{N_+}$ within 95% confidence limits, indicating no significant thermal effects in the nucleon mass. However, the splitting between the N_+ and its parity partner, N_-, changes at finite temperature, and is a precursor to the restoration of chiral symmetry before the

QCD phase transition. These observations not only constrain models of quantum hadrodynamics [59], but could also have implications for the analysis of heavy-ion collision data.

0.6 Summary and conclusions

In this synopsis, we summarized our study of baryons by using non-perturbative methods of lattice QCD. The significant part of the work dealt with spectroscopy of charm baryons. In this, we performed two complementary studies using two different non-perturbative techniques with distinct merits, and comparative study was performed between the results from both these studies, which gave us confidence in our results. A second part of this synopsis involved a study of baryon screening masses at finite temperature that could provide important information on the properties of the QCD medium across the transition temperature.

The detailed study of charmonia, both theoretically and experimentally, has provided crucial insights in our understanding of strong interaction. In contrast to that, charm baryons have not been studied comprehensively, though that can also provide similar information. In this work, we make the first attempt to study charm baryons comprehensively. An anisotropic action with 2+1 flavor dynamical clover and with temporal lattice spacing of about $(5.67\ \text{GeV})^{-1}$ was used. A large set of carefully designed baryonic interpolating operators with up to two derivatives were constructed and the newly developed distillation technique was employed to generate the correlation functions. A well-suited variational technique was utilized to extract the energy eigenstates with reliable spin-parity quantum numbers. The main results are shown in Figure 1, 2 and 3. Among the results most significant ones are the following predictions: $m_{\Omega_{ccc}} - m_{J/\psi} = 160 \pm 6$ MeV, $m_{B_{c^*}} - m_{B_c} = 80 \pm 8$ MeV, and $m_{\Omega_{ccb}} = 8050 \pm 10$ MeV. In the extracted spectra we found bands of states with alternating parities and increasing energies. Beside identifying the spin of a state we could also decode the structure of operators leading to that state : whether constructed by relativistic, non-relativistic, hybrid, non-hybrid types or a mixture of them all. However, for negative parity states and highly excited positive parity states, this identification is not possible since we do not include operators with more than two derivatives which will contribute to these states and so will change the relative contribution from various operators leading to such states. Similar to light and strange baryon spectra [35], we also found the number of extracted states of each spin in the three lowest-energy bands and the number of quantum numbers expected based

on weakly broken $SU(6) \times O(3)$ symmetry agree perfectly, *i.e.,* all the low lying charm baryon spectra remarkably resemble the expectations of quantum numbers from quark model [6, 7, 8] though we used relativistic as well as non-relativistic hybrid operators which are not present in such models.

In addition to the pattern of the spectra, we also studied various energy splittings that could give insights into spin-dependent interactions that exists between multiple charm quarks as well as charm quarks and the light or the strange quarks. In the heavy quark limit, the energy splitting due to spin-orbit coupling should vanish as it is proportional to the heavy quark masses. To check this, we identify a few states with the same L and S values from overlap factors of various operators and found that the spin-orbit energy degeneracy between these states are more or less satisfied both for bottom and charm quarks, justifying a heavy quark status for the charm quarks. More precise data are necessary to check the breaking of this degeneracy at the charm quark mass. We also evaluated some other energy splittings that mimics the binding energy of various baryon states, such as : $m_{\Omega_{bbb}} - \frac{3}{2}\, m_{\Upsilon_{\bar{b}b}}$, $m_{\Omega_{ccc}} - \frac{3}{2}\, m_{J/\psi_{\bar{c}c}}$ and $m_{\Omega_{sss}} - \frac{3}{2}\, m_{\phi_{\bar{s}s}}$. Significant quark mass dependence was observed for such splittings that can be modeled with a form $a + b/m_{PS}$, which assumes they will tend to a constant in the heavy quark limit. It is interesting to note that the heavy quark expansion gives a good fit with data at bottom, charm as well as strange masses.

It is to be noted that we did not use any multi-hadron operators in this calculation. Inclusion of those operators, particularly those involving light quarks, may affect some of the above conclusions, though to a lesser extent than their influence in the light hadron spectra. Also this calculation was carried out with one lattice spacing, one volume and at $m_\pi = 391$ MeV. In order to get precise estimate, which can be compared with experiments, this study needs to be repeated with multiple volumes and lattice spacings at lighter pion masses.

Complementary to the above work, we calculated charm and strange hadron spectra with the overlap fermions in the background of a set of 2+1+1 flavors HISQ gauge configurations. By adopting such a mixed action approach, we took advantage of the chiral symmetry and low quark mass limit of overlap fermions, and the advantage of having a large set of configurations with small discretization errors as well as small taste breaking effects. We were also able to simulate both light, strange as well as heavy fermions on the same lattice formalism with chiral fermions having no $\mathcal{O}(a)$ errors. Results obtained, in particular the splittings between various hadrons, including the hyperfine splitting in 1S charmonia, are encouraging and consistent with experiments.

This suggests that the overlap valence quarks on 2+1+1 flavor HISQ configurations is a promising approach to do lattice QCD simulation with light, strange and charm quark together in the same lattice formulation. We found the tuning of the charm quark mass with the kinetic mass, rather than the pole mass, improves the discretization errors. We also have the estimates for various charm and charm-strange hadrons. The splitting $(m_{\Omega_{ccc}} - \frac{3}{2}m_{J/\Psi})$, between J/Ψ and the unknown triply charm baryon Ω_{ccc} was found to be 145(10) MeV and 144(10) MeV, on our coarser and finer lattices respectively.

This is a complementary study of the first project to access the effect of discretization errors on extracted masses. In both the works, we calculated the Ω_{ccc} mass, for which the discretization error is maximum since all the three quarks are heavy. We observed that results from both the calculations are consistent with each other and are also consistent with a few other independent lattice calculations. This shows that the discretization errors entering in our estimates are in good control.

It is to be noted that we have not performed continuum and chiral extrapolations which will be performed later by ILGTI after adding another lattice spacing. The chiral extrapolation has to be done carefully by using mixed action partially quenched chiral perturbation theory [60] with proper mixed action discretization term Δ_{mix} [61].

In the second part of the work, we calculated thermal correlations in quenched QCD in channels with various hadronic quantum numbers, with a aim to access the behavior of baryons at finite temperature. The correlation functions are consistent with the usual picture of the QCD phase diagram : below T_c long-distance correlations are mediated by hadrons and above T_c these are mediated by weakly interacting quarks. Above T_c, at the temperature $T = 1.5T_c$, we found strong signals of approximate chiral symmetry restoration in the near degeneracy of screening masses of hadronic parity partners. In addition, we found, as before [54, 55, 56], that the correlation functions and screening masses are not far from those obtained in FFT, which is a model of non-interacting quarks. The estimates from this work is in consistence with previous results using clover quarks [55] and overlap quarks [56], while staggered quarks in the quenched approximation always indicated stronger deviations from FFT [57, 58].

Mesonic channels and the nucleon ground state show no thermal effects below T_c. However, the opposite parity excitation of the nucleon, S_{11}, is seen to move closer to the ground state signaling a precursor to chiral symmetry restoration. No such effects have been seen earlier either in the glue sector or with quarks, nor do we see any effect in the V/AV channels here. This is a new observation which can constrain models of quantum hadrodynamics, as well as have implications for the analysis of heavy-ion collision data.

This encourages for future study of baryonic correlators in a comprehensive way.

Bibliography

[1] P. W. Higgs, Phys. Lett. **12**, 132 (1964);
S. Chatrchyan *et al.* [CMS Collaboration], Phys. Lett. B **716**, 30 (2012) [arXiv:1207.7235 [hep-ex]];
G. Aad *et al.* [ATLAS Collaboration], Phys. Lett. B **716**, 1 (2012) [arXiv:1207.7214 [hep-ex]].

[2] RPP : J. Beringer et al. (Particle Data Group), Phys. Rev. D **86**, 010001 (2012).

[3] M. Mattson *et al.* [SELEX Collaboration], Phys. Rev. Lett. **89**, 112001 (2002) [hep-ex/0208014].

[4] B. Aubert *et al.* [BABAR Collaboration], Phys. Rev. D **74**, 011103 (2006) [hep-ex/0605075].

[5] Y. Kato *et al.* [Belle Collaboration], arXiv:1312.1026 [hep-ex].

[6] S. Capstick and W. Roberts, Prog. Part. Nucl. Phys. **45**, S241 (2000) and the references therein.

[7] E. Klempt and J. -M. Richard, Rev. Mod. Phys. **82**, 1095 (2010) and the references therein.

[8] V. Crede and W. Roberts, Rept. Prog. Phys. **76**, 076301 (2013) and the references therein.

[9] J. D. Bjorken, FERMILAB-CONF-85/69, Is the ccc a New Deal for Baryon Spectroscopy?, Int. Conf. on Hadron Spectroscopy, College Park, MD, Apr. 1985;

[10] S. Aoki, *et al.* [CP-PACS Collaboration], Phys. Rev. Lett. **84**, 238 (2000); Phys. Rev. D **79**, 034503 (2009).

[11] C. W. Bernard, *et al.*, Phys. Rev. D **64**, 054506 (2001) [hep-lat/0104002].

[12] C. T. H. Davies *et al.* [HPQCD and UKQCD and MILC and Fermilab Lattice Collaborations], Phys. Rev. Lett. **92**, 022001 (2004) [hep-lat/0304004].

[13] C. Aubin, *et al.*, Phys. Rev. D **70**, 094505 (2004) [hep-lat/0402030].

[14] S. Durr, *et al.*, Science **322**, 1224 (2008) [arXiv:0906.3599 [hep-lat]].

[15] T. Burch, *et al.*, Phys. Rev. D **81**, 034508 (2010).

[16] G. C. Donald, *et al.*, Phys. Rev. D **86**, 094501 (2012).

[17] Y. Namekawa *et al.* [PACS-CS Collaboration], Phys. Rev. D **84**, 074505 (2011).

[18] C. McNeile, *et al.*, Phys. Rev. D **86**, 074503 (2012) [arXiv:1207.0994 [hep-lat]].

[19] D. Mohler and R. M. Woloshyn, Phys. Rev. D **84**, 054505 (2011);
D. Mohler, S. Prelovsek and R. M. Woloshyn, Phys. Rev. D **87**, 034501 (2013).

[20] R. J. Dowdall, *et al.*, [HPQCD Collaboration], Phys. Rev. D **85**, 054509 (2012) [arXiv:1110.6887 [hep-lat]]; Phys. Rev. D **86**, 094510 (2012) [arXiv:1207.5149 [hep-lat]].

[21] E. B. Gregory, *et al.*, Phys. Rev. D **83**, 014506 (2011) [arXiv:1010.3848 [hep-lat]].

[22] N. Mathur, R. Lewis and R. M. Woloshyn, Phys. Rev. D **66**, 014502 (2002);
R. Lewis, N. Mathur and R. M. Woloshyn, Phys. Rev. D **64**, 094509 (2001).

[23] J. M. Flynn, *et al.*, [UKQCD Collaboration], JHEP **0307**, 066 (2003) [hep-lat/0307025].

[24] L. Liu, *et al.*, Phys. Rev. D **81**, 094505 (2010) [arXiv:0909.3294 [hep-lat]].

[25] G. Bali, *et al.*, J. Phys. Conf. Ser. **426**, 012017 (2013) [arXiv:1212.0565 [hep-lat]].

[26] R. A. Briceno, H. -W. Lin and D. R. Bolton, Phys. Rev. D **86**, 094504 (2012) [arXiv:1207.3536 [hep-lat]].

[27] S. Basak, *et al.*, [ILGTI] PoS LATTICE **2012**, 141 (2012) [arXiv:1211.6277 [hep-lat]]; PoS LATTICE **2013**, 243 (2013) [arXiv:1312.3050 [hep-lat]].

[28] S. Durr, G. Koutsou and T. Lippert, Phys. Rev. D **86**, 114514 (2012) [arXiv:1208.6270 [hep-lat]].

[29] Y. Namekawa *et al.* [PACS-CS Collaboration], Phys. Rev. D **87**, 094512 (2013).

[30] M. Peardon, *et al.*, [Hadron Spectrum Collaboration], Phys. Rev. D **80**, 054506 (2009).

[31] C. Michael, Nucl. Phys. B **259**, 58 (1985);
M. Luscher and U. Wolff, Nucl. Phys. B **339**, 222 (1990).

[32] J. J. Dudek, R. G. Edwards, N. Mathur and D. G. Richards, Phys. Rev. D **77**, 034501 (2008).

[33] S. Basak *et al.* [Lattice Hadron Physics (LHPC) Collaboration], Phys. Rev. D **72**, 074501 (2005).

[34] R. G. Edwards, J. J. Dudek, D. G. Richards and S. J. Wallace, Phys. Rev. D **84**, 074508 (2011).

[35] R. G. Edwards, N. Mathur, D. G. Richards and S. J. Wallace, Phys. Rev. D **87**, 054506 (2013).

[36] J. J. Dudek, *et al.*, Phys. Rev. Lett. **103**, 262001 (2009); Phys. Rev. D **82**, 034508 (2010).

[37] L. Liu, *et al.*, [HSC], JHEP **1207**, 126 (2012);
G. Moir, *et al.*, JHEP **1305**, 021 (2013).

[38] J. J. Dudek and R. G. Edwards, Phys. Rev. D **85**, 054016 (2012) [arXiv:1201.2349 [hep-ph]].

[39] M. Padmanath, R. G. Edwards, N. Mathur and M. Peardon, arXiv:1307.7022 [hep-lat];
arXiv:1311.4354 [hep-lat]; arXiv:1311.4806 [hep-lat].

[40] E. Follana *et al.* [HPQCD and UKQCD Collaborations], Phys. Rev. D **75**, 054502 (2007).

[41] A. Bazavov *et al.* [MILC Collaboration], Phys. Rev. D **87**, no. 5, 054505 (2013).

[42] S. Datta, S. Gupta, M. Padmanath, J. Maiti and N. Mathur, JHEP **1302**, 145 (2013).

[43] K. G. Wilson, Phys. Rev. D **10**, 2445 (1974).

[44] G. Burgers, F. Karsch, A. Nakamura and I. O. Stamatescu, Nucl. Phys. B **304**, 587 (1988); T. R. Klassen, Nucl. Phys. B **533**, 557 (1998); P. Chen, Phys. Rev. D **64**, 034509 (2001).

[45] R. G. Edwards, B. Joo and H. -W. Lin, Phys. Rev. D **78**, 054501 (2008) [arXiv:0803.3960 [hep-lat]].

[46] H. -W. Lin *et al.* [HSC], Phys. Rev. D **79**, 034502 (2009) [arXiv:0810.3588 [hep-lat]].

[47] S. Meinel, Phys. Rev. D **85**, 114510 (2012).

[48] M. J. Savage and R. P. Springer, Int. J. Mod. Phys. A **6**, 1701 (1991);
M. J. Savage and M. B. Wise, Phys. Lett. B **248**, 177 (1990).

[49] N. Brambilla, A. Vairo and T. Rosch, Phys. Rev. D **72**, 034021 (2005) [hep-ph/0506065];
S. Fleming and T. Mehen, Phys. Rev. D **73**, 034502 (2006) [hep-ph/0509313].

[50] H. Neuberger, Phys. Lett. B **417**, 141 (1998); ; *ibid.* B427 (1998) 353;
M. Luscher, Phys. Lett. B **428**, 342 (1998).

[51] S. Gupta, *et al.*, Science **332**, 1525 (2011).

[52] J. Cleymans and K. Redlich, *Phys. Rev. Lett.* 81 (1998) 5248;
P. Braun-Munzinger and J. Wambach, Rev. Mod. Phys. 81 (2009) 1031.

[53] C. E. DeTar and J. B. Kogut, *Phys. Rev. Lett.* 59 (1987) 399, *Phys. Rev.* D 36 (1987) 2828.

[54] K. D. Born *et al.*(MT_c Collaboration), *Phys. Rev. Lett.* 67 (1991) 302.

[55] S. Wissel *et al.*, *PoS* LAT-2005, 164; S. Wissel, Ph. D *dissertation* (2006).

[56] R. V. Gavai, S. Gupta and R. Lacaze, *Phys. Rev.* D 78 (2008) 014502.

[57] R. V. Gavai, S. Gupta and P. Majumdar, *Phys. Rev.* D 65 (2002) 054506.

[58] A. Gocksch, P. Rossi and Urs M. Heller, *Phys. Lett.* B 205 (1988) 334.

[59] R. Rapp and J. Wambach, *Adv. Nucl. Phys.* 25 (2000) 1.

[60] O. Bar, G. Rupak and N. Shoresh, Phys. Rev. D **67**, 114505 (2003);
J. -W. Chen, D. O'Connell and A. Walker-Loud, Phys. Rev. D **75**, 054501 (2007);
K. Orginos and A. Walker-Loud, Phys. Rev. D **77**, 094505 (2008) and references therein.

[61] M. Lujan, *et al.*, Phys. Rev. D **86**, 014501 (2012).

Publications

- S. Basak, S. Datta, A. T. Lytle, **M. Padmanath**, P. Majumdar and N. Mathur, PoS LATTICE **2013**, 243 (2013), [arXiv:1312.3050 [hep-lat]].
- **M. Padmanath**, R. G. Edwards, N. Mathur and M. Peardon, arXiv:1311.4806 [hep-lat], *conference proceedings* : CHARM 2013.
- **M. Padmanath**, R. G. Edwards, N. Mathur and M. Peardon, PoS LATTICE **2013**, 247 (2013), arXiv:1311.4354 [hep-lat].
- **M. Padmanath**, R. G. Edwards, N. Mathur and M. Peardon, arXiv:1307.7022 [hep-lat], *submitted to Phys. Rev.* D.
- S. Datta, S. Gupta, **M. Padmanath**, J. Maiti and N. Mathur, JHEP **1302**, 145 (2013) [arXiv:1212.2927 [hep-lat]].
- S. Basak, S. Datta, **M. Padmanath**, P. Majumdar and N. Mathur, PoS LATTICE **2012**, 141 (2012) [arXiv:1211.6277 [hep-lat]].

Outline of the thesis

In this thesis, I present my work on the non-perturbative studies of various aspects of baryon physics using lattice QCD. An outline of the works presented in the thesis is as follows :

- Spectroscopy of charm hadrons
  - Excited state charm baryon spectroscopy using clover fermions.
  - Charm hadron spectroscopy using overlap fermions.
- Nucleons at finite temperature.

The organization of this thesis is as described below.

In Chapter 1, I introduce the aforementioned works, covering the phenomenology in the respective aspects. I discuss the experimental and the theoretical advances in the spectroscopic studies and the future prospects from both experimental and theoretical point of view. After the phenomenological background and motivation, I discuss the works on *Excited state charm baryon spectroscopy* and *Charm hadron spectroscopy using overlap fermions*. The work on *Nucleons at finite temperature* is discussed briefly in the last section.

Chapter 2 serves as very brief review of the basics of the first principle non-perturbative technique, known as Lattice QCD, that we employ for our calculations. The review covers a short introduction to the QCD in the continuum followed by a section dedicated to the lattice regularization of QCD. A third section discusses the basics of simulations involved and an introduction to the conventional spectroscopy studies using lattice.

Chapter 3 is dedicated for the technical details related to the work on excited state spectroscopy. I begin by discussing the procedure involved in conventional spectroscopy studies using lattice QCD and the challenges that appear in the excited state spectroscopy. Individual sections are dedicated to explain the solutions, which include the

use of anisotropic lattice formalism, derivative based operator construction formalism and variational fitting techniques, to these challenges.

In Chapter 4, our results for charm baryons from the excited state spectroscopy studies are presented. The chapter is divided into three sections : 1) Triply charm baryons, 2) Doubly charm baryons and 3) Singly charm baryons and spectra for them are discussed in the respective sections. Along with I also discuss our calculations to assess the discretization errors entering our estimates. Separate subsections are used for various energy splittings, which carry the information about the binding energies of the extracted states. We also discuss various systematics involved in this calculation that have not been addressed.

In Chapter 5, I discuss the details and the results from our heavy hadron spectroscopy calculations using overlap fermions. In this chapter, we discuss the detailed study of the discretization errors in this non-perturbative approach, and make a comparative study of various estimates that we measure from this work and the previous one, along with estimates from other lattice and potential model calculations.

In Chapter 6, I discuss our study of hadron screening masses at finite temperature. Main emphasis has been given for the nucleonic channels, where we observe interesting behavior in the negative parity nucleonic channels indicating precursor effects for the chiral symmetry restoration in the nucleonic channels immediately below T_c.

In Chapter 7, we give a brief summary of the findings made in the works described in the thesis.

Chapter 1

Introduction

Understanding the building blocks of the universe and the fundamental laws of nature that govern the interactions between them is the primary aim of theoretical physics, with a hope that this understanding will help us explain all the complex natural phenomena around us. This view is known as reductionism. Success of such a view in atomic physics began with John Dalton's (1803) atomic theory, followed by Dmitri Mendeleev's proposal of atomic periodic table and the developments that followed till the early 20^{th} century. Atomic physics further got a substantial boost in its understanding about the atomic spectra and atomic substructure following Ernest Rutherford's Gold foil experiment, Niels Bohr's proposal of his atom model and, in particular, the development of quantum mechanics. The enormity of the success of quantum mechanics is such that it found applications in a wide variety of areas beyond atomic physics, including a great deal of modern technological inventions which revolutionized our life.

Particle physicists also believe in such a reductionist point of view in order to understand the proliferated collection of particles that were observed after the invention of cyclotron and the development of various particle accelerators. The rich spectra of light hadrons provided us with a framework for constructing a theory of strong interactions starting from the eightfold way to treating quarks and gluons as the fundamental degrees of freedom. The development including the unification of the electromagnetic and the weak interactions [1, 2, 3], followed by the proposal of Higgs field [4], which is believed to give mass to all the fundamental particles in the universe, gave the Standard Model of particle physics its modern form.

Though the discoveries of the neutral intermediate vector boson, the top quark, the τ-neutrino and the Higgs boson [5, 6] put the Standard Model of particle physics on solid

footing, there remains significant limitations in our understanding. Quantum Chromo Dynamics (QCD), a local non-Abelian gauge theory representing the $SU(3)$ sector in the Standard Model, is established to be the theory of strong interactions. The most desirable feature of QCD, the asymptotic freedom [7, 8], allowed successful application of perturbative techniques in explaining the observations in the high energy domain from various particle collider experiments. However, a complete understanding of the non-perturbative part of QCD in the low energy domain remains a challenge. The masses of the hadrons made of light quarks, in particular baryons, are observed to be an order of magnitude higher than the sum of the mass of the quarks that constitutes them. Baryons, particularly neutrons and protons, account for $\sim$99% of the mass of the visible universe. However, only $\sim$1% of the proton mass is explained by the Higgs mechanism. Hence it is very important to understand the origin of the mass that constitutes the major part of the visible universe. From various lattice studies, it is now understood that this mass comes from the non-perturbative nature of the strong interactions in the low energy domain. The calculation of the energy spectra of various hadrons is the main aim of this work.

1.1 Baryons

Baryons are relatively simple systems in which quintessentially confining character of multiple quarks is manifest and are sufficiently complex to shed light on physics hidden from us in the mesons. Understanding the baryon spectra is thus expected to answer a large series of questions on baryons and the interactions that exist within them [9]. A few questions for which the current day and the future baryon spectroscopy studies are expected to provide answers are the following. Can all baryon resonances be explained from QCD? What are the leading interactions that govern the spectra of baryons from the light to the heavy sector? Can we find signatures for the property of flavor independence of the QCD interactions? How much the mean field theories, like quark model calculations that are highly successful in explaining the low lying spectrum, will be successful in explaining the full resonance spectrum? Why are the 'missing resonances' missing? Missing resonances are those that are predicted by symmetric quark models but have not been observed. Even the diquark models, in which the diquark excitations are suppressed, predicts a lot more resonances than observed. Do they really exist in nature? What is the spectral pattern of the highly excited states? Are they organized in the form of spin-parity doublets or chiral multiplets of mass degenerate states having

identical spin and parity?

Though in its infancy, one also expects to understand a number of questions in the heavy baryon sector. The triply heavy baryons are expected to shed light into the quark dynamics in baryons, which is somewhat hidden by the chiral dynamics in the light baryons. The doubly charm spectrum will explain if it is dominantly governed by a charmonium-like heavy quark dynamics or a charm meson-like relativistic light quark dynamics around a static color source formed by the heavy-heavy diquark. While the spectra of singly charm baryons are expected to help us understand the hierarchy of the light quark excitations. Particularly, with the recent excitement in heavy hadron physics and fore-seeing the observations from large statistical samples that will be collected in many future and ongoing experiments [10, 11, 12, 13, 14, 15], a detailed understanding of the heavy baryon spectra is expected to provide insights into various aspects of the strong force that cannot be probed with light baryons.

1.2 Heavy hadrons in QCD

A comprehensive understanding of the theory of QCD in the strong coupling regime implies a rigorous determination and understanding of its bound states. If QCD is the correct theory, then one should be able to reproduce the physical hadron spectra from a high precision first principles non-perturbative calculation. Much like the role of atomic spectroscopy in the development of quantum mechanics, hadron spectroscopy, both theoretically and experimentally, has played a crucial role in understanding the nature of the fundamental strong force and its degrees of freedom. The dense spectra of hadrons with light quarks provided us with a framework for constructing the theory of strong interaction. The discovery of the heavier hadron, J/ψ meson, and the subsequent discoveries of other charmonia put this framework on a solid footing. These discoveries and the identification of these states as charm-anti-charm bound states took the concept of quarks from a mere mathematical construct to reality. The discovery of J/ψ meson triggered such a huge scientific interest that it was termed as the *November revolution*. The charm quark mass being heavy, the approximation that the charm quark and anti-quark are non-relativistic were found to be good for many predictions. Studies on various energy splittings provided crucial information on heavy quark-anti-quark potential, hyperfine and spin-orbit interactions, etc. The ground state charmonia, J/Ψ and η_c, gave the excellent analogs of hydrogen atom for strong interactions, which revealed the quark layer of substructure for hadrons. Potential models, consisting of non-relativistic

quark kinetic energy, a central confining potential, and spin-dependent interaction terms were found to be very successful in explaining various observed states. Recently, a tower of heavy hadron states, including the X's, Y's and Z's, has been discovered with unusual properties [16]. These discoveries have rejuvenated the heavy hadron spectroscopy tremendously and offer a bright promise in detailed understanding of various interesting aspects of the theory of strong interaction.

While the heavy quarkonia and other heavy flavored mesons have been studied quite extensively, the heavy baryon physics has received substantially less attention, even though they can provide similar insight in understanding the strong interaction. Experimentally nearly a score of singly charm baryons have been discovered, but only a few of the low lying states have been assigned the spin-parity quantum numbers based on experimental evidence [16]. A reliable determination of the quantum number of most of the observed states has not been made. For doubly charm baryons, only experiments at SELEX reported the discovery of five doubly charm baryon resonances and interpreted those as $\Xi^+_{ccd}(3443)$, $\Xi^+_{ccd}(3520)$, $\Xi^{++}_{ccu}(3460)$, $\Xi^{++}_{ccu}(3541)$ and $\Xi^{++}_{ccu}(3780)$ [17, 18]. Later they confirmed the $\Xi^+_{ccd}(3520)$ state in two different decay modes ($\Xi^+_{cc} \to \Lambda_c K^- \pi^+$; $\Xi^+_{cc} \to pD^+K^-$) at a mass of 3518.7 ± 1.7 MeV with an average lifetime of less than 33 fs [19]. However, these states have *not* been observed either by BABAR [20] or Belle [21, 22] in e^+e^- annihilation experiments. Along with the well-established triply flavored $\Delta(uuu)$ and strange $\Omega(sss)$ baryons, QCD predicts similar states built from charm quarks, the triply charm baryon, Ω_{ccc}. Such a state is yet to be observed. This could be because of the large energy threshold required for their production via either resonant or continuum production mechanisms, their very short lifetime and the very low reconstruction efficiency for the highly excited heavy hadron resonances, which follow cascade decays into multi-particle final states. The extremely low production rate hinders the identification of the spin-parity quantum numbers, even though the partial wave analysis is relatively simple in heavy hadrons in comparison with the light hadron spectra. Being a baryon-baryon collider experiment, SELEX, unlike BaBar and Belle, may have had huge cross section for the production of the charm baryons through continuum production mechanism from the QCD background. This could be a reason for the observation of the doubly charm baryon in SELEX experiments, while not in BaBar or Belle. One of the main aims of the proposed PANDA experiment at the Facility for Anti-proton and Ion Research (FAIR), Darmstadt, is to provide an ideal environment to study the heavy hadron physics. It will investigate anti-proton annihilations in the momentum range from 1.5 GeV to 15 GeV. The ongoing proton-proton collider experiments at LHCb aim at wide

range of physics programs covering many important aspects of heavy flavor physics. The high intensity baryon beams and the gluon rich reaction product from the baryon-baryon and the nucleus-nucleus collisions in both these experiments will allow high precision spectroscopy of heavy hadrons.

1.2.1 Potential model calculations

On the theoretical side, one expects that potential models will be able to describe, charm baryons [9, 23, 24], in particular the triply charm baryons, to a similar level of precision as their success in charmonia. The triply charm baryons may provide a new window for understanding the structure of baryons, as pointed out by Bjorken several years ago [25]. Just as the quark-anti-quark interactions are examined in charmonia, these studies can probe the interactions between multiple heavy quarks and heavy quarks with one or more lighter quarks. Various spin dependent splittings between baryons can provide information to constrain spin dependent potential terms, which are crucial in building successful Non-Relativistic QCD (NRQCD), pNRQCD and similar models [26, 27]. The low lying spectra of charm baryons have been studied theoretically using various approximate formulations [9, 23, 24] of QCD. These include potential model calculations with non-relativistic and relativistic heavy quarks utilizing various symmetries in a heavy quark system, calculations based on QCD sum rules and Regge phenomenology. These kind of calculations were performed as early as in late 1970's by Isgur and Karl [28, 29] where they studied baryons in a quark model framework inspired by QCD. These were followed by studies using a QCD motivated bag model [30]. Potential model calculations in non-relativistic quarks were performed in a number of works using simple variational methods [31] or by employing Faddeev formalism to solve the three body problem of baryons [32, 33, 34]. Taking into account the presence of the valence heavy flavor, calculations were performed based on heavy quark effective theory formulations [35], and with heavy quark spin symmetry constraints [36, 37, 38] to solve the non-relativistic three body problem. In Ref. [39] masses and mass relations between heavy baryons with one heavy quark using $1/m_Q$ and $1/N_c$ expansions were studied. Non-relativistic potential model calculations were also performed treating baryons as quark-diquark systems [40], where the excitations in the diquark are frozen or occur at significant higher energies. Calculations were also performed using NRQCD and its improvisations called pNRQCD formalisms, which were found to be successful in classifying the low lying charmonia and bottomonia [41, 42, 43, 44]. Owing to the fact that the NRQCD Lagrangian can be

derived in a systematic manner from QCD, these formulations were also used in many first principles lattice spectroscopic studies [45, 46, 47, 48]. Various forms of relativistic potentials were also used in many studies. For example, in Ref. [49] a relativized quark model with simple Breit-Fermi potential, combined with the spin-orbit interactions after accounting for the corrections from Thomas precession, was considered. Ref. [50] uses a relativistic potential for baryons constructed from a hyper-spherical expansion. Another approach was to extract the spectrum by solving the three body problem of baryons based on Bethe-Salpeter equations using relativistically covariant quark model in the instantaneous approximation [51]. In Ref. [52], the relativistic three quark equations were derived using dispersion relation techniques and were solved so as to extract the masses of charm baryons with orbital excitations. In Ref. [53] a constituent quark model with a full relativistic form for the light quarks and a velocity expanded relativistic potential for the heavy quarks up to second order was used. Other calculations were also performed based on QCD sum rules [54, 55], inspired by their success in explaining the low lying heavy quarkonium systems. Masses and mass relations among the heavy hadrons were studied assuming the quasi-linear Regge phenomenology ansatz for the heavy meson and heavy baryon spectra [56]. Although predictions from all these models for the low lying spectra are satisfactory, none of these models possess all the features of the full theory of QCD and many of them also does not possess the full relativistic nature. Further, it is questionable about the validity of the predictions for the extended baryons, where the dynamics could include features beyond the approximation made in these models. Hence, in the absence of any experimental discovery the only way to test these model-dependent calculations is to compare these with the results from first principles lattice QCD calculations.

1.2.2 Lattice spectroscopy

QCD, like other quantum field theories, needs to be regularized. Discretizing the space-time serves as an intutive non-perturbative regularization scheme for the theory by introducing a UV cut off through the lattice spacing, 'a'. A gauge invariant regularization of QCD is possible this way, which is often referred to as lattice QCD. Such a regularization combined with putting the theory on a finite sized box reduces the theory with infinite degrees of freedom to a theory with finite number of degrees of freedom and thus allowing to perform numerical computations of QCD. Expectation values of the QCD observables can be expressed as finite dimensional path integrals, which can directly be evaluated

with controlled systematics using Monte Carlo methods. At present, lattice QCD is the only *ab-initio* approach to access the non-perturbative aspects of QCD, that includes the QCD spectrum.

A quantitative description of the QCD spectra, particularly the charm baryons, using rigorous ab-initio computations like lattice QCD is important for a number of reasons. Firstly, many of the estimates of physical states from these calculations will be predictions and thus can naturally provide crucial inputs to the future experiments. Secondly, lattice results can provide guidance in identifying unknown quantum numbers (spin-parity) of the discovered states, based on what one expects from QCD. Moreover, it will be interesting to compare the low lying spectra of charm baryons computed from a first principles method to those obtained from potential models, which have been very successful for charmonia. It is expected that more information about interactions between multiple charm quarks and charm quark and light quark can be obtained by computing the excited state spectra of charm baryons, including in particular the spin-dependent energy splittings.

Lattice computations of hadron masses proceed through the calculations of the Euclidean two point correlation functions, followed by performing non-linear exponential fits to the long distance tail of these two point correlators, where only the ground state contribution dominates. Lattice computations of light hadron masses are well documented in the literature. Lattice studies with quenched approximation, which assume no quark loops in the theory, were found to give estimates that are accurate with respect to the observed values at $\sim$10% level [57, 58]. Light hadron spectroscopy calculations performed in the preceding couple of years with dynamical configurations, that included the quark loop effects from the light and strange flavors [59, 60], obtained an improvement in the estimates and the results were observed to be accurate with the physical values at 3% level of the statistical and systematic errors. Other dynamical calculations were also performed, which used the fermion discretizations like $O(a)$ improved Wilson action [61], domain wall fermion action [62, 63] and twisted mass fermions [64]. But all of these calculations compromised with one or other systematics involved. A notable work is by the BMW collaboration [65], where they performed a precise determination of the masses of the light hadron ground states, with controlled systematics that included the effects of light and strange sea quark effects, the chiral extrapolations, the infinite volume limit and the continuum limit. Their results were in excellent agreement with the experimental observations.

The study of heavy hadron spectroscopy using lattice QCD, mainly for the ground

state mesons, is quite mature. From early days of lattice QCD, impressive results were obtained for spectra as well as for decay constants of heavy mesons, for example, in Refs. [66, 67, 68, 69, 70, 71] and in many other works. Charmonium and bottomonium mass splittings, particularly the 1S hyperfine splittings, were studied in detail in different works using staggered quarks Asqtad improvement [72], Highly Improved Staggered Quarks (HISQ) [73, 74, 75, 76, 77]. Notably the estimates from Refs. [76, 77] included the quark loop effects up to the charm quark mass, various systematics including chiral, infinite volume and continuum extrapolations. Their results include a set of predictions along with a set of post-dictions, which are found to be in good agreement with the observed values. Considering the heavy mass of the charm quarks, Ref. [78, 79] used relativistic heavy quark formulation for the charm quarks, to determine the low lying spectra of charmonium and charm mesons.

For charm baryons, early calculations include those using quenched configurations [80, 81, 82]. Recently, the interest in lattice charm baryon spectroscopy has revived with quite a few calculations being reported. Ref. [83] used relativistic Fermilab formulation for the valence heavy quark and domain wall fermions for the valence light and strange quarks on $N_f = 2+1$ gauge configurations using improved Kogut-Susskind sea quarks to study the spin-1/2 singly and doubly charm baryons. $N_f = 2+1+1$ gauge configurations using HISQ action for sea quarks was utilized by Ref. [84], to study the ground state charm baryons, using relativistic heavy quark action for charm quarks and clover-Wilson fermions for light and strange quarks. The masses of low lying charm baryons are evaluated using two degenerate flavors of twisted mass sea quarks in Ref. [85]. There are a few dynamical calculations using clover-Wilson fermions [86, 87] and relativistic heavy quark action for charm quarks [88] aimed at spectroscopy of the low lying charm hadrons and improving the discretization errors using different discretization schemes for the heavy quarks [87].

1.2.3 Excited state spectroscopy

In spite of all these motivating results for low lying hadrons from lattice QCD, estimation of excited state spectrum remained a major challenge. Lattice results are available only for a few excited states [89, 90, 91, 92, 93, 94, 95] using usual local operators which fails to give higher radial and orbital excitations. This deficiency is mainly because the excited state contributions decay faster than those from the ground state. Hence the conventional fitting procedures fail to produce reliable estimate as the signals for the

excited states are swamped by those from the low lying states. One solution to study the excited states is to use very fine temporal resolution and scan early times so as to get stronger signals from the excited states. This can be achieved by using anisotropic lattices, where one uses a finer temporal lattice spacing in comparison with the spatial lattice spacing. Further, one can use a large set of operators that allow strong overlap with the excited states. Use of novel smearing technique, called distillation [96], aid in efficient computing of correlation functions between such large number of interpolating operators. Development of distillation and the proper utilization of fitting techniques, such as the generalized eigenvalue method [97, 98, 99], along with the derivative based operator construction formalism [100, 101], boosted the hadron spectroscopic studies, facilitating the determination of the excited state spectra [101, 102, 103, 104, 105, 106, 107, 108].

A significant part of this thesis consists of spectroscopy of charm baryons using two complementary non-perturbative approaches. The first, which constitutes the major part, employs these novel techniques mentioned above, enabling us to extract a tower of spin identified excited states for all charm baryons. In this work, we follow a well defined procedure developed and employed extensively for extracting excited states for light mesons [103, 104, 105], mesons containing charm quarks [106, 107], and light and strange baryons [101, 102, 108]. The procedure uses anisotropic lattice configurations with the light and strange quark dynamics included [109, 110]. The anisotropic discretization helps us obtain better resolution of the correlation functions, which is very helpful for extraction of excited states. The anisotropic gauge configurations utilized here are generated with $N_f = 2 + 1$ flavor clover improved Wilson fermions [109, 110]. The valence quarks, including the charm quark, are realized using clover action, which are $\mathcal{O}(am)$ improved at tree level in tadpole-improved perturbation theory [111]. Furthermore, we follow the derivative based operator construction formalism as described in Ref. [101]. This procedure proceeds in two steps : First we construct a large set of baryonic operators in the continuum. These operators transform as irreducible representations (irreps) of $SU(3)_F$ symmetry for flavor, $SU(4)_S$ symmetry for Dirac spins of quarks and $O(3)$ symmetry for orbital angular momenta, corresponding to a $SU(12) \otimes O(3)$ symmetry. If instead of the Dirac spinors with four components, Pauli spinors that are formed from purely the upper two components of the Dirac spinor in Dirac-Pauli representation are used, one would have obtained only an $SU(6) \otimes O(3)$ symmetry, where the $SU(6)$ is built up from the sub-groups according to $SU(6) = SU(3)_F \otimes SU(2)_S$. The $O(3)$ corresponds to the symmetry in the spatial part. These continuum operators are then subduced to various lattice irreducible representations to obtain lattice operators [101]. Finally, using

the novel technique called "distillation" [96], correlation functions for these operators are computed and the variational method is utilized to extract excited energies of charm baryons with one or more valence charm quark content as well as to reliably determine the spins of these states up to spin 7/2. We also computed several energy splittings, for example, hyperfine as well as spin-orbit splittings between various states. Being first of its kind in the excited charm baryon spectra calculation, this study serves as a foundation for many follow up studies, which may help us address many of the challenges in the baryon spectroscopy. The results from these studies were reported in Ref. [112, 113, 114].

Like any other lattice study, this work also possess certain systematics. The finite lattice spacing introduces a UV cut-off and the finite box size brings in an IR cut-off. It is very crucial that any physics extracted from these studies remains unaffected by these cut-offs. In order to have good control over the ma errors, we used the tree level tadpole improved clover action with $\mathcal{O}(ma_t)$ and $\mathcal{O}(ma_s)$ errors removed. We have not addressed other higher order terms, as the temporal lattice spacing is quite small. We also do not make a quantitative study of $\mathcal{O}(m^2a_s^2)$ errors. However, to study the charm physics, it is essential to have an action with discretization errors as small as possible. Further, one needs to perform lattice calculations with multiple lattice spacings on multiple lattice sizes; this is beyond the scope of this work. Furthermore, the light quark mass on the lattices we use is such that the pion mass is ~ 391 MeV. Along with the approach to the thermodynamic limit, one also needs to perform a chiral extrapolation due to the unphysical pion mass in these calculations, which again is beyond the scope of this work. Another caveat in the above study is that the clover action does not have chiral symmetry at finite lattice spacing, *i.e.*, we have not addressed the effects of chiral symmetry on observables. Though this may not affect the triply charm baryon spectra, charm baryons with valence light quark content could have some effects. Furthermore, it is also to be noted that we have not used any multi-hadron operators, which are expected to give significant implications in the extracted spectra. Hence, one also need to perform calculations considering multi-hadron operators. Keeping these caveats in mind in future it will be worthwhile to pursue same calculation by addressing all these systematics to make more precise quantitative predictions which can then confront experimental results.

1.2.4 Spectroscopy with chiral fermions

So as to complement the above calculation on spectroscopy of excited charm baryons, we perform a second non-perturbative calculation of the low lying charm hadron spectra

with highly controlled systematics. The main advantage of performing these calculations, which cover the second part of the work on spectroscopy of charm baryons, using the mixed action approach is the better control over the systematic errors that appear in the estimates. Mixed action approaches have been studied by many groups such as DWF valence on staggered fermion sea [63, 115, 116, 117], overlap valence on DWF sea [118], overlap valence on clover sea [119], and overlap valence on twisted fermion sea [120]. This calculation uses overlap valence quarks in the background of a large set of dynamical configurations generated with the one-loop, tadpole improved [111] Symanzik gauge action and the highly improved staggered quark (HISQ) fermion action [121, 122]. Taste violations, which were a generic problem with the unimproved staggered fermion action, were found to be small in the HISQ formalism [121]. The overlap formalism has exact chiral symmetry [123, 124] on the lattice and is automatically $\mathcal{O}(a)$ improved. By adopting such a mixed action approach, one can simultaneously get the advantage of having a large set of configurations with very small discretization errors as well as small taste breaking effects and the unbroken chiral symmetry as well as the low quark mass limit of overlap fermions. The overlap action also has some desirable features computationally, such as the adaptation of multi mass algorithms [125], which allows us to perform quark propagator construction for multiple quark masses very efficiently. One also gets the advantage of simulating both light, strange as well as heavy fermions on the same lattice formalism with chiral fermions having no $\mathcal{O}(a)$ errors. With a large set of quark masses being studied, we plan to perform a chiral extrapolation so as to get the estimates at the physical pion mass. With the above formulation we have calculated the ground state spectra of various charm hadrons and have made a comparative study between these two projects along with other results from literature where available. Agreement between these results from different approaches gives confidence in our estimates. The results from these studies were reported in Ref. [126, 127].

1.3 Hadrons at finite temperature

Following the zero temperature calculations involving the spectroscopy of the low lying hadrons, we are further interested in understanding how these physical states behave at finite temperature. QCD at finite temperature proceeds through a crossover transition between two phases : deconfined chirally symmetric phase at high temperatures to a confined chiral symmetry broken phase at low temperatures. It has been observed from many lattice calculations that this proceeds through a cross-over transition during this

change of phase. While in a pure gluonic field theory, this change of phase proceeds through a first order transition. The non-perturbative effects that dominate the low temperature regime of QCD, contributes at a significant level even at finite temperatures. In this work, we are interested in understanding how the degrees of freedom, in particular those with nucleon quantum numbers, that exists in the zero temperature QCD gets modified with increasing temperature.

In order to understand the thermal effects on the zero temperature degrees of freedom, we study the static correlation lengths that exist in a pure $SU(3)$ gauge theory above and immediately below the deconfinement transition temperature, T_c. Such static correlations that persist in the equilibrium thermodynamic system can be studied by introducing static probes into the equilibrium plasma and measuring the response of the medium. This response depends on the quantum numbers carried by the probes; so one can classify static correlators as glueball-like, meson-like and baryon-like probes with the usual quantum numbers of these quantities corrected for the fact that the static spatial symmetries are different from the Poincare group.

Meson-like screening masses have been studied in QCD in great detail [128, 129, 130, 131, 132, 133, 134, 135]. Baryons at finite temperature has not been studied in detail in recent past and a few notable works were in the late 1980's [128, 133]. Moreover, a detailed study of the baryon screening masses in the low temperature phase also has not been performed yet. In this work, we perform simulations of pure gauge theory for three different temperatures across the transition temperature and study screening correlators for mesonic and nucleonic resonances with clover fermions. The main emphasis, in this work, has been given to the nucleon channels, which are expected to provide important inputs to the study of baryon number fluctuations and thus to the experimental search for the critical point of QCD. The results from these studies were reported in Ref. [136].

1.4 Summary

In this chapter, we give a detailed discussion about the phenomenological and theoretical background in the spectroscopy calculations of baryons from lattice QCD. We begin with briefing the major questions that are expected to be answered with the experimental progress in the baryon spectroscopy, in Section 1.1. While in Section 1.2, we discuss the main part of the thesis work, that includes the charm baryon spectroscopy. We begin by emphasizing the experimental status and the theoretical developments from first principles lattice QCD calculations and quark model calculations of the low lying heavy

hadron spectrum. Following these discussions, we discuss our two main complementary non-perturbative calculations, which cover most part of this thesis, of the heavy baryon spectrum. The first calculation focuses on excited charm baryon spectroscopy using clover fermions (Section 1.2.3), while the second calculation performs a spectroscopy of the low lying heavy hadron states, with improved control over the systematics related the lattice formulation of QCD (Section 1.2.4).

In the last section, we discuss our studies on hadron screening masses to study the the nature of the strongly interacting matter at high temperatures. Main emphasis was given for the study of baryonic screening lengths above and immediately below the deconfinement transition temperature.

Chapter 2

Quantum ChromoDynamics on lattice

Quantum ChromoDynamics (QCD) is the established fundamental theory of strong interactions that governs the dynamics in a system of quarks and gluons. Along with the weak and the electromagnetic gauge theories, QCD, which is an $SU(3)$ gauge theory, constitutes the Standard Model of particle physics. Perturbation theory, which relies on the smallness of the coupling strength, provided an excellent tool to understand high energy regime of QCD [7, 8]. However, first principles studies of QCD at the low energy regime that includes spectroscopy, remained a highly non-trivial task.

The lattice formulation of QCD makes calculations of the QCD observables in the low energy regime possible. Introduced by Kenneth G. Wilson in 1974 [137], lattice QCD is a first principle non-perturbative regularization scheme that proceeds by putting the QCD action on a discretized Euclidean space-time array. On a finite lattice, with only finite number of degrees of freedom, it serves as a promising tool to study QCD using numerical techniques. This formalism is widely used in determining various QCD observables. The discretization introduces a UV cut-off, while the finite size of the lattice gives the system an IR cut-off. All the infinite dimensional path integrals representing physical observables become finite dimensional numerical integrals similar to those in statistical mechanics. One can then use the Markov-chain Monte Carlo methods, which have been widely in use for studies in statistical mechanics, to determine the observables in QCD.

This chapter is dedicated to a brief introduction to the theory of QCD on lattice. Section 2.1 discusses the continuum formulation of QCD, while Section 2.2 briefs how the QCD action is realized on the lattice and Section 2.3 details how simulations and

spectroscopy calculations are made using this lattice formulation of QCD.

2.1 QCD in the continuum

The QCD action in a four dimensional Euclidean space-time, with temporal extent at 0 and $\mathcal{T}$, can be written as [138, 139, 140]

$$S^E_{QCD}[\psi, \bar{\psi}, A] = S_F[\psi, \bar{\psi}, A] + S_G[A], \tag{2.1}$$

where

$$S_F[\psi, \bar{\psi}, A] = \sum_{f=1}^{N_f} \int_0^{\mathcal{T}} d\tau \int d^3x \; \bar{\psi}^{(f)}_{\alpha\, c}(x)\{(\gamma_\mu)_{\alpha\beta}(\delta_{cd}\partial_\mu + iA_\mu(x)_{cd}) + m^{(f)}\delta_{\alpha\beta}\delta_{cd}\} \; \psi^{(f)}_{\beta\, d}(x) \tag{2.2}$$

is the Fermion action and

$$S_G[A] = \frac{1}{2g^2} \int d^4x \; Tr[F_{\mu\nu}(x)F_{\mu\nu}(x)] \tag{2.3}$$

is the gluon action with the bare gauge coupling, g.

Here $\psi^{(f)}(x)$ is the Fermion field corresponding to a quark flavor, f, with mass $m^{(f)}$ and γ_μ is the Euclidean Dirac gamma matrix. $\{(\delta_{cd}\partial_\mu + iA_\mu(x)_{cd})\}$ is the gauge covariant derivative with A_μ being the gauge field, which can be decomposed as $A_\mu(x) = \sum_i \lambda^i A^i_\mu(x)$. Here λ^i's are the generators of the $SU(3)$ gauge group. $F_{\mu\nu}(x)$ is the field strength tensor, which can be expressed as $F_{\mu\nu}(x) = \sum_{i=1}^{8} F^{(i)}_{\mu\nu}(x)\lambda^i$, where $F^{(i)}_{\mu\nu}$ can be written in terms of the vector potential as

$$F^{(i)}_{\mu\nu} = \partial_\mu A^{(i)}_\nu(x) - \partial_\nu A^{(i)}_\mu(x) - f_{ijk}A^{(j)}_\mu(x)A^{(k)}_\nu(x), \tag{2.4}$$

where f_{ijk}'s are the structure constants.

This theory can be quantized using the Euclidean path integral formalism, in which the partition function for this system can be written as,

$$Z_{\mathcal{T}} = Tr(e^{-\mathcal{T}\hat{H}}) = \int D[\psi, \bar{\psi}, A] e^{-S^E_{QCD}[\psi, \bar{\psi}, A]}. \tag{2.5}$$

The expression in the center represents the partition function in the Hamiltonian operator formalism, where the self-adjoint operator, $\hat{H}$, is the Hamiltonian operator of the

system that measures the energy in the system and also governs the time evolution. The expression on the right is the partition function in the path integral formalism. The expectation value of an operator $\hat{O}$ is given by

$$\langle \hat{O} \rangle = \frac{1}{Z_{\mathcal{T}}} Tr(e^{-\mathcal{T}\hat{H}}\hat{O}) = \frac{1}{Z_T} \int D[\psi, \bar{\psi}, A] e^{-S^E_{QCD}[\psi,\bar{\psi},A]} O[\psi, \bar{\psi}, A]. \tag{2.6}$$

The usage 'partition function' for $Z_{\mathcal{T}}$ appears very natural, once we establish the structural equivalence between quantum field theory and statistical mechanics. For a canonical ensemble of spins (s), the expectation value of an observable O is given by

$$\langle O \rangle = \frac{1}{Z} \sum_{\{s\}} e^{-\beta H[s]} O[s]. \tag{2.7}$$

where $Z = \sum_{\{s\}} e^{-\beta H[s]}$ is the partition function, $1/\beta$ is the temperature in units of k_B and $H[s]$ is the Hamiltonian of the system. The similarity between eq. (2.6) and eq. (2.7) is very much evident. The Boltzmann factor, $e^{-\beta H[s]}$, is replaced by the weight factor, $e^{-S^E_{QCD}}$, and the summation over all spin configurations by the integral over the fields ψ, $\bar{\psi}$ and A_μ at all space-time points. The structural equivalence allows one to apply the numerical methods, like Monte Carlo techniques, originally developed in statistical mechanics, to quantum field theories.

2.2 Lattice formulation of QCD

Lattice QCD proceeds by the discretization of the space-time and thus regularizing the theory from UV divergences by introducing a cut-off. The theory is put on a finite sized box, so as to perform numerical computations, and this introduces an IR cut-off. The next step is to define the QCD action on lattice such that it is explicitly gauge invariant at any lattice spacing 'a'. Further, any such definition for the QCD action on the lattice should approach the continuum form in the limit, $a \to 0$.

The quark fields are placed on the lattice sites, followed by the discretization of the derivative terms. Naive discretization of the derivative terms in the action,

$$\Delta_\mu \psi(n) = \frac{1}{2a}(\psi(n + \hat{\mu}) - \psi(n - \hat{\mu})), \tag{2.8}$$

introduces terms involving fields at different space-time points resulting in gauge dependent expressions. For example, consider the term $\bar{\psi}(n)\psi(n + \hat{\mu})$: under a gauge

transformation,

$$\psi(n) \to \psi'(n) \to \Omega_\mu(n)\psi(n), \qquad \bar{\psi}(n) \to \bar{\psi}'(n) \to \bar{\psi}(n)\Omega^\dagger_\mu(n)$$

$$\text{and} \qquad \bar{\psi}(n)\psi(n+\hat{\mu}) \to \bar{\psi}(n)\Omega^\dagger_\mu(n)\Omega_\mu(n+\hat{\mu})\psi(n+\hat{\mu})$$

.

$U_\mu(n)$ is a new field living on the links between two lattice sites that is introduced so as to construct gauge invariant action. Then

$$\bar{\psi}(n)U_\mu(n)\psi(n+\hat{\mu}) \to \bar{\psi}'(n)U'_\mu(n)\psi'(n+\hat{\mu}) = \bar{\psi}(n)\Omega^\dagger_\mu(n)U'_\mu(n)\Omega_\mu(n+\hat{\mu})\psi(n+\hat{\mu})$$

is gauge invariant, given $U_\mu(n)$ transforms as

$$U_\mu(n) \to U'_\mu(n) = \Omega_\mu(n)U_\mu(n)\Omega^\dagger_\mu(n+\hat{\mu}).$$

Objects with such transformation properties in the continuum are the path ordered (P) exponential integral (eq. (2.9)) of the gauge field (A_μ) along a curve (C) connecting two points, x and y.

$$U(x,y) = P\ \exp\left(\int_C igAds\right). \tag{2.9}$$

Based on the transformation properties, $U_\mu(n)$s are interpreted as the lattice version of the gauge transporters in the continuum and hence the lattice gauge fields are introduced as

$$U_\mu(n) = \exp\left(iaA_\mu(n)\right). \tag{2.10}$$

Since $U_\mu(n)$ lives on the links connecting the adjacent sites, they are called as link variables. Thus, all the quark fields ψ and $\bar{\psi}$ live on the lattice sites, while the gauge fields live on the links between adjacent sites.

2.2.1 Gauge action on lattice

As mentioned above, the main requirement of any lattice definition of QCD action is that they should explicitly be gauge invariant and should have proper continuum limit. The gauge invariant objects that can be formed purely from link variables are various path ordered closed loops. With this information it is very straight forward to define the lattice form of gauge action in terms of these closed loops. The simplest definition of the

lattice gauge action, S_G, is given by

$$S_G[U] = \frac{2}{g^2} \sum_{n\in\Lambda} \sum_{\mu<\nu} Re\ Tr(I - U_{\mu\nu}(n)), \tag{2.11}$$

where $U_{\mu\nu}(n)$, called the plaquette, are the smallest closed loops constructed by the product of four link variables.

$$U_{\mu\nu}(n) = U_\mu(n)U_\nu(n+\mu)U_{-\mu}(n+\mu+\nu)U_{-\nu}(n+\nu), \tag{2.12}$$

where $U_{-\mu}(n+\mu) = U_\mu^\dagger(n)$.

Expressing this gauge action in terms of the field strength tensor in the continuum and the lattice spacing one gets

$$S_G[U] = \frac{a^4}{2g^2} \sum_{n\in\Lambda} \sum_{\mu,\nu} Tr[F_{\mu\nu}(n)^2] + O(a^2). \tag{2.13}$$

In general, it is advantageous to use a gauge action with improved discretization effects defined by adding contributions from the large loops constructed out of six or more link variables to the definition given in eq. (2.11). Such an improvement is called Symanzik improvement. In our spectroscopy calculations, we use such improved gauge actions with appropriate co-efficients, to correct for the $O(a^2)$ errors in eq. (2.11). The details are discussed in the respective sections.

2.2.2 Fermion action on lattice

The continuum action for a free Fermion is given by

$$S_{_F} = \int d^4x\ \{\bar{\psi}(x)\gamma_\mu\partial_\mu\psi(x) + m\bar{\psi}(x)\psi(x)\}, \tag{2.14}$$

where the Dirac indices are suppressed for convenience. Defining the lattice derivatives as symmetric differences, a naive discretization can be made as

$$S_{_F}^{naive} = \sum_{n,\mu} \bar{\psi}_n\gamma_\mu\Delta_\mu\psi_n + m\ \sum_n \bar{\psi}_n\psi_n = \sum_{m,n} \bar{\psi}_m D_{m,n}\psi_n, \tag{2.15}$$

where $\Delta_\mu\psi_n = \frac{1}{2a}(\psi_{n+\hat{\mu}} - \psi_{n-\hat{\mu}})$ and $D_{m,n} = \frac{1}{2}\sum_\mu \gamma_\mu\{\delta_{n+\hat{\mu},m} - \delta_{n-\hat{\mu},m}\} + m\delta_{m,n}$ is called the Dirac operator.

Since Fermions are anti-commuting in nature, they are described by the Grassmann numbers. Using Matthews-Salam formula [141],

$$\int \prod_{n=1}^{N} d\bar{\psi}_n \; d\psi_n \; e^{-\sum_{i,j=1}^{N} \bar{\psi}_i D_{i,j} \psi_j} = det[D] \tag{2.16}$$

the two point functions of the Fermionic fields or the Fermion propagator can be obtained as

$$\langle \psi_i \bar{\psi}_j \rangle = -D_{ij}^{-1}. \tag{2.17}$$

The lattice free propagator in the momentum space is given by

$$\frac{1}{a} D_{naive}^{-1}(p) = \frac{-i\gamma_\mu sin(p_\mu a) + ma}{\sum_\mu sin^2(p_\mu a) + m^2 a^2}. \tag{2.18}$$

A free Fermion propagator in the continuum, $D(p) = (i\gamma_\mu p_\mu + m)^{-1}$, has its pole at $p_\mu = (0,0,0,0)$. While for the naive discretization of Fermions on the lattice, one get additional poles at $p_\mu = (\pi,0,0,0)$, $p_\mu = (0,\pi,0,0)$, ..., $p_\mu = (\pi,\pi,\pi,\pi)$ (all the corners in a Brillouin zone). Hence in the continuum, we get sixteen poles representing sixteen Fermions instead of just one Fermion. This is the (in)famous Fermion doubling problem. Associated with this is a *no-go* theorem, which has important consequences on Fermion discretization schemes This *no-go* theorem was first formulated in the Ref. [142]. It states that describing the Fermionic fields on a lattice by a transitionally invariant ($D(x,y) = D(x-y)$) Hermitian matrix that preserves the chiral symmetry and have couplings that extend over a finite number of lattice spacings, one inevitably runs into the problem of *Fermion doubling*.

Wilson Fermions

One solution to get away with Fermion doubling is to force the unwanted solutions to be heavy in the continuum limit and thus retaining only one low energy solution. Wilson Fermions involve such a solution, where one adds an irrelevant operator constructed of two derivatives.

$$S^W = r\bar{\psi} D_W \psi = -\frac{r}{2a} \sum_{n,\mu} (\psi_{n+\mu} - 2\psi_n + \psi_{n-\mu}) \sim -\frac{ar}{2} \bar{\psi} D^2 \psi, \tag{2.19}$$

where D^W is called the Wilson term forces the doublers to be heavy. With this definition, the momentum space propagator becomes

$$\frac{1}{a}D^{-1}_{naive+W}(p) = \frac{1}{a}D^{-1}_{w}(p) = \frac{-i\gamma_\mu sin(p_\mu a) + ma + r\sum_\mu(\cos(p_\mu a) - 1)}{\sum_\mu sin^2(p_\mu a) + \{ma + r\sum_\mu(\cos(p_\mu a) - 1)\}^2} \tag{2.20}$$

While the doubler modes are lifted to energies that are of the order of $1/a$ at any non-zero r, the pole at $p_\mu = (0, 0, 0, 0)$ remains unchanged and thus retaining only one low energy solution.

The Wilson term is not chiral, due to the presence of a term proportional to the mass term in it, that causes explicit breaking of chiral symmetry. Thus the chirality of the Fermion action is sacrificed in this formulation according to the aforementioned *no-go* theorem. Consequently, the Wilson action may not be able to capture the subtle effects of the spontaneous chiral symmetry breaking. This explicit symmetry breaking due to the Wilson term cannot be rectified by further adding irrelevant terms to the lattice action and is inherent to the theory. Another unpleasant disadvantage with the Wilson Fermions is that the discretization errors appears at $O(a)$, unlike the case of naïve lattice Fermions, where the discretization errors start at $O(a^2)$.

Symanzik improved Wilson Fermions

Symanzik improvement program offers a clean solution to avoid the leading cut off effects. The basic idea is to use additional terms in the action with dimension, $d > 4$, and tune the respective co-efficients such that all contributions of order $O(a^{d-4})$ are removed. First application of this methodology to remove the $O(a)$ errors in Wilson Fermions is by Sheikholeslami and Wohlert [143]. They used the counter terms up to $O(a^5)$. The only effective term at $O(a^5)$ other than the Wilson term that contribute to this improvement is

$$S^{SW} = c_{SW}\bar{\psi}\sigma_{\mu\nu}F_{\mu\nu}\psi, \tag{2.21}$$

where $F_{\mu\nu}$, known as the clover term, is the imaginary part of the sum of the four oriented loops of link variables as shown in Figure 2.1. As was mentioned for the Wilson Fermions, the addition of irrelevant terms to the lattice action does not restore the explicitly broken chiral symmetry. Thus the chiral symmetry is broken in this formulation also, in accordance with the aforementioned *no-go* theorem.

For the tree level improvement, $c_{SW} = 1$. A non-perturbative evaluation of the co-efficient, $c_{SW}(g)$ has been performed by Luscher, *et al.* [144] and an empirical form for

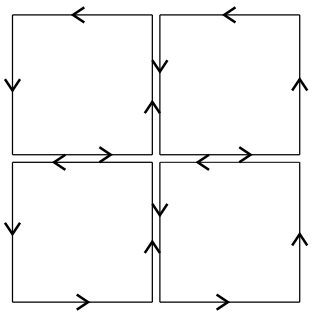

Figure 2.1: The 'clover' term

c_{SW} was obtained,

$$c_{SW} = \frac{1 - 0.656g^2 - 0.152g^4 - 0.054g^6}{1 - 0.922g^2}. \tag{2.22}$$

It is to be noted that this empirical form has been derived for isotropic lattices. While for the calculations using anisotropic lattices, we used the tree-level tadpole improved values for the spatial and temporal improvement co-efficients.

Staggered Fermions

The doublers contribute from each corner of the Brillouin zone. Staggered formulation ameliorates the doubling problem by reducing the size of the Brillouin zone from $1/a$ to $1/2a$. Effectively, the doubler Fermion degrees of freedom are distributed over a hypercube of lattice spacing 2a on the lattice. This method was originally suggested by Kogut and Susskind [145] and hence it is also known as Kogut-Susskind Fermions. The staggered Fermion action is given by

$$S_F^{ks} = \frac{1}{2a} \sum_{n,\mu} \bar{\chi}_n \alpha_\mu(n) \{\chi_{n+\hat{\mu}} - \chi_{n-\hat{\mu}}\} + m \sum_n \bar{\chi}_n \chi_n, \tag{2.23}$$

where $\alpha_\mu(n) = (-1)^{n_0+n_1+\ldots+n_{\mu-1}}$.

χ and $\bar{\chi}$ are the single component spinors. Because of the alternating nature of the sign of $\alpha_\mu(n)$, the natural unit for the staggered Fermion field is the 2^4 hypercube. The sixteen hypercube components are formed by four 'taste's of four 'Dirac component's. The taste degree of freedom corresponds to the residual doubler degree of freedom. On a finite lattice and for massless Fermions this action is invariant under

$$\psi \to e^{i\theta}\psi \qquad \& \qquad \psi \to e^{i\beta(\gamma_5 \otimes \tau_5)}\psi,$$

where τ_5 is the γ_5 matrix acting on the taste space. Thus the action has a remnant $U(1) \otimes U(1)$ chiral symmetry and this makes it useful in the study related to the chiral symmetry. With the partially preserved chiral symmetry, the assumption in the *no-go* theorem that is relaxed in this Fermion formulation is the remnant doubler degrees of freedom (taste) contributing to the low energy physics.

Associating different taste with different physical flavors were considered in many older works [146], but it was proved to be not a fruitful idea, because it is not possible to break the flavor symmetry by introducing different masses for different tastes. One alternative is to introduce new species of staggered field with its own mass for each flavor. But this comes with a penalty of having additional multiplicity : each flavor comes with its own four tastes. In common practice one uses one staggered Fermion for each flavor and take the fourth root of the Fermion determinant [146].

Overlap Fermions

One way to realize chiral Fermion on lattice is through overlap formulation invented by Narayanan and Neuberger [123]. The overlap action is given by

$$D_{ov} = 1 + \gamma_5 sgn(\gamma_5 D_w); \qquad sgn(\gamma_5 D_w) = \frac{\gamma_5 D_w}{\sqrt{\gamma_5 D_w \gamma_5 D_w}}, \tag{2.24}$$

where D_w is the Wilson Dirac Fermion operator and sgn denotes the matrix sign function. The operator possess a form of chiral symmetry on the lattice [147] :

$$\delta\psi = i\alpha\gamma_5(1 - a/2D_{ov})\psi \quad \& \quad \delta\bar{\psi} = i\alpha\bar{\psi}(1 - a/2D_{ov})\gamma_5, \tag{2.25}$$

that leaves the Fermion action invariant for any $a \neq 0$. In the continuum limit, this transformation reduces to the continuum definition of chiral transformation. Hence this is interpreted as exact chiral symmetry at $a \neq 0$ and thus the overlap operator is better suited for study of problems related to chiral symmetry. However, the presence of the matrix sign function makes the overlap operator highly non-local and so it is very expensive to implement it in numerical calculations. Thus the assumption of the local nature of the couplings in the Fermion formulation is relaxed in accordance with the *no-go* theorem.

One important symmetry of these lattice Dirac operators, that has very important

implications on numerical computations, is the γ_5-hermiticity :

$$(\gamma_5 D)^\dagger = \gamma_5 D \qquad or \qquad \gamma_5 D \gamma_5 = D^\dagger. \tag{2.26}$$

One important consequence of this property is that the eigenvalues of a γ_5-hermitian Dirac operator are either real or come in complex conjugate pairs. This implies that the Fermion determinant, which is the product of all the eigenvalues, is real and hence $det[D] = det[D^\dagger]$.

Followed by these definitions for the Fermion action in the free field theory, one can construct the Fermion action in the non-trivial gauge field theory by inclusion of the link variables, which acts as gauge transporters and make the action gauge invariant. In our calculations dealing with excited state spectroscopy, we use the $O(a)$ improved clover Fermion action on lattices with non-degenerate spatial and temporal lattice spacings (anisotropic lattices). While in the studies employing the MILC configurations, the dynamical simulations were carried out using a highly improved version of the staggered quarks (HISQ) [121] and the spectroscopy calculations used overlap quarks. In the finite temperature studies, the clover improved Wilson Fermions were used on isotropic lattices.

2.3 Numerical calculations using lattice QCD

In this section, we briefly discuss how simulations and spectroscopy calculations are performed numerically using the lattice formulation of the theory of QCD.

2.3.1 Simulations using lattice QCD

Following the discretization of the space-time and the definition of the gauge and the Fermion fields on the lattice, we move on to the discussion of how simulations are performed on the lattice. The Fermion fields are represented by anti-commuting Gramssmann valued field variables so as to satisfy the Fermi statistics. Since there is no existing realization of the Grassmann valued variables on a computer, one integrates out the Fermion degrees of freedom and obtain the partition function as

$$Z = \int D[U]\ e^{-S_G} \prod_{f=1}^{N_f} \det[D_f] \tag{2.27}$$

. Given eq. (2.26), for mass degenerate pair of quark flavors in dynamical simulations with a γ_5-hermitian Dirac operator, this weight factor ($\prod_{f=1}^{N_f} \det[D_f]$) will be positive definite real number, which is a requirement for the application of Monte Carlo methods.

$$\det[D]\det[D] = \det[D]\det[D^\dagger] = \det[DD^\dagger] \geq 0. \tag{2.28}$$

Monte Carlo techniques

Although the lattice formulation of the QCD in a finite sized box reduces the problem of infinite degrees of freedom to a problem of finite degrees of freedom, the partition function, Z, is still very large dimensional and naïve numerical integrations are not possible even on small lattice within finite time. The structural equivalence (Section 2.1) of the quantum field theories and statistical mechanics comes to aid here. Monte Carlo techniques, originally developed in the context of statistical mechanics, can be utilized to find a representative sequence of statistically independent field configurations, $\{\Omega\}$, on which the observables can be measured such that

$$\langle O(\Omega)\rangle_\Omega \simeq \frac{1}{Z}\sum_i e^{-S_i} O(\Omega_i). \tag{2.29}$$

The underlying idea behind the Monte Carlo methods is as follows : Since the number of configurations is very large, the weight factor for most of the configurations, Ω_i, is very small. Hence a simple set of randomly picked configurations from a uniform distribution would result in a very bad convergence of eq. (2.29) and so highly inefficient. In Monte Carlo technique, one performs an importance sampling, in which the configuration sequence is generated with a probability distribution $P(\Omega)$ equal to the weight factor in eq. (2.27).

$$P(\Omega) = \frac{1}{Z}\, e^{-S_G} \prod_{f=1}^{N_f} \det[D_f]. \tag{2.30}$$

Markov process is a method to generate such a sequence of configurations that represent the whole ensemble. The idea is to pick a new configuration, Ω', with a transition probability, $T(\Omega, \Omega')$, which depends only on the current configuration, Ω, and Ω'. The procedure is repeated, so that after some time of thermalisation, the equilibrium, which satisfies eq. (2.29), is reached. The transition probability, $T(\Omega, \Omega')$ should posses two important properties, so that it is a Markov process and hence guarantees the approach to the equilibrium distribution after the initial period of thermalisation.

1. *Strong ergodicity* : For every Ω and Ω',

$$T^N(\Omega, \Omega') > 0 \qquad \text{for every } \Omega \text{ and } \Omega'.$$

   In other words, every configuration should be reachable in finite number of updates, N.

2. The transition probability, $T(\Omega, \Omega')$, should be a map of $P(\Omega)$ to itself.

$$P(\Omega') = \int d\Omega P(\Omega) T(\Omega, \Omega') \qquad \text{for every } \Omega'.$$

It can be shown that the $\langle O(\Omega) \rangle$ evaluated on an ensemble generated from such a Markov chain indeed approaches the ensemble average, $\langle O \rangle$, with a statistical uncertainty of the order of $\frac{1}{\sqrt{n}}$. Here n is the number of configurations in the set, $\{\Omega\}$. Simulations for the finite temperature studies were performed using a combination of one heat bath and three over-relaxation updates [140]. While the gauge configurations, that were used in these spectrum calculations, were generated with the Rational Hybrid Monte Carlo algorithm [148, 149, 150]. The details of these algorithm and the other related subtleties related with the simulations are very huge that they themselves can cover the original size of this document. Hence we omit those and refer the interested reader to the Refs. [109, 122].

The major part of the computation resource in simulations goes into the evaluation of the Fermion determinants. So as to reduce the computational intensity, simulations can also performed after putting these Fermion determinants to unity. This approximation known as quenched approximation, is equivalent to neglecting all the creation/annihilation of the quark-anti-quark pairs in the vacuum. Though this is an acute unphysical approximation, it has been surprisingly successful in many spectroscopy studies.

The finite temperature studies that are discussed in this thesis are based on the quenched approximation, where there are no quark loops allowed in the gauge configurations, while both of our works on charm baryon spectroscopy employs dynamical configurations. The excited state spectroscopy studies employ $N_f = 2$ light and 1 strange quark fields in the configuration generation, where the charm quark fields follow the quenched approximation. While the MILC configurations used for spectroscopy calculations were generated with $N_f = 2$ light, 1 strange and 1 charm quark fields in the lattice action.

2.3.2 Spectroscopy on the lattice

All numerical simulations of lattice QCD begins with the determination of the low lying hadron masses. Since most of the masses are experimentally known to a high precision, the comparison of these to the numerical estimates is an important check to the lattice formulation of QCD. Other lattice QCD calculations, like matrix elements, thermodynamic properties, also begin with the spectroscopy calculation of the low lying hadron masses. In this section, we brief the theory behind conventional spectroscopy calculations.

Using the standard time evolution of a Hamiltonian system, a two point correlation function can be expressed as

$$\langle \hat{O}_i(t)\hat{O}_j^\dagger(0)\rangle = \frac{1}{Z_\mathcal{T}} Tr(e^{-\mathcal{T}H}e^{tH}\hat{O}_i e^{-tH}\hat{O}_j^\dagger), \tag{2.31}$$

where $Z_\mathcal{T}$, which is the partition function, which ensures proper normalization of the correlation function. In the limit of large $\mathcal{T}$, one can express the zero-momentum two point correlation function as a sum of contribution from the eigenstates at rest,

$$\lim_{\mathcal{T}\to\infty} \langle \hat{O}_i(t)\hat{O}_j^\dagger(0)\rangle = \sum_n \frac{\langle 0|\hat{O}_i|n\rangle\langle n|\hat{O}_j^\dagger|0\rangle}{2\ \Delta E_n}\ e^{-t\Delta E_n} = \sum_n \frac{Z_i^n Z_j^{n*}}{2\ \Delta E_n}\ e^{-t\Delta E_n}, \tag{2.32}$$

where $\Delta E_n = E_n - E_0$ is the energy difference of the eigenstate relative to the energy of the vacuum and the $Z_i^n = \langle 0|\hat{O}_i|n\rangle$ is referred to as the *overlap factors*, which carries the information about the quantum numbers of the states they represent. In Section 3.5, we will see these quantities are crucial in the determination of the spin of the extracted states. Since the calculation will be performed on a finite lattice, the $\sum_n$ is over a finite number of states. Assuming discrete spectrum in the low lying states, in the large t limit, the lowest lying state corresponding to ΔE_1 contributes significantly, while contribution from all other higher lying states can be neglected.

In brief, the first step in the lattice spectroscopy calculations is the identification / construction of the hadron interpolators [1], which are functionals of the lattice fields with the quantum number of the state one is interested in. Once the interpolators are identified / constructed, one evaluates the two point Euclidean correlation functions between them. Finally, the low lying spectrum can be extracted by performing non-linear fitting to the exponential fall of the correlation functions at large t, where the contribution from the excited sates can be neglected.

[1] Interpolator and operator refers to the same quantity and we use them here synonymously.

Consider an isovector meson operator, $O_M(x) = \bar{\psi}_u \Gamma \psi_d(x)$, where Γ carries the spin quantum numbers and the spatial description of the operator. The two point Euclidean correlators for this operator is then given by

$$\begin{aligned} \langle\ O_M(x)\ \bar{O}_M(y)\ \rangle &= \langle\ \bar{\psi}_u \Gamma \psi_d(x)\ \bar{\psi}_d \Gamma \psi_u(y)\ \rangle \\ &= -\ Tr\{\ \Gamma\ D_d^{-1}(x,y)\ \Gamma\ D_u^{-1}(y,x)\ \}, \end{aligned} \tag{2.33}$$

where $D_f^{-1}(x,y) = \langle \psi_f(x) \bar{\psi}_f(y) \rangle$. The negative sign appears due to the rearrangement of the Grassmann valued Fermion fields. From the above expression once can see that the expectation value factorizes with respect to the flavors, $\langle\ ...\ \rangle = \langle\ ...\ \rangle_{f_1} \langle\ ...\ \rangle_{f_2}$. Application of the Wick's theorem for each individual flavors expresses the correlation function as a product of the quark propagators as given in the second step of eq. (2.33). This procedure is called as Fermion contraction.

It can be seen from the eq. (2.33), the quark propagators carry no information about the quantum numbers in the interpolator and all the information about the quantum numbers of the state of interest are embedded in Γ factors. Hence, the computation of the quark propagators can be performed independently. More importantly, once all these quark propagators are computed, one can construct correlation functions for any interpolators of interest.

2.3.3 Quark propagators

To compute the hadron correlation functions, we will have to compute the quark propagators in each configurations. However, computing quark propagators from all the sites on the lattice to all the sites on the lattice (all-to-all) would not be feasible, due to the computational intensiveness and the huge memory requirement. For example, if we consider all-to-all propagators on the lattices that we use for the excited state spectroscopy ($16^3 \times 128$), quark propagator from each configuration consumes approximately 633 Terabytes of memory, which is enormously huge. The simplest solution, that is widely followed, is to put quark source (η_i) in just one point in space-time (point-to-all propagator) followed by construction of the quark propagators from them as the solutions of the matrix equations

$$D\ x_i = \eta_i, \tag{2.34}$$

where D is the Dirac matrix. However, for operators that are non-local, one may need to compute point-to-all propagators using quark sources at multiple space-time points. We

employ novel smearing techniques to circumvent these necessities, the details of which are described in the Section 3.4.7.

In general, this system of linear equations (eq. (2.34)) are solved by iterative methods such as Conjugate Gradient (CG) for symmetric positive definite matrices, the MINRES-method for symmetric non-definite matrices or Bi-Conjugate Gradient (BiCG) method for non-symmetric matrices. These details of the quark propagator generation are either described in brief or referred to literature in the respective sections.

2.4 Summary

In this chapter, we briefly discuss the QCD in the continuum (Section 2.1) and how it is formulated on a lattice, so as to perform numerical computations (Section 2.2 and 2.3). In Section 2.2, we discuss the details about the standard discretization scheme for the gauge fields and the various lattice realization of Fermionic fields along with the main pros and cons in each of the realizations. In Section 2.3, we briefly discuss the basic idea behind Monte Carlo simulations and the spectroscopy calculations using lattice QCD. This chapter serves as a fundamental building block for various topics discussed in later chapters.

Chapter 3

Excited state spectroscopy

As mentioned in the previous chapter, spectrum calculation proceeds by the construction of the two point correlation function on the lattice, followed by fitting them with non-linear fit forms and extracting the energy spectrum of QCD from the exponential fall of these correlation functions at large Euclidean times. While the ground state energy can be determined fairly straight forward from the correlations at large time, the extraction of the excited state spectra is highly non-trivial. This is because the signals from the excited state appears in the sub-leading exponentials and simple multi-dimensional fits are usually unstable. In this section, we start by discussing the conventional methodology in extraction of the ground state masses from the large time exponential fall-off in Section 3.1, followed by the challenges in excited state spectroscopy on the lattice in Section 3.2. Then we discuss the solutions of these challenges including the use of anisotropic lattices, construction of large basis of carefully designed interpolators, and a good fitting technique, which also aids in reliable spin identification in Section 3.3, 3.4 and 3.5.

3.1 Conventional spectroscopy from lattice

As discussed in the previous chapter, spectroscopy proceeds by constructing the two point correlation functions between the operators with the desired quantum numbers. Based on the spectral decomposition, the two point correlation function at large times behaves as

$$C(t) \sim Ae^{-Et}, \tag{3.1}$$

where E is the energy gap of the ground state from the vacuum. If the energy gap between the ground state and the excitations are large enough, the ground state can

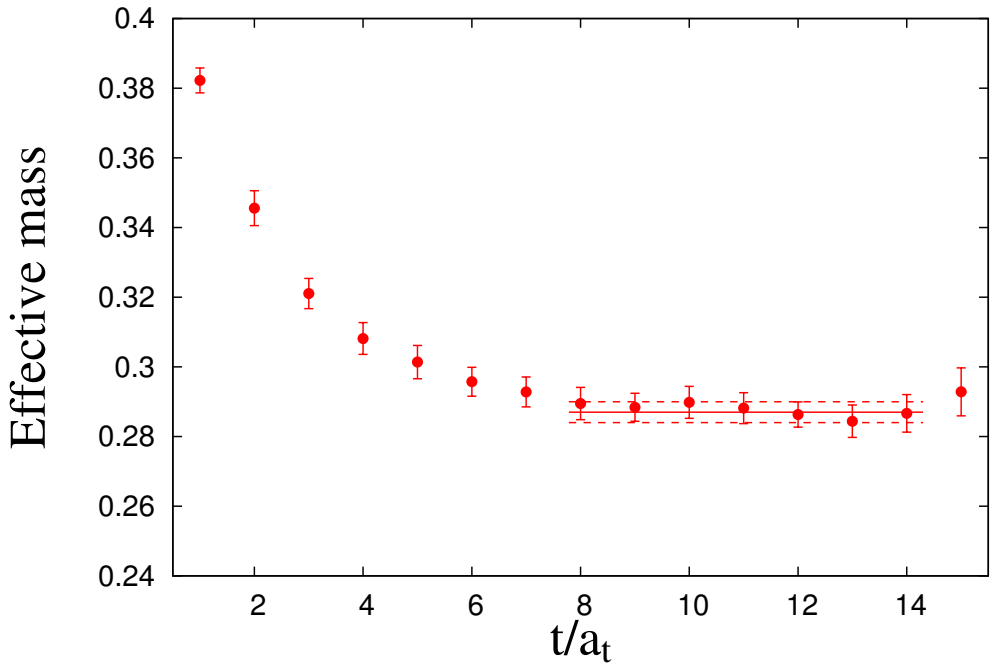

Figure 3.1: The plot of effective mass versus the time slice, showing the plateau in the effective mass at large times. At short times, the contribution from the excited states is clearly visible from the approach to the plateau. The fit value is an estimate using the fit range {8-14}.

be extracted reliably by fitting it with single exponential at large Euclidean times. The non-negligible contamination of the excited states will be evident as the instability in the fit range. This can also be viewed in terms a local fit estimate, known as *effective mass* or *local mass*, which is defined as

$$a_t \; m_{eff} = ln(\frac{C(t)}{C(t+1)}). \tag{3.2}$$

This quantity helps to visualize the decaying contribution from the excited states in the correlation function as the approach to plateau in effective masses.

The final step in the extraction is to compare the fit estimates with the plateau in the effective mass plot. This method is very efficient as the effective masses are very much visually appealing than the correlation functions itself, as the correlation function involves numbers that differ in magnitude by many orders. Thus, reliable fits can be made in those ranges with negligible contribution from the higher lying states to the

effective masses by ensuring a stable plateau in the fitted range of time slices. In Figure 3.1, we show a sample effective mass plot, where the best fit result (fit range {8-14}) is also plot. One need to be careful with the fact that, if the covariance between the time-slices are large then the good fit range may not pass through the effective masses.

3.2 Challenges in excited state heavy hadron spectroscopy

Though the basic procedure in all spectroscopy calculations on the lattice are similar and fairly straight forward, the challenges in the excited state heavy hadron spectroscopy are multiple fold. The first obvious difficulty is attributed to the heaviness of the quark in the heavy hadrons. The discretization errors in a lattice fermion action and the Fermionic observables are quoted in terms of the dimensionless quantity am, where m is the quark mass. The typical lattice spacings that are used for the light hadron spectroscopy ($\mathcal{O}(0.1\ fm)$), cannot be used for the heavy quark systems, as they will provide very large discretization errors to the estimates. For rapidly decreasing successive corrections from the higher order terms in am, one requires $am << 1$, so that one can neglect the contributions beyond some order of am. This requires one to use a lattice with very fine spacing between the lattice points, so that $am << 1$. Further, the physical states comprised of heavy quarks, being heavy, the correlations fall very rapidly with the Euclidean time. Employing very fine lattices in the calculation becomes a requirement due to this necessity for high temporal resolution at very early time slices.

The study of excited states also comes with various difficulties. Lepage analysis [151] of fluctuations in hadron correlations shows that while signal-to-noise ratio (SNR) in meson correlations is a constant with Euclidean time, the SNR in baryon correlations falls exponentially. The argument is as follows. The signal for mesons and baryons can be extracted from the respective correlations. While the fluctuations in such correlations are given by C^2, which goes as $\sigma_M^2(\tau) \sim e^{-2\ m_\pi \tau}$ for mesons and $\sigma_B^2(\tau) \sim e^{-3\ m_\pi \tau}$ in baryons. This is because each quark propagator is uncorrelated with any other in a gauge field and does not know which physical state it is part of. Hence the variance in the baryon correlations are dominated by the state with three pions, and hence $\sigma_B(\tau)$ falls much more slowly than the signal as $3/2 m_\pi < m_B$. Further, for the excited states,

the scenario is much worse as $3/2m_\pi << m_B^*$ and the SNR goes as

$$\lim_{\tau\to\infty} \frac{C_B(\tau)}{\sigma_B(\tau)} \propto \sqrt{N_{cfg}}\; e^{-(m_B^* - 3/2m_\pi)\tau} \tag{3.3}$$

Employing a very fine lattice serves as a naive solution here also. We can extract the energy of the resonances from very early time slices, where the signals from the desired correlations may not have eclipsed by the noise. But using very fine lattice spacings along all the four dimensions is extremely costly. So we follow a formalism, in which the temporal lattice spacing, along which the correlations are measured, is much finer compared to the spatial lattice spacings, while keeping the latter unchanged. This allows one to reduce the huge computational necessity that will arise from reducing lattice spacing in all four dimensions, while keeping the discretization errors under control. This formalism, known as anisotropic formalism [109, 152, 153, 154, 155], is briefly discussed in Section 3.3.

Another major difficulty is in the extraction of the excited state spectrum using conventional fitting procedures. In principle, one can perform multi-parameter fits to get the information about the higher excited states. But in general, the stability of the fits degrades very fast with the addition of each successive exponentials to the fit form. Hence it is desirable to have the correlation functions such that contributions from the higher lying states to the state being studied are suppressed, while keeping contribution from the state of interest intact. The solution to this problem is to perform a careful construction of large basis of interpolating operators, which can overlap strongly with various physical states. Marrying this with a novel smearing technique, called distillation, provides an efficient method to compute the two point correlation functions for the large basis of operators, in addition to suppressing the contribution from the higher lying states to the state being studied. Details of this construction of the operators and the use of distillation are discussed in detail in Section 3.4.

In addition to the computation of the correlation functions with improved signal from the physical states, one also require to have a good analysis procedure in their extraction along with precise determination of the respective quantum numbers. A reliable identification of the spin-parity quantum numbers of a state is highly non-trivial on the lattice. We use the variational fitting method so as to extract the spectrum of baryon states from the matrix of correlation functions using large basis of interpolators. Section 3.5 discusses the details about the variational fitting method. We also discuss the procedure we follow to identify the quantum number of the extracted state from these lattices with

single lattice spacing using the overlap factors, Z_i^n.

3.3 Anisotropic lattice

A possible solution for the issues related to the discretization errors as well as the rapid decay of the temporal correlations is to increase the temporal resolution by adopting a very fine lattice spacing along the Euclidean time direction, while keeping the spatial lattice spacing same. This reduces the huge computational efforts that would have come from reducing the spacing in all lattice directions [109, 152, 153, 154, 155]. In this work, we adopt such an anisotropic dynamical lattice formulation to extract the highly excited charm baryon spectra.

We use the anisotropic $N_f = 2 + 1$ flavor dynamical gauge configurations generated by the Hadron Spectrum Collaboration (HSC)[109]. For the gauge sector, a Symanzik-improved action was used. With tree level tadpole improved coefficients [111], the action is given by

$$S_G^{\xi}[U] = \frac{\beta}{N_c \gamma_g} \left(\sum_{x,s<s'} \left[\frac{5\mathcal{P}_{ss'}}{3u_s^4} - \frac{\mathcal{R}_{ss'}}{12u_s^6} \right] + \sum_{x,s} \left[\frac{4\mathcal{P}_{st}}{3u_s^2 u_t^2} - \frac{\mathcal{R}_{st}}{12u_s^4 u_t^2} \right] \right), \tag{3.4}$$

where $\mathcal{P}$ is the plaquette and $\mathcal{R}$ is the 2+1 rectangular Wilson loop. In order to preserve the positive definiteness of the transfer matrix, length-two rectangle in time were omitted from the action. The coupling g^2 appears in the $\beta = \frac{2N_c}{g^2}$. The parameter γ_g is the bare gauge anisotropy and u_s and u_t are the spatial and temporal tadpole improvement factors, dividing the spatial and temporal gauge links respectively. This action has leading discretization errors $O(\alpha_s^4, a_t^2, g^2 a_s^2)$.

For fermions, we use an anisotropic Shekholeslami-Wohlert fermion (clover) action, with tree level tadpole improvement and three dimensional stout link smeared gauge fields. In terms of the dimensionless variables, $\hat{m}_0 = m_0 a_t$, $\hat{\nabla}_\mu = a_\mu^2 \nabla_\mu$, $\hat{\Delta}_\mu = a_\mu \Delta_\mu$, the 'Wilson operator' : $\hat{W}_\mu = \hat{\nabla}_\mu - \frac{\gamma_\mu}{2}\hat{\Delta}_\mu$ and the clover term : $\hat{F}_{\mu\nu} = a_\mu a_\nu F_{\mu\nu}$, the fermion action is given by

$$\begin{aligned} S_F^{\xi}[U, \bar{\psi}, \psi] \;=\; & \sum \bar{\psi}(x) \frac{1}{\tilde{u}_t} (\tilde{u}_t \hat{m}_0 + \hat{W}_t + \frac{1}{\gamma_f} \sum_s \hat{W}_s \\ & - \frac{1}{2} \left[(\frac{\gamma_g}{\gamma_f} + \frac{1}{\gamma_g^r}) \frac{1}{2\tilde{u}_t \tilde{u}_s^2} \sum_s \sigma_{st} \hat{F}_{st} + \frac{1}{\gamma_f u_s^3} \sum_{s<s'} \sigma_{ss'} \hat{F}_{ss'} \right]) \psi(x), \end{aligned} \tag{3.5}$$

where γ_f is the bare fermion anisotropy, γ_g^r is the renormalized gauge anisotropy, $\tilde{u}_s$ and $\tilde{u}_t$ are the spatial and temporal tadpole improvement factors associated with the three dimensional stout smeared gauge fields and $\sigma_{\mu\nu} = \frac{1}{2}[\gamma_\mu, \gamma_\nu]$. Finer details of the formulation, the determination of the tadpole factors and the improvement co-efficients, the tuning of the anisotropy coefficients and the algorithms employed in the simulation of these lattices are detailed in the Ref. [109].

Lattice size	$a_t m_\ell$	$a_t m_s$	N_{cfgs}	m_K/m_π	m_π/MeV	$a_t m_\Omega$
$16^3 \times 128$	-0.0840	-0.0743	96	1.39	391	0.2951(22)

Table 3.1: Properties of the gauge-field ensembles used. N_{cfgs} is the number of gauge-field configurations.

The important lattice parameters required for this work is summarized in the Table 3.1. The temporal lattice spacing, a_t, was determined using the Ω-baryon mass measured on these ensembles [110]. This leads to $a_t^{-1} = 5.67(4)$ GeV. On these lattices we find $m_c a_t << 1$, which validates the use of these lattices to study the charm physics. With an anisotropy close to 3.5, $a_s = 0.12$ fm. This gives a spatial extent of about 1.9 fm, which would be sufficient to study charm baryons, in particular doubly and triply charm baryons.

The charm quarks were not included in the sea during generation of these lattices. It is expected that the effects due to the absence of the dynamical charm quark loops in this calculation will be small, as the disconnected diagrams are OZI suppressed. Liu, *et al.* [106, 107] initiated the study of charm hadron spectroscopy using these lattices and the construction of clover fermion perambulators (equivalent of quark propagator, see Section 3.4.7). The action parameters for the charm quark, including the fermion anisotropy and the temporal and the spatial clover co-efficients, are obtained by ensuring that the mass of the η_c meson takes its physical value and its dispersion relation at low momentum is relativistic. In their studies, the preliminary tests they made to estimate the contribution of disconnected diagrams to the hyperfine splitting in charmonium showed that this contribution is negligibly small.

3.4 Construction of baryon operators

After addressing the issue of discretization, the next challenge is to construct a large basis of baryon interpolating operators, such that they project on to the desired states

of interest. In this section, we discuss the construction of baryon interpolating operators using up to two derivatives, such that they project up to $J = \frac{7}{2}$ states with both even and odd parities. We follow the prescription given in [101]. The details about the construction of the operators used for the study also provides insight into the results obtained from the numerical studies. Since our calculations are performed in a hyper-cubic lattice, all the operators that we use should be classified according to the symmetry on the lattice, rather than the full symmetry of the continuum space-time. As the lattice spacing is made quite small, we expect to recover the symmetry of the continuum space-time. Since we are only interested in spectroscopy, restricting ourselves to the zero-momentum correlations, we require that our operators should transform according to the irreps of the double-cover octahedral group, O_h^D. The methodology involves first constructing a basis of baryon interpolating operators in the continuum with well-defined continuum spin-parity quantum numbers. These continuum operators are then subduced/reduced to the irreducible representations (irrep) of the double-cover octahedral group on the lattice. The correlation functions, constructed out of these octahedral operators, are expected to show rotational symmetry breaking artefacts in these calculations due to the reduced symmetry on a lattice. However, we observe, as will be discussed in Section 3.6, an effective rotational symmetry from the primary spin identification tests and that the symmetry breaking effects are very small. In the next section, we will be discussing these tests in detail with examples.

3.4.1 Continuum baryon interpolating operators

All hadrons are color singlet objects and thus they form totally anti-symmetric combinations in the color indices of its constituents. Since baryons are fermions made of three quarks, their interpolating operators excluding the color part should be totally symmetric combinations of all the quark labels representing flavor, spin and the spatial structure. The overall flavor-spin-spatial structure of a continuum baryon interpolating operator with quantum numbers, J^P, can be decomposed into a combination as

$$O^{[J^P]} = \left[\mathcal{F}_{\Sigma_F} \otimes \mathcal{S}_{\Sigma_S} \otimes \mathcal{D}_{\Sigma_D}\right]^{J^P}, \tag{3.6}$$

where $\mathcal{F}$, $\mathcal{S}$ and $\mathcal{D}$ are flavor, Dirac spin and spatial projection operators respectively and the subscripts stands for the symmetry in the respective subspaces. For every baryon operator, we must combine the symmetry projection operators such that the resulting

baryon operator, excluding the color part, is overall symmetric. In the next subsection, we discuss the general symmetry constructions possible for three objects, based on which we construct the symmetry projection operators in individual subspaces.

3.4.2 General symmetry combinations

Before we start with construction of the continuum operators, let us look at the definite symmetries for three objects that can be labeled by x, y and z, where the first object is labeled by x, the second is labeled by y and third by z. There are four definite permutation symmetry combinations: Symmetric (S), Mixed-Symmetric (MS), Mixed-Anti-symmetric (MA) and Antisymmetric (A). They are as follows

$$\begin{aligned}
\{xyz\}_{_S} &= N_{_S}\,[\; xyz + yxz + zyx + yzx + xzy + zxy \;] \\
\{xyz\}_{_{MS}} &= N_{_{MS}}\,[\; xyz + yxz + zyx + yzx - 2xzy - 2zxy \;] \\
\{xyz\}_{_{MA}} &= N_{_{MA}}\,[\; xyz - yxz + zyx - yzx \;] \\
\{xyz\}_{_A} &= N_{_A}\,[\; -xyz + yxz + zyx - yzx + xzy - zxy \;]
\end{aligned} \tag{3.7}$$

The objects x, y and z could be identical as well, depending on which the normalization constants $N_{_S}$, $N_{_{MS}}$, $N_{_{MA}}$ and $N_{_A}$ change. For example, when all of them are different, $N_{_S} = \frac{1}{\sqrt{6}}$, and when all of them are the same, $N_{_S} = 1$. The convention used for mixed symmetries is the same as used in [101], where the MS and MA are according to whether the first two labels are symmetric or antisymmetric.

As described in eq. (3.6), baryon operators are constructed from direct products of the different projection operators corresponding to the flavor, spin and the spatial derivative labels. Each of these labels can be arranged according to the symmetry combinations above, following which they have to be combined with each other in order to make an overall symmetric object. The general rules for carrying out direct product between the symmetry combinations of independent sets to make different overall symmetries are as follows [101] :

$$\begin{aligned}
\{1\}_{_S}\{2\}_{_S} &= \{1,2\}_{_S}, & \{1\}_{_S}\{2\}_{_{MS}} &= \{1,2\}_{_{MS}}, \\
\{1\}_{_S}\{2\}_{_{MA}} &= \{1,2\}_{_{MA}}, & \{1\}_{_S}\{2\}_{_A} &= \{1,2\}_{_A}, \\
\{1\}_{_A}\{2\}_{_S} &= \{1,2\}_{_A}, & \{1\}_{_A}\{2\}_{_{MS}} &= \{1,2\}_{_{MA}}, \\
-\{1\}_{_A}\{2\}_{_{MA}} &= \{1,2\}_{_{MS}}, & \{1\}_{_A}\{2\}_{_A} &= \{1,2\}_{_S},
\end{aligned}$$

$$\frac{1}{\sqrt{2}}(+\{1\}_{MS}\{2\}_{MS} + \{1\}_{MA}\{2\}_{MA}) = \{1,2\}_{S},$$
$$\frac{1}{\sqrt{2}}(-\{1\}_{MS}\{2\}_{MS} + \{1\}_{MA}\{2\}_{MA}) = \{1,2\}_{MS},$$
$$\frac{1}{\sqrt{2}}(+\{1\}_{MS}\{2\}_{MA} + \{1\}_{MA}\{2\}_{MS}) = \{1,2\}_{MA},$$
$$\frac{1}{\sqrt{2}}(-\{1\}_{MS}\{2\}_{MA} + \{1\}_{MA}\{2\}_{MS}) = \{1,2\}_{A}, \tag{3.8}$$

3.4.3 Flavor symmetry structures

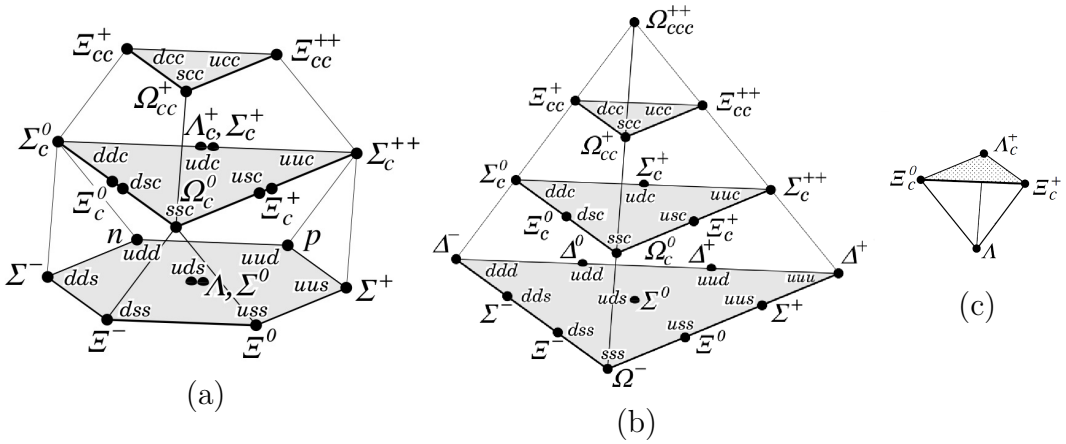

Figure 3.2: The $SU(4)$ multiplets of baryons containing u, d, s and c flavors [16]. (a) 20_M-plet containing the light-strange $SU(3)$ octet, (b) 20_S-plet containing the light-strange $SU(3)$ decuplet and (c) 4_A-plet containing the light-strange $SU(3)$ singlet

Figure 3.2 shows the $SU(4)_F$- classification of the baryons containing the u, d, s and c flavor quarks. The lowest plane in all these diagrams represent the octet, decuplet and the singlet in the light-strange $SU(3)_F$ symmetric flavor sector. With the approximation that $m_u \sim m_d$ (the theory has an approximate isospin symmetry) and m_s being only an order of magnitude heavier, we see in nature that this multiplet structure is nearly followed. But due to very heavy mass of the charm quark, we believe that there could be very strong mixing between various multiplets in the physical states. Though this symmetry is greatly broken to the large non-degeneracy in the masses, these provide a good bookkeeping systematics for the large set of baryons that are allowed based on quark models. The layers, except the lowest, constitutes of the charm baryons. With only three different flavors simultaneously possible, the flavor wave functions of the charm baryon operators can be constructed to be members of $SU(3)_F$ multiplets as $3 \otimes 3 \otimes 3 = 10_S \oplus 8_{MS} \oplus$

$8_{MA} \oplus 1_A$. These represent a subset of states from the larger group of $SU(4)_F$ which has a decomposition based on symmetry considerations as $4 \otimes 4 \otimes 4 = 20_S \oplus 20_{MS} \oplus 20_{MA} \oplus 4_A$. Table 3.2 contains the details of the flavor symmetry constructions possible for various charm baryons.

20_M					
	I	I_z	S	$\mathcal{F}_{MS}$	$\mathcal{F}_{MA}$
Λ_c^+	0	0	0	$\frac{1}{\sqrt{2}}(\|cud\rangle_{MS} - \|udc\rangle_{MS})$	$\frac{1}{\sqrt{2}}(\|cud\rangle_{MA} - \|udc\rangle_{MA})$
Σ_c^{++}	1	+1	0	$\|uuc\rangle_{MS}$	$\|uuc\rangle_{MA}$
Σ_c^{+}	1	0	0	$\|ucd\rangle_{MS}$	$\|ucd\rangle_{MA}$
Σ_c^{0}	1	−1	0	$\|ddc\rangle_{MS}$	$\|ddc\rangle_{MA}$
$\Xi_c^{\prime +}$	$\frac{1}{2}$	$+\frac{1}{2}$	−1	$\|ucs\rangle_{MS}$	$\|ucs\rangle_{MA}$
$\Xi_c^{\prime 0}$	$\frac{1}{2}$	$-\frac{1}{2}$	−1	$\|dcs\rangle_{MS}$	$\|dcs\rangle_{MA}$
Ξ_c^{+}	$\frac{1}{2}$	$+\frac{1}{2}$	−1	$\frac{1}{\sqrt{2}}(\|cus\rangle_{MS} - \|usc\rangle_{MS})$	$\frac{1}{\sqrt{2}}(\|cus\rangle_{MA} - \|usc\rangle_{MA})$
Ξ_c^{0}	$\frac{1}{2}$	$-\frac{1}{2}$	−1	$\frac{1}{\sqrt{2}}(\|cds\rangle_{MS} - \|dsc\rangle_{MS})$	$\frac{1}{\sqrt{2}}(\|cds\rangle_{MA} - \|dsc\rangle_{MA})$
Ω_c^{0}	0	0	−2	$\|scs\rangle_{MS}$	$\|scs\rangle_{MA}$
Ξ_{cc}^{++}	$\frac{1}{2}$	$+\frac{1}{2}$	0	$\|ccu\rangle_{MS}$	$\|ccu\rangle_{MA}$
Ξ_{cc}^{+}	$\frac{1}{2}$	$-\frac{1}{2}$	0	$\|ccd\rangle_{MS}$	$\|ccd\rangle_{MA}$
Ω_{cc}^{+}	0	0	−1	$\|ccs\rangle_{MS}$	$\|ccs\rangle_{MA}$

20_S				
	I	I_z	S	$\mathcal{F}_S$
Σ_c^{++}	1	+1	0	$\|uuc\rangle_S$
Σ_c^{+}	1	0	0	$\|ucd\rangle_S$
Σ_c^{0}	1	−1	0	$\|ddc\rangle_S$
Ξ_c^{+}	$\frac{1}{2}$	$+\frac{1}{2}$	−1	$\|ucs\rangle_S$
Ξ_c^{0}	$\frac{1}{2}$	$-\frac{1}{2}$	−1	$\|dcs\rangle_S$
Ω_c^{0}	0	0	−2	$\|ssc\rangle_S$
Ξ_{cc}^{++}	$\frac{1}{2}$	$+\frac{1}{2}$	0	$\|ccu\rangle_S$
Ξ_{cc}^{+}	$\frac{1}{2}$	$-\frac{1}{2}$	0	$\|ccd\rangle_S$
Ω_{cc}^{+}	0	0	−1	$\|ccs\rangle_S$
Ω_{ccc}^{++}	0	0	0	$\|ccc\rangle_S$

4_A				
	I	I_z	S	ϕ_A
Λ_c^{+}	0	0	0	$\|udc\rangle_A$
Ξ_c^{+}	$\frac{1}{2}$	$+\frac{1}{2}$	−1	$\|ucs\rangle_A$
Ξ_c^{0}	$\frac{1}{2}$	$-\frac{1}{2}$	−1	$\|dcs\rangle_A$

Table 3.2: Flavor symmetry structures for charm baryons. I in the first column stands for the isospin, I_z in the second column is for the third component of isospin and S in the third column is for the strangeness.

With only one kind of flavor available, the Ω_{ccc} baryon, like the Δ and Ω baryons, appears only in the S flavor construction. While all those baryons with two of the quarks having identical flavor, which is different from that of the third quark, can appear in the S, the MS and the MA flavor constructions. The doubly charm baryons, Σ_c and the Ω_c baryons falls in this category. While the Ξ_c baryon that have all the three quarks in three

different flavor can appear in all the symmetry constructions. Λ_c baryon, for which all three quark flavors are different, being an isospin singlet, can appear only with MS, MA and A flavor constructions.

3.4.4 Dirac spin symmetries

The Dirac matrices in the Dirac-Pauli representation can be expressed as a direct product of two $SU(2)$ components : one for ordinary spin (s-spin) and the other for intrinsic parity (ρ-spin), where the $SU(2)$ components are generated by 2×2 Pauli matrices corresponding to the two component Pauli spinor ($\begin{smallmatrix}+\\-\end{smallmatrix}$) [100]. This representation of Dirac matrices is convenient for constructing the symmetry combinations that exists in the Dirac labels. Expressed in terms the $SU(2)_\rho \otimes SU(2)_\sigma$ matrices, $\gamma_4 = \rho_3 \otimes \sigma_4$, where $\rho_3 = diag[1,-1]$ and $\sigma_4 = diag[1,1]$. Thus the Dirac index $\mu = 1,2,3,4$ is equivalent to a two-dimensional superscript corresponding to ρ-spin ($\rho = +1,-1$) and a two-dimensional subscript corresponding s-spin ($\sigma = +1,-1$), and the quark field may be expressed as $\psi^\mu = q^\rho_\sigma$. The mapping of Dirac indices (μ) to the ρ and s labels are as given in Table 3.3(a). We refer to the ρ value as ρ-parity because of its role in the parity transformations (γ_4 is the parity transformation operator).

Using a two component Pauli spinor, σ-spin, and the formula in eq. (3.7), one gets the following symmetry combinations for a three quark system, with total spin $\frac{3}{2}$, $\frac{1}{2}$ and $\frac{1}{2}$ for the symmetric (S), mixed symmetric (MS) and mixed antisymmetric (MA) combinations respectively.

$$
\begin{aligned}
S: \quad & \left|\tfrac{3}{2},+\tfrac{3}{2}\right\rangle = \left|+++\right\rangle_S; \qquad \left|\tfrac{3}{2},+\tfrac{1}{2}\right\rangle = \left|++-\right\rangle_S; \\
& \left|\tfrac{3}{2},-\tfrac{1}{2}\right\rangle = \left|+--\right\rangle_S; \qquad \left|\tfrac{3}{2},-\tfrac{3}{2}\right\rangle = \left|---\right\rangle_S; \\
MS: \quad & \left|\tfrac{1}{2},+\tfrac{1}{2}\right\rangle = \left|+-+\right\rangle_{MS}; \qquad \left|\tfrac{1}{2},-\tfrac{1}{2}\right\rangle = -\left|-+-\right\rangle_{MS}; \\
MA: \quad & \left|\tfrac{1}{2},+\tfrac{1}{2}\right\rangle = \left|+-+\right\rangle_{MA}; \qquad \left|\tfrac{1}{2},-\tfrac{1}{2}\right\rangle = -\left|-+-\right\rangle_{MA}.
\end{aligned}
\tag{3.9}
$$

Only the operators formed by considering a two component Pauli spinor ($\rho = +1$), which form the upper two components of the four component Dirac spinor (μ), appear in the leading order in a velocity expansion of any baryon operator. The baryon operators constructed purely from such a two component Pauli spinor is hence non-relativistic in nature. Those based on the lower components of Dirac spinors are relativistic. A full relativistic formulation requires consideration of the $\rho = -1$ sector as well, hence one uses the full four component Dirac spinor instead of the two component Pauli spinor.

The symmetry constructions for the ρ-spins also follow similarly. The direct product of the ρ-spin and the σ-spin follows the rules as described in eq. (3.8), and yields sums of three-quark terms in which each quark has a ρ and s label representing its Dirac index. The construction of the symmetry combinations for full four component Dirac spinor using the symmetry patterns from ρ-spin and s-spin is detailed in Table 3.3(b).

Dirac	ρ	s
1	+	+
2	+	−
3	−	+
4	−	−

(a)

D	IR	Emb	$\mathcal{S} = \rho \otimes s$
S	$\frac{1}{2}$	1	$\frac{1}{\sqrt{2}}\big(+ \|\rho\rangle_{MS}\|s\rangle_{MS} + \|\rho\rangle_{MA}\|s\rangle_{MA}\big)$
	$\frac{3}{2}$	1, 2	$\|\rho\rangle_S\|s\rangle_S$
MS	$\frac{1}{2}$	1, 2	$\|\rho\rangle_S\|s\rangle_{MS}$
		3	$\frac{1}{\sqrt{2}}\big(- \|\rho\rangle_{MS}\|s\rangle_{MS} + \|\rho\rangle_{MA}\|s\rangle_{MA}\big)$
	$\frac{3}{2}$	1	$\|\rho\rangle_{MS}\|s\rangle_S$
MA	$\frac{1}{2}$	1, 2	$\|\rho\rangle_S\|s\rangle_{MA}$
		3	$\frac{1}{\sqrt{2}}\big(+ \|\rho\rangle_{MS}\|s\rangle_{MA} + \|\rho\rangle_{MA}\|s\rangle_{MS}\big)$
	$\frac{3}{2}$	1	$\|\rho\rangle_{MA}\|s\rangle_S$
A	$\frac{1}{2}$	1	$\frac{1}{\sqrt{2}}\big(- \|\rho\rangle_{MS}\|s\rangle_{MA} + \|\rho\rangle_{MA}\|s\rangle_{MS}\big)$

(b)

Table 3.3: (a) : Mapping of Dirac spin indices to ρ and s labels. (b) Table taken from Ref. [101] : Symmetries of Dirac spin states based on direct products of ρ-spin and s-spin states for three quarks. $|\rho\rangle_{\Sigma_\rho}$ and $|s\rangle_{\Sigma_s}$ refer to a ρ-spin and s-spin state with Σ_ρ and Σ_s symmetries respectively. Direct products of the ρ-spin and s-spin states yield sums of three-quark terms in which each quark has a ρ and s label. These two labels together determines each quark's Dirac index according to (a).

From the above discussion, it is clear that using spatially local constructions the total spin of baryon can have only two values, 1/2 or 3/2. The flavor and non-relativistic spin can be combined in an approximate spin flavor $SU(6)$ whereby the multiplets are $6 \otimes 6 \otimes 6 = 56_S \oplus 70_M \oplus 70_M \oplus 20_A$. These can again be decomposed into flavor $SU(3)$ multiplets as $56 = {}^4 10 \oplus {}^2 8$, $70 = {}^2 10 \oplus {}^4 8 \oplus {}^2 8 \oplus {}^2 1$, $20 = {}^2 8 \oplus {}^4 1$, where the superscript (2S+1) gives the spin for each particle in the $SU(3)$ multiplet. The wave functions of the 56-plet can be combined with local or non-local spatial projections to make the non-color component of the wave function symmetric, while the wave functions of the 70 and 20-plets require some non-local excitations of the spatial part to make the overall non-color component of the wave function symmetric. With the four component Dirac spinors, the actual construction of the operators corresponds to $SU(12)$, which is built up from the subgroups according to $SU(12) = SU(3)_F \otimes SU(2)_\rho \otimes SU(2)_s$. The details of the local operators constructed from the symmetries in the flavor and Dirac spin sector, forming the $SU(12)$ group, is tabulated in the Table 3.4.

Σ	$^{SU(3)}_{SU(2)}$	$N_{\rm nr}$	$N_{\rm r}$		
S	$(\mathbf{10},\mathbf{4})$	1	1	$\phi_{\mathsf{S}}\chi_{\mathsf{S}}$	
	$(\mathbf{10},\mathbf{2})$		1	$\phi_{\mathsf{S}}\chi_{\mathsf{S}}$	
	$(\mathbf{8},\mathbf{4})$		1	$\frac{1}{\sqrt{2}}(\phi_{\mathsf{MS}}\chi_{\mathsf{MS}}+\phi_{\mathsf{MA}}\chi_{\mathsf{MA}})$	
	$(\mathbf{8},\mathbf{2})$	1	2	$\frac{1}{\sqrt{2}}(\phi_{\mathsf{MS}}\chi_{\mathsf{MS}}+\phi_{\mathsf{MA}}\chi_{\mathsf{MA}})$	
	$(\mathbf{1},\mathbf{2})$		1	$\phi_{\mathsf{A}}\chi_{\mathsf{A}}$	
M	$(\mathbf{10},\mathbf{4})$		1	MS $\phi_{\mathsf{S}}\chi_{\mathsf{MS}}$	MA $\phi_{\mathsf{S}}\chi_{\mathsf{MA}}$
	$(\mathbf{10},\mathbf{2})$	1	2	$\phi_{\mathsf{S}}\chi_{\mathsf{MS}}$	$\phi_{\mathsf{S}}\chi_{\mathsf{MA}}$
	$(\mathbf{8},\mathbf{4})$	1	1	$\phi_{\mathsf{MS}}\chi_{\mathsf{S}}$	$\phi_{\mathsf{MA}}\chi_{\mathsf{S}}$
	$(\mathbf{8},\mathbf{4})$		1	$\frac{1}{\sqrt{2}}(-\phi_{\mathsf{MS}}\chi_{\mathsf{MS}}+\phi_{\mathsf{MA}}\chi_{\mathsf{MA}})$	$\frac{1}{\sqrt{2}}(\phi_{MS}\chi_{\mathsf{MA}}+\phi_{\mathsf{MA}}\chi_{\mathsf{MS}})$
	$(\mathbf{8},\mathbf{2})$		1	$\phi_{\mathsf{MS}}\chi_{\mathsf{S}}$	$\phi_{\mathsf{MA}}\chi_{\mathsf{S}}$
	$(\mathbf{8},\mathbf{2})$	1	2	$\frac{1}{\sqrt{2}}(-\phi_{\mathsf{MS}}\chi_{\mathsf{MS}}+\phi_{\mathsf{MA}}\chi_{\mathsf{MA}})$	$\frac{1}{\sqrt{2}}(\phi_{\mathsf{MS}}\chi_{\mathsf{MA}}+\phi_{\mathsf{MA}}\chi_{\mathsf{MS}})$
	$(\mathbf{8},\mathbf{2})$		1	$\phi_{\mathsf{MA}}\chi_{\mathsf{A}}$	$\phi_{\mathsf{MS}}\chi_{\mathsf{A}}$
	$(\mathbf{1},\mathbf{4})$		1	$\phi_{\mathsf{A}}\chi_{\mathsf{MA}}$	$\phi_{\mathsf{A}}\chi_{\mathsf{MS}}$
	$(\mathbf{1},\mathbf{2})$	1	2	$\phi_{\mathsf{A}}\chi_{\mathsf{MA}}$	$\phi_{\mathsf{A}}\chi_{\mathsf{MS}}$
A	$(\mathbf{10},\mathbf{2})$		1	$\phi_{\mathsf{S}}\chi_{\mathsf{A}}$	
	$(\mathbf{8},\mathbf{4})$		1	$\frac{1}{\sqrt{2}}(\phi_{\mathsf{MS}}\chi_{\mathsf{MA}}-\phi_{\mathsf{MA}}\chi_{\mathsf{MS}})$	
	$(\mathbf{8},\mathbf{2})$	1	2	$\frac{1}{\sqrt{2}}(\phi_{\mathsf{MS}}\chi_{\mathsf{MA}}-\phi_{\mathsf{MA}}\chi_{\mathsf{MS}})$	
	$(\mathbf{1},\mathbf{4})$	1	1	$\phi_{\mathsf{A}}\chi_{\mathsf{S}}$	
	$(\mathbf{1},\mathbf{2})$		1	$\phi_{\mathsf{A}}\chi_{\mathsf{S}}$	

Table 3.4: Local baryon operators classified according to symmetry of the flavor and the four component Dirac spin. The first element inside the braces in the second column shows the dimensionality of the $SU(3)_{\mathcal{F}}$ representation, while the second element shows the dimensionality of the Dirac spin projections. The third column is the number of Dirac spin embeddings in non-relativistic ($\rho = +$) construction, while those constructions involving the lower two components also are shown in the fourth column. The multiplicity of operators in the non-relativistic case is 56_S, 70_{MS}, 70_{MA} and 20_A, and corresponds to the conventional non-relativistic $SU(6)$ construction. The relativistic construction, which involves both positive and negative parity operators, corresponds to the reduction of $SU(12)$. Table taken from [101].

3.4.5 Spatial projection operator symmetries

In order to project the higher spin baryons ($J > 3/2$) and the excited baryon states, one needs to employ baryon operators that create states with angular and radial excitations. Such excitations can be explored using baryon operators with non-local behavior. Covariant derivatives defined in Ref. [100] are incorporated into the three quark operators in order to obtain suitable representations that transform like orbital angular momentum. First the covariant derivatives are combined in the definite symmetries with respect to

their action on the three quark fields. At the single derivative level, there are two relevant symmetry combinations transforming like an $L = 1$ object. They are

$$\begin{aligned} L = 1; \quad D^{[1]}_{MS}(m) &= \frac{1}{\sqrt{6}}\{2D^{(3)}_m - D^{(1)}_m - D^{(2)}_m\}, \\ D^{[1]}_{MA}(m) &= \frac{1}{\sqrt{2}}\{D^{(1)}_m - D^{(2)}_m\}, \end{aligned} \tag{3.10}$$

where the different m-components in $D^{(q)}_m$, which acts on the q-th quark, are given by

$$D^{(q)}_{\pm 1} = \pm\frac{i}{2}(D^{(q)}_x \pm iD^{(q)}_y), \quad D^{(q)}_0 = -\frac{i}{2}D^{(q)}_z \tag{3.11}$$

The superscript inside the square brackets in eq. (3.10), stands for the number of derivatives in the operator being represented. There is no totally antisymmetric construction of the one derivative and the symmetric combination $D^{(1)} + D^{(2)} + D^{(3)}$ is a total derivative that gives zero when applied to a baryon with zero momentum. Totally symmetric baryon operators with one derivative are constructed by applying eq. (3.10) to the mixed symmetric spin-flavor operators as given in Table 3.4.

$$\psi^{[1]}_S = \frac{1}{\sqrt{2}}\big(D^{[1]}_{MS}\psi^{[0]}_{MS} + D^{[1]}_{MA}\psi^{[0]}_{MA}\big), \tag{3.12}$$

where the superscripts in brackets indicate the number of derivatives in the operator.

The two derivative baryon operators are constructed as follows. Initially, definite symmetry combinations of two derivatives are formed using the single derivatives, based on the same general rules of combination of two symmetry labels (see eq. (3.8)). The three quark symmetry combinations with two derivatives that transform like $L = 0, 1, 2$ are as follows,

$$\begin{aligned} L = 0, 2; D^{[2]}_S &= \frac{1}{\sqrt{2}}\{D^{[1]}_{MS}D^{[1]}_{MS} + D^{[1]}_{MA}D^{[1]}_{MA}\}, \\ L = 0, 2; D^{[2]}_{MS} &= \frac{1}{\sqrt{2}}\{-D^{[1]}_{MS}D^{[1]}_{MS} + D^{[1]}_{MA}D^{[1]}_{MA}\}, \\ L = 0, 2; D^{[2]}_{MA} &= \frac{1}{\sqrt{2}}\{D^{[1]}_{MS}D^{[1]}_{MA} + D^{[1]}_{MA}D^{[1]}_{MS}\}, \\ L = 1; D^{[2]}_A &= \frac{1}{\sqrt{2}}\{-D^{[1]}_{MS}D^{[1]}_{MA} + D^{[1]}_{MA}D^{[1]}_{MS}\}. \end{aligned} \tag{3.13}$$

Using these two derivative symmetric constructions one can construct the totally symmetric baryon interpolators by applying them on the local baryon operators. They are as follows.

$$\psi_S^{[2]} = D_S^{[2]}\psi_S^{[0]}; \quad \frac{1}{\sqrt{2}}(D_{MS}^{[2]}\psi_{MS}^{[0]} + D_{MA}^{[2]}\psi_{MA}^{[0]}); \quad D_A^{[2]}\psi_A^{[0]}, \tag{3.14}$$

where no total derivatives are considered in these constructions. In Table 3.5, we give the different derivative operators that can be constructed using two derivatives.

	L=0,2	L=1
S	$(\mathrm{qqq})_{1_c}$	0
M	$(\mathrm{qqq})_{1_c}$	$[(\mathrm{qqq})_{8_c}\ \mathrm{G}_{8_c}]_{1_c}$
A	0	$(\mathrm{qqq})_{1_c}$

Table 3.5: Summary of the bound state interpretations of the two derivative structures. Table taken from Ref. [108]

The subset of operators, as given in Table 3.5, that follows the MS and MA constructions, with angular momentum, $L = 1$, corresponds to a commutation of the two gauge-covariant derivatives acting on the same quark field [108]. Note that such operators form color singlet object, $[(qqq)_{8_c}G_{8_c}]_{1_c}$, as a combination of the three quarks in color octet and a gluon field, G. Such operators vanish in a theory without the gauge fields and corresponds to the chromomagnetic components of the gluonic field strength tensor. This leads to the identification of the so-called *hybrid* operators, as they are formed out of a hybrid combination of quark and gluon fields. As will be observed later, operators that are proportional to the gluon field strength tensor are essential in obtaining some states in the spectrum.

These spatial projection operators with definite symmetries are then combined with the symmetry combinations constructed out of the Dirac spin projection operators using the standard Clebsch-Gordan formula of SU(2) in order to obtain operators with good J in the continuum. Table 3.6 shows the details of the allowed spin-parity patterns of the non-relativistic local and non-local operators for various symmetries in the flavor sector. We show the constructions up to two derivatives. Using non-relativistic components alone, it is not possible to construct a negative parity state with a spin higher than 5/2, even with operators that include two derivatives. Use of relativistic operators along with non-relativistic ones enables us to extract states with spin up to 7/2 for both the parities.

We follow the same naming convention as used in Ref. [101]. As an example, Ω_{css} oper-

ator with spin and parity of the three quarks as $\frac{3}{2}^-$, with two derivatives coupled into $L = 2$ and total spin and parity $J^P = \frac{7}{2}^-$, is denoted as $\left(\Omega_{css,S} \otimes (\frac{3}{2}^-_{1,M}) \otimes D^{[2]}_{L=2,M}\right)^{J^P=\frac{7}{2}^-}$, where the subscripts show the definite symmetries in different labels. Accounting for the orbital motion classifies the total symmetry in a non-relativistic approach to be $SU(6) \otimes O(3)$ super-multiplets with the $O(3)$ describing the orbital motion. With four component Dirac spinors, the construction of the operators corresponds to $SU(12) \otimes O(3)$.

3.4.6 Subduction into lattice irreps

Discretization reduces the symmetry of the space from $O(3)$ to O_h^D. The eigenstates of the lattice Hamiltonian transforms as irreps of the O_h^D. With the reduced symmetry, the continuum states get separated across the lattice irreps. Restricting the operators in the continuum to the symmetries allowed by the lattice generates the representations of these continuum operators that are reducible under O_h^D. Subduction is this method of generating the representations of the continuum irreducible operators, which are reducible under O_h^D in terms of the lattice irreps. Once the continuum operators are constructed, we subduce them to the irreps of the octahedral group.

The octahedral group consists of 24 group elements, each corresponding to a rotation that leaves invariant a cube, or an octahedran embedded within the cube. When the objects that are rotated involve half-integer values of angular momentum, the number of group elements doubles to extend the range of rotational angles from 2π to 4π, forming doubled-valued representations of the octahedral group, giving the irreps for half integer spins also. Spatial inversion commutes with all rotations and together with identity forms a two-element point group simply doubling the number of group elements.

The eight irreps of the double-valued representations of the octahedral group include A_1, A_2, E, T_1 and T_2 for integer spins and G_1, G_2 and H for half-integer spins. The continuum spins are distributed over these eight irreps on a lattice. Since we consider only baryons, we discuss only the appearance of the continuum spins over different lattice irreps for half integer spins (G_1, G_2 and H). The irreps of the octahedral group are determined only by the s-spins and the derivative structures. A $J = 1/2$ spin state appears only in G_1 irrep. A spin of $J = 3/2$ appears only in H irrep. A continuum spin of $J = 5/2$ distributes itself across G_2 and H irrep, while $J = 7/2$ appears over G_1, G_2

				$N(J^P)$						
F	N_D	L	S	$\frac{1}{2}^+$	$\frac{3}{2}^+$	$\frac{5}{2}^+$	$\frac{7}{2}^+$	$\frac{1}{2}^-$	$\frac{3}{2}^-$	$\frac{5}{2}^-$
S_F	0	0	$\frac{3}{2}$		1					
	1	1	$\frac{1}{2}$					1	1	
	2	0	$\frac{1}{2}$	1						
	2	0	$\frac{3}{2}$		1					
	2	**1**	$\mathbf{\frac{1}{2}}$	**1**	**1**					
	2	2	$\frac{1}{2}$		1	1				
	2	2	$\frac{3}{2}$	1	1	1	1			
A_F	1	1	$\frac{1}{2}$					1	1	
	2	0	$\frac{1}{2}$	1						
	2	1	$\frac{3}{2}$	1	1	1				
	2	**1**	$\mathbf{\frac{1}{2}}$	**1**	**1**					
	2	2	$\frac{1}{2}$		1	1				
M_F	0	0	$\frac{1}{2}$	1						
	1	1	$\frac{1}{2}$					1	1	
	1	1	$\frac{3}{2}$					1	1	1
	2	0	$\frac{1}{2}$	1						
	2	0	$\frac{1}{2}$	1						
	2	0	$\frac{3}{2}$		1					
	2	**1**	$\mathbf{\frac{1}{2}}$	**1**	**1**					
	2	**1**	$\mathbf{\frac{3}{2}}$	**1**	**1**	**1**				
	2	1	$\frac{1}{2}$	1	1					
	2	2	$\frac{1}{2}$		1	1				
	2	2	$\frac{3}{2}$	1	1	1	1			
	2	2	$\frac{1}{2}$		1	1				

Table 3.6: The number of operators of a given J^P that can be constructed from up to two derivatives acting on non-relativistic quark spinors. N_D indicates the number of covariant derivatives, S indicates the total spin of the quarks and L indicates the total orbital angular momentum. The row indicated in bold face contains the two-derivative *hybrid* operators, which vanish in the absence of a non-trivial gluon field.

and H. A simple mathematical notation of this phenomena of subduction is given by

$$\Omega^J{}_{n\Lambda,r} = \sum_m \mathcal{S}^{J,m}{}_{n\Lambda,r}\ \Omega^J_m, \tag{3.15}$$

where $\Omega^{J}{}_{n\Lambda,r}$ is the lattice operator that is the r^{th} row of the n^{th} embedding of the irrep: Λ on the continuum spin J, subduced from a continuum spin operator Ω^{J}_{m}. The $\mathcal{S}^{J,m}{}_{n\Lambda,r}$ are called the subduction coefficients.

Ω_{ccc}	G_1		H		G_2	
	g	u	g	u	g	u
Total	20	20	33	33	12	12
Hybrid	4	4	5	5	1	1
NR	4	1	8	1	3	0

(a)

Ξ_{cc}, Ω_{cc}	G_1		H		G_2	
$(S_f + M_F)$	g	u	g	u	g	u
Total	55	55	90	90	35	35
Hybrid	12	12	16	16	4	4
NR	11	3	19	4	8	1

(b)

Table 3.7: The number of lattice operators for triply (left) and doubly (right) charm baryons obtained after subduction to various irreps of operators with up to two covariant derivatives. The number of non-relativistic (NR) and hybrid operators for each irreps and for both parities are given.

Σ_c, Ω_c	G_1		H		G_2	
$(S_f + M_F)$	g	u	g	u	g	u
Total	55	55	90	90	35	35
Hybrid	12	12	16	16	4	4
NR	11	3	19	4	8	1

(a)

Λ_c	G_1		H		G_2	
$(M_F + A_F)$	g	u	g	u	g	u
Total	53	53	86	86	33	33
Hybrid	12	12	16	16	4	4
NR	10	3	17	4	7	1

(b)

Ξ_c	G_1		H		G_2	
$(S_F + M_F + A_F)$	g	u	g	u	g	u
Total	116	116	180	180	68	68
Hybrid	24	24	32	32	8	8
NR	23	6	37	10	15	2

(c)

Table 3.8: The number of lattice operators for different singly charm baryons obtained after subduction to various irreps of operators with up to two covariant derivatives. The number of non-relativistic (NR) and hybrid operators for each irreps and for both parities are given.

Considering the ρ-parity involved, one can classify these irreps into even and odd parity versions, indicated by the subscripts g (gerade) and u (ungerade). The parity of the baryon operator is determined from it $\rho \times (-1)^L$, where $\rho = \rho_1\rho_2\rho_3$ and L is the

angular momentum from the derivatives and ρ_i is the ρ-value of the i^{th} quark. For non-relativistic operators, $\rho_1 = \rho_2 = \rho_3 = 1$ always, hence its parity is solely determined by the orbital angular angular momentum.

Table 3.7 and Table 3.8 shows the total number of relativistic and non-relativistic operators constructed using the above procedure for various charm baryons. They also contain the number of non-relativistic and hybrid operators used for various charm baryons.

3.4.7 Distillation

Having constructed a large set of operators, it is possible to calculate their diagonal and off-diagonal correlation functions to extract excited states by using variational methods. However, construction of correlation functions with so many operators, particularly for the operators with one or more derivatives, is very computationally intensive as it needs extra inversions for non-local sources. The total time needed for the construction of correlation function could be as intensive as gauge field generations. To avoid this we use a recently developed novel technique, called the "*distillation method*" [96]. Using this method, one can efficiently construct a large number of correlation functions with multiple operators. Moreover, this method automatically includes a smearing process, a requirement for suppressing the high frequency modes that do not contribute significantly to the low energy regime in the spectrum and thus increases the relative contributions from the low lying states in the correlation functions. As a smearing function, the constraint on the distillation operator is that it should preserve as many symmetries as possible while effectively removing the contribution from the short distance modes.

A gauge covariant source, with a shape similar to a Gaussian is obtained by Jacobi smearing [156], where one uses a gauge covariant second order three dimensional lattice Laplacian operator,

$$-\nabla^2_{xy}(t) = 6\delta_{xy} - \sum_{j=1}^{3}\{\tilde{U}_j(x,t)\delta_{x+\hat{j},y} + \tilde{U}^{\dagger}_j(x-\hat{j},t)\delta_{x-\hat{j},y}\}, \tag{3.16}$$

where the gauge fields may be constructed from an appropriate covariant gauge field smearing algorithm. The high energy modes of this operator is suppressed by exponentiating it, $\exp(\sigma\nabla^2(t))$, with a smearing weight, σ. The resulting smoothened operator is applied on the quark fields (ψ) to construct the smeared quark fields ($\tilde{\psi}$). The suppression of the high energy modes of the Jacobi smearing operator means that only a small number of modes contribute significantly to the smeared quark fields, $\tilde{\psi}$.

The distillation technique [96] replaces the exponentiation of the Laplacian by an outer product over the low lying eigenmodes of the discretized gauge covariant Laplacian,

$$\Box_{xy}(t) = V_{xz}(t)V^{\dagger}_{zy}(t) = \sum_{k=1}^{N} \xi^{(k)}_{x}(t)\xi^{(k)\dagger}_{x}(t), \tag{3.17}$$

where $\xi^{(k)}_{x}$ are a finite number, $N << N_s^3 N_c$, of eigenvectors of ∇^2 evaluated on the background of spatial gauge fields of the time slice t, once the eigenvectors have been sorted by the eigenvalues. The number of modes, N (volume dependent), should be sufficient to sample the required angular structure of the low lying hadronic states, but is small compared to the number of sites on a time slice. Once the eigenvectors are sorted by the eigenvalues, in terms of $V(t)$, the k^{th} column of $V(t)$ contains the k^{th} eigenvector of ∇^2 evaluated on the background of the spatial gauge fields of time-slice t. This is the projection operator onto the subspace, V_N, spanned by the N lowest lying eigenmodes, so $\Box^2 = \Box$. When N is the same as N_c times the number of sites on a time-slice, then the distillation operator becomes identity, and the fields acted upon are unsmeared. In this calculation, we used 64 eigenvectors from four time slices in construction of the baryon correlation functions.

The Laplace operator inherits many symmetries of the vacuum. It transforms like a scalar under rotations, is covariant under gauge transformation and is parity and charge conjugation invariant. If the action of one of these symmetries on the Laplace operator maps ∇^2 onto $\tilde{\nabla}^2$, then there is a unitary transformation, R on the vector space spanned by the eigenmodes of the Laplacian such that

$$R\tilde{\nabla}^2 R^{\dagger} = \nabla^2. \tag{3.18}$$

This implies that if v is an eigenvector of ∇^2, then Rv is an eigenvector of $\tilde{\nabla}^2$. Considering the definition of the distillation operator, the transformed operator must obey

$$R\tilde{\Box}R^{\dagger} = \Box, \tag{3.19}$$

and so the correlation functions constructed using the distilled fields have same symmetry properties on the lattice as those constructed using the Laplacian methods.

Distilled baryon correlation functions

Here we discuss the application of the distillation technique in the construction of the hadron correlation functions and a smart representation of the correlation functions in terms of the eigenvectors of the discretized gauge covariant Laplacian, which will make their computation efficient. We take the case of the isospin-$\frac{1}{2}$ baryon as an illustrative example. A generalization is straight forward. A general baryon annihilation operator can be written as

$$O_i(t) = \epsilon^{abc} S^i_{\alpha\beta\gamma} (\mathbf{\Gamma}_1 \Box d)^a_\alpha (\mathbf{\Gamma}_2 \Box u)^b_\beta (\mathbf{\Gamma}_3 \Box u)^c_\gamma, \tag{3.20}$$

where u and d are the quark fields; $\mathbf{\Gamma}_j$ is a spatial operator, including possible spatial displacements, acting on quark j; a, b, c are the color indices, and α, β and γ are the spin indices; S encodes the spin structure of the operator, and is constructed so that the operator has the desired quantum numbers. Using eq. (3.20), we construct the baryon correlation function as

$$C_{ij}(t',t) = \epsilon^{abc}\bar{\epsilon}^{\bar{a}\bar{b}\bar{c}} S^i_{\alpha\beta\gamma} \bar{S}^{*j}_{\bar{\alpha}\bar{\beta}\bar{\gamma}} \langle [(\mathbf{\Gamma}_1 \Box d)^a_\alpha (\mathbf{\Gamma}_2 \Box u)^b_\beta (\mathbf{\Gamma}_3 \Box u)^c_\gamma (t')] . [(\bar{d}\Box\bar{\mathbf{\Gamma}}_1)^{\bar{a}}_{\bar{\alpha}} (\bar{u}\Box\bar{\mathbf{\Gamma}}_1)^{\bar{a}}_{\bar{\alpha}} (\bar{u}\Box\bar{\mathbf{\Gamma}}_1)^{\bar{a}}_{\bar{\alpha}} (t)] \rangle, \tag{3.21}$$

where the bar over S and $\mathbf{\Gamma}$ indicate these are from the creation operator. Inserting the outer product representation for distillation operator, we can write the baryon correlator as

$$C_{ij}(t',t) = \Phi^{i,(p,q,r)}_{\alpha\beta\gamma}(t') \Phi^{j,(\bar{p},\bar{q},\bar{r})}_{\bar{\alpha}\bar{\beta}\bar{\gamma}}(t) \times [\tau^{p\bar{p}}_{\alpha\bar{\alpha}}(t',t) \tau^{q\bar{q}}_{\beta\bar{\beta}}(t',t) \tau^{r\bar{r}}_{\gamma\bar{\gamma}}(t',t) - \tau^{p\bar{p}}_{\alpha\bar{\alpha}}(t',t) \tau^{q\bar{r}}_{\beta\bar{\gamma}}(t',t) \tau^{r\bar{q}}_{\gamma\bar{\beta}}(t',t)], \tag{3.22}$$

$$\text{where} \qquad \Phi^{i,(p,q,r)}_{\alpha\beta\gamma} = \epsilon^{abc} S^i_{\alpha\beta\gamma} (\mathbf{\Gamma}_1 \xi^{(p)})^a (\mathbf{\Gamma}_2 \xi^{(q)})^b (\mathbf{\Gamma}_3 \xi^{(r)})^c \tag{3.23}$$

and $\tau^{p\bar{p}}_{\alpha\bar{\beta}}(t',t) = \xi^{\dagger(\bar{p})}(t') M^{-1}_{\alpha\beta}(t',t) \xi^{(p)}$. $\Phi^{i,(p,q,r)}_{\alpha\beta\gamma}$ has a well defined momentum and all the information about the quantum numbers of the operator goes into this quantity. While $\tau^{p\bar{p}}_{\alpha\bar{\beta}}(t',t)$ is called the operator independent 'perambulator' with no explicit momentum projections. Hence the perambulators can be computed independently between any source and sink. In principle, once the τ has been computed and stored, the correlation of any local or non-local source and sink operators can be computed.

Note that both the Φ's and τ's are $4N \times 4N$ matrices. Such a decomposition of the correlation functions reduces the cost of their computation substantially. Firstly, such a decomposition enables efficient computation of correlation functions with a large basis of interpolating operators at both the source and the sink time slices. It also enables a momentum projection at both the source and the sink time slices, in contrast

with conventional spectroscopy, where a momentum projection only at sink is possible. Furthermore, it also reduces the costs of computations involving all-to-all quark propagators, since calculation of all elements of a perambulator requires only $4N$ inversions of the Dirac matrix, in contrast to $12N_s^3$ inversions for conventional all-to-all quark propagators. Thus, the 'distillation' technique allows one to perform computations involving disconnected diagrams, multihadron operators, etc. also, with limited computation resources.

3.5 Variational fitting technique

After constructing two point correlation functions (see eq. (2.31)) for a large basis of interpolating operators, the next task is the extraction of the spectrum from these matrix of correlation functions in a reliable way. We employ a variational fitting method [97, 98, 99] for this purpose. The construction of the large basis of operators has been discussed in detail in the previous section. The basic idea of variational fitting technique is to solve a generalized eigenvalue problem of the form

$$C(t)v_\alpha = \lambda_\alpha C(t_0)v_\alpha, \tag{3.24}$$

where $C(t)$ is the matrix of correlators at time-slice t. The orthonormality condition for the generalized eigenvectors is $v_\alpha^\dagger C(t_0)v_\beta = \delta_{\alpha\beta}$. The '*principal correlators*' λ_α, as a function of the times-lice, representing the physical two point correlation functions, are formed from the generalized eigenvalues of the correlation matrices on the respective time-slices and can be shown to behave at large times as

$$\lambda_\alpha(t) = e^{-m_\alpha(t-t_0)}(1 + \mathcal{O}(e^{-|\delta m|(t-t_0)})), \tag{3.25}$$

where m_α is the mass of a state labeled by α and δm is the energy splitting from the nearest excited state to α. The eigenvectors form a $dim(C) \times dim(C)$ matrix V that transform the interpolating operators into an optimum linear combination to overlap with the $dim(C)$ lightest states accessible to them. These eigenvectors should be time independent to the extent that the correlator is saturated by the lightest $dim(C)$ states. In practice, one solves the eigenvalue problem on each time-slice and obtain eigenvectors that can vary with t. The $C(t_0)$-orthogonality of these eigenvectors are then utilized to order these eigenvectors across the time slices. Examining the form of the eigenvalue in

eq. (3.24) with the substitution of the spectral decomposition in eq. (2.32) one finds that $Z_i^\alpha = (V^{-1})_i^\alpha \sqrt{2m_\alpha} e^{m_\alpha t_0/2}$. The inverse of this eigenvector matrix is trivial to compute owing to the orthonormality property $V^\dagger C(t_0) V = I \Rightarrow V^{-1} = V^\dagger C(t_0)$.

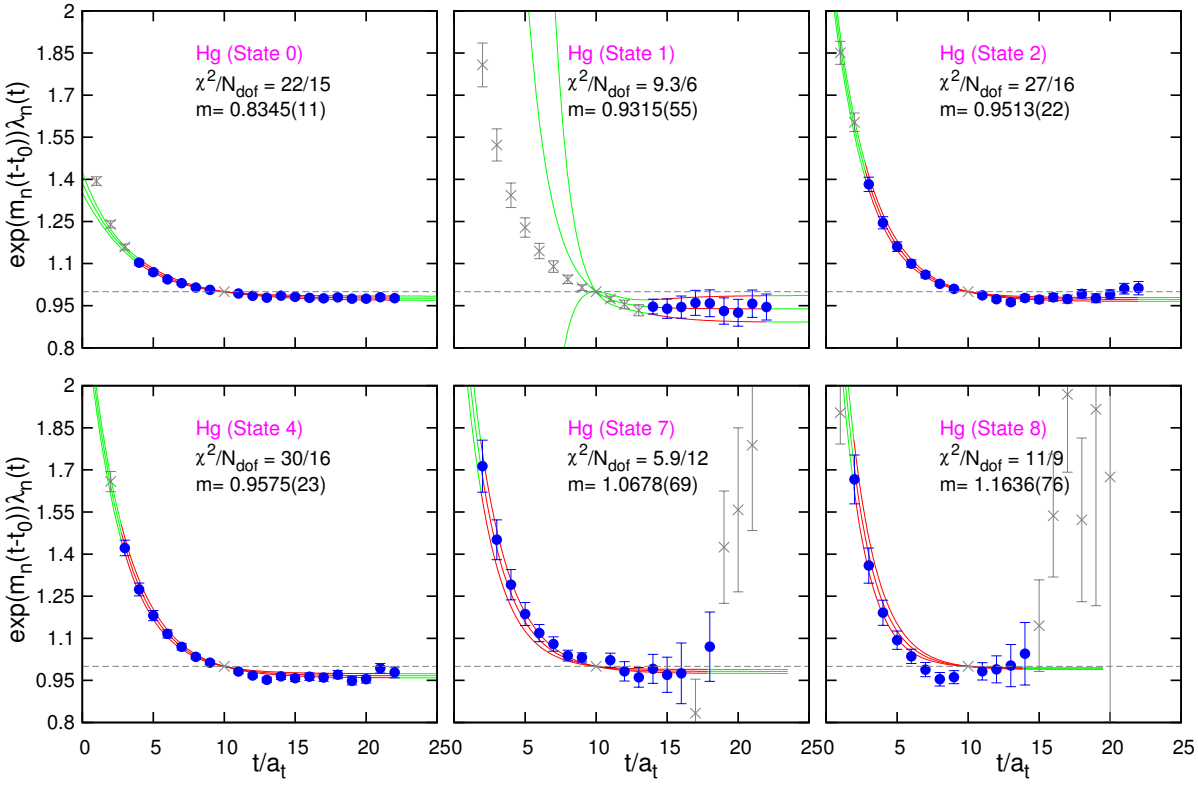

Figure 3.3: Principal correlator fits for six Ω_{ccc} states in irrep H_g that will be identified as $J^P = 3/2^+$ based on the procedure described in the Section 3.7. Fits are obtained using eq. (3.27). Data points are obtained from $e^{m_n(t-t_0)}\lambda_n(t)$ and the lines show the fits and one sigma-deviation according to the fitting form $e^{m_n(t-t_0)}\lambda_n(t) = 1 - A_n + A_n e^{-(m'_n - m_n)(t-t_0)}$, with $t_0 = 10$; the gray points are not included in the fits.

The selection of the parameter t_0 plays a crucial role as in practice one works with a limited number of interpolating operators. The eigenvectors are forced by the solution procedure to be orthogonal on the metric $C(t_0)$, which will be a good approximation to the true orthonormality, defined in continuum with an infinite number of states and operators, if the correlator at t_0 is dominated by the lightest $dim(C)$ states. The choice of the optimum t_0 is governed by two factors. The contribution from the excited states pushes the optimum value of t_0 to larger values where they would have died down significantly in the correlators, while the fall in the signal-to-noise ratio with the Euclidean time slice

urges one to keep t_0 to be as small as possible. A remedy for this is to define a χ^2 like quantity, so as to gauge how well the generalized eigenvalue problem describes the correlators for any given t_0, as [99]

$$\chi^2 = \frac{1}{\frac{1}{2}N(N+1)(t_{max}-t_0) - \frac{1}{2}N(N+3)} \sum_{i,j\geq i} \sum_{t,t'=t_0+1}^{t_{max}} (C_{ij}(t) - C_{ij}^{rec.}(t)) \mathcal{C}_{ij}^{-1}(t,t') (C_{ij}(t') - C_{ij}^{rec.}(t')) \tag{3.26}$$

where $N = dim(C)$ and $\mathcal{C}$ is the data covariance matrix for the correlator C_{ij} computed with jackknife statistics. For a given value of t_0, one gets the estimates for the masses and the overlap factors (Z) by solving the eigenvalue problem and then fitting the principal correlators. Using these mass and overlap factor estimates one can reconstruct the correlator matrix using the spectral decomposition in eq. (2.31). $C_{ij}^{rec.}$ are the correlation functions obtained from the reconstruction procedure discussed above. The optimum value of t_0 is chosen based on the minimum of the chi-square like quantity defined in eq. (3.26).

After the diagonalization procedure to obtain the optimum linear combination representing the physical states, we extract the energy of a state by fitting the dependence of λ_n on $t - t_0$ to the form,

$$\lambda_n(t, t_0) = (1 - A_n) e^{-m_n(t-t_0)} + A_n e^{-m'_n(t-t_0)}, \tag{3.27}$$

with three fit parameters m_n, m'_n and A_n. We find that allowing a second exponential stabilizes the fits and the resulting second exponential decreases rapidly with large t_0, implying that $m'_n >> m_n$. In Figure 3.3, we plot some examples of fits to six Ω_{ccc} principal correlators in irrep H_g, where the fitted states will be identified with $J^P = \frac{3}{2}^+$. The fits approach the constant value, $1 - A_n$, for large t, and they approach one if a single exponential dominates. This is seen to be the case for most of our fits.

3.6 Rotational symmetry and cross correlations

After the construction of the matrix of two point correlation functions for a large basis of interpolating operators and the extraction of the physical states employing a reliable advanced fitting technique, what remains is to make a precise determination of the quantum numbers of the extracted physical states. One primary goal of lattice calculations such as this one is such an identification of the continuum quantum numbers for the extracted physical states. As discussed earlier, lattice possess only a reduced symmetry

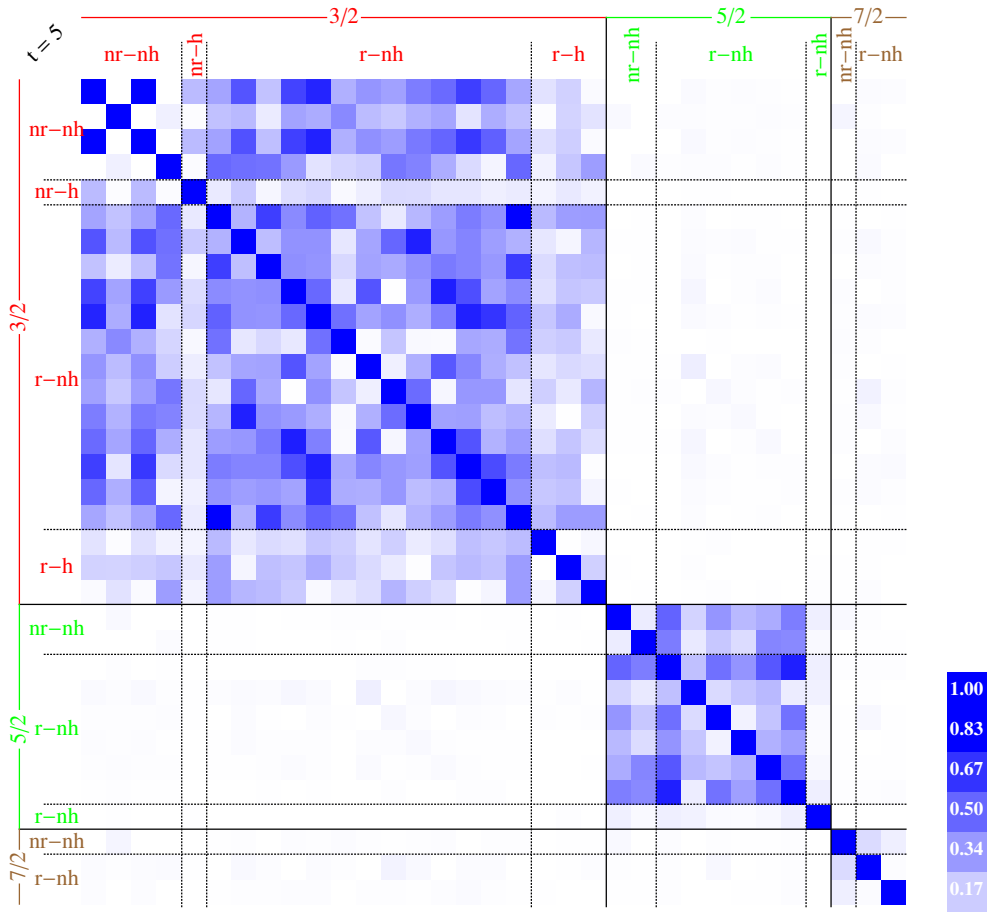

Figure 3.4: The normalized correlation matrix, $C_{ij}/\sqrt{C_{ii}C_{jj}}$, of ccc baryon at $t/a_t = 5$ for the H_g irrep averaged over all the configurations. Operators are ordered such that those subduced from spin 3/2 appear first followed by spin 5/2 and then spin 7/2.

of the continuum. And hence the physical states in the continuum gets subduced over the lattice irreps. In the continuum limit, the rotational symmetry should be restored. If the lattice is fine enough, one should be able to observe the effects of the restoration of the rotational symmetry. The use of smeared fields in construction of interpolating operators should help in making this restoration more directly observable. With the aim of creating a more direct link between the lattice operators and the physical quantum numbers, operators were constructed first in the continuum and then subduced onto the lattice irreps. Therefore, it is useful to determine whether these lattice operators exhibit a remnant of the continuum rotational symmetry on the lattice.

To check this, in Figure 3.4, we plot the normalized two point correlation functions $(C_{ij}/\sqrt{C_{ii}C_{jj}})$ of triply charm baryons in the H_g irrep at time separation 5 averaged

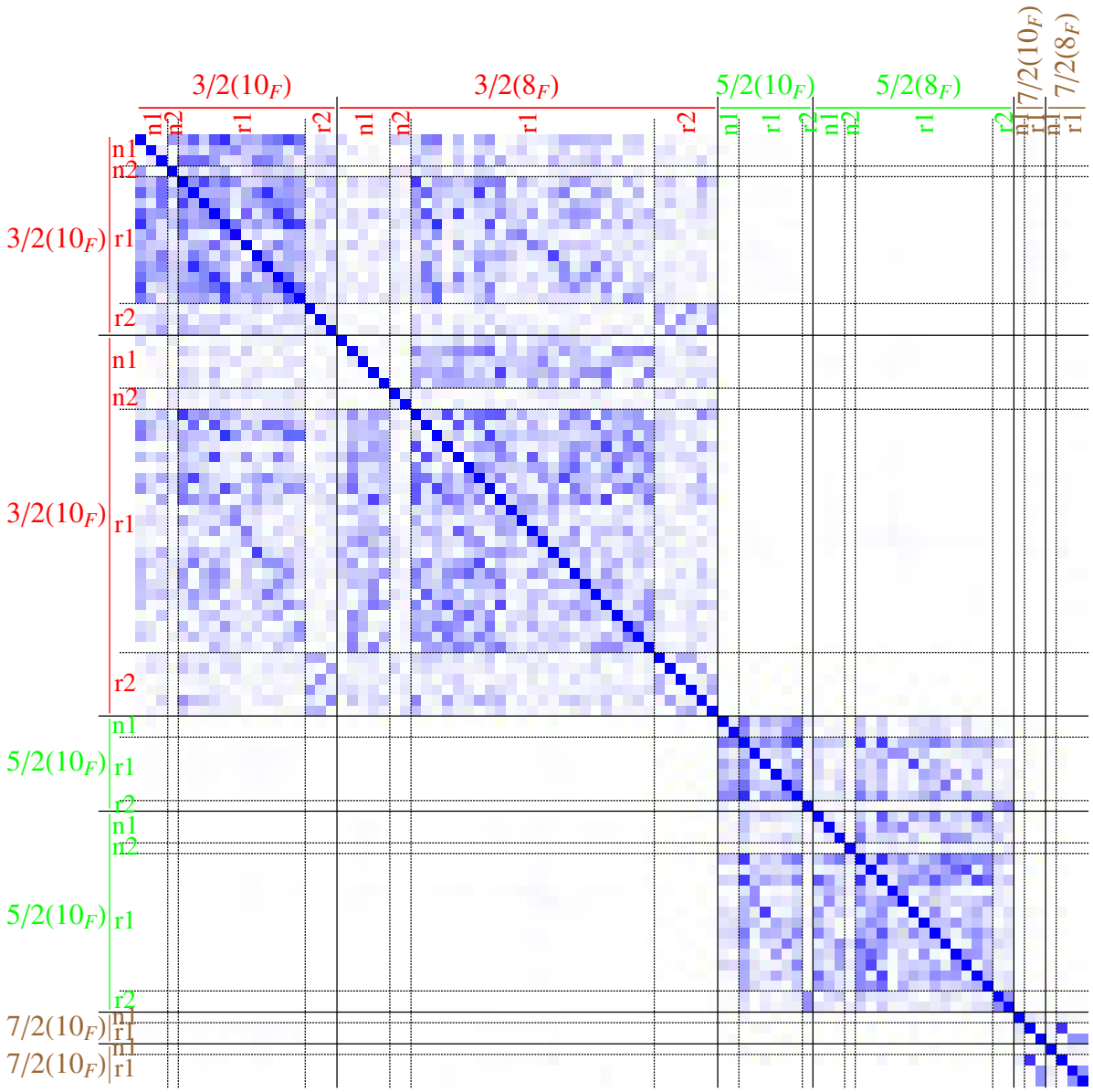

Figure 3.5: The normalized correlation matrix, $C_{ij}/\sqrt{C_{ii}C_{jj}}$, of Ω_{ccs} baryon at $t/a_t = 5$ for the H_g irrep averaged over all the configurations. Operators are ordered such that those subduced from spin 3/2 appear first followed by spin 5/2 and then spin 7/2.

across all the configurations used in the study. The normalization ensures all the diagonal entries are unity, while cross correlations are always less than 1. There are 33 operators used in this irrep, including operators up to two derivatives. The solid lines divide these operators subduced from continuum spins $\frac{3}{2}$, $\frac{5}{2}$ and $\frac{7}{2}$, and the dashed lines are used for separating operators defined above with various abbreviations (nr : non-relativistic, nh :

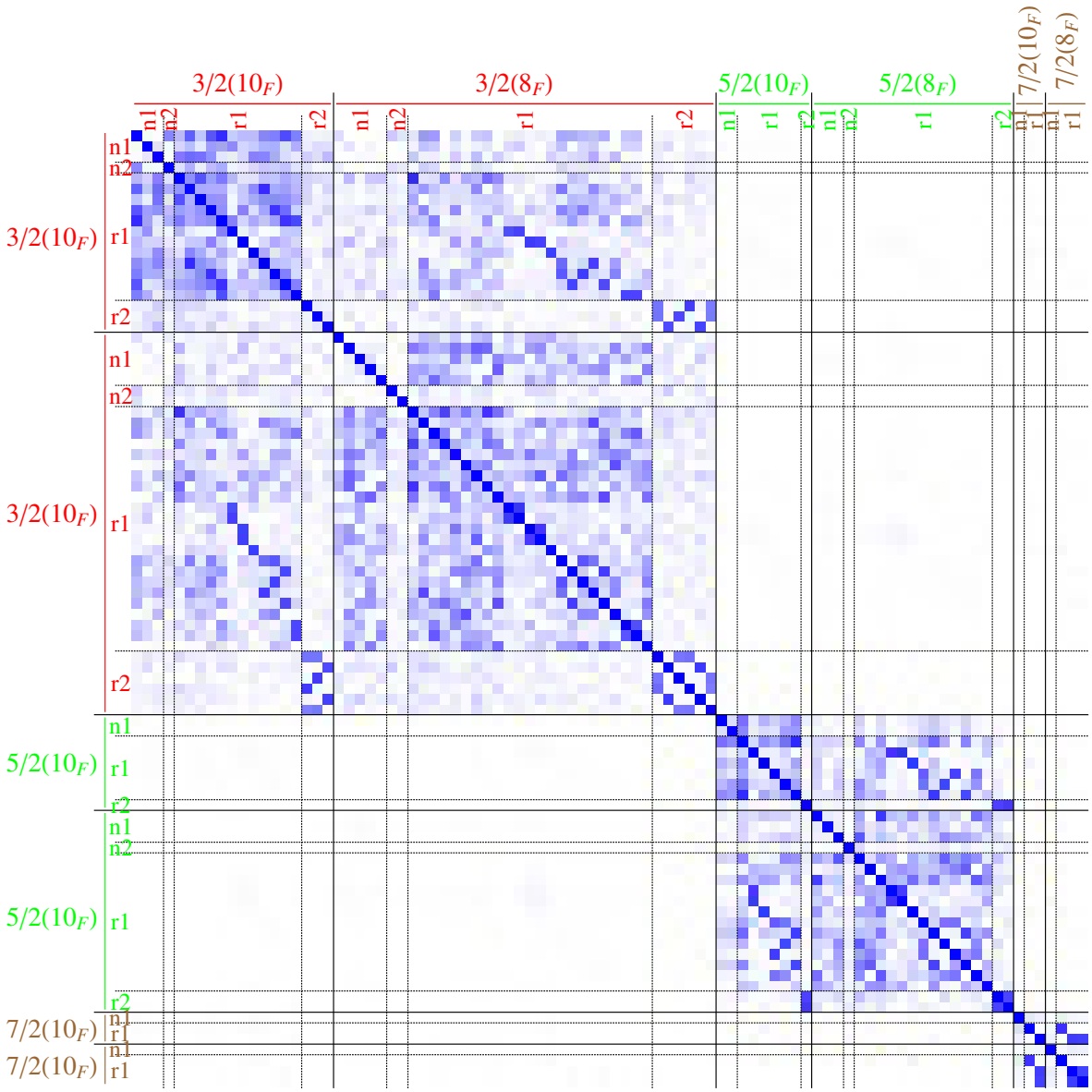

Figure 3.6: The normalized correlation matrix, $C_{ij}/\sqrt{C_{ii}C_{jj}}$, of Ω_{css} baryon at $t/a_t = 5$ for the H_g irrep averaged over all the configurations. Operators are ordered such that those subduced from spin 3/2 appear first followed by spin 5/2 and then spin 7/2.

non-hybrid, r : relativistic and h : hybrid). A breaking of the rotational symmetry on the lattice is expected to reflect in these plots in terms of the relatively large magnitude of the cross correlations between lattice operators with different continuum spin in comparison with the diagonal elements. The matrix plot can be trivially seen to show a block diagonal pattern in the various continuum spin labels. We observe similar patterns of block diagonal structure in correlation functions of other irreps as well as correlation

functions of different irreps in other charm baryons. For example, we show in Figure 3.5 and Figure 3.6 the matrix plot of correlation for the Ω_{ccs} and Ω_{css} baryons. The solid lines in these plots divides different continuum spin operators with varying flavor symmetry constructions, while the dashed lines divide various abbreviations (n1 : non-relativistic and non-hybrid, n2 : non-relativistic and hybrid, r1 : relativistic and non-hybrid, r2 : relativistic and hybrid). As mentioned above, one can trivially observe a block diagonal structure along the boundaries of different continuum spins. Similar patterns were also observed for the light ant the strange baryons [102]. These observations suggest that after subduction a remarkable degree of rotational symmetry remains in the lattice operators. And this fact gives us confidence in our ability to make unambiguous spin-identification for the charm baryons.

This analysis also aids in identifying the mixing between different operators. For example, it is evident from Figure 3.4 that there is strong mixing between 'nr-nh' and 'r-nh' type operators and comparatively weak mixing between 'h' and 'nh'-type operators. As was observed in Ref. [157], we also found additional suppression of mixing for operators with a given J, but with different L and S, compared to those with the same J, as well as the same L and S. For example, for the operators $O_1 = [(\frac{3}{2}^+_{1,S}) \otimes D^{[0]}_{L=0,S}]^{\frac{3}{2}} H_{g1}$ and $O_2 = [(\frac{3}{2}^+_{1,S}) \otimes D^{[2]}_{L=0,S}]^{\frac{3}{2}} H_{g1}$ both of which have $J = 3/2, L = 0, S = 3/2$, the matrix element $M_{12} = C_{12}/\sqrt{C_{11}\mathcal{C}_{22}} = 0.99$. On the other hand, the mixings of these operators with $O_3 = [(\frac{3}{2}^+_{1,S}) \otimes D^{[2]}_{L=2,S}]^{\frac{3}{2}} H_{g1}$ which has $J = 3/2, L = 2, S = 3/2$ are $M_{13} = 0.0026$ and $M_{23} = 0.0031$. This suppression of mixing is however evident only for the non-relativistic operators. We found that for some relativistic operators mixing enhanced between operators with same J but different L and S, compared to those with same J, L and S. This observation, particularly in the non-relativistic sector can be explained in terms of the heaviness of the charm/bottom quark. Being heavy, the spin-orbit interaction is significantly small and hence L and S acts as good quantum numbers separately. Hence those operators with same L and S values can be expected to show strong correlations as their quantum numbers match, while a cross correlation between operators with different L and S may not be significant. Similar observations can also be made in the other charm baryons also.

These plots also aid in qualitative understanding of how much the $SU(4)_F$ symmetry is violated due to very heavy charm quark mass compared to the light and strange quark masses. These violations of the flavor symmetry are expected to reflect in these matrix plots in terms of the cross correlation (mixing) between the operators from different flavor symmetry combinations. One can easily observe in Figure 3.5 and Figure 3.6 that,

the non-hybrid operators from the 10_F flavor combination, corresponding to S, show significant mixing with non-hybrid operators in the 8_F flavor combination, corresponding to MS and MA. A similar observation can also be made between the hybrid operators in two different multiplets. It is also very clear from the figures that this mixing is very strong in the singly charm baryons. Similar observations are also made in other irreps and different irreps in other charm baryons.

3.7 Spin identification

One main goal, which is a highly non-trivial task, in these lattice calculations is to ensure that any state identified can be assigned continuum quantum numbers in a reliable way. In principle, the spin of a hadron state can be determined by extracting the spectrum at various lattice spacings and then extrapolating to the continuum limit. In the continuum limit, where the $SO(3)$ symmetry gets restored, the emergence of energy degeneracies between the lattice irreps will aid us in identifying the continuum spin of the state. However, there are difficulties with this procedure. Firstly, this requires high precision calculations with successively finer lattice spacings, and hence with increasing computational demand. With the current computational resources, this procedure is hence impractical. Secondly, in the continuum limit, the spectrum can exhibit degeneracies not just arising from $SO(3)$ symmetry restoration, but also due to the physical degeneracies, like the ones due to hyperfine splittings and spin-orbit splittings. This raises the problem of identifying degeneracies due to lattice discretization unambiguously.

An alternative approach, which was detailed in Ref. [99] and used in the calculations of light baryons [101, 102], light mesons [103], charm mesons as well as heavy-light mesons [106, 107], was followed by us in these calculations. The main ingredient is the overlap factor, Z_i^n, as defined in eq. (2.32). To identify the states with spin 1/2 and 3/2 are fairly straight forward. A state with spin $\mathcal{S}$ should have large overlap factors with those operators, which are subduced from continuum spin $\mathcal{S}$. The operators with largest overlap factors to this state not only determine the quantum numbers, but also the spin and spatial structure of this state. Figure 3.7, Figure 3.8 and Figure 3.9 shows the matrix plot of normalized Z_i^n values of various states across various operators for Ω_{ccc}, Ω_{ccs} and Ω_{css} baryons respectively. The normalization of Z_i^n is given by $\frac{Z_i^n}{max_n[Z_i^n]}$, so that for a given operator the largest overlap across all states is unity. It is very easy from this plot to identify the spin of the state from the operators corresponding to darker pixels for a given state. As one can see, that the low lying states correspond to first seven

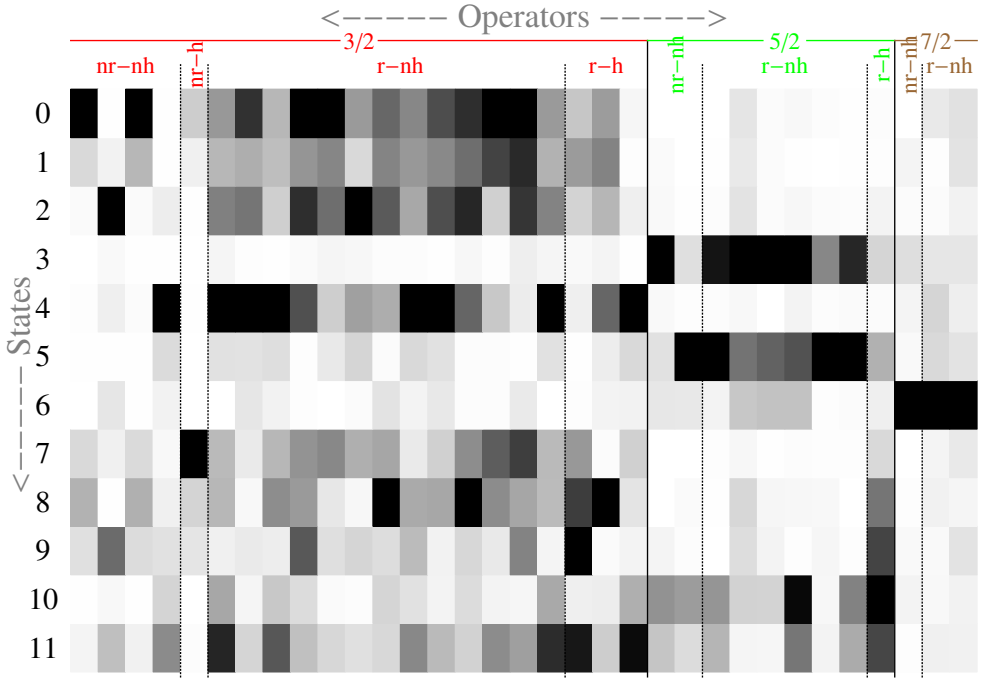

Figure 3.7: "Matrix" plot of values of overlap factor, Z_i^n, of an operator i to a given state n, as defined by eq. (2.32) for Ω_{ccc} baryon. Z_i^n are normalized according to $\frac{Z_i^n}{max_n[Z_i^n]}$, so that for a given operator the largest overlap across all states is unity. The normalized magnitudes of various operator overlaps to states in the H_g irrep are shown. Darker pixel indicates larger values of the operator overlaps. Various type of operators, for example, non-relativistic (nr) and relativistic (r) operators, as well as hybrid (h) and non-hybrid (nh) operators are indicated by column labels. In addition, the continuum spins of the operators are shown by 3/2, 5/2 and 7/2. Here one can associate state 6 with quantum number $J^P = \frac{7}{2}^+$, the states 3, 5 and 10 with $J^P = \frac{5}{2}^+$, and the rest with $J^P = \frac{3}{2}^+$. The states 7 and 9 are predominantly hybrid in nature, while states 4, 8 and 10 are found to have substantial overlap with non-hybrid operators.

states in Ω_{ccc} have very strong non-relativistic content. They also have contribution from the relativistic operators. The higher lying states can be seen to have very little overlap with the non-relativistic operators, while they overlap very significantly with the relativistic operators. Similar observation can also be made to identify the low lying states as strongly non-relativistic in nature for the other charm baryons, which is evident from the plots for Ω_{ccs} and Ω_{css} baryons. For states with spin 1/2 and 3/2, which gets subduced simply over single irrep, G_1 and H respectively, this procedure is sufficient for identification.

One can also identify certain states in these plots that have overlap with 5/2 and 7/2 spin, and not with the 3/2. However, spin - 5/2 and 7/2 states appear in multiple

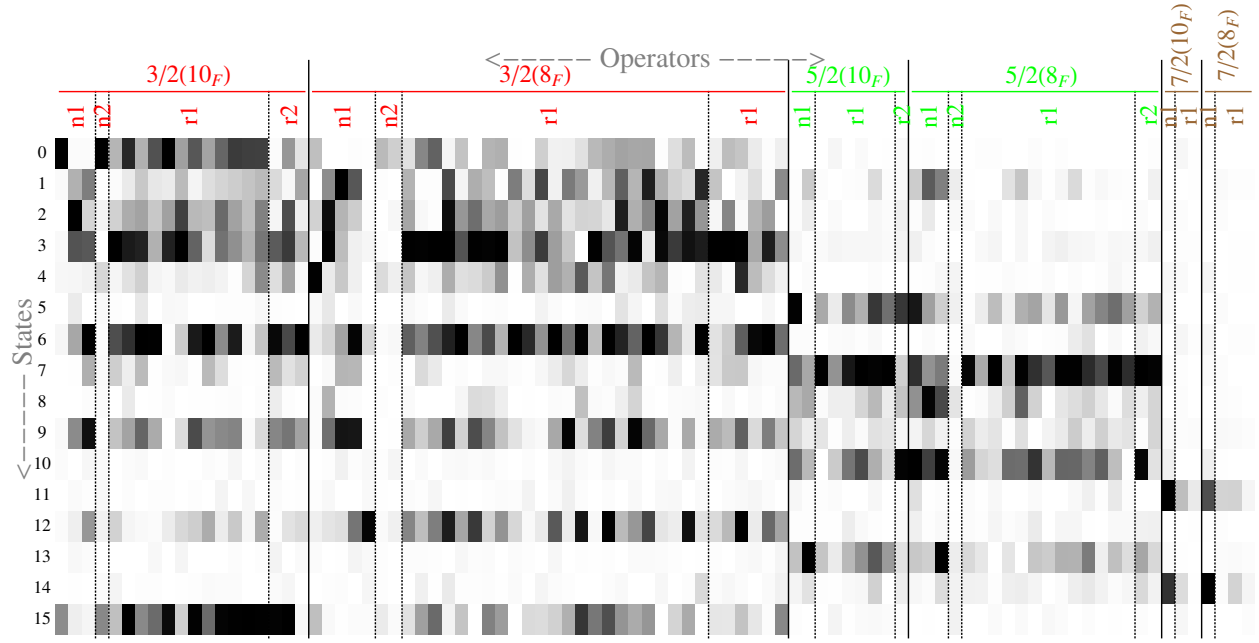

Figure 3.8: Same as in Figure 3.7, but for Ω_{ccs} baryon.

lattice irreps, as in these cases, the continuum operator is subduced to multiple lattice irreps. Identification of spin of these states is made by identifying the Z_i^n degeneracies

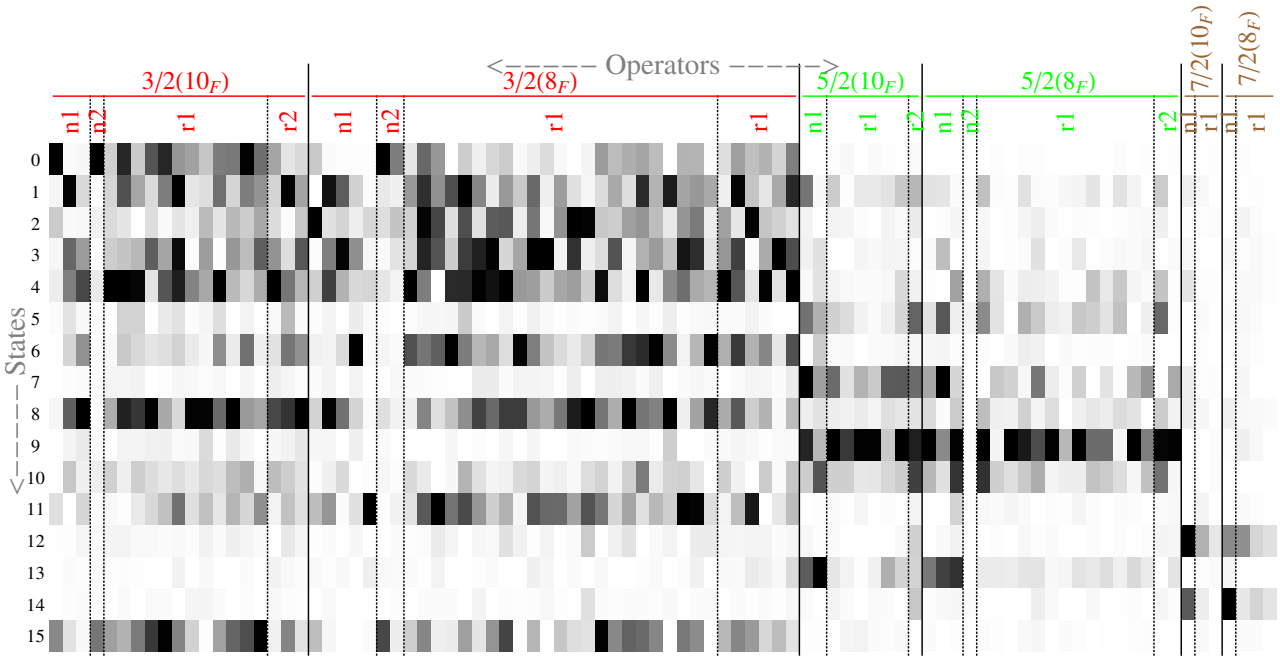

Figure 3.9: Same as in Figure 3.7, but for Ω_{css} baryon.

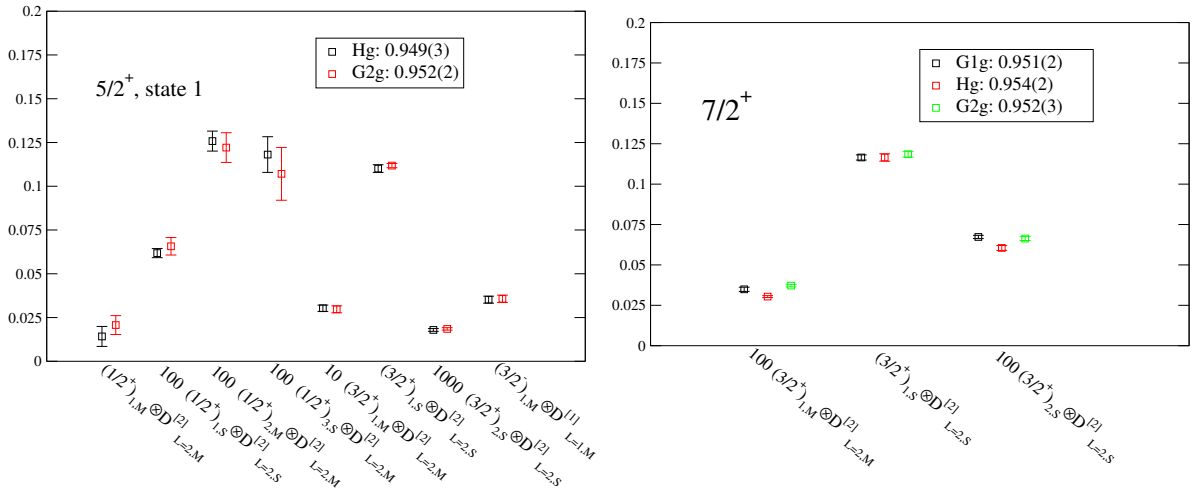

Figure 3.10: A selection of Z-values for Ω_{ccc} baryon states conjectured to be identified with $J^P = \frac{5}{2}^+$ (left) and $\frac{7}{2}^+$ (right). Operators in consideration, which overlap to these states, are mentioned as the x-axis tick labels. Z-values obtained for a given operator, but from different irreps, are found to be consistent to each other which helps to identify the spin of a given state.

between states across different irreps. In the continuum limit, for a given physical state, the overlap factors obtained from different operators, which are subduced from the same continuum operators should become equal. They should nearly be equal even on a finite lattice, if the rotational symmetry breaking effects are small. Hence in order to confirm the identification of a state with a given spin $> 3/2$, one has to compare the magnitudes of overlap factors of those operators, which are subduced into different irreps. In Figure 3.10 and Figure 3.11, we show a selection of Z values for a set of Ω_{ccc} and Ω_{ccs} states respectively, across a set of operators with matching overlaps. A degeneracy between the Z-values is clearly evident in these plots helping in identification of the states with spin $> 3/2$. After confirming the matching overlap factors, it is also necessary to check whether the energy of the identified state also matches over the irreps. The legends in these plots contains the ma values obtained for each of these states in the respective irreps. Comparing those estimates one can see that the spin identification made in these plots are valid. In Figure 3.12 and Figure 3.13, we show the histogram plots of normalized Z values of a selection of low lying Ω_{ccc} and Ω_{ccs} states identified to be spin 1/2(black), 3/2(red), 5/2(green) and 7/2(blue) for the positive parity, respectively. The normalization of the Z values follows the same definition as used in the Figure 3.7. Once this is made, we perform a simultaneous fitting of the respective principal correlators over the irreps to get the final mass. Figure 3.14 and Figure 3.15 show two examples of

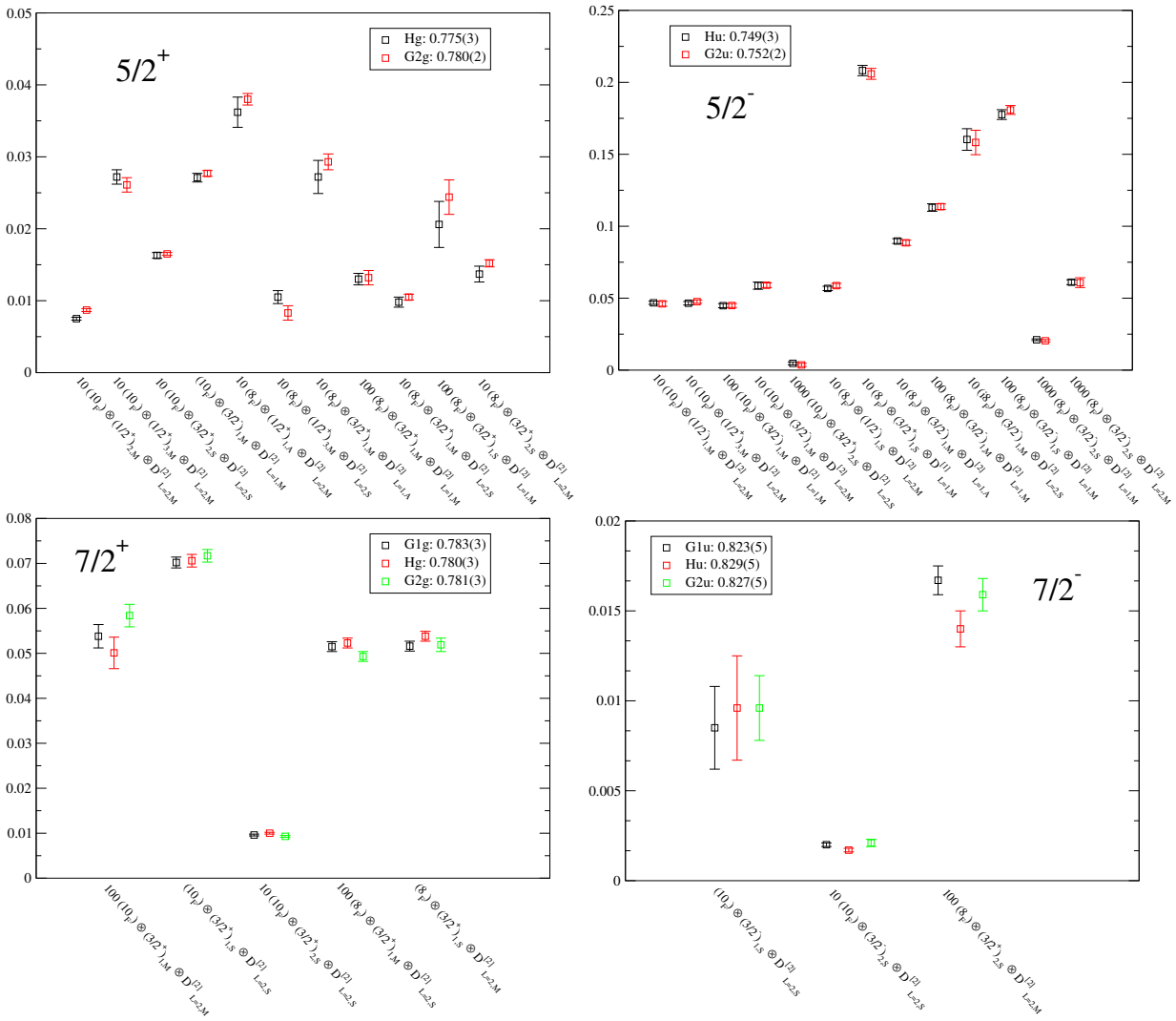

Figure 3.11: A selection of Z-values for Ω_{ccs} baryon states conjectured to be identified with $J^P = \frac{5}{2}^+$ (top left), $J^P = \frac{5}{2}^-$ (top right), $\frac{7}{2}^+$ (bottom left) and $\frac{7}{2}^-$ (bottom right). Operators in consideration, which overlap to these states, are mentioned as the x-axis tick labels. Z-values obtained for a given operator, but from different irreps, are found to be consistent to each other which helps to identify the spin of a given state.

such simultaneous fits performed for a state with spin 5/2 and 7/2 respectively.

3.8 Summary

This chapter discusses various details about the techniques used in the excited charm baryon spectroscopy calculations. We begin this chapter discussing the conventional methodology followed in spectroscopy calculations (Section 3.1), following which we dis-

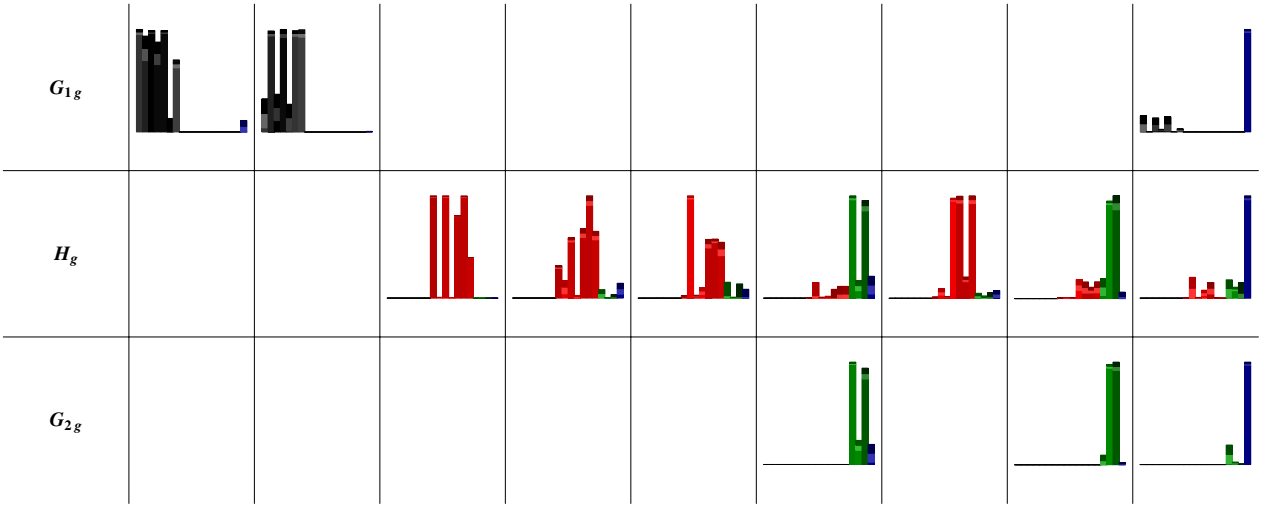

Figure 3.12: Histogram plot showing normalized overlap factor, Z, of a few operators onto some of the lower-lying Ω_{ccc} states in each of the lattice irreps. The overlaps are normalized according to $\frac{Z_i^n}{max_n[Z_i^n]}$ s that the largest overlap across all states for a given operator is unity. Black bars correspond to spin-1/2 state, red for spin-3/2, green for spin-5/2 and blue represents spin-7/2 states. Lighter and darker shades at the top of each bar represent the one-sigma statistical uncertainty.

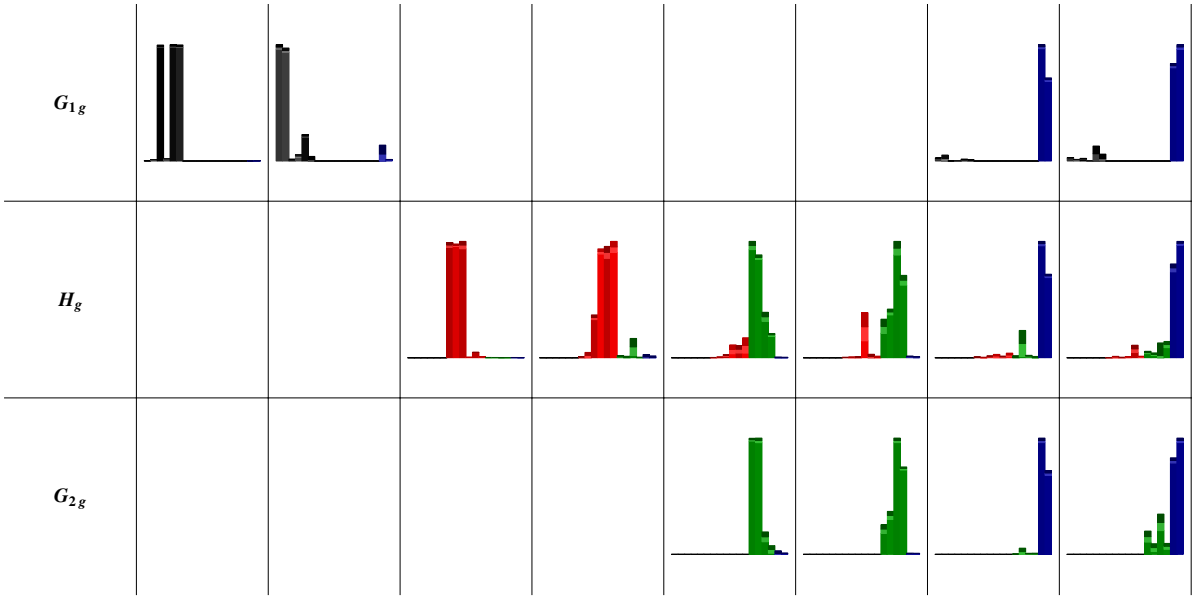

Figure 3.13: Same as the Figure 3.12, but for Ω_{ccs} baryon.

cuss about the challenges in the excited state spectroscopy (Section 3.2). In Section 3.3, 3.4 and 3.5 we discuss how the use of anisotropic lattices, the derivative-based operator construction formalism, and the variational fitting method help us meet these challenges.

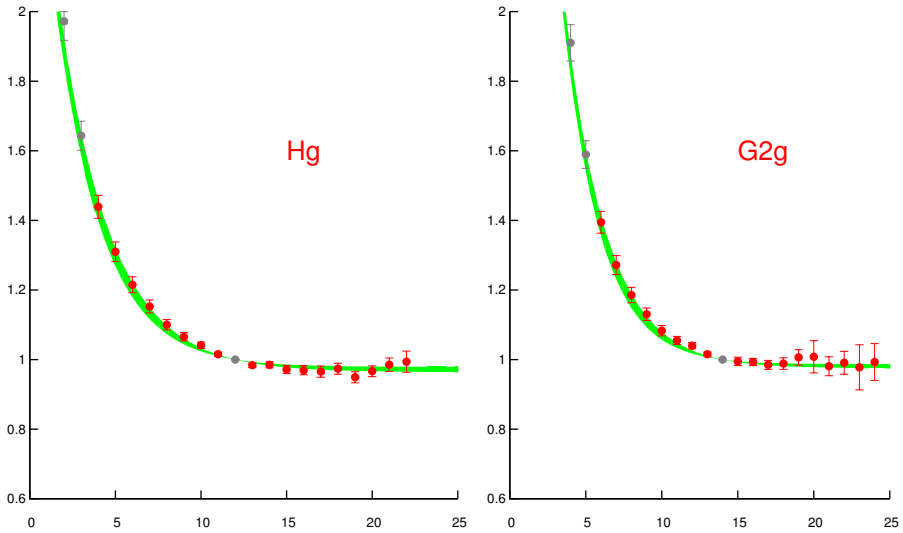

Figure 3.14: The joint fits of principal correlators identified to be the same 5/2 state obtained from H_g and G_{2g} irrep. The red point are those included in the fit, while the grey points are excluded.

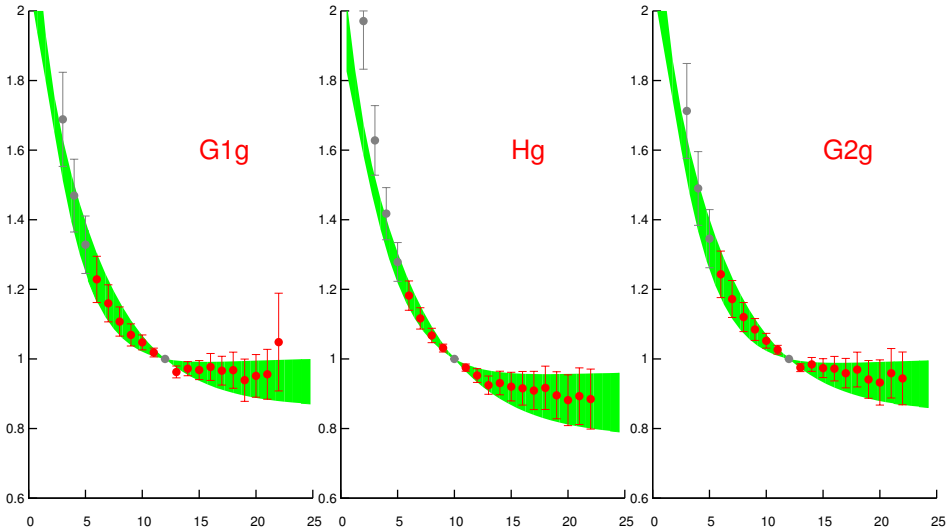

Figure 3.15: The joint fits of principal correlators identified to be the same 7/2 state obtained from G_{1g}, H_g and G_{2g} irrep. The red point are those included in the fit, while the grey points are excluded.

In the last two sections, 3.6 and 3.7, we discuss how a reliable identification of the quantum numbers of a state is made. In short, this chapter discusses all the major technical details related with the calculations referred in the next chapter.

Chapter 4

Charm baryon spectrum

In this chapter, we present our results on the spectra of charm baryons with spins up to 7/2 and for both the parities. Results for the extracted masses are quoted in terms of various energy splittings. This convention is preferable, as it is expected to reduce the impact of various systematic errors that could arise from the uncertainty in determination of the quark mass parameters as well as the discretization of the lattice action. Particularly, we consider the option of subtracting out the valence charm quark content in the spectrum, as the contribution for the discretization errors from the charm quark is larger than the light quarks. Various spin dependent energy splittings between the extracted states are also considered and compared with similar splittings at light, strange and bottom quark masses, wherever possible. We divide the discussion of results in three separate sections for the charm baryons with three, two and one flavor in the valence sector, respectively.

4.1 Triply charm baryons

With three valence charm quarks, triply charm baryons are the heaviest of all the baryons made of u, d, s and c quarks. The triply-charmed baryons may provide a new window for understanding the structure of baryons, as pointed out by Bjorken several years ago [25]. A comprehensive study of the excitation spectra of these states, where the complications of light-quark interaction are absent, can provide information about the quark confinement mechanism as well as elucidating our knowledge about the nature of the strong force by providing a clean probe of the interplay between perturbative and non-perturbative QCD [158]. Just as the quark-antiquark interactions are examined in charmonia, these

studies will probe the quark-quark interactions in the charm baryons. The flavor content being similar to $\Delta(uuu)$ and $\Omega(sss)$, only symmetric flavor combination is allowed for the triply charm baryons. Table 3.7(a) shows the total number of operators including up to two derivatives that we use in our calculations.

4.1.1 The spectrum

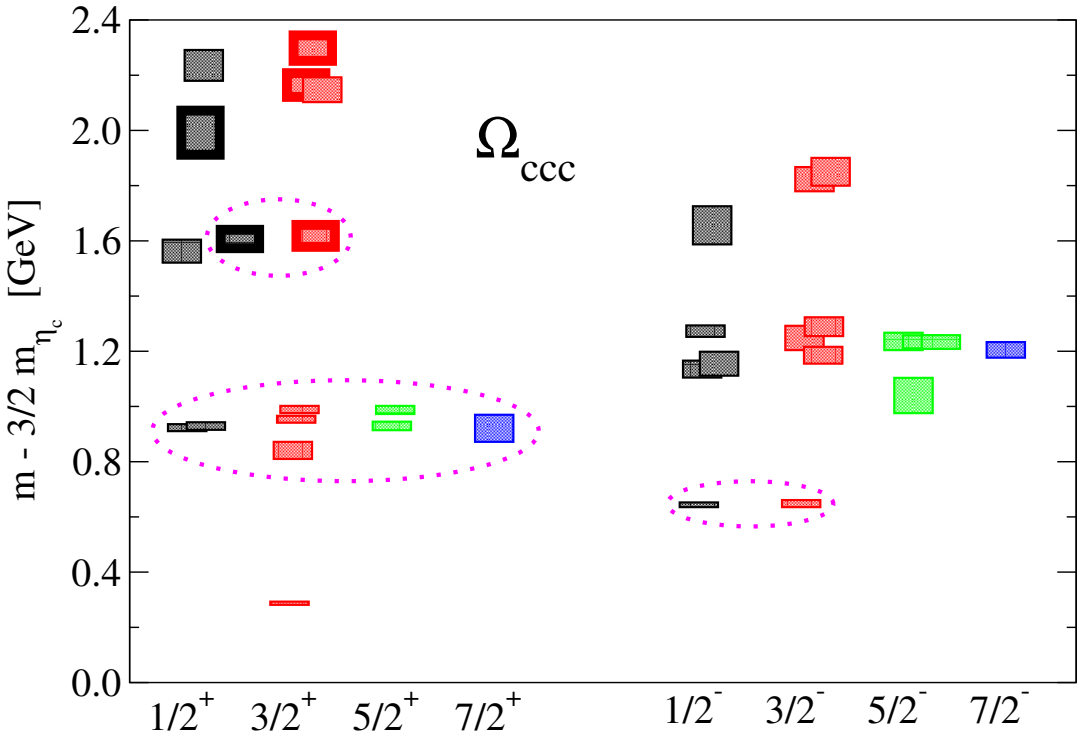

Figure 4.1: Spin identified relativistic spectra of triply-charmed baryons with respect to $\frac{3}{2}m_{\eta_c}$. The boxes with thick borders corresponds to the states with strong overlap with hybrid operators. The states inside the pink ellipses are those with relatively large overlap to non-relativistic operators.

Figure 4.1 shows the relativistic spectrum of triply charm baryons as splitting from 3/2 times the mass of η_c meson, while Table 4.1 contains the estimates. The factor of $\frac{3}{2}$ corrects for the different number of valence charm quarks in triply-charmed baryon and charmonium states. As mentioned earlier, plotting in this splitting is expected to reduce the possible discretization errors in the estimates. Boxes with thicker borders correspond to those with a greater overlap onto operators proportional to the field strength tensor as discussed in the previous chapter and might consequently be *hybrid* states. The states inside the pink ellipses have relatively large overlap with non-relativistic operators.

$\frac{1}{2}^+$	$\frac{3}{2}^+$	$\frac{5}{2}^+$	$\frac{7}{2}^+$	$\frac{1}{2}^-$	$\frac{3}{2}^-$	$\frac{5}{2}^-$	$\frac{7}{2}^-$
0.923(13)	0.287(6)	0.930(15)	0.921(49)	0.644(9)	0.648(13)	1.040(64)	1.205(28)
0.929(14)	0.841(31)	0.988(15)		1.136(31)	1.186(31)	1.233(25)	
1.563(33)	0.954(13)			1.155(43)	1.248(44)	1.234(24)	
1.607(42)	0.989(13)			1.273(21)	1.289(34)	1.236(32)	
1.992(80)	1.618(40)			1.656(69)	1.823(44)		
2.236(56)	2.147(46)				1.850(51)		
	2.165(43)						
	2.298(46)						

Table 4.1: Relativistic spectrum $m_{\Omega_{ccc}} - \frac{3}{2}\, m_{\eta_c}$ in units of GeV.

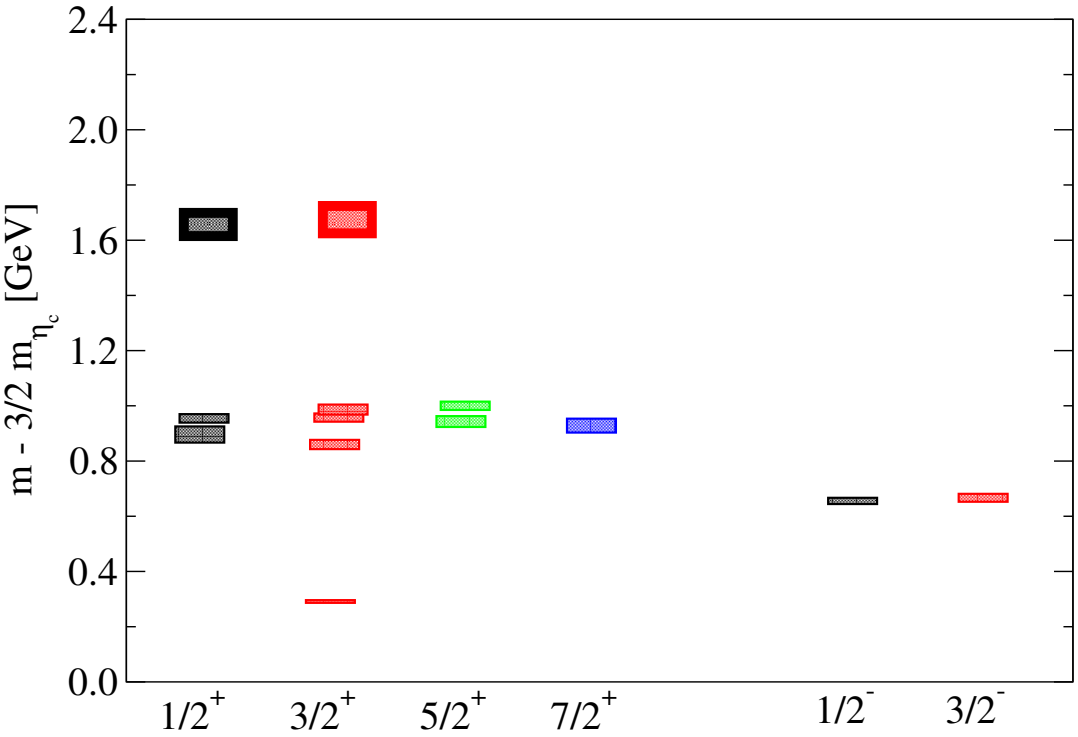

Figure 4.2: Spin identified non-relativistic spectra of triply-charmed baryons with respect to $\frac{3}{2}m_{\eta_c}$. The boxes with thick borders corresponds to the states with strong overlap with hybrid operators.

An analysis of the spectrum using only the non-relativistic operators is presented in the Figure 4.2. One can easily see that the low lying states in the relativistic spectrum (Figure 4.1) looks the same as in the non-relativistic spectrum. This supports the non-relativistic nature of the low lying spectrum of triply charm baryons. The main difference between Figure 4.1 and Figure 4.2 is the absence of negative parity states with spin higher

than 3/2 in the non-relativistic spectrum. This is because with the two component Dirac spinor ($\rho = +1$) and using up to two derivatives, one can construct operators that has continuum quantum numbers only up to spin 3/2 for negative parity. A similar non-relativistic spectrum was studied for the triply bottom baryons in Ref. [157]. The main difference with the set of operators used in that calculation is the inclusion of the hybrid operators in this work, which provides access to two higher lying states with spin 1/2 and 3/2, represented using boxes with thick borders in Figure 4.2.

In the low lying bands of states, up to the second band, the pattern of states expected based on and $SU(6) \otimes O(3)$ symmetry is as mentioned in Table 3.6. With only symmetric flavor structure allowed for triply charm baryons, only a symmetric spin pattern can combine with a local spatial structure to give a totally symmetric baryon wavefunction, modulo the color part. Hence the ground state is formed by a spin-3/2 (H_g) local structure. The first excited band is formed from the states with overlap on to the one derivative operators. One derivative operators possess only MS and MA construction with $L = 1$. Hence they can combine only with MS and MA spin constructions to give a totally symmetric spin-spatial projection operator. Thus, two negative parity states ($1/2^-$ and $3/2^-$) are formed in the first excitation band as a result of the spin-orbit interaction between the spin-1/2 (G_{1g}) structure and the orbital angular momentum of $L = 1$. With two derivatives, a set of positive parity states with a range of spins from $\frac{1}{2}$ to $\frac{7}{2}$ is expected in the second excitation band based on a model with $SU(6) \otimes O(3)$ symmetry. All these patterns up to the second excitation band is clearly evident in the full spectrum determined by this calculation, as shown in Figure 4.1. This agreement of the number and pattern of low lying states between the lattice spectra obtained in this work and the expectations based on non-relativistic quark spins implies a clear signature of $SU(6) \times O(3)$ symmetry in the spectra. Such $SU(6) \times O(3)$ symmetric nature of spectra was also observed in Ref. [102]. It is not meaningful to interpret the higher excited states, that are extracted in this calculation, in terms of $SU(6) \times O(3)$ symmetry due to the following reasons. We have not included non-relativistic operators with three derivatives and as the relativistic operators are expected to have strong overlaps with the higher excited states, it is not clear how the relative importance of all the relevant operators overlapping to that state will change in the presence of non-relativistic operators having three or more number of derivatives. For the same reasons, it is also not possible to identify negative parity states with strong *hybrid* content.

4.1.2 Investigating lattice artifacts

For a simulation carried out at a finite lattice cut-off, the results obtained will differ from their continuum counterparts and the difference can be understood in a Symanzik expansion in powers of the lattice spacing. Usually, the best means of removing these artifacts is to perform calculations at a range of lattice spacings and to use the expansion to extrapolate to the limit of vanishing lattice spacing. In this study, we do not have sufficient data to carry out this extrapolation. So we follow a calculation similar to the one that was made in Ref. [106] so as to get an estimate on how much our spectrum is affected with the corrections from the discretization.

In Ref. [106], a simple experiment was carried out to provide a crude estimate of the systematic uncertainty due to spatial discretization artifacts. The charm quark action is discretized using an action that removes the $\mathcal{O}(a_s)$ effects at the tree-level. To assess if radiative corrections to the co-efficient of the improvement term in the charm-quark action could lead to significant changes in physical predictions, a second calculation was carried out after the spatial clover co-efficient was boosted from its tree-level value, $c_s = 1.35$ to $c_s = 2$. In the charmonium study, it was observed that this new ad-hoc value for c_s is found to increase the hyperfine spitting $(m_{J/\psi} - m_{\eta_c})$, from its tree level estimate, by ~ 45 MeV and take it to its physical value. A very similar shift was observed in other low lying states in the charmonium spectrum indicating a similar magnitude of uncertainty in their estimation. Higher lying states do not show any statistically significant difference between the two charm quark actions.

With three valence charm quarks, triply charm baryons is expected to posses the maximum discretization errors among the charm baryons. We perform a similar calculation using the charm quark action with $c_s = 2.0$, where we computed the two point correlation functions for the triply charm baryons. Figure 4.3 and Figure 4.4 shows the energy splitting, $m_{\Omega_{ccc}} - 3/2 m_{\eta_c}$, of positive and negative parity, respectively, for various states that we extracted using the two charm quark actions. Here the factor of $\frac{3}{2}$ corrects for the different number of valence charm quarks in a triply-charmed baryon and the η_c meson. A very similar shift, to that observed in charmonia, is observed in the lowest few states, indicating a similar scale of uncertainty in this calculation for triply charm baryons also. The lowest few states, where this shift is observed, has been shown in insets of the plots for clarity. The higher lying triply charm states also do not show any statistically significant shifts between the estimates from the two calculations.

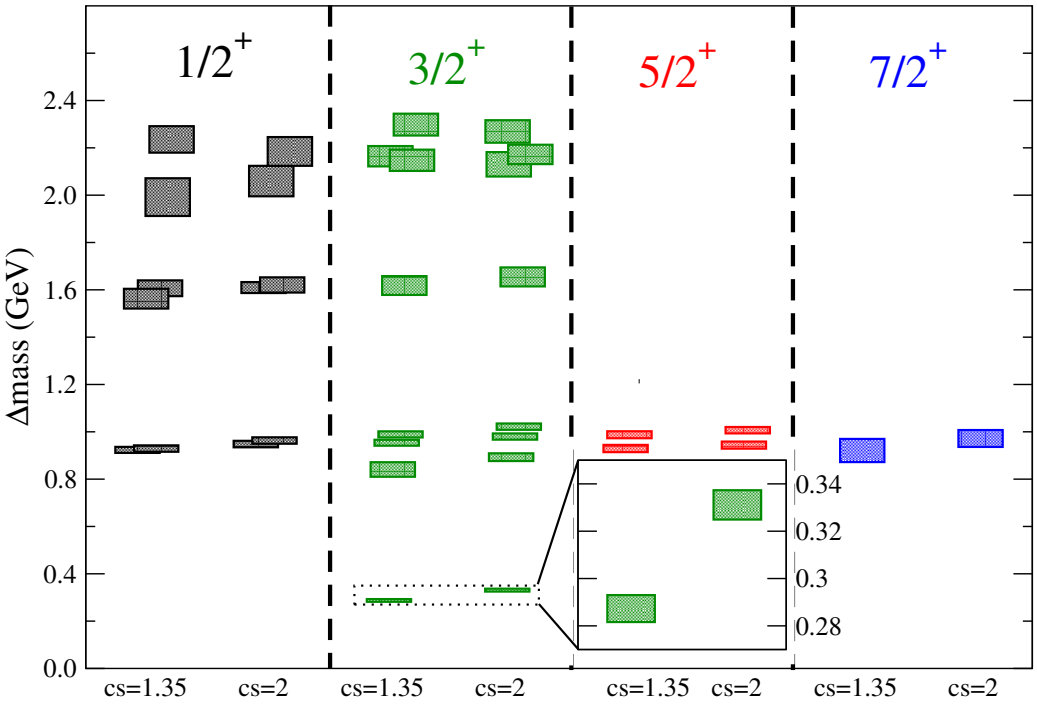

Figure 4.3: Comparison of the positive parity triply charm baryon spectrum from the two calculations; one using the tree level tadpole improved spatial clover co-efficient, $c_s = 1.35$, and the other using ad-hoc boosted value, $c_s = 2.0$, to study the systematics coming from the discretization. The spectrum is in terms of the energy splittings from 3/2 times the mass of the η_c meson in the respective calculations.

4.1.3 Valence quark mass dependence of energy splittings

Spin-dependent splittings between the triply-flavored baryons provide an insight into interactions between three confined quarks with the same mass. We consider now the dependence of these splittings on the mass of the valence quarks.

As presented in Table 3.6, operators with increasing numbers of gauge-covariant derivatives (which can correspond to non-zero orbit angular momentum in a quark model) create states with numerous values of total spin J. For example, we construct flavor (F) decuplet states with $D = 2, S = \frac{3}{2}$ and $L = 2$ with the combination $\{10F_S \otimes (S)_S \otimes (D)_S\}$, where S in the subscript stands for symmetric combinations, as defined in Ref. [101]. In this way of construction, we get four quantum numbers with $J^P = \frac{1}{2}^+, \frac{3}{2}^+, \frac{5}{2}^+$ and $\frac{7}{2}^+$. In the heavy quark limit, the spin-orbit interaction vanishes since the interaction term is inversely proportional to the square of the quark mass. States corresponding to quantum numbers ($|L, S, J^P\rangle \equiv |2, \frac{3}{2}, \frac{1}{2}^+\rangle, |2, \frac{3}{2}, \frac{3}{2}^+\rangle, |2, \frac{3}{2}, \frac{5}{2}^+\rangle$ and $|2, \frac{3}{2}, \frac{7}{2}^+\rangle$) will thus be degenerate in the heavy quark limit. Similarly, two states with quantum numbers $J^P = \frac{1}{2}^-$ and

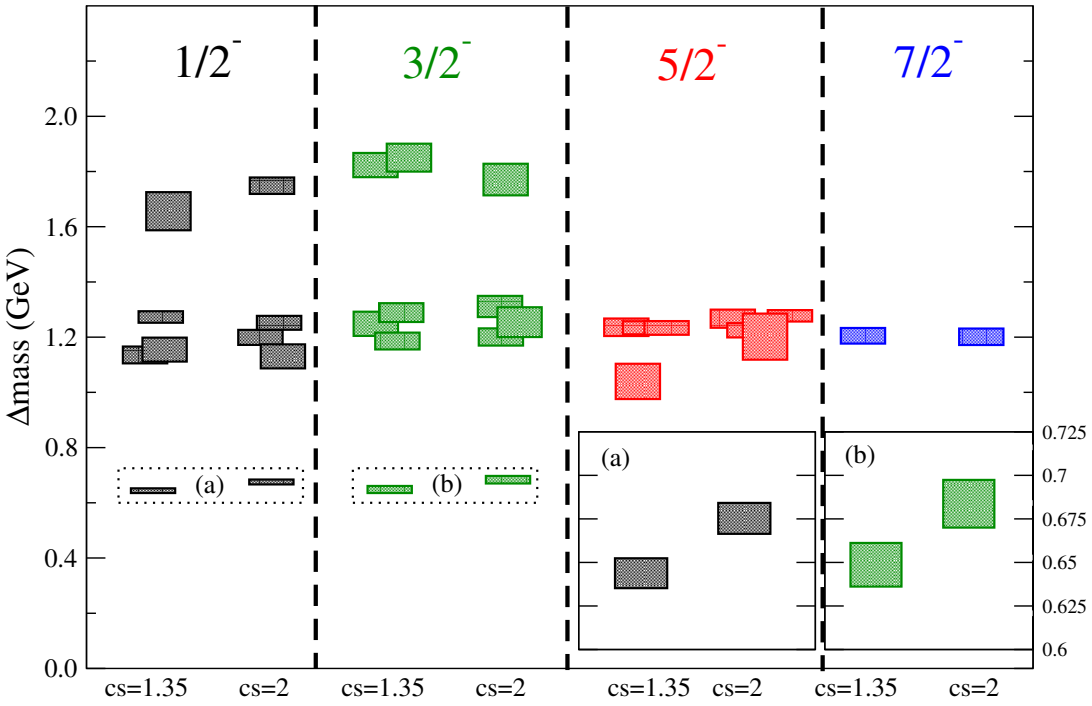

Figure 4.4: Comparison of the negative parity triply charm baryon spectrum from the two calculations; one using the tree level tadpole improved spatial clover co-efficient, $c_s = 1.35$, and the other using ad-hoc boosted value, $c_s = 2.0$, to study the systematics coming from the discretization. The spectrum is in terms of the energy splittings from 3/2 times the mass of the η_c meson in the respective calculations.

$\frac{3}{2}^-$ with $L = 1$ and $S = \frac{1}{2}$ will also be degenerate in the heavy quark limit. In Figure 4.5, we plot absolute values of energy differences between energy levels which originate from the spin-orbit interaction of the following $(L\,, S)$ pairs : $(2,\frac{3}{2}$ –in the left column), $(2,\frac{1}{2}$ –in the middle column) and $(1,\frac{1}{2}$ –in the right column). We plot these spin-orbit energy splittings at various quark masses corresponding to following triple-flavored baryons : Δ_{uuu}, Ω_{sss}, Ω_{ccc} and Ω_{bbb}. We identified the states with these (L, S) pairs by finding the operators, which incorporate these pairs and which have major overlaps to these states. These energy differences are obtained from the ratio of jackknifed correlators, which in general, reduce error bars by canceling systematic corrections in these correlators. For bottom baryons we use data from Ref. [157] and for light and strange baryon results from Ref. [102] are used.

It should be noticed that energy levels shown for bottom baryons are obtained from only non-relativistic operators [157]. For charm baryons, we show results from the full set of operators (including relativistic and non-relativistic operators) as well as from only

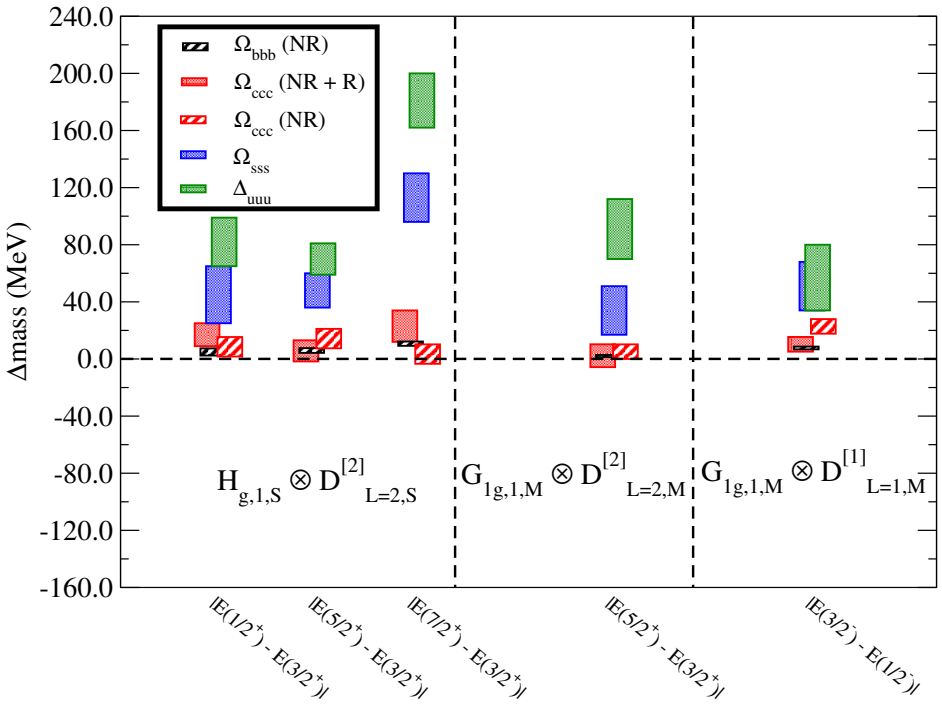

Figure 4.5: Energy splittings between states with same L and S values, starting from light to heavy baryons. For Ω_{bbb}, results are with only non-relativistic operators [157]; for Ω_{ccc}, results from relativistic and non-relativistic as well as only non-relativistic operators are shown, and for light and strange baryons results are with relativistic and non-relativistic operators [102]. These results are obtained from fitting the jackknife ratio of the correlators which helps to get smaller error bar in splittings. The left column is for the states with $D = 2, S = \frac{3}{2}$ and $L = 2$. The symbol $H_{g,1,S}$ refers to the first embedding of irrep H_g in the totally symmetric Dirac spin combination, while $D^{[2]}_{L=2,S}$ refers to spatial projection operators with two derivatives in a totally symmetric combination, and with orbital angular momentum two. Similarly, the middle column is for the states with $D = 2, S = \frac{1}{2}$ and $L = 2$. Here irrep is G_{1g} and both Dirac and derivative are in a mixed symmetric combination. In the right column these negative parity states have $D = 1, S = \frac{1}{2}$ and $L = 1$. Here again irrep is G_{1g} and both Dirac and derivative are in a mixed symmetric combination.

non-relativistic operators, and for light and strange baryons the splittings results are obtained also with the full set operators. In some cases, we find that the inclusion of the relativistic operators increase error bars. As one can observe that the degeneracy between these spin-orbit split states is more or less satisfied both for bottom and charm quarks. However, data with higher statistics is necessary to identify the breaking of this degeneracy at charm quark. For $\Delta(uuu)$ and $\Omega(sss)$ some of these splittings are non-zero. This is expected because of the presence of the light quark masses in the denominator of

the spin-orbit interaction, which enhance these splittings.

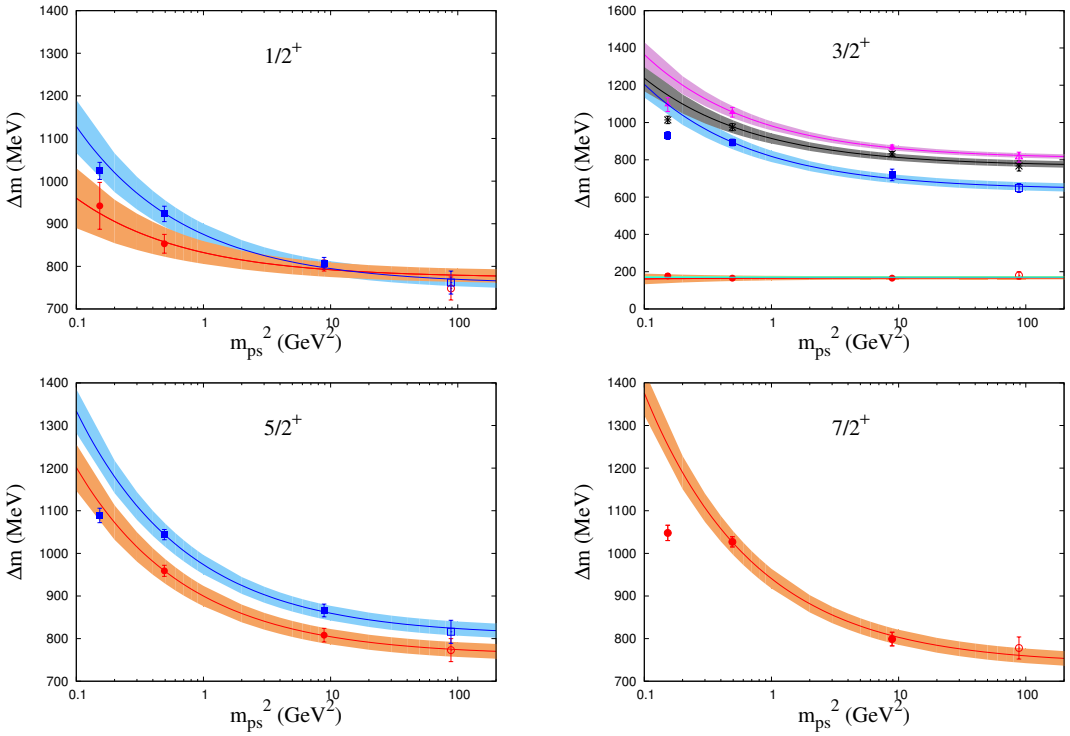

Figure 4.6: Energy splittings of a few positive parity triple-flavored baryons from vector meson (T_1^{--}) ground state are plotted against the square of the pseudoscalar masses. Data at charm quark are from this work, while light and strange quark results are from Ref. [102] which uses the same gauge field configurations. Data points for bottom quark are shown by open symbols and are taken from Ref. [157], which uses non-relativistic action. A factor 3/2 is multiplied with vector meson masses to account for the difference in the flavor content between baryons and mesons. The fits are performed assuming a form $a + b/m_{ps}$, inspired by HQET [39], (except for $\frac{3}{2}^+$ ground state, where data are also fitted with a constant, which gave better χ^2/dof). The light quark data has not been considered in the fits though the fit estimates are extrapolated to light quark masses.

We also compared how energy splittings change between light and heavy baryons. Some of these, such as the hyperfine splitting, vanish in the heavy quark limit while others become constant. However, most splittings tend to be higher at lighter quark masses where relativistic effects are prominent. We determined the energy difference between the triply-flavored baryons with respect to the vector mesons with two constituents of the same flavor. To make a comparison, which is independent of the quark mass in the heavy quark limit, we subtract $\frac{3}{2}$ of the vector meson mass, where this factor simply takes account of the difference in the flavor content between baryons and mesons. It is

to be noted here that the light and strange vector mesons are isoscalar in nature, while for the charm and the strange vector mesons the disconnected diagrams were omitted in the calculations so as to reduce the computational costs. It is expected that the contributions from such disconnected diagrams will be very small, since such diagrams are OZI suppressed. Specifically we consider following splittings: $m_{\Delta_{uuu}} - \frac{3}{2} m_{\omega_{\bar{u}u}}$, $m_{\Omega_{sss}} - \frac{3}{2} m_{\phi_{\bar{s}s}}$, $m_{\Omega_{ccc}} - \frac{3}{2} m_{J/\psi_{\bar{c}c}}$ and $m_{\Omega_{bbb}} - \frac{3}{2} m_{\Upsilon_{\bar{b}b}}$. These splittings mimic the binding energies of triple-flavored states and thus it is interesting to compare these as a function of quark masses. In Figure 4.6 and Figure 4.7, we plot these splittings, for the ground-state and a few excitations as a function of the square of the pseudoscalar meson masses. For $\Delta^{++}(uuu)$ and Ω_{sss} baryons, results are from Ref. [102], while for Ω_{bbb}, we use results from Ref. [157]. Notice that most of the splittings in various spin parity channels decrease with quark mass.

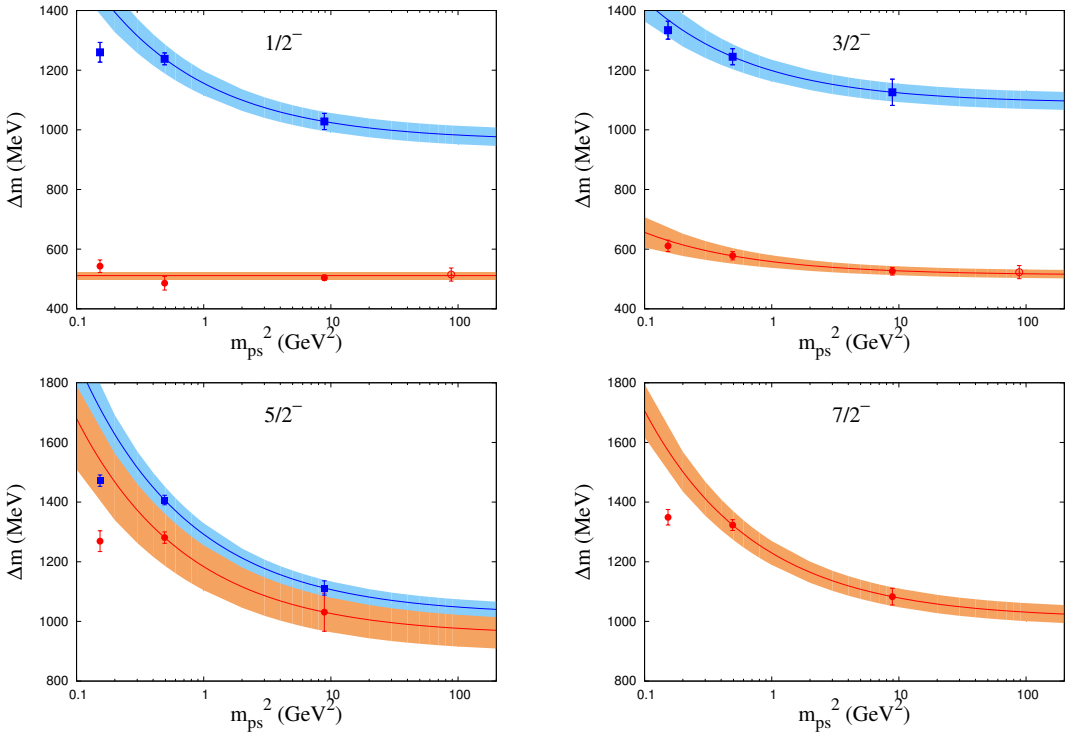

Figure 4.7: Energy splittings of a few negative parity triple-flavored baryons from vector meson (T_1^{--}) ground state are plotted against the square of the pseudoscalar masses. Details same as in Figure 4.6. The fits are performed assuming a form $a+b/m_{ps}$, inspired by HQET [39], except for $\frac{1}{2}^-$ ground state, where data are also fitted with a constant, which gave better χ^2/dof.

In the heavy quark limit, naively one can expand the mass of a heavy hadron, with

State	a	b	χ^2/DOF	State	a	b	χ^2/DOF
$\frac{1}{2}^+$	773 (16)	59 (22)	1.876	$\frac{1}{2}^-$	511 (12)		?????
$\frac{1}{2}^+$	758 (16)	117 (19)	0.411	$\frac{1}{2}^-$	963 (31)	193 (27)	10.89
$\frac{3}{2}^+$	168 (9)	-2.0 (9)	0.474	$\frac{3}{2}^-$	513 (14)	45 (15)	0.085
$\frac{3}{2}^+$	170 (5)		?????				
$\frac{3}{2}^+$	640 (22)	179 (21)	0.558	$\frac{3}{2}^-$	1089 (30)	109 (20)	0.200
$\frac{3}{2}^+$	765 (17)	149 (21)	1.228				
$\frac{3}{2}^+$	805 (12)	177 (21)	0.179				
$\frac{5}{2}^+$	760 (17)	140 (16)	0.009	$\frac{5}{2}^-$	954 (61)	230 (50)	10.33
$\frac{5}{2}^+$	807 (17)	167 (15)	0.148	$\frac{5}{2}^-$	1021 (26)	271 (26)	28.54
$\frac{7}{2}^+$	739 (17)	201 (16)	0.687	$\frac{7}{2}^-$	1009 (30)	220 (27)	17.41

Table 4.2: The fit estimates for the parameters in the fit form, $a + b/m_{_{ps}}$ (inspired by HQET), for different states from various quantum channels. The states are identified between this table and the figures 4.6 and 4.7 by keeping the colors consistent between them.

n heavy quarks, as $M_{H_{nq}} = n\ m_Q + A + B/m_Q + \mathcal{O}(1/m_{Q^2})$ [39]. Though in Ref. [39] such an expansion is argued for singly charm baryons, here we assume it to work for hadrons with multiple quarks. Hence, the energy splittings between heavy hadrons, that take into account the difference in the heavy flavor content, can be expressed in the form $a + b/m_Q$ and similarly in the heavy quark limit with $a + b/m_{ps}$. Note this form is not expected to be valid for light hadrons. Using this function, we fitted the data obtained for $m_{\Omega_{bbb}} - \frac{3}{2}\, m_{\Upsilon_{\bar{b}b}}, m_{\Omega_{ccc}} - \frac{3}{2}\, m_{J/\psi_{\bar{c}c}}$ and $m_{\Omega_{sss}} - \frac{3}{2}\, m_{\phi_{\bar{s}s}}$. Because of the very different behavior in the chiral limit, the light quark points, $m_{\Delta_{uuu}} - \frac{3}{2}\, m_{\omega_{\bar{u}u}}$ are excluded from the fit. For the cases where data for the bottom quark are not available (mainly for negative parity cases), fitting is done using only the two data at charm and strange masses. While there is no good reason for the heavy-quark inspired functional form to model the data at the strange quark mass, a good fit is still found. We also extrapolate fit results to lighter pion masses and observe that for many cases they pass through the light quark points though those points are *not* included in these fits. However, as mentioned before, one should not use this extrapolation to get splittings at lighter quark masses as is evident in many cases where data points fall significantly below the fit. It is worth noting that that the energy splittings for the spin-$\frac{3}{2}^+$ and spin-$\frac{1}{2}^-$ ground states are almost constant, even when varying the quark mass from light to bottom. In fact, we observe better fit with a constant term for these splittings. Table 4.2 tabulates the fit estimates for the parameters

in the fit form, $a + b/m_{ps}$ (inspired by HQET), for different states from various quantum channels.

4.2 Doubly charm baryons

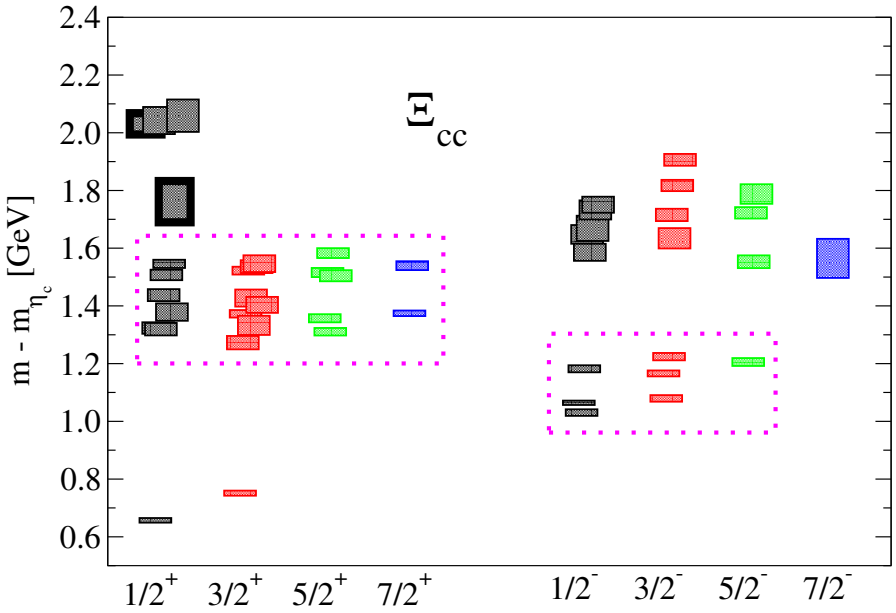

Figure 4.8: Spin identified Ξ_{cc} baryon spectra for both parities and with spin up to 7/2. Energy splittings of the Ξ_{cc} baryons from the mass of m_{η_c} meson, which has same number of charm quarks, are shown here. The states inside the magenta boxes are those with relatively larger overlap to non-relativistic operators and the states with thick borders corresponds to the states with strong hybrid content. The number of states inside these boxes matches with the expectations based on non-relativistic quark spins, as shown in Table 3.6. This agreement of the number of low lying states between the lattice spectra obtained in this work and the expectations based on non-relativistic quark spins implies a clear signature of $SU(6) \times O(3)$ symmetry in the spectra.

Doubly charm baryons are interesting systems as they provide a unique opportunity to get insights into the nature of strong force in the presence of slow relative motion of the heavy quarks along with the relativistic motion of a light quark. The study of their excited state spectra and various energy splittings will help us understand how the collective degrees of freedom gives rise to excitations in these systems. A comparison of these excitations with corresponding spectra of singly and triply charm baryons, where the number of charm quark is one less and more respectively, will be helpful to get information

about quark-quark interactions within these systems. A doubly-heavy baryon can be treated as a bound state of a heavy antiquark and a light quark ($qQQ \leftrightarrow q\bar{Q}$) in the limit when the typical momentum transfer between the two heavy quarks is larger than Λ_{QCD} [159, 160]. In this limit of quark-diquark symmetry, definite predictions of the spin dependent energy splittings can be made [42, 161]. It is thus interesting to study those spin splittings based on first principles to check whether charm quark is heavy enough to respect this quark-diquark symmetry.

With two valence charm quarks, doubly charm baryons are the second heaviest baryons of the $SU(4)$ flavor family. The flavor pattern being similar to the Σ^{++} baryon (suu), the allowed flavor symmetry combination are symmetric, mixed-symmetric and mixed-antisymmetric. Table 3.7(b) shows the total number of operators including up to two derivatives, we have used in our calculations.

4.2.1 The spectrum

$\frac{1}{2}^+$	$\frac{3}{2}^+$	$\frac{5}{2}^+$	$\frac{7}{2}^+$	$\frac{1}{2}^-$	$\frac{3}{2}^-$	$\frac{5}{2}^-$	$\frac{7}{2}^-$
0.676(08)	0.770(9)	1.329(13)	1.393(10)	1.049(11)	1.098(12)	1.224(14)	1.583(68)
1.338(22)	1.291(23)	1.376(14)	1.558(15)	1.083(8)	1.185(10)	1.572(22)	
1.342(20)	1.351(33)	1.523(19)		1.201(12)	1.243(13)	1.741(20)	
1.397(30)	1.391(13)	1.534(16)		1.604(30)	1.653(35)	1.806(34)	
1.456(21)	1.422(28)	1.602(17)		1.666(32)	1.734(21)		
1.526(18)	1.446(30)			1.687(44)	1.836(20)		
1.564(14)	1.541(14)			1.751(33)	1.925(21)		
1.780(72)	1.555(22)			1.769(28)			
2.049(37)	1.565(29)						
2.061(47)							
2.078(56)							

Table 4.3: Relativistic spectrum $m_{\Xi_{cc}} - m_{\eta_c}$ in units of GeV.

In Figure 4.8 and Figure 4.9, we show the spin identified full spectra, that we extracted on our lattices, of Ξ_{cc} and Ω_{cc} baryons, respectively, as splittings from η_c meson, while Table 4.4 and Table 4.3 contains the respective estimates. The states inside the magenta boxes are those with relatively larger overlap to non-relativistic operators and the states with thick borders corresponds to the states with strong hybrid content.

Similar to the case of the triply charm baryons, an analysis of the number of pattern of the states in the spectrum for both the doubly charm baryons points to a spectrum based

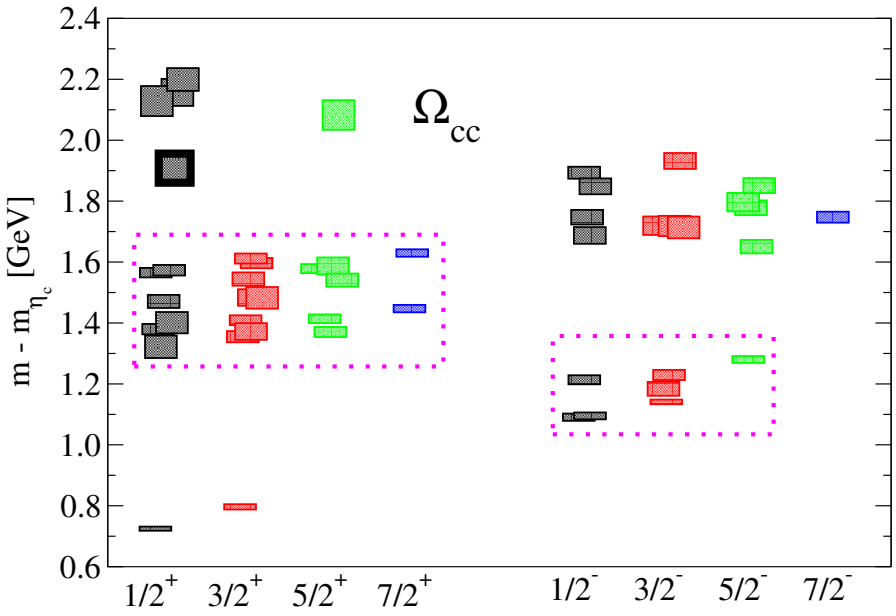

Figure 4.9: Spin identified spectra of Ω_{cc} baryons for both parities and with spin up to 7/2. Energy splittings of the Ω_{cc} states from the mass of η_c meson, which has same number of charm quark, are shown here. All other details are same as in Figure 4.13.

$\frac{1}{2}^+$	$\frac{3}{2}^+$	$\frac{5}{2}^+$	$\frac{7}{2}^+$	$\frac{1}{2}^-$	$\frac{3}{2}^-$	$\frac{5}{2}^-$	$\frac{7}{2}^-$
0.720(7)	0.792(9)	1.362(16)	1.438(12)	1.084(12)	1.134(8)	1.272(11)	1.736(18)
1.314(37)	1.345(18)	1.405(14)	1.620(12)	1.088(11)	1.176(23)	1.640(22)	
1.371(17)	1.364(27)	1.531(21)		1.206(15)	1.222(17)	1.767(24)	
1.391(35)	1.400(16)	1.569(15)		1.677(27)	1.703(35)	1.786(30)	
1.462(21)	1.473(35)	1.577(28)		1.736(24)	1.708(33)	1.840(25)	
1.555(15)	1.475(27)	2.070(48)		1.837(26)	1.709(30)		
1.563(17)	1.535(22)			1.882(20)	1.920(26)		
1.896(47)	1.587(17)						
2.115(49)	1.602(16)						
2.143(44)							
2.186(37)							

Table 4.4: Relativistic spectrum $m_{\Omega_{cc}} - m_{\eta_c}$ in units of GeV.

on non-relativistic quark models. With two flavor symmetry constructions possible, doubly charm baryons allows two local non-relativistic operators : one from the combination of spin 1/2 (G_{1g}) and the other from the combination of spin 3/2 (H_g) with local spatial structure, giving rise to two positive parity operators with total angular momentum 1/2 and 3/2, respectively. While the set of one derivative operators posses a pattern of

(3,3,1,0) with the total angular momentum $J = (\frac{1}{2}, \frac{3}{2}, \frac{5}{2}, \frac{7}{2})$, the two derivative operators form a pattern of (6,8,5,2) with the total angular momentum $J = (\frac{1}{2}, \frac{3}{2}, \frac{5}{2}, \frac{7}{2})$. Figure 4.8 and Figure 4.9 shows this pattern is very clearly followed in the low lying three bands with the allowed quantum numbers as mentioned above. It is to be pointed out that in our calculation, we use the whole set including non-relativistic and relativistic operators and still we obtain the number and pattern of states allowed by purely non-relativistic operators. This agreement of the number of low lying states between the lattice spectra obtained in this work and the expectations based on non-relativistic quark spins implies a clear signature of $SU(6) \times O(3)$ symmetry in the spectra. As mentioned in the previous section, such a symmetry based on non-relativistic quarks is observed in the triply charm baryons and in the light baryons [102]. Note that there are no 7/2 operators with negative parity that can be constructed purely with non-relativistic quarks, and the signal for the extracted state is a result of the inclusion of the relativistic operators. We also able to identify a few states which has strong overlap to hybrid operators. Though there are more number of non-relativistic operators with hybrid nature in Table 3.6, we could not clearly identify those. We expect a data with higher statistics will aid in extracting the signals from those states. Further, one cannot argue an $SU(6) \otimes O(3)$ symmetry for the higher lying states to these non-relativistic bands, because of same reasons as described for triply charm baryons. Identification of the negative parity states with hybrid content also suffers from this ambiguity.

Since both the doubly charm baryons have the same flavor structure, pqq, and hence the same allowed flavor symmetry combinations, the interpolators used in their spectroscopy are similar. They differ only in their flavor content. Hence one expects a similar pattern in their spectra also. To check such a similarity in the spectra of doubly charm baryons, in Figure 4.10 and Figure 4.11, we show the extracted positive and negative parity spectra, respectively, in terms of another type of energy splittings. For each spin, left column is for splittings of $\Xi_{cc} - D$ and the right column is for $\Omega_{cc} - D_s$ splittings. By subtracting out D and D_s mesons from Ξ_{cc} and Ω_{cc} baryons we effectively leave only the excitation of one charm quark in both cases. One would thus naively expect that both spectra will be equivalent. This is almost true for the lowest state in each spin parity channel, except for negative parity spin-7/2 state, as can be observed in Figure 4.10 and Figure 4.11. That state is obtained from relativistic operators and it is expected that such naive expectation may not hold there. This is also true for other excited states, where the contribution from relativistic operators are much larger. The inset figures in Figure 4.10 are for the positive parity ground states of spin-1/2 and spin-3/2 baryons.

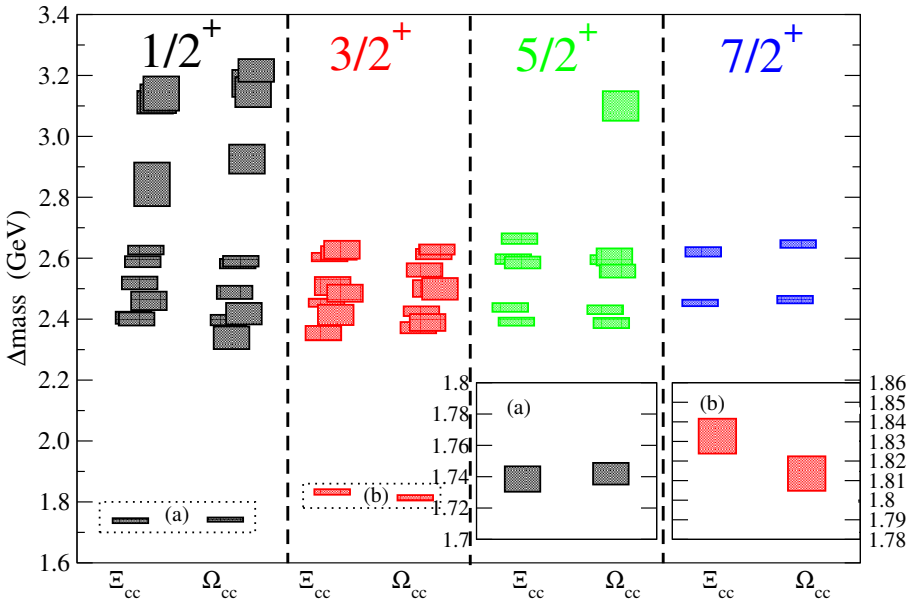

Figure 4.10: Energy splittings of positive parity Ξ_{cc} and Ω_{cc} baryons from D and D_s mesons, respectively. For each spin, left column is for splittings of $\Xi_{cc}(ccu)$ baryons from the ground state $D(cu)$ meson and the right column is for splittings of $\Omega_{cc}(ccs)$ baryons from the ground state $D_s(cs)$ meson. The inset figure are for the positive parity ground states of spin-1/2 and spin-3/2 ground states. Results for D and D_s mesons are taken from Ref. [107].

Results for D and D_s mesons are taken from Ref. [107].

As mentioned in the introduction that the experimental discovery of doubly heavy baryons is quite unsettled. It is thus important to compare the ground state spectra of the two doubly heavy baryons obtained by different calculations. In Figure 4.12 we show the ground state results of $J^P = \frac{1}{2}^+$ and $\frac{3}{2}^+$ Ω_{cc} baryons, obtained in this work, along with other lattice as well as various model results. In Figure 4.13, we show the ground state results of $J^P = \frac{1}{2}^+$ and $\frac{3}{2}^+$ of Ξ_{cc} baryons, obtained in this work, along with the only experimental (SELEX) result and other lattice as well as various model results. The discretization scheme for charm quarks followed by the other lattice calculations are as follows : Mathur, *et. al* [80]→NRQCD; Briceno, *et. al* [84] and PACS-CS [88] →relativistic heavy quark formalism; ILGTI [127] → overlap fermions; and Bali, *et. al* [86]→clover Wilson fermions. Our results are at pion mass 391 MeV, results for PACS-CS [88] and Briceno *et. al* [84] are extrapolated to the physical pion mass, while ILGTI [127] and Bali, *et. al* [86] results are at pion mass 340 MeV and 348 MeV respectively. The lattice spacing in the temporal direction (a_t) for this work is 0.035 fm, the lattice

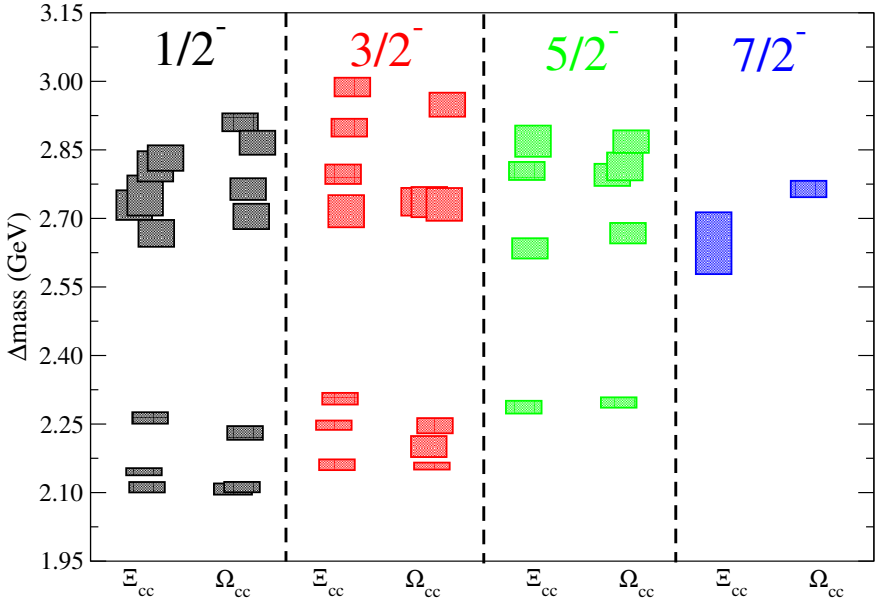

Figure 4.11: Energy splittings of negative parity Ξ_{cc} and Ω_{cc} baryons from D and D_s mesons, respectively. For each spin, left column is for splittings of $\Xi_{cc}(ccu)$ baryons from the ground state $D(cu)$ meson and the right column is for splittings of $\Omega_{cc}(ccs)$ baryons from the ground state $D_s(cs)$ meson. Results for D and D_s mesons are taken from Ref. [107].

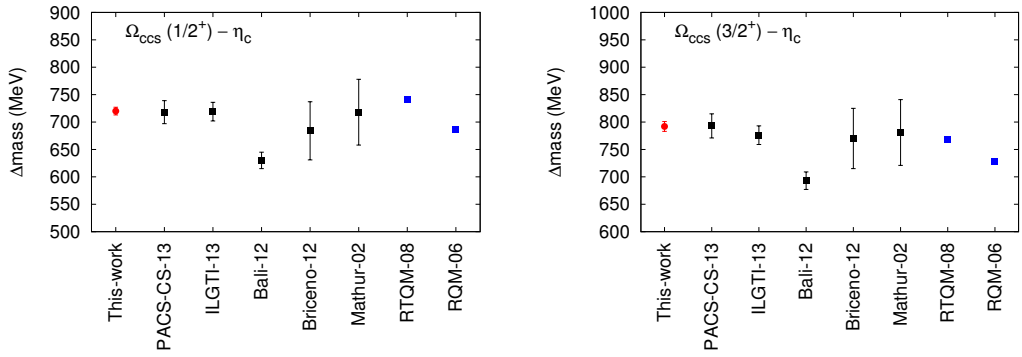

Figure 4.12: Ground state masses of spin-1/2 and spin-3/2 doubly charm Ω_{cc} baryons as a splitting from η_c meson mass. Our results are shown by the red filled circle. Other lattice as well as model results are also shown.

constants in other lattice calculations are as follows : PACS-CS $a_t = 0.09$ fm, Bali *et. al* $a_t = 0.08$ fm and for ILGTI $a_t = 0.0582$ fm. Results from only Briceno *et. al* are extrapolated to the continuum.

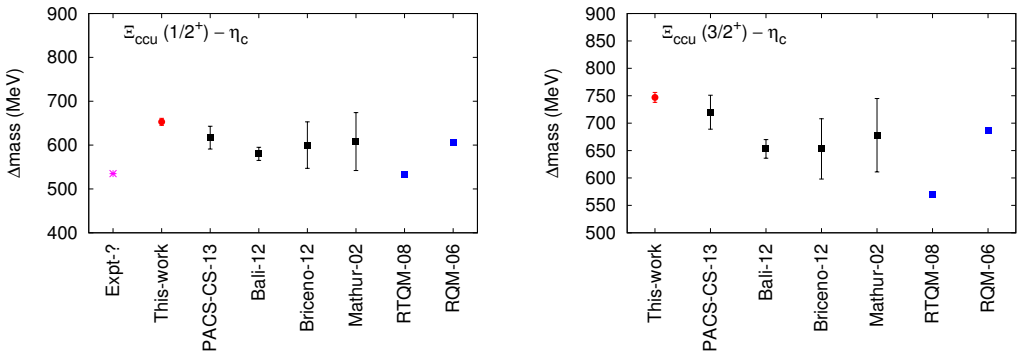

Figure 4.13: Ground state masses of spin-1/2 and spin-3/2 doubly-charmed Ξ_{cc} baryons as a splitting from η_c meson mass. Our results are shown by the red filled circle. Our u quark mass is not physical and have a pion mass 391 MeV, while results for PACS-CS [88], and Briceno *et. al* [84] are extrapolated to the physical pion mass, while ILGTI [127] and Bali, *et. al* [86] results are at pion mass 340 MeV and 348 MeV respectively.

4.2.2 Investigating lattice artifacts

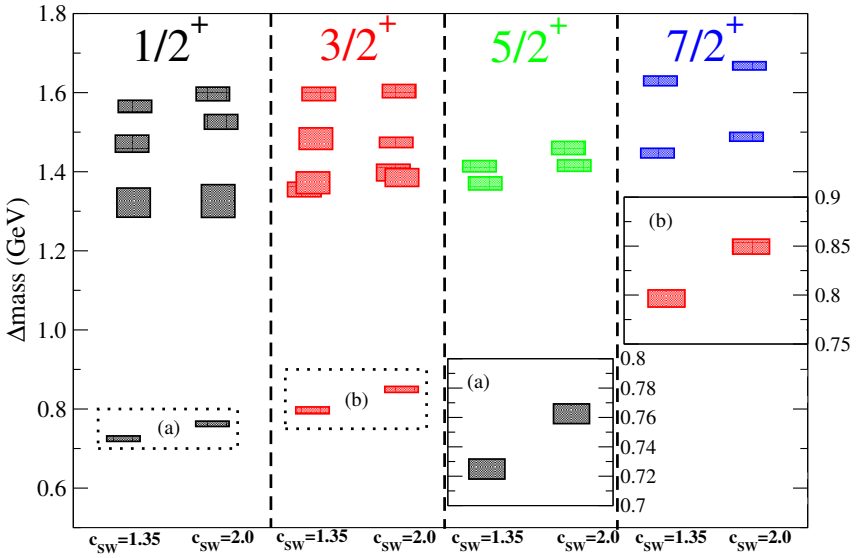

Figure 4.14: Comparison of a few low lying positive parity Ω_{cc} baryon states from the two calculations; one using the tree level tadpole improved spatial clover co-efficient, $c_s = 1.35$, and the other using ad-hoc boosted value, $c_s = 2.0$, to study the systematics coming from the discretization. The spectrum is in terms of the energy splittings from m_{η_c} in the respective calculations.

As in our previous study for triply charm baryons [112], to check the systematic uncertainty due to spatial discretisation artifacts, we carried another calculation in which the spatial clover co-efficient was boosted from its tree-level tadpole improved value,

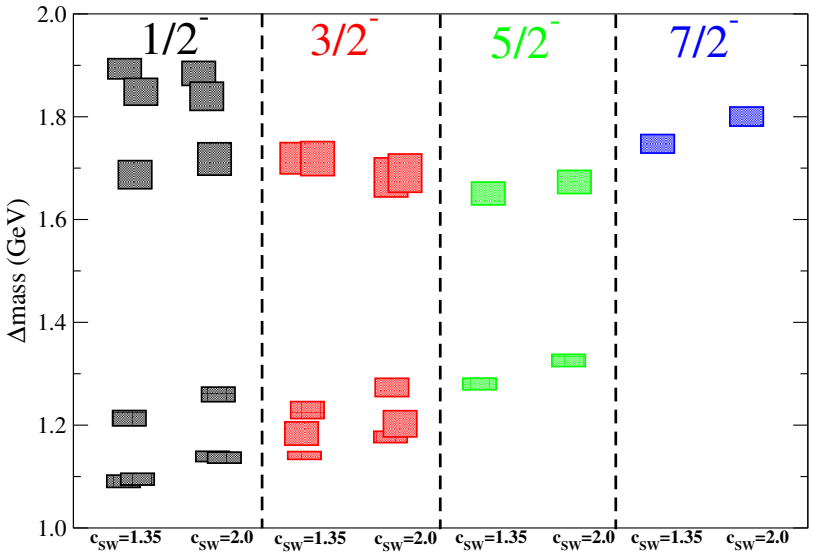

Figure 4.15: Comparison of a few low lying negative parity Ω_{cc} baryon states from the two calculations; one using the tree level tadpole improved spatial clover co-efficient, $c_s = 1.35$, and the other using ad-hoc boosted value, $c_s = 2.0$, to study the systematics coming from the discretization. The spectrum is in terms of the energy splittings from m_{η_c} in the respective calculations.

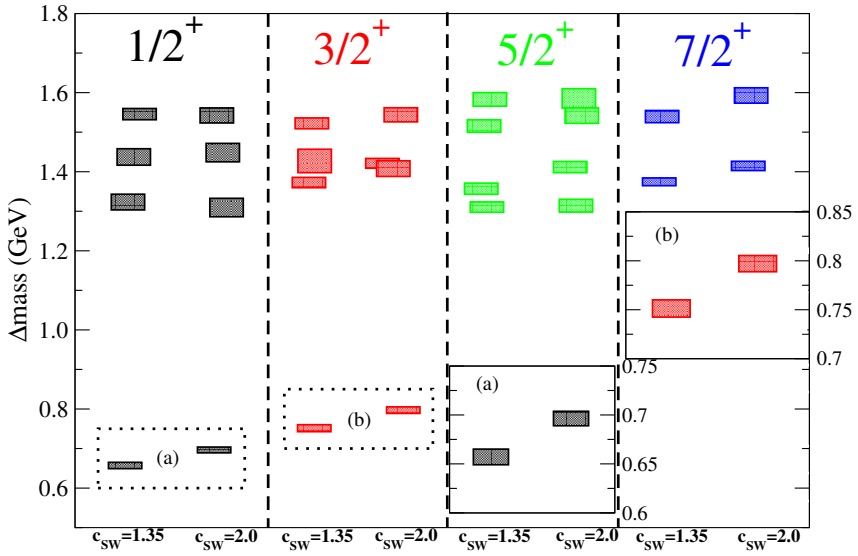

Figure 4.16: Comparison of a few low lying positive parity Ξ_{cc} baryon states from the two calculations; one using the tree level tadpole improved spatial clover co-efficient, $c_s = 1.35$, and the other using ad-hoc boosted value, $c_s = 2.0$, to study the systematics coming from the discretization. The spectrum is in terms of the energy splittings from m_{η_c} in the respective calculations.

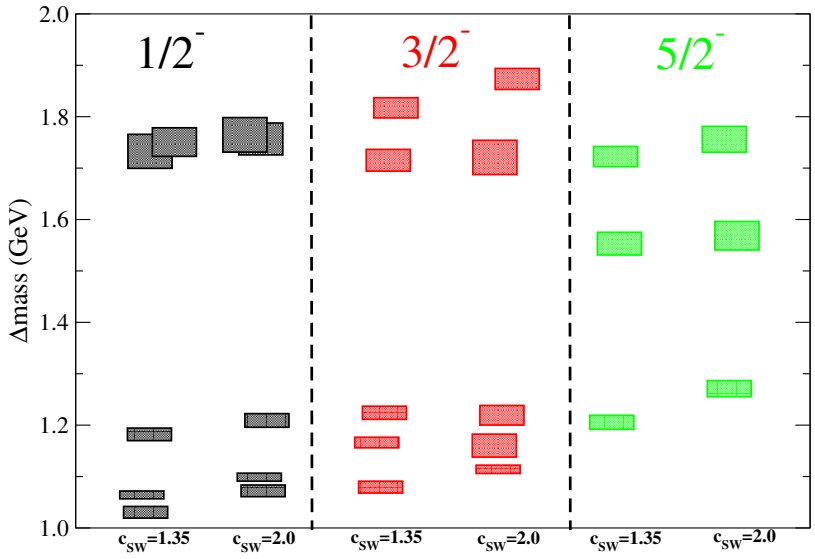

Figure 4.17: Comparison of a few low lying negative parity Ξ_{cc} baryon states from the two calculations; one using the tree level tadpole improved spatial clover co-efficient, $c_s = 1.35$, and the other using ad-hoc boosted value, $c_s = 2.0$, to study the systematics coming from the discretization. The spectrum is in terms of the energy splittings from m_{η_c} in the respective calculations.

$c_s = 1.35$ to $c_s = 2$. At this boosted value the new extracted hyperfine splitting was found to be physical [106]. The mass splittings were found to have increased by ∼45 MeV between two calculations. For doubly charm baryon also we performed similar analysis with the boosted spatial clover co-efficient. Figure 4.14, 4.15, 4.16 and 4.17 shows the comparison of a few low lying doubly charm baryons using the two different charm quark actions. We find a similar shift in the low lying doubly charm baryon energies, indicating a similar scale of uncertainty in this calculation. While for the higher excited states this shift seems to have eclipsed by the statistical uncertainties.

4.2.3 Energy splittings in doubly charm baryons

The energy splittings between various excitations in a spectra provide important information about the nature of interactions needed to excite those states. The energy splittings also provide inputs for building models which can describe these states successfully. The most notable spin dependent baryon energy splitting that one always considers is the hyperfine splittings between $\frac{3}{2}^+$ and $\frac{1}{2}^+$ states (for example, splitting between Δ and nucleon). For doubly charm baryons, we also compute this splitting and show in Figure 4.18 for Ξ_{cc} (left plot) and Ω_{cc} (right plot) baryons. Our results are compared with other

lattice results as well as with various model results. As one can see that our estimates are in very good agreement with other lattice estimations.

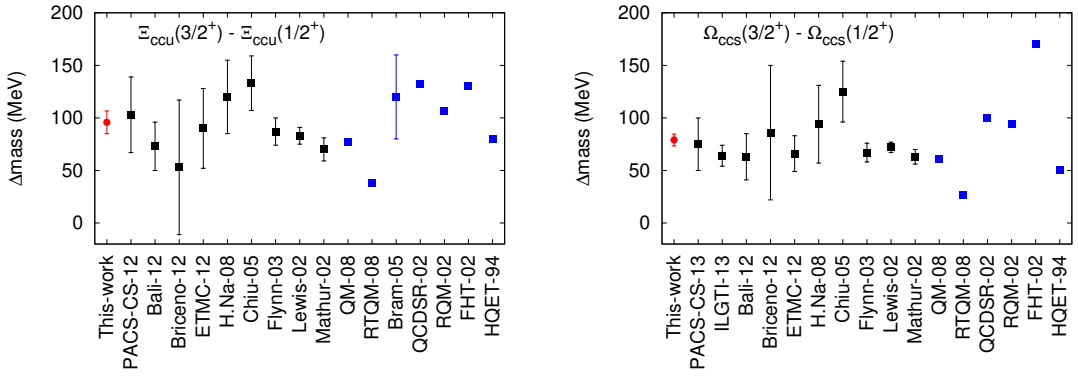

Figure 4.18: Hyperfine mass splittings between spin-$\frac{3}{2}^+$ and spin-$\frac{1}{2}^+$ states of Ξ_{cc} (left plot) and Ω_{cc} (right plot) baryons are compared for various lattice and model results. Our results are shown by red filled circle. Pion mass in these calculations is 391 MeV, while results for PACS-CS [88], and Briceno *et. al* [84] are extrapolated to the physical pion mass, while ILGTI [127] and Bali, *et. al* [86] results are at pion mass 340 MeV and 348 MeV respectively.

In Figure 4.19, we compare these hyperfine splittings for Ξ_{cc} and Ω_{cc} baryons as a function of quark mass. In the x-axis of that figure, we use the square of the pseudoscalar meson mass (m_{ps}), while y-axis shows hyperfine splittings at those pseudoscalar meson masses. Along with Ξ_{cc} and Ω_{cc}, we also show splittings between spin-$\frac{3}{2}$ and spin-$\frac{1}{2}$ states of Ω_{ccc} baryon. The later splittings is not hyperfine in nature. For the Ω_{ccc} baryons, we take the spin-orbit splittings between $E_3(\frac{3}{2}^+)$ and $E_0(\frac{1}{2}^+)$ states, which have same L and S values corresponding to the 7^{th} row in S_F in Table 3.6.

In Figure 4.20, we show energy splittings of the ground states of each spin-parity channel from the lowest state in that parity channel. For the positive parity, the lowest state is $J^P = \frac{1}{2}^+$ and for negative parity the lowest state is $J^P = \frac{1}{2}^-$. It is interesting to note that both for Ξ_{cc} and Ω_{cc} this splittings are almost same. This indicates that the interquark interactions, which are responsible for these splittings, are similar in these two different type of baryons. The negative parity 7/2 state is a result of the inclusion of the relativistic operators and doesn't appear in a purely non-relativistic spectrum constructed using up to two derivatives. So the contribution to that state from a possible three derivative operator is unclear and hence the disagreement may change after its inclusion.

Motivated by the success of HQET inspired fit form in understanding the quark

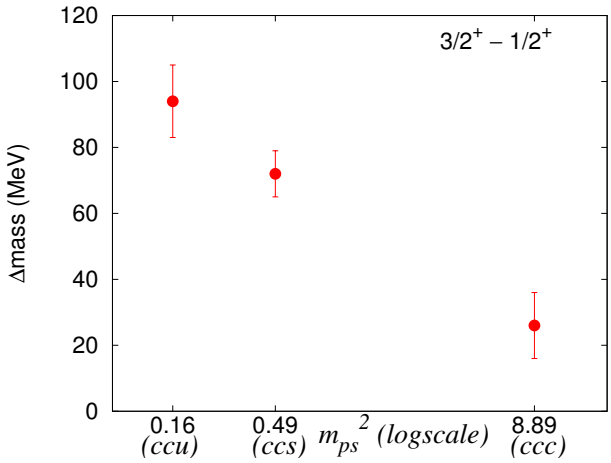

Figure 4.19: Mass splittings between spin-$\frac{3}{2}^+$ and spin-$\frac{1}{2}^+$ states are compared for $\Xi_{cc}(ccu)$, $\Omega_{cc}(ccs)$ and $\Omega_{ccc}(ccc)$ baryons. For Ω_{ccc}, mass splitting is between $E_0(1/2^+)$ and $E_3(3/2^+)$ states, which is actually due to spin-orbit coupling, while for Ξ_{cc} and Ω_{cc}, these are between respective ground states and are due to hyperfine splittings.

mass dependence of energy splittings in triple flavored baryons, we fit similar energy splittings for doubly charm baryons. However, there is a difference in doubly charm baryons. So as to show quark mass dependence one need to include triply-charmed baryons also. In the study of triple flavored baryons, states at different quark masses are obtained from same operators and so they are easy to compare. However, states at doubly charmed-baryons and triply-charmed baryons are not obtained from same set of operators except for positive parity spin 3/2 states. We thus consider energy splittings only for this state. In specific, we calculate the following energy splittings : $\Xi^*_{cc}(ccu) - D_u(\bar{c}u)$, $\Omega^*_{cc}(ccs) - D_s(\bar{c}s)$ and $\Omega^*_{ccc}(ccc) - \eta_c(\bar{c}c)$, and $\Xi^*_{cc}(ccu) - D^*_u(\bar{c}u)$, $\Omega^*_{cc}(ccs) - D^*_s(\bar{c}s)$ and $\Omega^*_{ccc}(ccc) - J/\psi(\bar{c}c)$ and plot in Figure 4.21. Absorbing the mass of the one remnant valence charm quark in to the additive parameter,'a', we again fit these splittings with a form $a + b/m_{ps}$, which was used for triply charm baryons, and obtain good fits. We also like to point out that energy splittings at very light quark masses should not be calculated using the above form and is valid only in the heavy quark domain.

It is interesting to note that one can extrapolate the fitted results to bottom mass to obtain the energy splittings of $\Omega^*_{ccb}(\frac{3}{2}^+) - B_c$ and $\Omega^*_{ccb}(\frac{3}{2}^+) - B^*_c$ at the mass of B_c meson. Using these splittings, we can empirically predict the mass splitting of $B^*_c - B_c$ by taking the difference between $\Omega^*_{ccb}(\frac{3}{2}^+) - B_c$ and $\Omega^*_{ccb}(\frac{3}{2}^+) - B^*_c$. Further, one can predict the mass of Ω^*_{ccb} by taking input for the mass of only discovered charm-bottom meson [16], assuming it is as a pseudoscalar meson with mass 6277 MeV, using the splitting $\Omega^*_{ccb}(\frac{3}{2}^+) - B_c$.

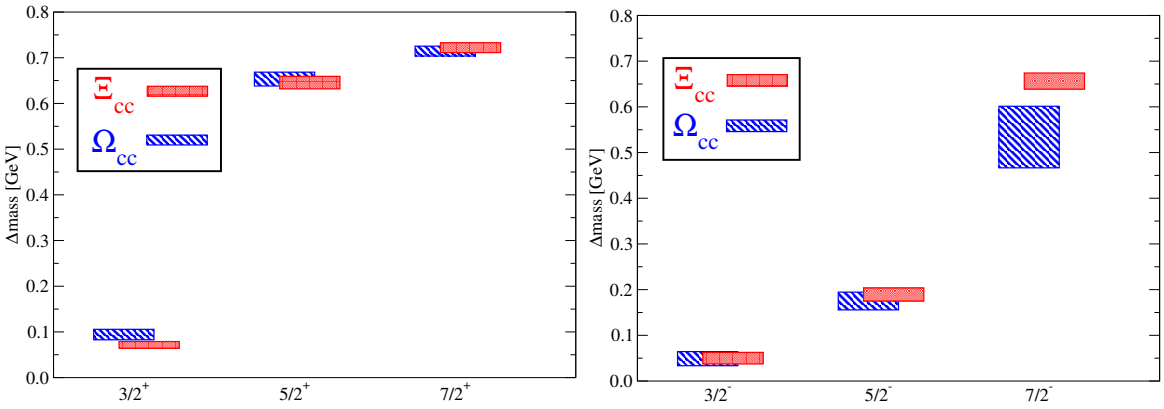

Figure 4.20: Energy splittings (in units of GeV) between the ground states of different spins are shown for positive (top two) and negative parity (bottom two) doubly-charmed baryons. Left two plots are for Ξ_{cc} and right two are for Ω_{cc} baryons. For positive parity, the lowest state has $J^P = \frac{1}{2}^+$ and for negative parity the lowest state has $J^P = \frac{1}{2}^-$.

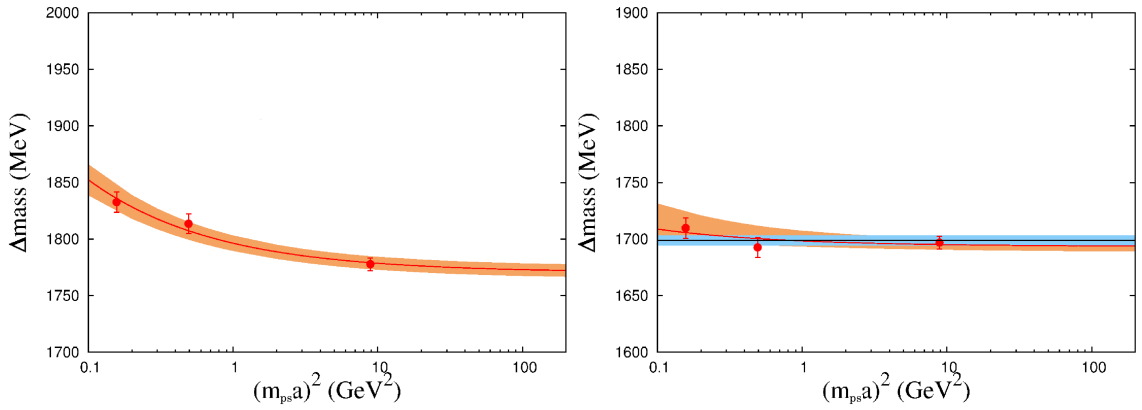

Figure 4.21: Energy splittings between positive parity spin-3/2 baryons and pseudoscalar meson as well as vector mesons are plotted against the square of the pseudoscalar masses. Left figure is the splittings of : $\Xi^*_{cc}(ccu) - D_u(\bar{c}u)$, $\Omega^*_{cc}(ccs) - D_s(\bar{c}s)$ and $\Omega^*_{ccc}(ccc) - \eta_c(\bar{c}c)$, and right figure includes following splittings : $\Xi^*_{cc}(ccu) - D^*_u(\bar{c}u)$, $\Omega^*_{cc}(ccs) - D^*_s(\bar{c}s)$ and $\Omega^*_{ccc}(ccc) - J/\psi(\bar{c}c)$; they are plotted against the square of the pseudoscalar masses (i.e., at D_u , D_s) and η_c mass. We fit the quark mass dependence with a form $a + b/m_{ps}$ (right figure is also fitted with a constant term). The fitted results are shown by solid lines with shaded regions as one sigma error bars.

This way we obtain the mass splitting of $B^*_c - B_c$ as 80 ± 8 MeV (fitting with a form $a + b/m_{ps}$) and 76 ± 7 MeV (fitting with a constant term). This result agrees very well with the results obtained in potential models [162]. However, this result does not agree with other lattice QCD prediction [74, 75, 163], which provided much lower values. It will be interesting to study the lattice cut-off effect on the hyperfine splittings of these hadrons with the possibility of future discovery of B^*_c meson. By taking $m_{B_c} = 6277$

MeV, our other prediction, the mass of $\Omega^*_{ccb}(3/2^+)$ is 8050 $\pm$ 10 MeV, which is consistent with the results from various models [30, 34, 38, 50] and a recent lattice calculation [164].

4.3 Singly charm baryons

Singly charm baryons have received significant scientific attention, mainly due to the recent experimental discoveries at various particle colliders like, SELEX, CDF, D0, Belle *etc.* In contrast to the triply and doubly charm baryons, the production and identification of singly charm baryons are relatively easier in hadron-hadron colliders as well as in electron-positron colliders. Particularly, the new Beijing Spectrometer and Belle II has great potential for accumulating large number of events and thus help us understand more about single charm baryons. The PANDA experiment, a GSI future project, and the LHCb are also expected to provide huge amount of information on charm baryon spectrum.

Considering the experimental prospects, it is very timely to study the singly charm baryons using a first principle non-perturbative calculation. That will serve various purposes : understanding the structure of already discovered states, assigning quantum numbers to ambiguous states and finally predicting states, which can be searched experimentally. After triply and doubly charm baryons, we studied singly charm baryons with the same detailing. However, for singly charm baryons the number of channels are many more, namely, $\Lambda_c(cud)$, $\Sigma_c(cuu)$, $\Xi_c(cus)$, and $\Omega_c(css)$. In the presence of one or two light quarks, the dynamics of these particles become much more complicated and hence they provide a unique opportunity to study the interaction between one or more light quarks in the presence of a heavy quark. These systems provide an excellent laboratory to study the dynamics of the light quark in the heavy quark environment, such as those controlled by the chiral symmetry. In a heavy quark effective theory, the two light quarks in the singly charm baryon can often be considered as a diquark system, similar to the case in doubly charm baryons. In the heavy quark limit, the spin-spin interactions between the heavy quark and the diquark will vanish and hence the diquark spin will be a good quantum number and will have implications in the singly charm spectrum as degeneracies between the spin-spin coupled states.

4.3.1 The spectrum

In this case, the number of possible interpolating operators are more than triply and doubly charm baryons as was shown in Table 3.8. We considered a large set of interpolating operators, as high as 180 (in H_g irrep for Ξ_c baryons), in construction of the correlation functions. In the analysis, we considered the full set of relativistic and non-relativistic operators for all the singly charm baryons, except for the Ξ_c, where we used only the non-relativistic operators. We show our results for the spectra of singly charm baryons in Figure 4.22, 4.23, 4.25 and 4.26, while the respective estimates are tabulated in the Tables 4.5, 4.6, 4.7 and 4.8. As in the previous cases, we plot the spectra in terms of the mass splittings instead of the absolute values. This is because the mass splittings are expected to suffer less from the discretization errors, as they gets canceled between the individual masses. In these plots, we show the mass splittings of these channels from 0.5 m_{η_c}, where the effects of charm quark discretization cancels out.

As in the previous cases, we observed that the pattern of the extracted low-lying states are remarkably similar to the expectation from a model with broken $SU(6) \times O(3)$ symmetry. As previously, the low lying bands that have relatively large overlap with the non-relativistic operators are shown with magenta boxes. Similarly the states with significant overlap with the operators proportional to the field strength tensor are painted with thick borders, and are identified as strongly hybrid in nature.

$\frac{1}{2}^+$	$\frac{3}{2}^+$	$\frac{5}{2}^+$	$\frac{7}{2}^+$	$\frac{1}{2}^-$	$\frac{3}{2}^-$	$\frac{5}{2}^-$	$\frac{7}{2}^-$
1.072(10)	1.185(10)	1.827(21)	1.058(25)	1.443(12)	1.524(12)	1.522(22)	2.105(37)
1.825(15)	1.825(20)	1.838(21)	1.822(16)	1.448(10)	1.533(10)	2.093(27)	
1.872(18)	1.825(40)	1.916(21)		1.612(13)	1.626(12)	2.083(38)	
1.883(25)	1.883(13)	1.950(29)		2.122(26)	2.092(19)	2.138(30)	
1.892(16)	1.904(20)	2.055(30)		2.165(31)	2.257(16)		
1.918(16)	1.943(20)			2.180(25)	2.261(28)		
2.022(19)	1.979(17)			2.193(28)	2.310(24)		
2.591(30)	2.027(23)			2.251(27)			
2.533(28)	2.033(18)			2.340(20)			
	2.511(35)						

Table 4.5: Relativistic spectrum $m_{\Sigma_c} - 0.5\ m_{\eta_c}$ in units of GeV.

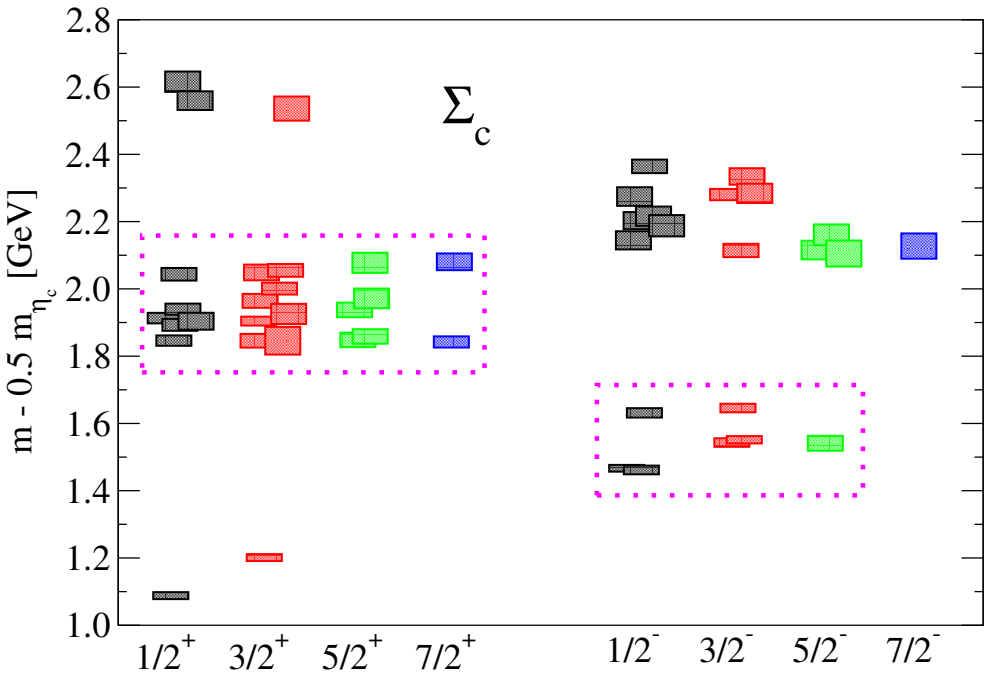

Figure 4.22: Results on the spin identified spectra of Σ_c for both even and odd parities *w.r.t.* 0.5 m_{η_c}. The keys are same as in Figure 4.1.

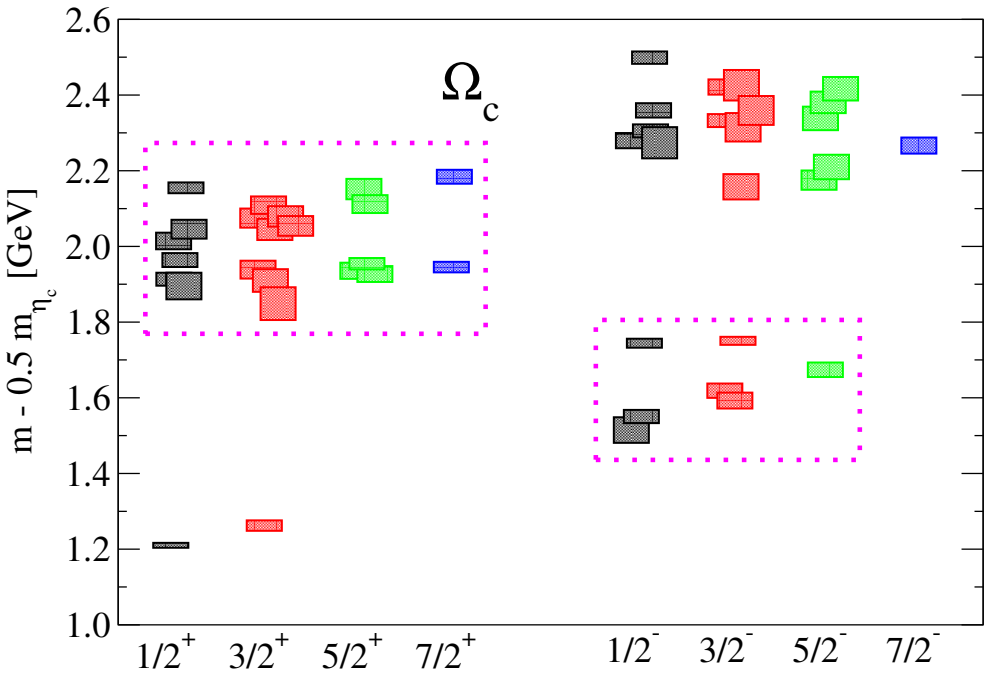

Figure 4.23: Results on the spin identified spectra of Ω_c for both even and odd parities *w.r.t.* 0.5 m_{η_c}. The keys are same as in Figure 4.1.

$\frac{1}{2}^+$	$\frac{3}{2}^+$	$\frac{5}{2}^+$	$\frac{7}{2}^+$	$\frac{1}{2}^-$	$\frac{3}{2}^-$	$\frac{5}{2}^-$	$\frac{7}{2}^-$
1.210(6)	1.262(14)	1.927(21)	1.945(14)	1.515(34)	1.593(21)	1.674(19)	2.267(21)
1.895(35)	1.849(43)	1.936(21)	2.184(18)	1.550(17)	1.619(19)	2.175(25)	
1.913(17)	1.910(30)	1.954(15)		1.744(12)	1.750(10)	2.210(32)	
1.964(18)	1.939(24)	2.112(24)		2.274(41)	2.157(33)	2.338(31)	
2.014(22)	2.045(28)	2.152(27)		2.280(20)	2.315(38)	2.381(28)	
2.046(25)	2.054(26)			2.305(17)	2.333(17)	2.417(31)	
2.059(74)	2.075(25)			2.360(19)	2.359(38)		
2.155(14)	2.079(27)			2.499(16)	2.421(20)		
2.258(90)	2.109(23)				2.426(40)		

Table 4.6: Relativistic spectrum $m_{\Omega_c} - 0.5\ m_{\eta_c}$ in units of GeV.

4.3.2 Σ_c and Ω_c baryon

The Σ_c^{++} and Ω_c baryons have the same flavor structure : pqq. The allowed flavor symmetries are similar to that of the doubly charm baryons, where one can have S flavor structure and MS/MA flavor structure. Thus the spectrum of these two baryons should resemble the spectrum obtained for the doubly charm baryons. This is quite evident from the Figure 4.22 and Figure 4.23. In Figure 4.24, we show the hyperfine splittings of the Ω_c and Σ_c baryons in units of MeV. Alongside we plot the estimates from various lattice calculations available in the literature and quark model calculations. We also show the experimental value in the plot with a magenta filled polygon in each of the plots. We see a reasonably good agreement between various lattice calculations, though our estimate for the Σ_c hyperfine splitting lies above the experimentally observed value. One important caveat in these calculations is that the light pion mass is heavier than its experimental value and the disagreement between our estimate and the experimental value is mainly due to this unphysical pion mass. The box size of the lattice used in these calculations is $L \sim 1.9fm$. The finite size effects in singly charm baryons can be expected to be larger than the corresponding effects in triply and doubly charm baryons. Hence, a systematic study of finite size effects is also necessary, which is beyond the scope of the current work.

4.3.3 Λ_c baryon

The Λ_c baryons are those with quark content udc and can have an A or MS/MA flavor structure, which corresponds to Λ_c-singlet and Λ_c-octet respectively. The difference between the Λ_c-octet and the Σ_c^+ is that the latter is a part of the isospin triplet, while the

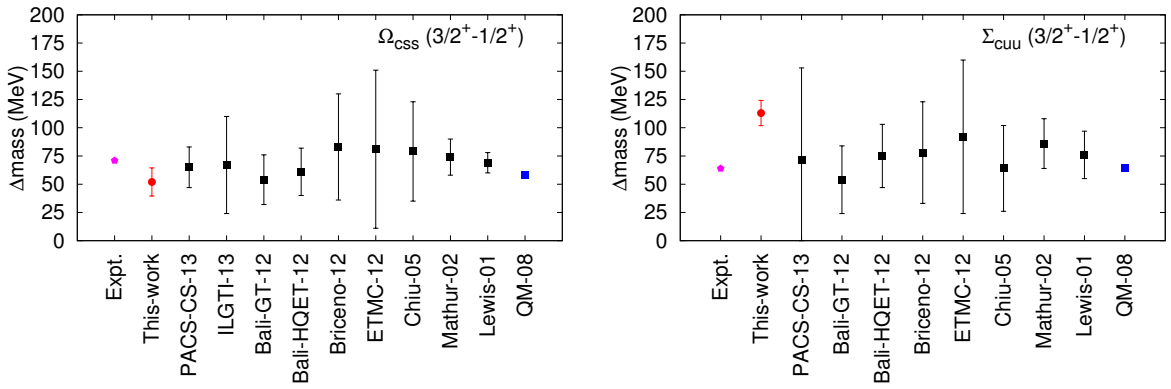

(a) (b)

Figure 4.24: Hyperfine splittings in Ω_c and Σ_c baryons(in MeV). The estimates from this calculation has been quoted in red filled circles, while estimates from other lattice calculations in black squares, and a quark model calculation in blue square. The experimentally observed value is quoted as magenta filled polygon. Pion mass in these calculations is 391 MeV, while results for PACS-CS [88], and Briceno *et. al* [84] are extrapolated to the physical pion mass, while ILGTI [127] and Bali, *et. al* [86] results are at pion mass 340 MeV and 348 MeV respectively.

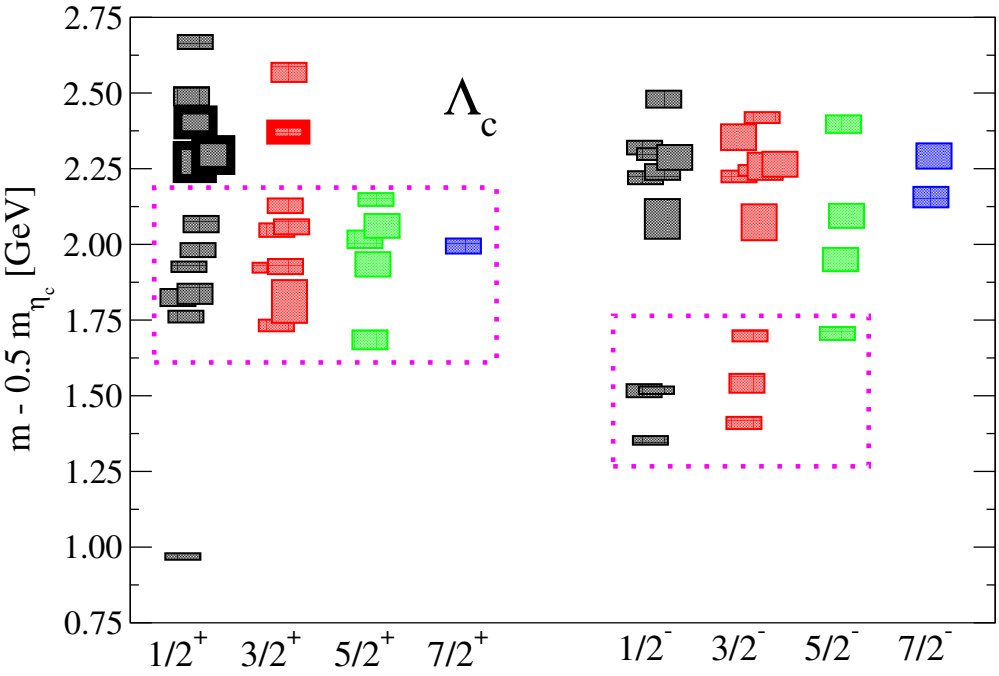

Figure 4.25: Results on the spin identified spectra of Λ_c for both even and odd parities *w.r.t.* 0.5 m_{η_c}. The keys are same as in Figure 4.1.

$\frac{1}{2}^+$	$\frac{3}{2}^+$	$\frac{5}{2}^+$	$\frac{7}{2}^+$	$\frac{1}{2}^-$	$\frac{3}{2}^-$	$\frac{5}{2}^-$	$\frac{7}{2}^-$
0.969(11)	1.732(19)	1.685(31)	1.995(25)	1.353(14)	1.410(20)	1.706(22)	2.156(34)
1.761(19)	1.811(70)	1.934(40)		1.517(22)	1.541(31)	1.950(39)	2.292(42)
1.825(28)	1.923(16)	2.017(29)		1.518(12)	1.698(18)	2.094(40)	
1.837(33)	1.927(25)	2.061(39)		2.084(66)	2.073(59)	2.397(29)	
1.926(17)	2.047(22)	2.148(21)		2.220(21)	2.224(19)		
1.981(23)	2.058(25)			2.239(26)	2.244(18)		
2.067(27)	2.128(24)			2.287(41)	2.258(45)		
2.272(55)	2.371(26)			2.298(19)	2.265(41)		
2.295(51)	2.568(32)			2.320(23)	2.354(43)		
2.403(41)				2.480(28)	2.419(18)		
2.489(30)							
2.669(23)							

Table 4.7: Relativistic spectrum $m_{_{\Lambda_c}} - 0.5\ m_{\eta_c}$ in units of GeV.

former forms an isospin singlet. The details of the flavor structure is shown in Table 3.2. Since there is no totally antisymmetric spin combination that can be constructed from a purely non-relativistic formalism, one requires angular momentum structure through non-local behavior to construct a flavor-singlet Λ_c interpolating operator. Figure 4.25 shows the spectrum of Λ_c, where one can observe only one state in the low lying band. This state has significant overlap with the flavors MS/MA with non-relativistic spin 1/2. As observed for the other channels, the numbers and the pattern of the first negative parity band and the first excited positive parity band agrees with the non-relativistic predictions. It is to be noted that the energy ordering of the low lying two positive parity states are in accordance with the experimental observation.

4.3.4 Ξ_c baryon

The Ξ_c baryons, with quark content usc, can have S, A or MS/MA flavor structure, which correspond to Ξ_c-decuplet, Ξ_c-singlet and Ξ_c-octet respectively. Within Ξ_c-octet flavor structure, one has two possibilities. If we assume an us-spin symmetry, similar to the isospin that describes the symmetry between u and d quarks, there are two possible MS/MA combinations : the Ξ_c-octet and the $\Xi_c^{'}$-octet. The latter is a part of the us-spin triplet, of which Ω_c and Σ_c^{++} are included, while the former is a us-spin singlet. As in the case of Λ_c, due to the absence of a totally antisymmetric spin combination that can be constructed from a purely non-relativistic formalism, one requires angular momentum

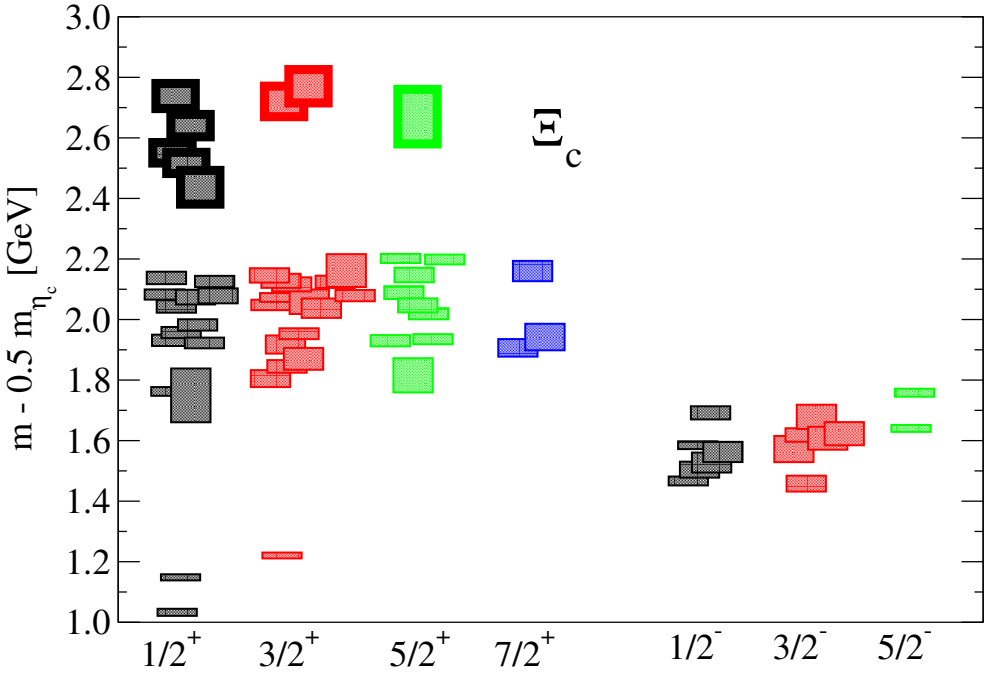

Figure 4.26: Results on the spin identified spectra of Ξ_c for both even and odd parities *w.r.t.* 0.5 m_{η_c}. The keys are same as in Figure 4.1.

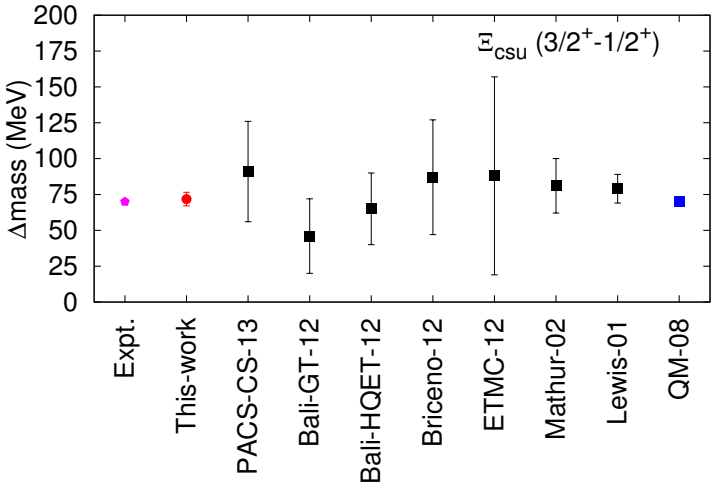

Figure 4.27: Hyperfine splittings in Ξ_c baryon(in MeV). The estimates from this calculation has been quoted in red filled circles, while estimates from other lattice calculations in black squares, and a quark model calculation in blue square. The experimentally observed value is quoted as magenta filled polygon.

structure through non-local behavior to construct a flavor-singlet Ξ_c interpolating operator. Hence the low lying spectra for Ξ_c baryon will have two spin 1/2 states from the

$\frac{1}{2}^+$	$\frac{3}{2}^+$	$\frac{5}{2}^+$	$\frac{7}{2}^+$	$\frac{1}{2}^-$	$\frac{3}{2}^-$	$\frac{5}{2}^-$	$\frac{7}{2}^-$
1.033(12)	1.221(10)	1.856(16)	1.985(14)	1.467(15)	1.458(26)	1.640(11)	
1.148(10)	1.805(28)	1.930(19)	2.019(22)	1.504(26)	1.572(43)	1.758(13)	
1.738(55)	1.845(21)	1.935(17)	2.180(22)	1.528(33)	1.608(38)		
1.762(14)	1.870(36)	2.019(19)		1.563(13)	1.619(22)		
1.923(18)	1.917(30)	2.030(18)		1.585(13)	1.622(38)		
1.931(19)	1.953(18)	2.089(21)		1.692(22)	1.679(40)		
1.957(18)	2.037(17)	2.147(24)					
1.982(19)	2.048(15)	2.164(21)					
2.043(21)	2.059(40)	2.198(16)					
2.074(24)	2.037(32)	2.202(15)					
2.078(25)	2.079(19)	2.670(90)					
2.083(17)	2.116(23)						
2.126(19)	2.125(20)						
2.138(21)	2.128(23)						
2.280(42)	2.146(24)						
2.437(56)	2.162(54)						
2.517(35)	2.721(51)						
2.551(34)	2.771(55)						
2.640(37)							
2.738(42)							

Table 4.8: Relativistic spectrum $m_{\Lambda_c} - 0.5\ m_{\eta_c}$ in units of GeV.

Ξ_c-octet and $\Xi_c^{'}$-octet operators and a spin 3/2 state with the Ξ_c-decuplet flavor structure. This can clearly be observed in Figure 4.26. We have calculated the correlation matrix for all of them. However, being too many in numbers, it is quite difficult to put together all these operators in our framework of variational fitting code. Hence, in this work, we use a smaller set comprising only the non-relativistic operators for fitting, and the Ξ_c spectrum shown in Figure 4.26 is non-relativistic. In Figure 4.27, we show the hyperfine splitting between the $3/2^+$ and $1/2^+$ ground states of Ξ_c baryon. Alongside we show the estimates from other lattice calculations and quark model estimate. The experimental value is shown as magenta filled polygon.

4.3.5 Energy splittings : A preliminary study

One important caveat in these calculations of the excited state charm baryon spectroscopy is that the pion mass used, $m_\pi = 391$ MeV. This unphysical heavy pion mass can give serious implications in the spectrum, where one expects the light quark chiral dynamics

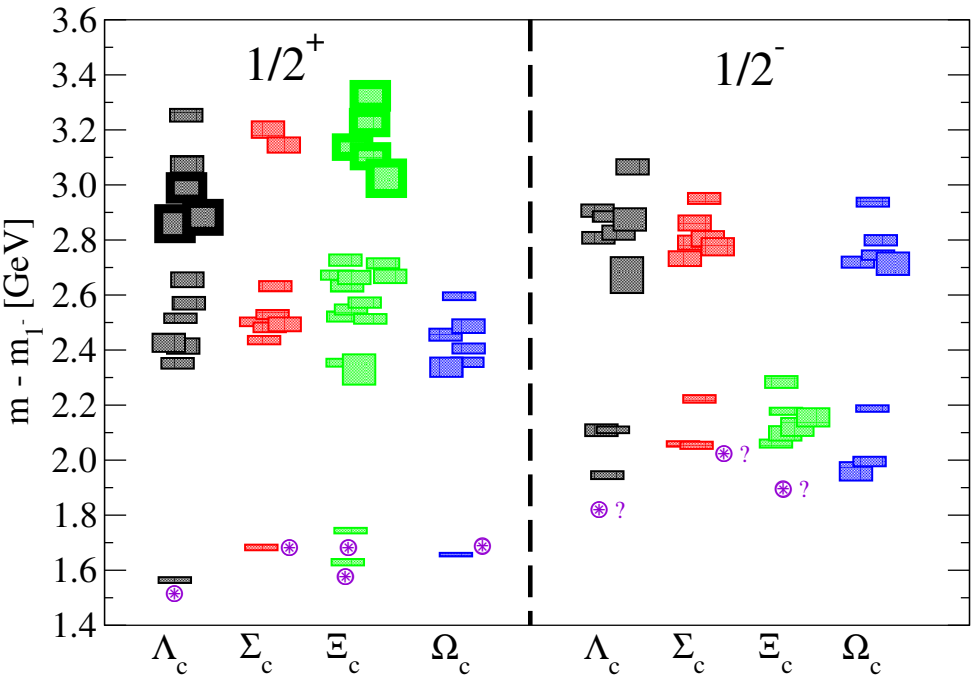

Figure 4.28: Spectra of spin 1/2 singly charm baryons shown as their splitting from the light vector mesons, such that the effective valence content in the splitting is a charm quark. Explicitly we consider the following splittings : $\Lambda_c(cud) - \rho(\bar{u}d)$, $\Sigma_c(cuu) - \rho(\bar{u}u)$, $\Xi_c(cus) - K^*(\bar{u}s)$ and $\Omega_c(css) - \phi(\bar{s}s)$.

to play a significant role. So as to make a comparative study of light quark effects in the singly charm baryons, we consider the splitting of the singly charm baryons with respect to the corresponding light vector mesons, such that there is only one remnant valence charm quark in the splitting. In other words, we consider the splittings, $\Lambda_c(cud) - \rho(\bar{u}d)$, $\Sigma_c(cuu) - \rho(\bar{u}u)$, $\Xi_c(cus) - K^*(\bar{u}s)$ and $\Omega_c(css) - \phi(\bar{s}s)$. This is a good choice, since to the leading order all these splittings should have the same discretization errors and the same effect of the light quark dynamics, making a comparative study between the singly charm baryon spectra possible. In Figure 4.28, 4.29, 4.30 and 4.31, we plot the spectra of the singly charm baryons, as the splittings mentioned above, corresponding to the spin 1/2, 3/2, 5/2 and 7/2 respectively. We also plot the experimental values (violet circled star) of the low lying singly charm states in these plots. Question marks are given beside those states that for which the quantum numbers are not certain (even based on quark model assumptions). It is very clear that the pattern of the low lying states, particularly for $1/2^+$ and $3/2^+$ channels, is almost the same between the experimental estimates and the results from our calculations. The little disagreement in the low lying spectra with the experimental numbers could be because of the various systematics that we will be

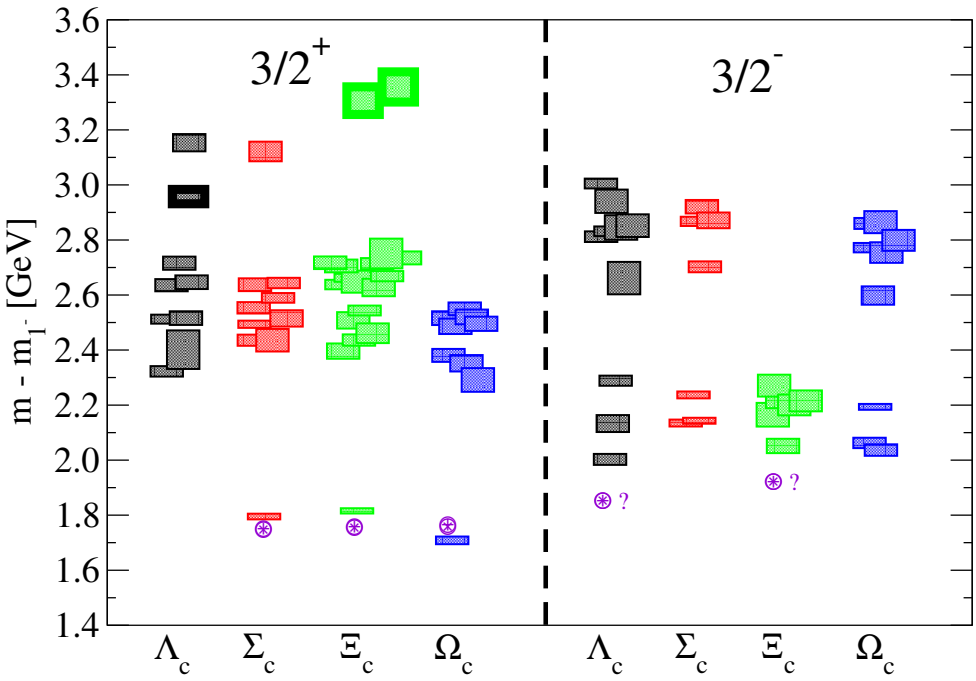

Figure 4.29: Spectra of spin 3/2 singly charm baryons shown in terms of the splittings : $\Lambda_c(cud) - \rho(\bar{u}d)$, $\Sigma_c(cuu) - \rho(\bar{u}u)$, $\Xi_c(cus) - K^*(\bar{u}s)$ and $\Omega_c(css) - \phi(\bar{s}s)$.

discussing in Section 4.4. This observation calls for a detailed study of the singly charm baryon spectra, with improved control over the systematics, particularly with lighter pion mass as well as with multi-hadron operators.

4.4 Caveats in excited state spectroscopy

Lattice computations should be accompanied with a study of the systematics associated with the formulation of the theory on lattice, so as to validate and compare the results obtained from these calculations with the actual values. The discretization of the space-time introduces a UV cut off proportional to the inverse of the lattice spacing $(1/a)$. The systematics from this UV cut off is in general quantified in terms of the dimensionless quantity, 'am', m being the quark mass. One in general considers complicated lattice formalisms, that has the discretization errors up to different orders of 'ma' removed. In this study, in order to have good control over the discretization errors, we use the tree level tadpole improved (mean field improvement [111]) clover fermion action, which has no $\mathcal{O}(ma_t)$ and $\mathcal{O}(ma_s)$ errors. We have not considered any higher order terms as the temporal lattice spacing is quite small. However, for the charm quarks the discretization

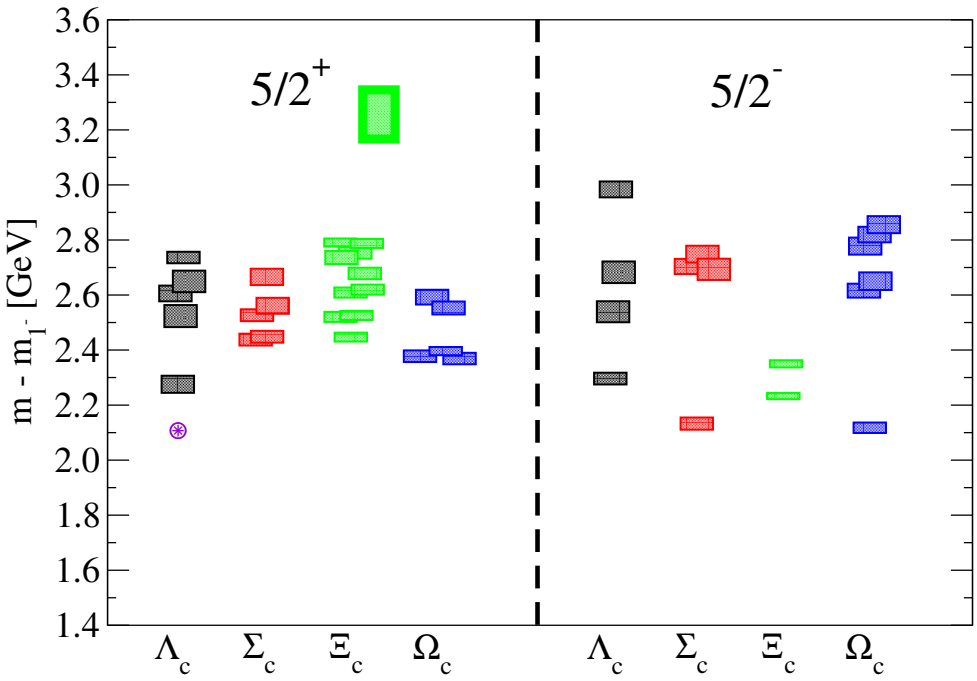

Figure 4.30: Spectra of spin 5/2 singly charm baryons shown in terms of the splittings : $\Lambda_c(cud) - \rho(\bar{u}d)$, $\Sigma_c(cuu) - \rho(\bar{u}u)$, $\Xi_c(cus) - K^*(\bar{u}s)$ and $\Omega_c(css) - \phi(\bar{s}s)$.

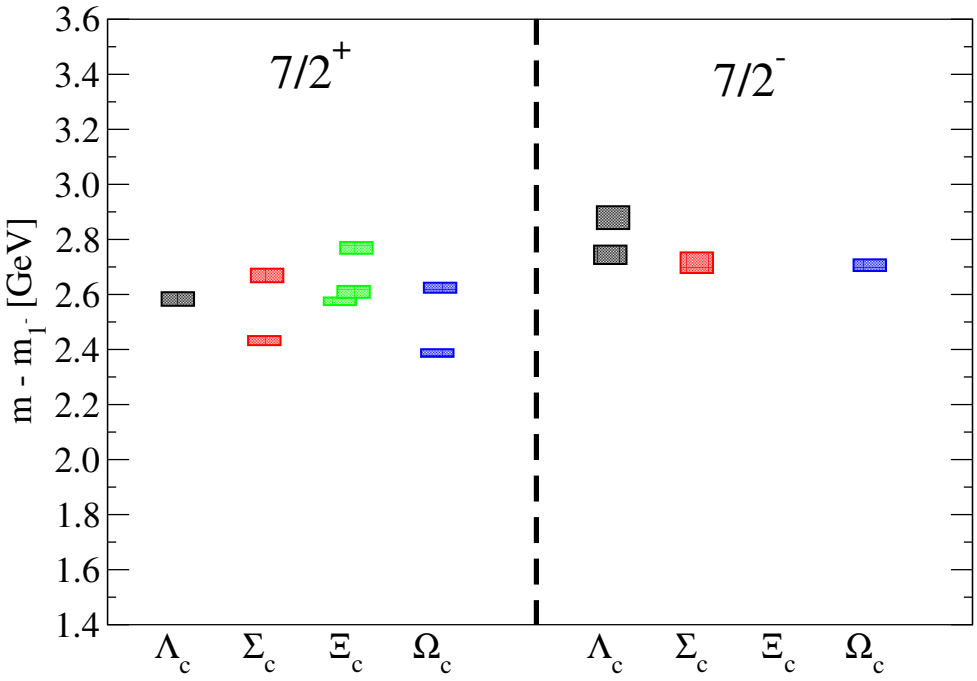

Figure 4.31: Spectra of spin 7/2 singly charm baryons shown in terms of the splittings : $\Lambda_c(cud) - \rho(\bar{u}d)$, $\Sigma_c(cuu) - \rho(\bar{u}u)$, $\Xi_c(cus) - K^*(\bar{u}s)$ and $\Omega_c(css) - \phi(\bar{s}s)$.

errors is significantly larger than the light and strange quarks on a given lattice. The study of heavy hadrons using lattice QCD has this inherent problem, since at these masses, with currently available lattices, the condition $ma_t << 1$ and $ma_s << 1$, in general is not satisfied leading to larger systematic errors. In such a case, one require to perform a continuum extrapolation of the estimates from calculations using multiple lattices with very fine lattice spacings : this is beyond the scope in these excited state spectroscopy calculations.

Another systematics that enter the lattice calculations is due to the finite box size, which is limited by the available computational resources. To ensure negligible finite size effects in these systems, in general one makes sure that the lattice size, L, is at least 4 times the Compton wavelength of the lightest state in that lattice. In our calculations, $m_\pi L = 3.77$ and hence we expect the finite size effects to be under control. An infinite volume extrapolation is necessary to have the estimates free of finite size effects : This is also beyond the scope of the previous work, as excited baryon spectroscopy calculations involving larger lattices calls for very large computational requirements, which is currently beyond the limit of the available resources.

A third systematics in lattice QCD calculations is related to the light quark masses that are used in the calculations. The computational cost for calculations involving fermions increases as the quark mass decreases and hence the studies involving lighter quark masses are highly CPU intensive. The light quark mass used in these calculations corresponds to a pion mass of ~ 391 MeV, which is greater than the physical pion mass. Hence, along with the continuum and the infinite volume extrapolations, one need to perform a chiral extrapolation, which is not possible with just one light quark mass available in these calculations. With all these caveats related to the lack of study of systematics in mind, confronting this calculation with another non-perturbative study with better control over the systematics, will be a good check to validate the smallness of the systematic errors in our results from calculations in the previous chapters.

Finally we have not used the multi-hadron operators in our basis of operators. These operators couples efficiently onto multi-hadron scattering states having the same quantum number as the resonance states. As an example, while studying ρ resonance, one needs to include $\pi\pi$ two-particle operators along with regular 1^{--} operator set. To match the appropriate quantum number one use the technique of moving frames where the total momentum of the system is nonzero. This has been demonstrated in Ref. [166], where ρ resonance has been studied in great details. This is also true for Δ, $S_{11}(1535)$ resonance, where one needs to use $N\pi$ operators to study these resonances. Other higher particle

decay channel operators also need to be included for comprehensive study of resonances. These additional operators will increase the number of levels that can be extracted and hence the resonance parameters can be evaluated from the extensive mapping of the energy dependence of the scattering amplitudes. In this calculation, one should also use these multi-hadron operators in the basis of operators. Inclusion of those operators, particularly those involving light quarks, may affect some of the above conclusions. However, due to the presence heavier quark(s), influence of these multi-hadron operators may be lesser for charm baryons, particularly for triply and doubly charm baryons, than their influence in the light baryons.

4.5 Summary, conclusions and future prospects

In this work, we present results from the first non-perturbative calculation on the excited state spectroscopy of the charm baryons, with three, two and one valence charm quarks and with spin up to 7/2. Employing a large set of operators classified according to the irreps of the lattice symmetries, constructed out of derivative based operator formalism using up to two derivatives, we extracted approximately 20 states for each of the charm baryons, along with a reliable identification of the spin-parity quantum numbers for each of these states. Beside identifying the spin of a state we are also able to decode the structure of operators leading to that state : whether constructed by relativistic, non-relativistic, hybrids, non-hybrid types or a mixture of them all. We discussed the results in three sections, dedicated for triply, doubly and singly charm baryons respectively.

The spectra for the triply, doubly and singly charm baryons are shown in Figure 4.1, 4.9, 4.8, 4.22, 4.23, 4.25 and 4.26. Similar to light and strange baryon spectra [102], we also find the number of extracted states of each spin in the three lowest-energy bands and the number of quantum numbers expected based on weakly broken $SU(6) \times O(3)$ symmetry agree perfectly, *i.e.,* all the charm baryon spectra remarkably resemble the expectations of quantum numbers from non-relativistic quark model [28, 29, 165]. It is to be noted that in these calculations, we use the full set of operators (non-relativistic and relativistic) and still the spectra behaves to be non-relativistic.

Discretization errors are of major concern for heavy hadron spectroscopy. Since a calculation involving multiple lattice spacing is beyond the scope of this work, we follow a similar analysis procedure, as was performed in Ref. [106]. To assess if radiative corrections to the co-efficient of the improvement term in the charm quark action could lead to significant changes in physical predictions, we perform a second calculation using

a boosted spatial clover co-efficient, $c_s = 2$, from its tree level tadpole improved value, $c_s = 1.35$. A very similar shift of ~ 45 MeV, to that found in charmonia, was observed for the lowest few states of triply and doubly charm baryons, indicating a similar scale of uncertainty in this calculation of charm baryons also. The higher lying charm baryon states do not show any statistically significant shifts between the estimates from the two calculations.

Various energy splittings, including splittings due to hyperfine and spin-orbit coupling, are also evaluated for all these baryons. In the triply charm baryons we performed a quantitative study of the spin-orbit coupling to understand how good is the heavy quark approximation for the charm quarks, by comparing them with the respective splitting for triply light, strange and bottom baryons. We find degeneracy between these spin-orbit split states is more or less satisfied both for bottom and charm quarks. However, data with higher statistics is necessary to identify the breaking of this degeneracy precisely at charm quark. The energy splitting of the triply charm baryon spectrum, from the isoscalar vector meson (irrep T_1^{--}) ground state is also evaluated. These splittings are compared with similar ones obtained at other quark masses. For the splitting, which mimics the binding energy of these states, significant quark mass dependence is observed for ground as well as for first few excited states, except for the $J^P = 3/2^+$ and $J^P = 1/2^-$ ground states. These splittings can be modeled with a form $a + b/m_{\rm ps}$ to show their expected quark mass dependence, which assumes they will tend to a constant in the heavy quark limit. It is interesting to note this form gives a good fit with data at bottom, charm as well as strange quark masses. For some of them, we observe that the extrapolated fit lines pass through the light quark data points even through they are not included in the fit.

For doubly and singly charm baryons, we calculated hyperfine mass splittings between spin-$\frac{3}{2}^+$ and spin-$\frac{1}{2}^+$ states and compared those with various other lattice as well as model results. We also evaluated mass splittings between ground states of spin-$\frac{3}{2}$ and spin-$\frac{1}{2}$ states at both parities. To study the quark mass dependence of these splittings we compared results for $\Xi_{cc}(ccu)$, $\Omega_{cc}(ccs)$ and $\Omega_{ccc}(ccc)$ baryons for which there is a common 'cc' diquark and a varying quark from 'u' to 'c'. Encouraged by a successful fitting of the mass splittings in triple flavored baryons, we studied similar mass splittings. Here also we find that a heavy quark motivated form $a + b/m_{ps}$ can fit quite successfully energy splittings like : $\Xi^*_{cc}(ccu) - D_u(\bar{c}u)\,, \Omega^*_{cc}(ccs) - D_s(\bar{c}s)$ and $\Omega^*_{ccc}(ccc) - \eta_c(\bar{c}c)$, and $\Xi^*_{cc}(ccu) - D^*_u(\bar{c}u)\,, \Omega^*_{cc}(ccs) - D^*_s(\bar{c}s)$ and $\Omega^*_{ccc}(ccc) - J/\psi(\bar{c}c)$. From the fitted results we are able to predict $B^*_c - B_c = 80 \pm 8$ MeV and $\Omega^*_{ccb}(3/2^+) = 8050 \pm 10$ MeV. The study

of energy splittings of singly charm baryons is ongoing and we expect similar interesting results from that sector also. The method used here to study charm baryons can also be employed for similar study of bottom baryons. Considering experimental importance and prospects we will carry out such calculation in future.

There are various systematics that are unattended in this calculation, which include various extrapolations like chiral extrapolation, continuum limit and infinite volume extrapolation. Furthermore, it is also to be noted that we have not used any multi-hadron operators, which are expected to give significant implications in the extracted spectra. Hence, one also need to perform calculations considering multi-hadron operators. However, this calculation is the first of its kind in the excited charm baryon spectra calculation and hence this study serves as a foundation for many follow up studies, which may help us address many of the challenges in the heavy baryon spectroscopy.

Chapter 5

Spectroscopy using chiral fermions

In this chapter, we discuss another independent non-perturbative calculation to determine the low lying charm baryon spectrum with improved control over the systematics. This alternative calculation was made with a hope that confronting our ground state studies with the excited state calculations will give us an idea of the systematic errors appearing in our excited state spectrum calculations. We give a brief introduction of this calculation in Section 5.1 and Section 5.2. As mentioned earlier, discretization errors are of major concern in charm baryon spectroscopy. In Section 5.3, we detail our attempts to quantify the discretization errors that enters in these calculations, by studying the dispersion relation for the pseudoscalar charmonia. In Section 5.4, we discuss our results on charmonia, charm-strange mesons and charm baryons. There we make comparison of estimates from this studies with the experimental estimates, wherever available. We also make comparison of estimates from this calculation and our studies of excited state spectroscopy, wherever available. Finally, in Section 5.5, we summarize the findings in these calculations.

5.1 Mixed action formalism

In order to study the systematics due to the discretization errors in our previous study, we thus performed another calculation with a chiral action with the overlap fermions [123, 124], which is automatically $\mathcal{O}(a)$ improved. However, using overlap action for the dynamical quarks is still prohibitively costly, except with fixed topology [167]. A substantially less expensive approach is to adopt a mixed action formulation with chiral fermions as valence quarks in a background of existing highly improved gauge field configurations.

Mixed action approaches have been studied by many groups such as DWF valence on staggered fermion sea [63, 115, 116, 117], overlap valence on DWF sea [118], overlap valence on clover sea [119], and overlap valence on twisted fermion sea [120]. The Indian Lattice Gauge Theory Initiative (ILGTI) has adopted this mixed action approach and this part of my thesis is related to my work in that project. This calculation uses a large set of dynamical configurations generated during the past few years by MILC [122] with the one-loop, tadpole improved Symanzik gauge action and highly improved staggered quark (HISQ) fermion action [121]. Two degenerate light quarks, a strange and a charm sea quark field were included in the generation of these dynamical configurations. With very small magnitude of taste violations in comparison with the unimproved staggered quarks, HISQ provides an efficient lattice fermion formulation that demands very less computational requirements in contrast with the overlap action in simulation.

The valence quarks in this calculation are realized using the overlap formalism [123, 124], which has many desirable features. The overlap formalism has exact chiral symmetry [124] on the lattice and is automatically $\mathcal{O}(a)$ improved. By adopting such a mixed action approach, one can get advantage of the chiral symmetry and low quark mass limit of overlap fermions, and the advantage of having a large set of configurations with small discretization errors as well as small taste breaking effects. One also gets the advantage of simulating both light, strange as well as heavy fermions on the same lattice formalism with chiral fermions having no $\mathcal{O}(a)$ errors. The overlap action also has some desirable features computationally, such as the adaptation of multi mass algorithms [125]. However, we will have to encounter the usual systematics related to mixed action and partial quenching [169, 170, 171]. With the above formulation we have calculated the ground state spectra of various charm hadrons and have made a comparative study between these two projects along with other results from literature. Agreement between these results from different approaches gives confidence in our previous estimates. The results from these studies were reported in the Ref. [127, 126]

5.2 Numerical details

In this calculation, we used two sets of dynamical 2+1+1 flavors HISQ lattice ensembles, generated by the MILC [122] : $32^3 \times 96$ lattices with lattice spacing $a = 0.0877(10)\ fm$ and $48^3 \times 144$ lattices with lattice spacing $a = 0.0582(5)\ fm$. The gauge action used in these calculations is a one-loop, tadpole improved Symanzik gauge action that included 1×1 and 1×2 planar Wilson loops and a $1 \times 1 \times 1$ 'parallelogram'. The co-efficients of

these terms are calculated perturbatively and are tadpole improved. As mentioned above, the sea quark fields were realized using the HISQ action, which ensured the quark action is order a^2 improved. The use of HISQ action, instead the naïve staggered quark action, ensured very small taste-symmetry violations. The lattice spacings of these lattices mentioned above were determined by equating the Ω baryon mass measured on these ensembles to its physical value. Our estimates for the lattice spacings, as mentioned above, are consistent with the estimates as measured by MILC using the r_1 parameter [122], which are $a = 0.0888(8)$ fm and $a = 0.0582(4)$ fm respectively. The strange and charm masses are set at their physical values, while $m_l/m_s = 1/5$ for both lattices. The details of these configurations are summarized in Ref. [122]. The results reported here were obtained from 110 configurations on the coarser lattice, and 65 configurations on the finer lattice.

For valence quarks we used overlap action [124]. The overlap Dirac operator has the following definition for massive fermions :

$$D_{ov} = (\rho + \frac{m}{2}) + (\rho - \frac{m}{2})\gamma_5 sgn(\gamma_5 D_w); \qquad sgn(\gamma_5 D_w) = \frac{\gamma_5 D_w}{\sqrt{\gamma_5 D_w \gamma_5 D_w}}, \tag{5.1}$$

where sgn denotes the matrix sign function, D_w is the Wilson Dirac fermion operator and $\rho = 1/2\kappa - 4$ here is a negative mass parameter. Lüscher showed that on the lattice one can define the chiral transformation as [147],

$$\delta\psi = i\alpha\gamma_5(1 - \frac{a}{2}D_{ov})\psi \quad \& \quad \delta\bar{\psi} = i\alpha\bar{\psi}(1 - \frac{a}{2}D_{ov})\gamma_5, \tag{5.2}$$

which reduces to the proper continuum form in the continuum limit. For any $a \neq 0$, the overlap action remains invariant under this lattice chiral transformation. While the Wilson fermion action is ultra-local having only up to second derivative terms in it, in overlap fermions the condition of ultra-locality is sacrificed to preserve the exact chiral symmetry on the lattice in accordance with the Nielson-Ninomiya theorem. The advantage of the overlap fermion over Wilson fermion is the presence of the exact chiral symmetry. But since the operator contains a matrix sign function, its numerical studies require more computational resources than the Wilson fermion formulation.

Hence, for the numerical implementation of massive overlap fermions the methods used by the χQCD collaboration [168, 172] were followed. The gauge configurations were first fixed to Coulomb gauge and then HYP smeared [173]. Low mode deflation technique was employed in the inversion of the Hermitian Wilson Dirac operator ($\gamma_5 D_w$). In these

calculations, we projected out 350 and 160 low lying Wilson eigenmodes for the coarser and the finer lattices, respectively, using Arnoldi algorithm. The matrix *sign* function of the Hermitian Wilson Dirac operator in the overlap Dirac operator is calculated with 22^{nd} degree Zolotarev rational polynomial approximation [174, 175]. We used periodic boundary condition in the spatial and anti-periodic in the temporal directions. Using both point and wall sources and sinks, we calculated various hadron two point correlation functions. The adaptation of the multi mass algorithms on overlap action helped us to calculate the quark propagators over a wide range of quark masses with $10-12\%$ overhead. Our extracted pseudoscalar meson masses are within the range $400-5130$ MeV and $230-4000$ MeV for the coarser and finer lattices respectively. The valence strange quark mass was tuned by setting the $\bar{s}s$ pseudoscalar mass to 685 MeV [176]. At heavy quark masses, one need to be careful about the discretization errors. The charm mass is tuned by setting the spin-averaged 1S state mass, $(m_{\eta_c}+3m_{J/\psi})/4$, to its physical value, where we take into account the kinetic mass, as defined below, in the definition of mass. As in the previous sections, in the following sections also, we will discuss our estimates for mesons and baryons mostly in terms of energy splittings as those have less systematics compared to extracted energies.

5.3 Discretization errors

Since ma is not very small, we need to be careful about discretization errors. Overlap action does not have $\mathcal{O}(ma)$ errors. In order to estimate the size of discretization errors coming from higher orders of ma, we look at the energy-momentum dispersion relation of the 1S charmonia. A naive construction of finite-momentum meson correlation functions by projecting the point-point meson correlation function to a suitable momentum is in general noisy, and require large statistics. Hence in these calculations of dispersion relations, we use a momentum induced wall source to construct the quark propagators, which are later used to project the meson correlators to suitable momentum. Below we briefly discuss this method, which is found to improve the SNR ratio significantly in the finite momentum correlators with much less statistics [127].

5.3.1 Finite momentum meson correlators

The mode expansion of a quark propagator from a point source is given by

$$S(x'_\mu; x_\mu) = \frac{1}{L^3\ N_t} \sum_{k_\mu} e^{ik_\mu(x_\mu - x'_\mu)} \tilde{S}(k_\mu). \tag{5.3}$$

A quark propagator constructed out of a momentum ($k_{1,m} = \frac{2\pi m}{L}$) induced wall source is defined as :

$$\begin{aligned} \sum_{x'_1,x'_2,x'_3} e^{ik_{1,m}x'_1} S(x'_\mu; x_\mu) &= \sum_{x'_1,x'_2,x'_3} \frac{e^{ik_{1,m}x'_1}}{L^3\ N_t} \sum_{k_\mu} e^{ik_\mu(x_\mu - x'_\mu)} \tilde{S}(k_\mu), \\ &= \frac{e^{ik_{1,m}x_1}}{N_t} \sum_{k_4} e^{ik_4(x_4 - x'_4)} \tilde{S}(k_{1,m}, 0, 0, k_4), \\ &= S(x_1, x_4; x'_4; k_{1,m}). \end{aligned} \tag{5.4}$$

With $m = 0$, we get back the wall source,

$$\sum_{x'_1,x'_2,x'_3} S(x'_\mu; x_\mu) = \frac{1}{N_t} \sum_{k_4} e^{ik_4(x_4 - x'_4)} \tilde{S}(0, 0, 0, k_4) = S(x_4; x'_4). \tag{5.5}$$

Construction of finite momentum meson correlation function follows by introducing another phase factor in the final momentum projection, so as to compensate the phase factor that was introduced in the source. Local meson interpolating operators possess the form $\bar{\psi}\Gamma\psi(x)$, where Γ carries the quantum numbers. With the use of momentum induced wall sources, the finite momentum correlation functions for such operators can be written as

$$\begin{aligned} &\sum_{x,y,z} e^{-ik_{1,n}x_1} \langle \bar{\psi}\Gamma\psi(x) \bar{\tilde{\psi}}^m \Gamma' \tilde{\psi}^0(x') \rangle \\ &\qquad = \sum_{x,y,t} Tr\{\Gamma S(x_1, x_4; x'_4; k_{1,m}) \Gamma\gamma_5 S^\dagger(x_4; x'_4)\gamma_5\}\ e^{-ik_{1,n}x_1} \\ &\qquad = Tr\{\frac{\Gamma}{N_t} \sum_{k_4} e^{ik_4(x_4 - x'_4)} \tilde{S}(k_{1,m}, 0, 0, k_4) \\ &\qquad\quad \times \frac{\Gamma\gamma_5}{N_t} \sum_{k'_4} e^{-ik'_4(x_4 - x'_4)} \tilde{S}(0, 0, 0, k'_4)\gamma_5\} \sum_{x_1} e^{i(k_{1,m} - k_{1,n})x_1}, \end{aligned} \tag{5.6}$$

and

$$\sum_{x,y,z} e^{-ik_{1,n}x_1} \langle \bar{\psi}\Gamma\psi(x)\bar{\tilde{\psi}}^m\Gamma'\tilde{\psi}^0(x')\rangle = \begin{cases} M(k_{1,m}) & \text{if } m = n \\ 0 & \text{if } m \neq n \end{cases} \tag{5.7}$$

Here $\tilde{\psi}^m(x')$ is the momentum induced quark source field with a phase factor, $e^{ik_{1,m}x'_1}$, and $M(k_{1,m})$ is the finite momentum meson propagator with a momentum, $k_{1,m}$.

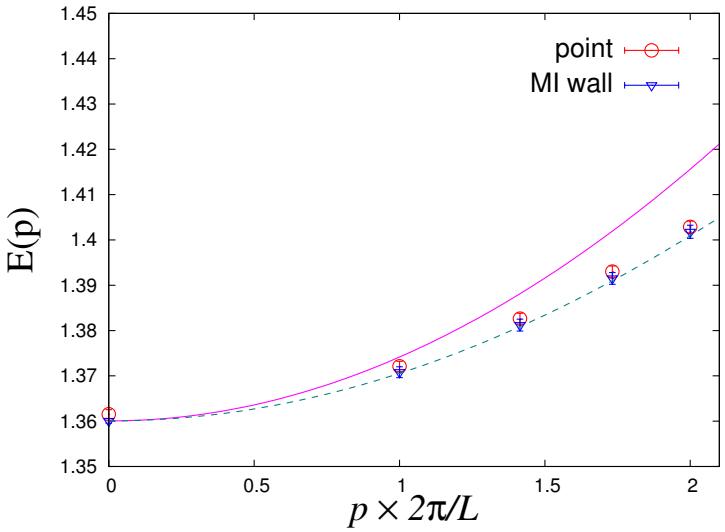

Figure 5.1: Energy-momentum dispersion relation for the η_c on the coarser lattices with $a = 0.09$ fm. Also shown are the continuum relativistic dispersion relation (solid line), and the lattice dispersion relation (dashed line) for the standard scalar action.

Employing this method and simple point source, we calculated pseudoscalar meson mass at various external momenta $p^2 = n^2\ (2\pi/L)^2$, with $n \leq 2$. While the momentum induced wall requires a separate inversion for each momenta, that is more than compensated by the improvement in the signal, as shown in Figure 5.1. In this figure, we show both point source and momentum induced wall source results for the coarser lattice. Also shown are the continuum dispersion relation, $E^2 = m^2 + p^2$, and the lattice dispersion relation for the standard scalar action with $O(m^2a^2)$ error, $\sinh^2(E(p)a/2) = (\sinh^2(ma/2))^2 + \sin^2(pa/2)$. Note that the wall source results are from 8 configurations, but the statistical error is already comparable to that from 100 configurations with the point source. While substantial deviation from the continuum dispersion relation is seen, the lattice scalar dispersion relation seems to explain the data quite well.

For a more quantitative analysis, we follow the standard practice of introducing an effective "speed-of-light" c through $E^2(p) = m^2 + p^2c^2$. The value of c obtained using

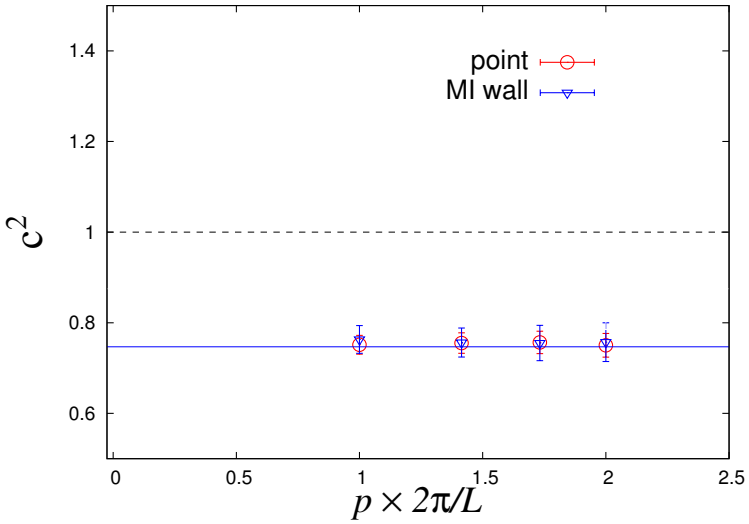

Figure 5.2: $c^2 = (E^2(p) - E^2(p = 0))/p^2$ calculated for η_c at various values of p, on lattices with $a = 0.09$ fm. Solid horizontal lines represent the estimate $ma/\sinh(ma)$, suggested by the lattice scalar action.

this relation and $E(p)$ at various p are shown in Figure 5.2. As the figure shows, we get $c^2 \sim 0.75$ on our coarser lattices. Using quenched overlap fermions, on an even coarser lattice, Ref. [177] found $c^2 \sim 1$ for the charm. However, on our dynamical lattices, we obtained c^2 values similar to that obtained in the literature with clover action, indicating a similar size of cutoff in the overlap action as that in the clover. The c^2 values are well-approximated by the estimate $ma/\sinh(ma)$, suggested by the lattice scalar action.

With such a large deviation of c from unity, the discretization errors entering due to uncertainty in the tuning of charm mass could be very large. In a second attempt, we used an expansion of the energy-momentum dispersion relation in powers of $\mathbf{p}a$, assuming $\mathbf{p} << m_0$ & $1/a$,

$$E(p)^2 = M_1^2 + \frac{M_1}{M_2}\mathbf{p}^2 + O(\mathbf{p}^4) = M_1^2 + \mathbf{p}^2 c^2. \tag{5.8}$$

Here M_1 is the called pole mass, $E(0)$: which is the same as rest mass in our previous definition, and M_2 is called the kinetic mass (M_1/c^2). The difference between M_1 and M_2 is a measure of $\mathcal{O}(ma)$ cutoff effects. As highlighted in Ref. [178], in the so-called Fermilab interpretation, since M_2 controls the non-trivial physics of a heavy hadron system, in using a relativistic action for heavy quarks, one should use M_2 to measure the masses. In Figure 5.3, we show $E(p)^2$ for various momenta for the pseudoscalar meson on our finer lattices. The green line is for the continuum dispersion relation, $E^2 = m^2 + p^2$, while the blue line is the fitted dispersion relation with $c = 0.96(2)$. For coarser lattices

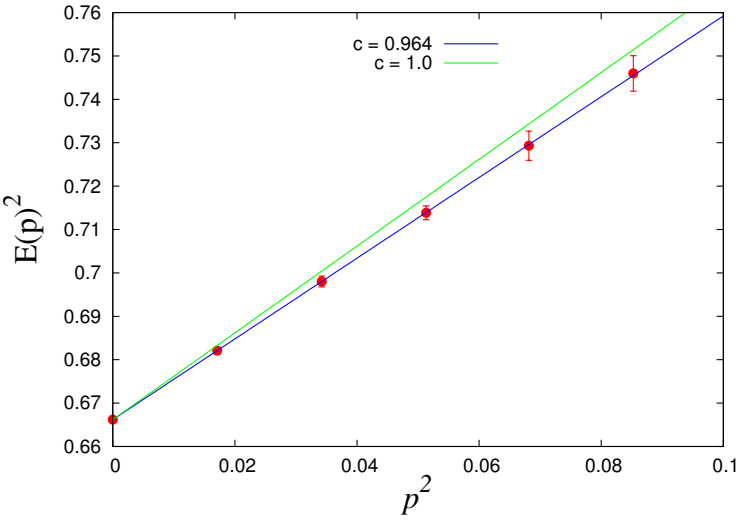

Figure 5.3: Energy-momentum dispersion relation for the pseudoscalar meson at charm mass on the finer lattices. Blue line is with c = 0.96(2) obtained by fitting our data while green line is with c = 1.

we obtain $c = 0.92(3)$. With a better estimate for c, kinetic mass proved to be a good candidate to be used for tuning the charm quark mass, as mentioned in the previous section.

5.4 Results

In this section, we discuss our results from these calculations. We studied pseudoscalar meson masses in a broad range of energies spanning between $400 - 5130$ MeV and $230 - 4000$ MeV for the coarser and finer lattices respectively. Figure 5.4 shows two plots of m_π versus m_q for the range of quark masses we performed the computations for coarser and finer lattices respectively.

We start our discussion with various energy splittings in mesons, including hyperfine splittings, in the following section. Following which, we discuss our estimates for various charm baryons, and their comparison with our previous calculations and other lattice determinations in literature.

5.4.1 Hyperfine splitting in 1S charmonia

The hyperfine splitting in 1S charmonia is one of the most well studied physical quantities in lattice charmonium calculations over the year, and until very recently [72, 73]

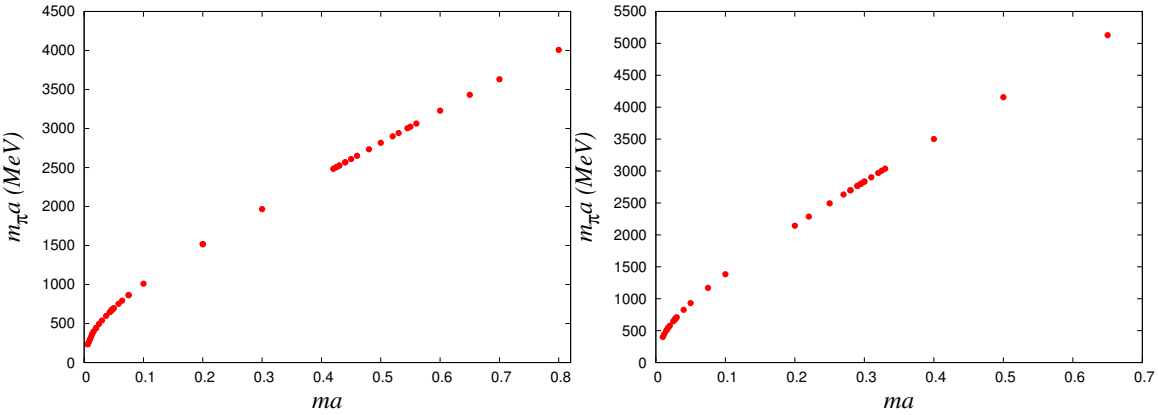

Figure 5.4: m_π versus m_q for a broad range of quark masses, where the computations were performed, for (left) coarser and (right) finer lattices. Our quark masses 'ma' are always less than 1 and $m_c a = 0.29$ and 0.425 for finer and coarser lattices respectively.

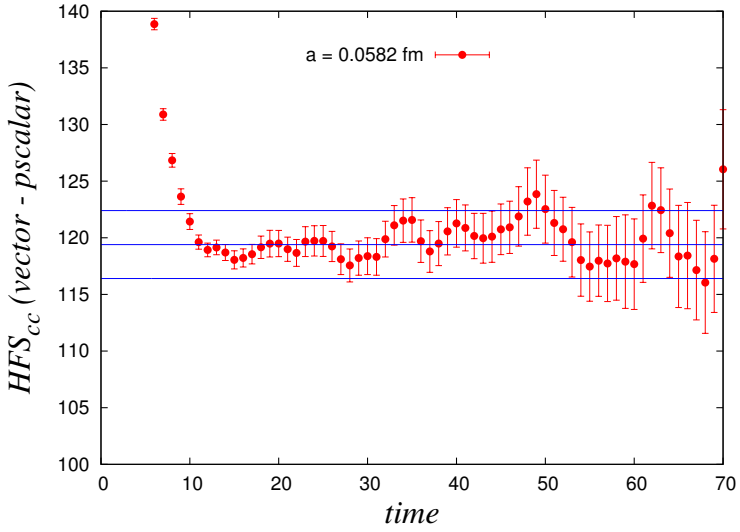

Figure 5.5: Effective hyperfine splitting in 1S charmonia for wall-point correlators for lattices with spacing 0.0582 fm. Horizontal lines show the fit results with one sigma error.

lattice results were found to be smaller than the experimental value ($\sim$ 116 MeV). This underestimation is now understood to be mainly due to the discretization error associated with the charm quark action and the quenched approximation. The effects due to the discretization errors are evident in the results from the excited state spectroscopy calculations using a tree level tadpole improved c_s value, where this hyperfine splitting is found to be $\sim$40MeV below the experimental value. In this study, we calculated this splitting. In Figure 5.5, we show the effective splittings between vector and pseudoscalar

correlators (jackknifed) at the tuned charm mass for wall-point correlators on finer lattices. horizontal lines shown are the fit results, with one sigma error bar. Our final estimate for this hyperfine splitting are 125(6) MeV and 119(3) MeV corresponding to coarser and finer lattices respectively. A com

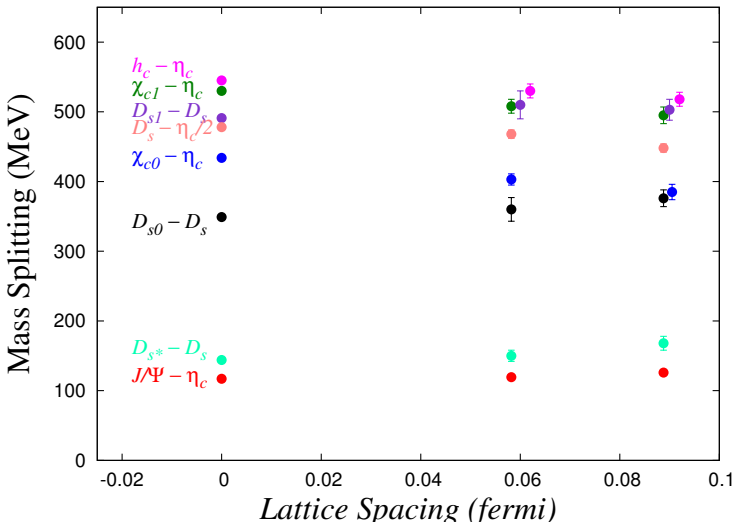

Figure 5.6: Meson mass splitting for charmonia and charmed-strange mesons at two lattice spacings. Experimental values are shown in the left side.

5.4.2 Energy splittings in charmonia and charmed-strange mesons

Beside 1S hyperfine splittings, it is also important to consider energy splittings between various other charmonia. In Figure 5.6, we plot energy splittings between axial, scalar and tensor charmonia from pseudoscalar charmonium. In addition to this, we also calculate charmed-strange mesons with various quantum numbers. Energy splittings between these mesons are plotted in Figure 5.6. It was observed that tuning of charm mass by using kinetic mass has brought these splittings more closer to experimental values than those obtained using the rest mass [127]. After adding one more lattice spacing, the continuum extrapolation will be carried out in future.

5.4.3 Charmed baryons

Our main motivation is to compare baryon masses calculated in this formalism with those obtained from the excited state spectroscopy study. Here we investigate that by studying the ground state spectra of charm baryons with one or more charm quark content, e.g.,

with quark content css, ccs, and ccc on these lattices. To project out the baryon states with 1/2 spin, we use the following standard local interpolating operators :

$$\Omega_{cc} \Rightarrow \epsilon^{abc}[c_a^T C\gamma_5 s_b]c_c \quad \text{and} \quad \Omega_c \Rightarrow \epsilon^{abc}[s_a^T C\gamma_5 c_b]s_c,$$

with $C = \gamma_4\gamma_2$ being the charge conjugation matrix. For spin 3/2 baryons, we choose the following operators :

$$\Omega_{ccc} \Rightarrow \epsilon^{abc}[c_a^T C\gamma_\mu c_b]c_c, \quad \Omega_{cc} \Rightarrow \epsilon^{abc}[c_a^T C\gamma_\mu s_b]c_c \quad \text{and} \quad \Omega_c \Rightarrow \epsilon^{abc}[s_a^T C\gamma_\mu c_b]s_c.$$

However, these operators has both spin 1/2 and 3/2 projections in them. At zero momentum the corresponding correlation functions using these operators can be written as

$$C_{ij}(t) = (\delta_{ij} - \frac{1}{3}\gamma_i\gamma_j)C_{3/2}(t) + \frac{1}{3}\gamma_i\gamma_j C_{1/2}(t),$$

where i and j are the spatial Lorentz indices and $C_{3/2}(t)$ is the correlation function for spin 3/2 state [179]. By choosing the appropriate Lorentz components, the spin 3/2 part of the correlation function, $C_{3/2}(t)$, can be extracted and used to calculate the mass of the spin 3/2 baryons.

The discretization effects will be maximum for triply charmed baryons since they have three heavy charm quarks, followed by doubly charmed baryons made with two charm quarks. Hence we first compare the results of Ω_{ccc} obtained from these two independent studies. The mass splittings $\Omega_{ccc} - \frac{3}{2}J/\Psi$ are shown in Figure 5.7. The factor 3/2 accounts for the difference in the valence charm quark content in the baryons and the mesons. The blue rectangles represent the results from this work for the two different lattice spacings, while the rectangles in red are results from the work discussed in the previous section. The two red points corresponds to the estimates from the tree-level clover coefficient $c_s = 1.35$ and at a boosted value of $c_s = 2$ (see Section 4.1.2), which gives correct charmonium hyperfine splitting, $J/\psi - \eta_c$. The consistency between the red and blue squares is evident. We also plot results from other lattice calculations (violet : Ref. [87], green : [88]). These can also be seen to be consistent with our estimates. We have omitted the estimate from Ref. [84], as the error bar was very large, though consistent with our estimates. Different variety of discretization used in above references. Our calculations were with anisotropic clover and overlap fermions, while Ref. [87] used Brillouin quraks and Ref. [88] used relativistic heavy quark action for the heavy quarks.

The agreement between our calculations and furthermore with results from other lat-

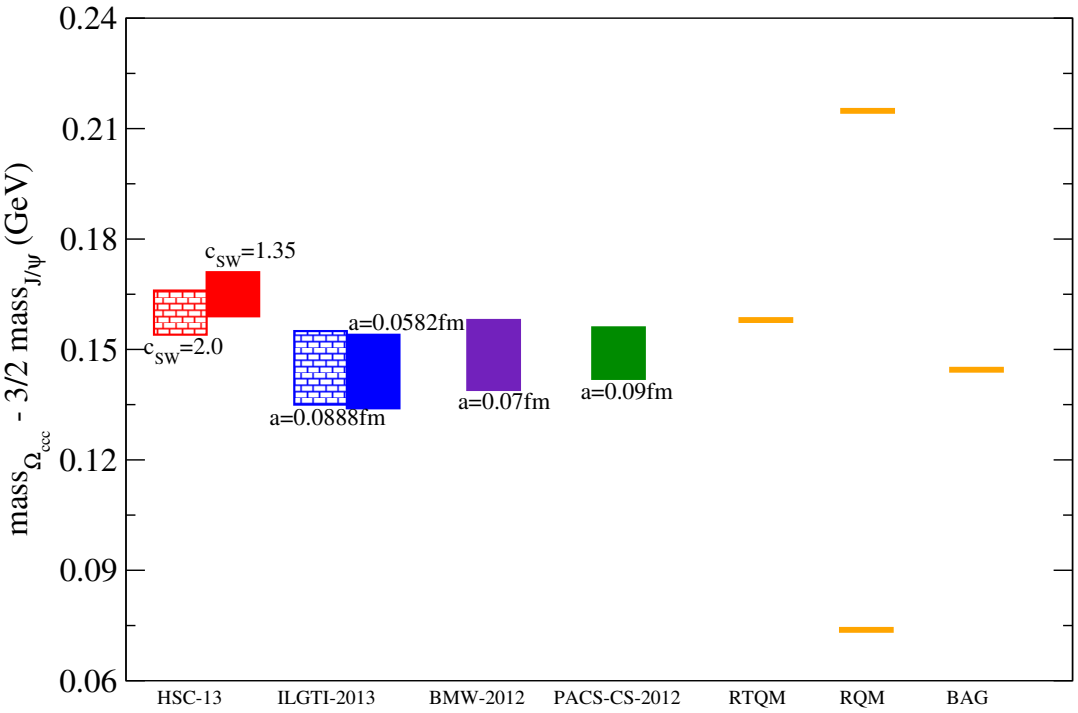

Figure 5.7: Mass splitting of the ground state of $J^P = \frac{3}{2}^+$ Ω_{ccc} from J/ψ meson. A factor 3/2 is multiplied with J/ψ mass to account for the difference in the number of charm quarks in baryons and mesons. This mass splitting mimics the binding energy of the ground state Ω_{ccc}. Results of this mass splitting from this work (blue boxes) are compared with those obtained from calculations discussed in the previous section (red box). Along with we compare estimates that are available from various lattice and quark model calculations available in the literature.

tice calculations gives us confidence in our estimates from the excited state spectroscopy calculations. While this consistency in results also make our calculations using overlap fermions itself serve an excellent formalism to study heavy quark systems. We also quote a few quark model calculations (orange) in the Figure 5.7, to show how potential models stand in predictions for the triply charm systems. As one can see that, though the relativistic calculations by Martynenko [50] and bag model calculations by P. Hasenfratz [30] lie in the range of lattice predictions, a relativistic calculation by Migura, *et al.*, accounting for the spin dependence of the confining potential in two different ways gives widely different estimates [51]. This plot can potentially provide crucial input to the future discovery of Ω_{ccc}.

Next we calculate various spin splittings for doubly charm baryons where one also expect larger discretization error. We have already shown the numbers from this calculation in Figure 4.18 and Figure 4.24 while comparing the numbers from the previous

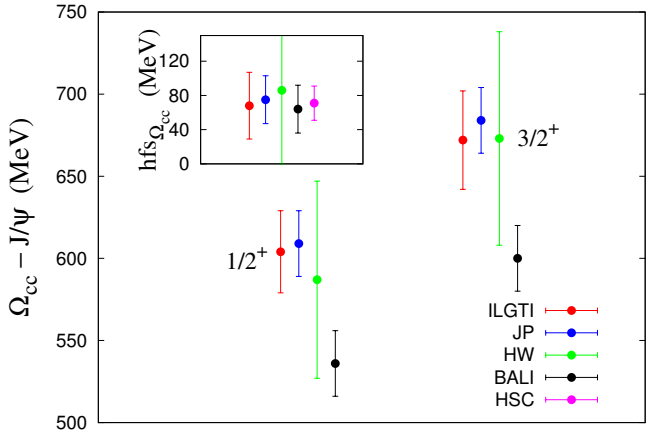

Figure 5.8: Mass splittings of $\Omega_{cc} - J/\Psi$. The inset plot shows the hyperfine splitting in this channel. Also shown are other lattice determinations.

calculations with results from various lattice calculation. For a completeness, we show the results here again. We find our results from the excited stated spectroscopy calculations and the calculations using overlap fermions are consistent with each other. We also find similar consistency of our results with estimates from other lattice calculations. In Figure 5.8, we show the results for $1/2^+$ and $3/2^+$ ground states for the Ω_{cc} baryon in terms its splitting from $m_{J/\psi}$. Along side we plot estimates from other lattice determinations. It is to be noted that these baryons are yet to be measured experimentally. The inset plot shows the corresponding hyperfine splitting. Our results for both the splittings are consistent with other lattice results [80, 84, 86, 88, 114]. This agreement further boosts the confidence in our results from our excited stated spectroscopy calculation and the applicability of overlap fermions in heavy quark systems. In Figure 5.9, we plot our estimates for the Ω_c baryons. It shows the 1/2 and 3/2 ground states for the Ω_c baryon for both the parities. We also quote the experimental numbers also in the plot, so as to have a comparison. While there are observations for the positive parity states, the negative parity states are yet to be measured experimentally. In the inset plot, we show the hyperfine splitting in this baryon, and make a comparison with other lattice estimates. Once again the consistency in our findings validates the credibility in our results.

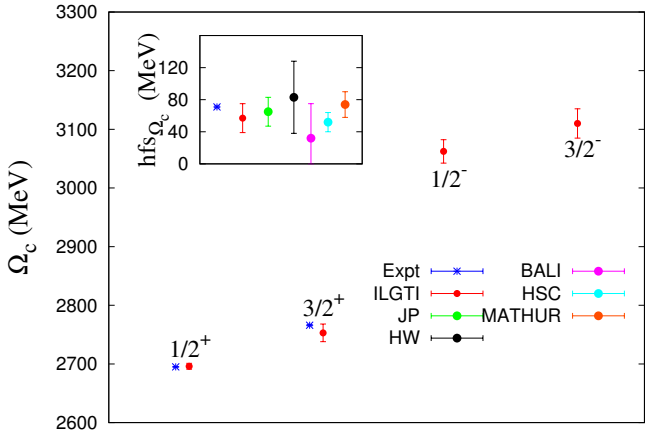

Figure 5.9: Ground states of Ω_c for even and odd parities. The inset plot shows the hyperfine splitting in this channel. Also shown are other lattice determinations, along with the experimental values, where available.

5.5 Summary, conclusions and future prospects

In this chapter, we discuss an alternative dynamical lattice QCD calculation of the low lying heavy hadron states. The main motivation is to compare the results between two independent calculations by two different type of discretization and then get an estimate of the discretization effects in energy spectra. Using a mixed action approach, we utilized the highly desirable features of small discretization errors and small taste breaking effects of the HISQ action and the small discretization effects and the low quark mass limit of the overlap fermion action. We are thus able to study a long range of pseudoscalar meson masses from $230 - 5000$ MeV. By tuning the charm quark mass using the kinetic mass, we made sure the discretization errors due to the uncertainty in the charm mass tuning is small. And at this tuned charm mass, we extracted the meson and the baryon spectra containing one or more charm quarks. We observed that results from our two independent methods are consistent with each other. Furthermore, we made a comparative study of our results with results from other lattice calculations and quark model calculations. The consistency within the lattice calculations and the agreement of those with the experimental values, wherever available, validates the credibility in both of our calculations. Thus, this calculation serves simultaneously as a complementary study to compare the results from our previous calculations and as an independent study with improved control over the systematics that gives predictions about the low lying charm hadron spectrum.

Chapter 6

Baryons at finite temperature

6.1 Introduction

In this chapter, we will describe our investigations of the nature of the strongly interacting matter at high temperatures using baryonic probes. The QCD matter undergoes a change of phase when its temperature is varied: from a chiral symmetry broken state of color singlet objects called hadrons at low temperatures to a deconfined chiraly symmetric state of the quark gluon plasma at high temperatures. It has been observed from many lattice calculations that there is no sharp phase transition but a cross-over from the hadronic to the deconfined state. One the other hand, in a pure gluonic field theory, this change of phase proceeds through a first order transition. In this work, we focused on the hadronic correlation lengths that exist in a pure $SU(3)$ gauge theory above and immediately below the deconfinement transition temperature, T_c. These correlations will help us understand the non-perturbative nature of QCD with varying temperature.

The starting point of the lattice computations of the correlation lengths in QCD medium at finite temperature, T, is the thermodynamic partition function,

$$\mathcal{Z} = Tr\{e^{-\beta_T \ H_{QCD}}\}, \tag{6.1}$$

where H_{QCD} is the QCD Hamiltonian and $\beta_T = 1/T$ ($k_B = 1$). This partition function can be expressed as a path integral of the QCD action, S_{QCD} (eq. (3.5)), over a four dimensional Euclidean space-time with a compactified temporal direction of extent $\beta_T = 1/T$,

$$Z_{\mathcal{T}} = \int D\psi D\bar{\psi} DA_\mu e^{-S_{QCD}}. \tag{6.2}$$

At finite temperature, the fermion and the gauge fields must satisfy anti-periodic and periodic boundary conditions along the temporal direction respectively due to the trace relation

$$\psi(\bar{x}, t + 1/T) = -\psi(\bar{x}, t), \qquad A^a_\mu(\bar{x}, t + 1/T) = A^a_\mu(\bar{x}, t) \tag{6.3}$$

After discretizing the space-time, the physical volume of the system is $V = N_s^3 a^3$ and $T = 1/(N_t a)$, where N_s an N_t are the number of lattice points along the spatial and the temporal directions.

We study the QCD medium at finite temperatures by looking at the static correlation functions,

$$\begin{aligned} O(z) &= \frac{1}{\mathcal{Z}} Tr(h(z)h(0)e^{-\beta_T \ H_{QCD}}) \qquad \text{and} \\ O(z) &|_{z\to\infty} = b \exp\left[-\mu(T) z\right]. \end{aligned} \tag{6.4}$$

Static correlation lengths (μ) indicates the spatial distance beyond which the effects of putting a test hadron in the medium is screened. This response depends on the quantum numbers carried by the probes; so one can classify static correlators as glueball-like, meson-like and baryon-like probes with the usual quantum numbers of these quantities corrected for the fact that the static spatial symmetries are different from the Poincare group.

Meson-like screening masses have been studied in QCD in great detail [128, 129, 130, 131, 132, 133, 134, 135]. Baryons at finite temperature has not been studied in detail in recent past and a few notable works were in the late 1980's [128, 133]. Moreover, a detailed study of the baryon screening masses in the low temperature phase also has not been performed yet. In this work, we perform simulations of pure gauge theory for three different temperatures across the transition temperature and study screening correlators for mesonic and nucleonic resonances with clover fermions. The main emphasis, in this work, has been given to the nucleon channels, which are expected to provide important inputs to the study of baryon number fluctuations and thus to the experimental search for the critical point of QCD.

The organization of this chapter is as follows. In Section 6.2 we discuss technical details related to the simulation, inversion and analysis, including the details of interpolating operators used and their asymptotic fit forms. In Section 6.3 and Section 6.4 we display the results for mesonic and baryonic channels, respectively, for temperatures above and immediately below T_c. In Section 6.5, we compare our results on screening

masses with the estimates from free theory and the other existing lattice calculations. Section 6.6 summarizes and concludes this study of hadrons at finite temperature. Appendices 6.A and 6.B discusses two technical aspects related with these calculations, which interested reader is referred to in the main section in this chapter.

6.2 Runs and measurements

T/T_c	$N_\tau \times N_s^3$	β	N_{conf}	c_{SW}	κ
0	32×16^3	6.03	71	1.7333	0.1345, 0.1347
0.95	8×32^3	6.03	94	1.7333	0.1345, 0.1347
1.5	8×32^3	6.332	67	1.5667	0.1345, 0.1350, 0.1355

Table 6.1: The simulation and measurement parameters used in this work. β is the bare coupling for the Wilson gauge action, c_{SW} is the clover coefficient (determined non-perturbatively using eq. (2.22)), and κ is the hopping parameter in the improved Wilson-Dirac operator.

The hadronic correlation functions with mesonic and baryonic quantum numbers were constructed out of clover-improved Wilson quarks [143], in zero and finite temperature ensembles generated using the Wilson gauge action. The finite temperature configurations were generated on lattices with lattice spacing $a = 1/(8T)$ with $T = 0.95T_c$ and $1.5T_c$. The spatial size of the lattice, L, was tuned such that $LT = 4$. We use the notation $L = N_s\, a$ and $V_4 = V/T$. Zero temperature measurements were carried out on $(2L) \times L^3$ lattices with coupling $\beta = 6.03$, which corresponds to the same lattice spacing as the finite temperature run below T_c [180, 181]. The box size, L, is sufficiently large (> 4 times the Compton wavelength of the lightest state on the lattice) in all our lattices, as a result of which finite volume effects are under control. A zero temperature study at $\beta = 6.332$, corresponding to the thermal ensemble above T_c was not made, but the corresponding choice of κ was made so that we could use a previous study [182]. Details of the simulation and measurement parameters are tabulated in Table 6.1. With the choices of κ listed for $\beta = 6.332$, the values of m_π/T_c are 1.52, 2.58, and 3.31 respectively.[1].

The zero momentum correlation functions for the mesonic channels are,

$$S_{_H}(t) = \sum_{\mathbf{x}} \langle H^\dagger(\mathbf{x}, t) H(\mathbf{0}, 0) \rangle, \qquad \text{where} \qquad H(\mathbf{x}, t) = \bar{\psi}(\mathbf{x}, t) \Gamma_{_H} \psi(\mathbf{x}, t), \tag{6.5}$$

[1]Discussion on a subtle aspect related to the studies has been omitted from the main text and has been discussed in detail in the Appendix 6.A

where $\psi(\mathbf{x}, t)$ is the quark field at time t and spatial point $\mathbf{x}$ (we will also use the component notation $\mathbf{x}_1 = x$, $\mathbf{x}_2 = y$ and $\mathbf{x}_3 = z$). The sum over all spatial sites of the point-to-point correlator projects on to zero spatial momentum. All Dirac, flavor, and color indices are summed. $\Gamma_{_H}$ is an appropriate Dirac, flavor matrix which gives the quantum numbers of the meson, H. In actual practice, we replaced the point source of eq. (6.5) by a wall source (see eq. (5.5)). Wall source allows the suppression of high momenta modes, especially above T_c, allowing more accurate study of the screening masses, which are related to the long distance behavior of the static correlation function in eq. (6.5). Wall source being a gauge non-invariant source, this required gauge fixing; we fixed to the Coulomb gauge.

We used $\Gamma_{_{PS}} = \gamma_5$ for the isovector pseudoscalar (PS), $\Gamma_{_S} = 1$ for the isovector scalar (S), $\Gamma_{_V} = \gamma_i$ for the vector (V) and $\Gamma_{_{AV}} = \gamma_i\gamma_5$ for the isovector axial vector (AV) channels. For the $T = 0$ measurements, we considered propagation in the time direction as shown in eq. (6.5), and since all the orthogonal directions are equivalent, we summed the V and AV propagators over the three polarizations $i = 1, 2, 3$. For the screening correlators all the polarizations of the V and AV are not equal, and we summed over only $i = 1$ and 2.

Masses and screening masses can be obtained without renormalization. They were estimated, as described in Section 3.1, by fitting to an assumed cosine-hyperbolic form, and looking for agreement with effective masses. Statistical errors on masses are obtained by a jackknife procedure. The propagation of statistical errors is done by jackknife when they could be correlated, and by adding in quadrature when they are independent.

(a) (b) (c)

Figure 6.1: Quark line diagrams which couples with scalar propagator in the full theory. In the quenched theory (c) does not contribute.

Though analysis of meson correlators is straight forward, scalar correlators in quenched calculations require special care. There have been several calculations to study the isovector scalar meson (a_0) at zero temperature with the $\bar{\psi}\psi$ interpolation field in the quenched approximation [183, 184, 185]. In all these works the scalar correlation functions were found to change the signature between the source point and $N_\tau/2$ violating spectral positivity. In this work, we make the observation of similar interesting unphysical behaviors of the scalar correlators at finite temperature (see for example Figure 6.2). An expla-

nation of this behavior based on quenched chiral perturbation theory (QχPT) has been discussed in [183, 185]. Unlike full QCD, the contributions to the scalar correlator in the quenched approximation comes only from diagrams Figure 6.1(a) and Figure 6.1(b). The diagram Figure 6.1(b) is equivalent to the propagation of $\eta - \pi$ intermediate state along significant fraction of the time in the correlation function, in contrast with the diagram Figure 6.1(a), which corresponds to the propagation of a scalar excitation. The negative value of the $\bar{\psi}\psi$ correlator appears due to the absence of the diagrams like in Figure 6.1(c), and hence does not compensate for the coupling of scalar with the $\eta - \pi$ ghost state appearing due to the presence of Figure 6.1(b). In quenched calculations the intermediate $\eta - \pi$ state is equivalent to $\pi - \pi$ state and hence we use twice the mass of the pseudoscalar excitation in our studies to estimate its binding energy.

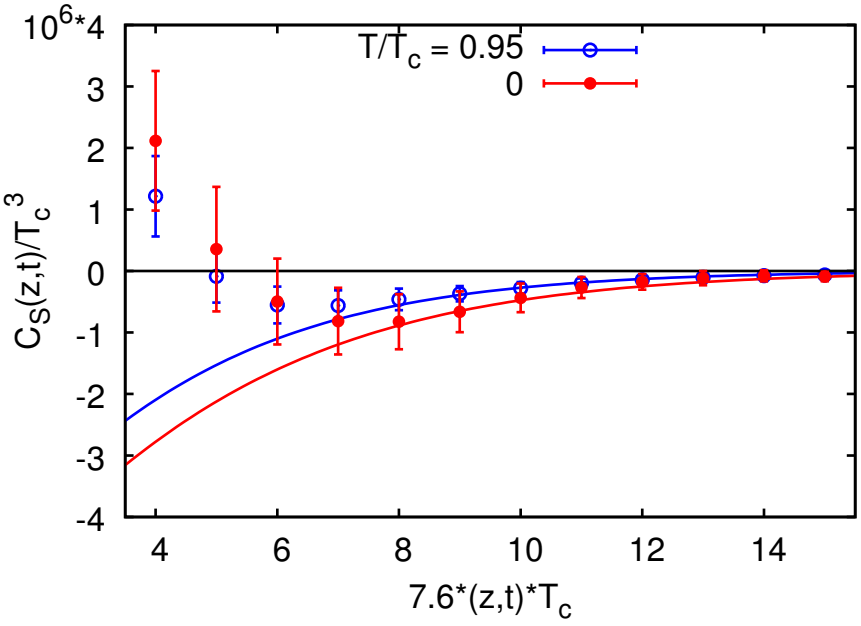

Figure 6.2: Scalar correlation functions below the deconfinement transition temperature, T_c: for temperatures $T = 0$ (red) and $T/T_c = 0.95$ (blue) and $m_\pi/T_c = 1.99$. The continuous curves are the fit estimates using the asymptotic fit forms predicted by quenched chiral perturbation theory (eq. (6.6)).

In references [183, 185], it has been argued that the large time behavior of the zero temperature scalar correlator in the quenched theory is given by

$$\begin{aligned} S^{Q\chi PT}(t) \quad &= b\left\{\exp\left[-m_s t\right] + \exp\left[-m_s(N_t - t)\right]\right\} \\ &-a_s\left\{(1 + m_\pi t)\exp(-E_{\eta'\pi} t) + (1 + m_\pi(N_t - t))\exp(-E_{\eta'\pi}(N_t - t))\right\}. \quad (6.6) \end{aligned}$$

The negative term is explicitly due to the quenched ghost. $m_{\pi/S}$ are the masses of the PS and S meson, $E_{\eta'\pi}$ is the energy of the ghost state ($E_{\eta'\pi} = 2m_\pi - E_{\rm int}$) and $-a_s$ is the coupling to the ghost. Since the ghost exactly cancels a physical term, these two parameters are physical. For sufficiently small m_π the second term dominates at intermediate distances, leading to negative values for the correlator. Though the asymptotic form in eq. (6.6) has been derived for zero temperature, in our calculations we have used the same form at finite temperature to study the thermal effects for the scalar meson. The continuous lines in Figure 6.2 are the best fit curves describing the unphysical coupling, obtained by fitting the tail of the correlation functions with the coupling term as in eq. (6.6). This negative dip becomes prominent as one decreases the quark mass.

The $\mathrm{SU}_L(2) \times \mathrm{SU}_R(2)$ chiral symmetry of the QCD vacuum is restored above T_c. The anomalous $\mathrm{U}_A(1)$ remains broken asymptotically, although its effects are seen to be small at temperatures of $1.5T_c$. The most straightforward consequence of this is that the S/PS and the V/AV correlators should become pairwise degenerate in the high temperature phase. The observation of some breaking of this symmetry has been an issue of some interest recently [134]. Here we introduce a new measure for this symmetry—

$$R_{_H} = \frac{1}{N_t - 1} \sum_{t=1}^{N_t - 1} \frac{\langle S_{_{H_+}}(t) - S_{_{H_-}}(t) \rangle}{\langle S_{_{H_+}}(t) + S_{_{H_-}}(t) \rangle}, \tag{6.7}$$

where $S_{_{H_\pm}}(t)$ are parity partner correlators (for the screening correlators t is replaced by z and N_t by N_s), and the angular brackets are averages over the gauge ensemble. The correlators at $t = 0$ are left out of the sum to avoid problems with time doublers. We will use the convention of taking the positive parity partner for the label H. When chiral symmetry is broken we expect $R_{_H} \simeq \mathcal{O}(1)$.

One subtlety in computing $R_{_H}$ is that the lattice mesonic currents need to be renormalized to connect them with the continuum currents, before $S_{_H}$ could be used to compute $R_{_H}$. For quarks of mass m_q, the lattice operators, $H(\mathbf{x}, t)$, are multiplicatively renormalized to

$$Z_{_H}(g^2)\Big(1 + b_{_H}(g^2) a m_q\Big) H(\mathbf{x}, t), \tag{6.8}$$

where a is the lattice spacing, $g^2 = 6/\beta$, and $am_q = (\kappa - \kappa_c)/2$. We use the results in the $\overline{MS}$ scheme where the renormalization constants are determined at the scale of $1/a$. For non-perturbatively improved clover fermions, the factors $Z_{_{V,AV}}$ and $b_{_V}$ have been calculated non-perturbatively [186], where the following interpolating formulae are

found:

$$Z_V = \frac{1 - 0.7663g^2 + 0.0488g^4}{1 - 0.6369g^2}, \qquad Z_{AV} = \frac{1 - 0.8496g^2 + 0.0610g^4}{1 - 0.7332g^2},$$
$$b_V = \frac{1 - 0.6518g^2 + 0.1226g^4}{1 - 0.8467g^2}. \tag{6.9}$$

For the other coefficients, we use the expression from the one-loop, tadpole improved perturbation theory [187]:

$$Z_{PS,S} = u_0\Big(1 - z_{PS,S}\tilde{g}^2\Big), \tag{6.10}$$

where u_0 is the tadpole factor, $\langle P\rangle = u_0^4$, $\tilde{g}^2 = g^2/u_0^4$, and the one-loop coefficients $z_{PS,S}$ as obtained from [188] are $z_{PS} = 0.107 - 0.019\tilde{c}_{SW} + 0.017\tilde{c}_{SW}^2$ and $z_S = 0.026 + 0.065\tilde{c}_{SW} - 0.012\tilde{c}_{SW}^2$ where $\tilde{c}_{SW} = u_0^3 c_{SW}$. The one-loop order tadpole-improved forms of b_H can be written as

$$b_H = \frac{1}{u_0}\Big(1 + b_H^1\tilde{g}^2\Big). \tag{6.11}$$

where one obtains from the calculations of [189] the values $b_{PS}^1 = 0.109$, $b_S^1 = 0.070$, and $b_{AV}^1 = 0.069$, computed for the tree-level $\tilde{c}_{SW} = 1$.

For the nucleon operator we used

$$N_\alpha(\mathbf{x}, t) = \varepsilon_{abc}(C\gamma_5)_{\beta\delta}\psi_\alpha^a(\mathbf{x}, t)\psi_\beta^b(\mathbf{x}, t)\psi_\delta^c(\mathbf{x}, t), \tag{6.12}$$

where α, β, and γ are Dirac indices, a, b, and c are color indices, ε is the Levi-Civita symbol, and C is the charge conjugation operator. The projection of the correlation function on to vanishing spatial momentum is performed by the usual means of summing over $\mathbf{x}$ at $T = 0$ where we imposed periodic boundary conditions in all directions. However, at finite temperature, anti-periodic boundary conditions must be imposed on quark fields in the Euclidean time direction. As a result, the screening correlator must be projected to the lowest Matsubara frequency [128]. The parity projection operators for the correlator whose propagation is measured in the direction μ is

$$\mathcal{P}_\pm^\mu = \frac{1}{2}(1 \pm \gamma^\mu). \tag{6.13}$$

The zero momentum correlators of the two parities of the nucleon can be fitted to the

behavior expected of a Wilson fermion—

$$\begin{aligned} S_{N_+}(t) &= c_+ \exp\left[-\bar{\mu}_{N_+} t\right] + c_- \exp\left[-\bar{\mu}_{N_-}(N_t - t)\right] \\ S_{N_-}(t) &= c_- \exp\left[-\bar{\mu}_{N_-} t\right] + c_+ \exp\left[-\bar{\mu}_{N_+}(N_t - t)\right]. \end{aligned} \tag{6.14}$$

Because of the admixture from opposite parity states, these correlators change sign across the middle of the lattice. It is to be noted that this structure is also expected for the excited baryon spectrum for both the parities. It is because our construction and the analysis were always concentrated on the temporal ranges close to the source point in the forward temporal direction, we did not encounter this behaviour in Chapter 4. In this work, we study this structural behaviour in the nucleon correlations to study the chiral symmetry across T_c. For this, we used the absolute value of the correlators above. We note that R_N does not require knowledge of Z_N, because the parity partners are generated by the same lattice operator. For the $T = 0$ measurement, where $\bar{\mu}_{N^\pm} = m_{N^\pm}$. For the finite temperature measurement where we replace t by z, we have

$$\mu^2_{N^\pm} = \bar{\mu}^2_{N^\pm} - \sin^2(\pi/N_t), \tag{6.15}$$

where we have subtracted the contribution coming from the anti-periodic boundary along the temporal direction [128].

6.3 The meson sector

κ	m_π/T_c	m_V/T_c	m_{AV}/T_c
0.1345	2.20 ± 0.03	3.55 ± 0.06	5.6 ± 0.4
0.1347	1.99 ± 0.03	3.53 ± 0.08	5.5 ± 0.5

Table 6.2: Meson masses in units of T_c at $T = 0$ and $\beta = 6.03$.

The analysis of meson masses at $T = 0$ follows the procedure described in Section 3.1. The results are collected in Table 6.2. We choose to express all results in units of T_c for two reasons. First, because quenched QCD is not open to experimental tests and hence quoting numbers in MeV units is based on assumptions which cannot be tested. We prefer to quote ratios of quantities, which are computable in practice. Second, because in quenched QCD the critical coupling is known with high precision, and $N_t = 8$ is within

the scaling region [190], the statistical and systematic errors involved in using this as a scale are completely under control.

m_π/T_c	H	μ_H/T_c	μ_H/m_H
2.20	PS	2.18 ± 0.02	0.99 ± 0.02
	V	3.45 ± 0.06	0.97 ± 0.02
	AV	5.18 ± 0.09	0.93 ± 0.06
1.99	PS	1.97 ± 0.02	0.99 ± 0.02
	V	3.31 ± 0.07	0.94 ± 0.03
	AV	5.1 ± 0.1	0.92 ± 0.08

Table 6.3: Meson screening masses, μ_H at $T = 0.95T_c$ in units of T_c and the corresponding $T = 0$ meson mass, m_H.

The analysis of most mesonic correlators below T_c is equally straightforward. The only subtlety has been mentioned earlier: since the zero momentum screening correlator is measured for separations along the z-direction, the three polarizations states of the V and AV are two spatial and one temporal. The temporal polarizations have behavior distinct from the spatial polarizations [191]. We measure the screening masses of the spatial polarizations only. Our main results for the screening masses below T_c are summarized in Table 6.3. Our results shown in Table 6.3 indicates that the pole mass of the mesons is hardly affected by temperature.

	$T = 0$		$T = 0.95T_c$	
m_π/T_c	$E_{\rm int}/m_\pi$	χ^2/dof	$E_{\rm int}/m_\pi$	χ^2/dof
2.20	0.6 ± 0.2	1.92	-0.1 ± 0.8	0.25
1.99	0.5 ± 0.2	1.28	0.1 ± 0.7	0.57

Table 6.4: $E_{\rm int}$ in units of m_π obtained by fitting the scalar correlator with the fit form in eq. (6.6).

We treat the scalar correlator separately because of its distinctive behavior in correlation functions compared to those for other mesons as shown in Figure 6.2. Table 6.4 contains the measure of the binding energy (E_{int}), in units of m_π, extracted by fitting the scalar correlation functions with the functional form in eq. (6.6) at both $T = 0$ and for $T < T_c$. $E_{\rm int}$ at $T = 0$ is non-zero at the 95% significance level for both values of m_π which we used. While the finite temperature measurements are statistically indistinguishable from these, they are consistent with zero within errors, due to the larger

fit errors at $T > 0$. It is interesting to note that the central values of $E_{\rm int}$ at $T > 0$ lie outside the 2σ errors of the $T = 0$ measurement.

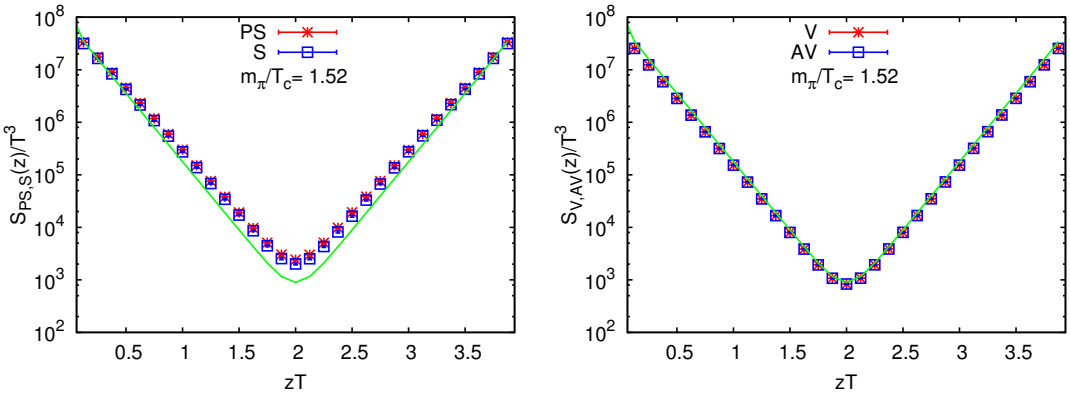

(a) (b)

Figure 6.3: A signal of restored chiral symmetry above T_c is that (a) the PS and S correlators and (b) the V and AV correlators become degenerate. The continuous curves are correlation functions in a FFT; in order to remove trivial artifacts, these have been computed on a lattice of the same size.

As described in the previous section, chiral symmetry restoration in the high temperature phase of QCD is signaled by pairwise equality of correlators which are related to each other by parity. This is the case shown in Figure 6.3[2]. The figure also shows that the correlation functions are not too far from those expected in a theory of non-interacting quarks (also called the free field theory, FFT).

At $T = 0$ in the V/AV sector we found $R_V = 0.73 \pm 0.02$; at $T = 0.95T_c$ this drops marginally to $R_V = 0.59 \pm 0.02$ for both the bare quark masses we have used. This indicates that chiral symmetry remains strongly broken up to $0.95T_c$. A simple model of V/AV mixing below T_c was presented in [192] using a mixing parameter ϵ, which can be adapted to our use by writing schematically

$$S_V(T) = (1-\epsilon)S_V(0) + \epsilon S_{AV}(0), \qquad \text{and} \qquad S_{AV}(T) = (1-\epsilon)S_{AV}(0) + \epsilon S_V(0). \quad (6.16)$$

This gives $R_V(T) = (1-2\epsilon)R_V(0)$. Using the values quoted above, we find $\epsilon = 0.10 \pm 0.02$. In the unquenched theory one may expect much larger values of this parameter below T_c [192]. We observed that at $T = 1.5T_c$ the value of R_V drops as a power of the quark mass, vanishing as m_π vanishes (see Figure 6.4). However, there is no dependence of R_S

[2]The quantity in the x-axis is a dimensionless measure of the lattice extension in units of the temperature, T. It is thus labeled, and runs from $0 \to 4$, because for the finite temperature lattices $LT = 4$.

on the quark mass.

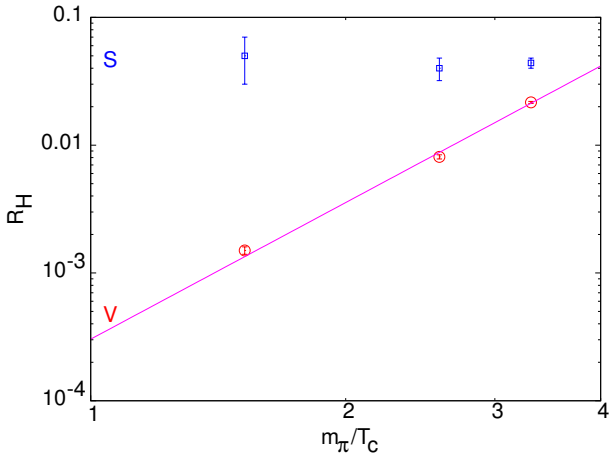

Figure 6.4: Above T_c, R_S is found to be almost independent of m_π/T_c. However, R_V goes to zero as a power of m_π/T_c, showing that correlation functions of the parity partners V and AV do become exactly degenerate in the limit.

We have extracted screening masses, μ_H from the correlation functions. We found that effective masses showed a good plateau which agreed with fits, unlike previous experience with Wilson quarks at $T > T_c$ [130]. The main reason for this is the use of wall source and the details are explored in Appendix 6.B instead of a point source, where some effective mass plateaus are also displayed. Our results for the screening masses are collected in Table 6.5. The pairwise degeneracy of the masses is quite evident. It is also evident that the screening masses are close to that expected in a theory of free quarks. The screening masses in the S/PS channel are 7–9% smaller than that in the free theory, whereas in the V/AV channel they are within 2–3% of the free theory.

m_π/T_c	μ_{PS}/T	μ_S/T	μ_V/T	μ_{AV}/T	μ_{N_+}/T	μ_{N_-}/T
1.52	5.54 ± 0.02	5.59 ± 0.04	5.88 ± 0.02	5.89 ± 0.02	8.72 ± 0.10	8.68 ± 0.10
2.58	5.56 ± 0.02	5.59 ± 0.02	5.90 ± 0.02	5.91 ± 0.02	8.75 ± 0.10	8.73 ± 0.10
3.31	5.61 ± 0.02	5.65 ± 0.02	5.95 ± 0.02	5.96 ± 0.02	8.82 ± 0.08	8.77 ± 0.09

Table 6.5: Hadron screening masses at $T = 1.5T_c$ for three different masses of quarks. In FFT all the mesonic (baryonic) screening masses are expected to be 5.99 (8.44), 5.995 (8.456) and 6.01 (8.48) on our lattices, when the bare quark mass is tuned to give $m_\pi/T_c = 1.52$, 2.58 and 3.31 respectively.

6.4 The baryon sector

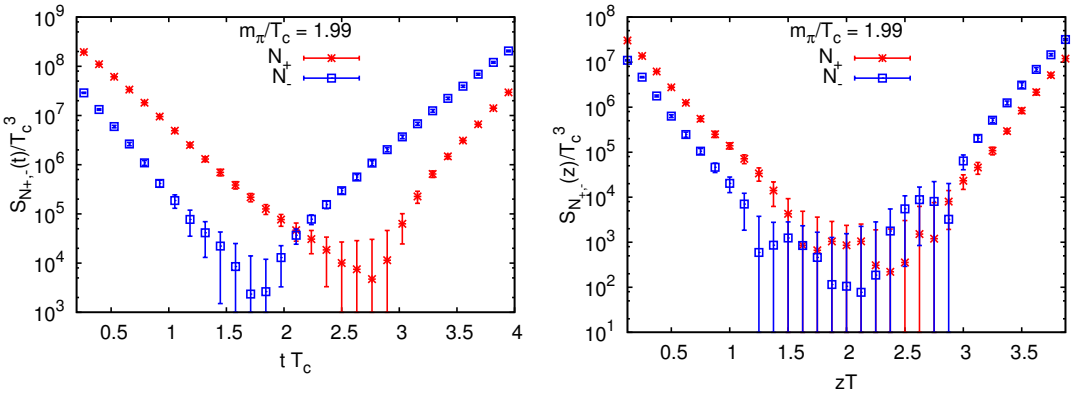

(a) (b)

Figure 6.5: Nucleon correlators at (a) $T = 0$ and (b) $T = 0.95T_c$. Both sets are asymmetric, showing that the nucleon, N_+ and its parity partner, N_-, are not degenerate.

Analysis of baryon correlators requires more care than meson correlators. This is because states of opposite parity contribute to each parity projected correlator, as explained in eq. (6.14) and shown in Figure 6.5. This contribution from the parity partners that are non-degenerate due to chiral symmetry breaking causes the asymmetric behavior in the nucleon correlation function, as is evident from Figure 6.5(a). As a result, both the fitting procedure and the extraction of effective masses is more complex than the analysis for mesons. In addition, the projection of the screening correlator on to zero momentum requires a twist to compensate for the thermal boundary condition [128]. The subsequent extraction of a screening mass from the nucleon correlator also requires the subtraction of (see eq. (6.15)) resulting in additional loss of precision.

In Figure 6.5, it would appear that the finite temperature correlators are more nearly symmetric than those at $T = 0$. Whether or not there is an early onset of chiral symmetry restoration can be probed by constructing the measure R_N, defined by eq. (6.7). At $T = 0$ we find $R_N = 0.88$ when $m_\pi/T_c = 2.20$ and 0.89 at the lower quark mass. At finite temperature these change to $R_N = 0.8$ and 0.83 respectively. Contrary to the visual impression created by Figure 6.5, once the covariances between the $N_\pm$ correlators are accounted for, the correlation functions themselves do not show any tendency towards early restoration of chiral symmetry. In fact if we adapt the model of eq. (6.16) to this case, we find a mixing parameter $\epsilon = 0.04$ in the nucleon sector, which is even smaller than that found for the V/AV at the same temperature.

m_π/T_c	m_{N_+}/T_c	μ_{N_+}/T_c	m_{N_-}/T_c	μ_{N_-}/T_c
2.20	5.10 ± 0.10	5.3 ± 0.2	6.8 ± 0.4	6.6 ± 0.4
1.99	4.9 ± 0.1	5.28 ± 0.14	6.7 ± 0.5	6.4 ± 0.7

Table 6.6: Nucleon masses at $T = 0$ and screening masses at $T = 0.95T_c$.

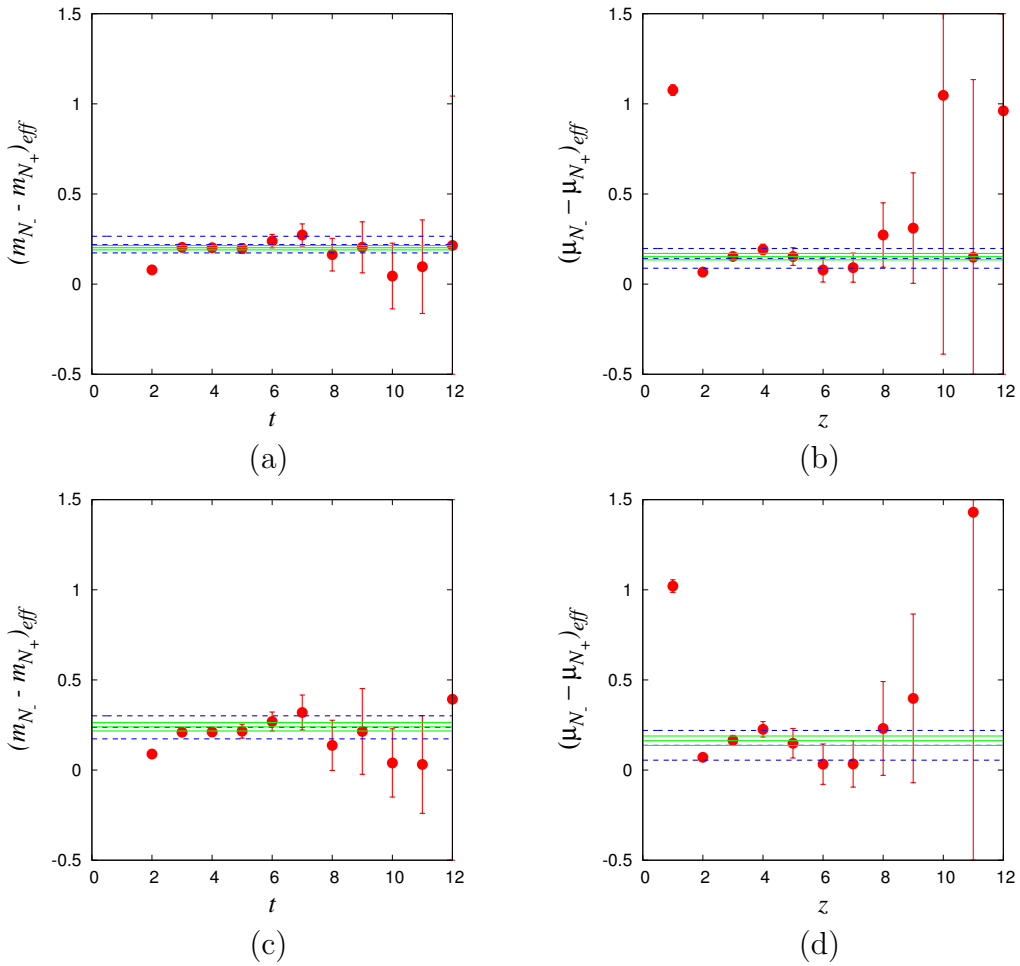

Figure 6.6: The analysis of mass splittings between N_+ and N_- for $m_\pi/T = 2.20$ at (a) $T = 0$ and (b) $T = 0.95T_c$ and for $m_\pi/T = 1.99$ at (c) $T = 0$ and (d) $T = 0.95T_c$. The data points are effective masses, the band between the dashed lines is obtained by taking the difference of screening masses. The band between the full lines is obtained by direct fits to the splitting between the two masses, and gives the results shown in eq. (6.17).

The results of fitting the masses is shown in Table 6.6. Here we indeed find some precursor effects of chiral symmetry restoration in the form of a thermal shift in the mass splitting between the baryon and its parity partner. We measured the splitting by the

ratio of the correlators, S_{N_+}/S_{N_-}, and extract the mass difference, Δm, by fitting to an exponential form $\exp(-\Delta m t)$. Since this method takes care of covariances between the correlators S_{N_+} and S_{N_-}, we expect to control statistical errors better. The fit can be cross checked against the equivalent of effective masses for the ratio. Such checks are exhibited in Figure 6.6. The resulting values are

$$\begin{aligned} \frac{m_{N_-} - m_{N_+}}{T_c} &= \begin{cases} 1.53 \pm 0.09 & (m_\pi/T_c = 2.20) \\ 1.82 \pm 0.17 & (m_\pi/T_c = 1.99) \end{cases} \\ \text{and} & \\ \frac{\mu_{N_-} - \mu_{N_+}}{T_c} &= \begin{cases} 1.15 \pm 0.14 & (m_\pi/T_c = 2.20) \\ 1.24 \pm 0.20 & (m_\pi/T_c = 1.99) \end{cases} . \end{aligned} \tag{6.17}$$

$\frac{m_\pi}{T_c}$	$\frac{\mu_V}{m_V}$	$\frac{\mu_{N_+}}{m_{N_+}}$	$\frac{\mu_{AV}-\mu_V}{m_{AV}-m_V}$	$\frac{\mu_{N_-}-\mu_{N_+}}{m_{N_-}-m_{N_+}}$
2.20	0.97 ± 0.02	1.05 ± 0.05	0.86 ± 0.16	0.75 ± 0.10
1.99	0.94 ± 0.03	1.07 ± 0.04	0.89 ± 0.22	0.68 ± 0.12

Table 6.7: Thermal shifts in masses and mass splittings at $T = 0.95T_c$; μ_H denotes the screening length in the hadronic channel H, and m_H the mass at $T = 0$. The ratio of mass splittings suggest that, unlike in the case of vector-like mesons, nucleonic correlations show some precursor effects to chiral symmetry restoration immediately below T_c.

In Table 6.7, we show the thermal shifts in the masses and the mass splittings in nucleonic and vector-like parity partners, in terms of the ratio of masses and the ratio of mass splittings between non-zero temperature and zero temperature. We find that $\mu_H = m_H$ within 95% confidence limits, indicating no significant thermal effects in the vector meson, V and nucleon, N_+. Nor do we observe a thermal shift in the mass splittings between the V and the AV (axial vector) mesons. However, we find that in the nucleon sector the mass of the opposite parity nucleon moves closer to the ground state immediately below T_c. This is the most definite evidence to date about precursor effects to chiral symmetry restoration immediately below T_c. The thermal effects in the parity partner nucleon is, hence, significant and these observations not only constrain models of quantum hadrodynamics [192], but could also have implications for the analysis of heavy-ion collision data.

Above T_c the correlators for $N_\pm$ become symmetric and degenerate (see Figure 6.7). We find $R_N = 0.230 \pm 0.005$ when $m_\pi/T_c = 3.31$, $R_N = 0.146 \pm 0.006$ for $m_\pi/T_c = 2.58$

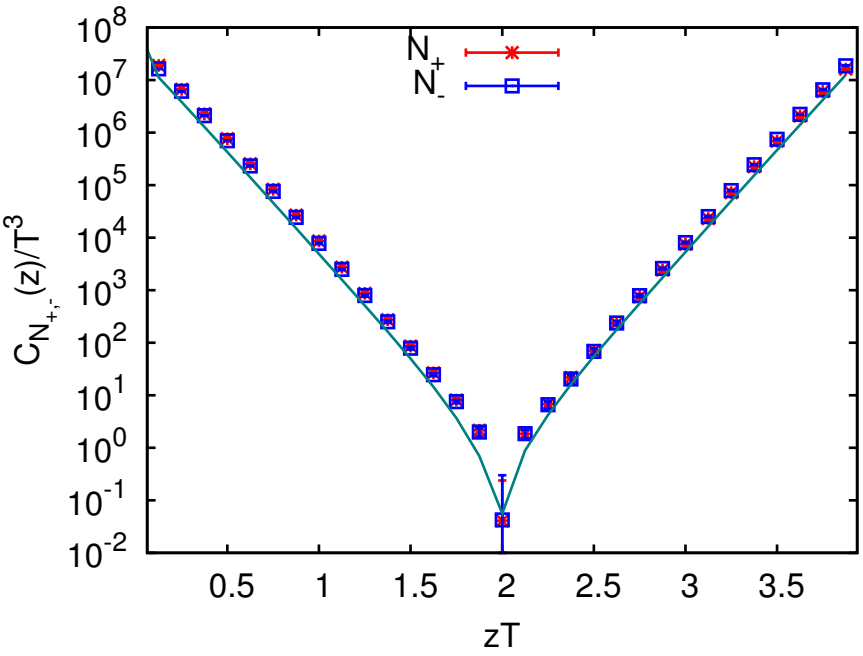

Figure 6.7: Nucleon and its parity partner correlators at 1.5 T_c. The degeneracy in the correlators signal the restored chiral symmetry at this temperature. The continuous curves are correlation functions in a FFT; in order to remove trivial artifacts, these have been computed on a lattice of the same size.

and $R_N = 0.076 \pm 0.009$ for $m_\pi/T_c = 1.52$. These lead to a vanishing of R_N as a power of m_π/T_c. Chiral symmetry restoration is also seen in the fitted screening masses, displayed in Table 6.5. As in the meson sector, the screening masses are within 3–4% of those expected in a theory of free quarks.

6.5 Hadrons above T_c and free field theory

Above T_c, at the temperature $T = 1.5T_c$, we found strong signals of approximate chiral symmetry restoration in the near degeneracy of screening masses of all the hadronic parity partners, evident in Table 6.5. We also observed the correlation functions and screening masses are not far from those obtained in FFT, which is a model of non-interacting quarks. For mesonic channels, this observation has been already made in Refs. [129, 132, 130, 131, 134]. To make a quantitative statement on these observation, in the Figure 6.8, we show the ratio of screening masses for mesonic and nucleonic quantum channels at $T = 1.5T_c$ in the interacting theory to the free theory. Alongside we also show the estimates from other lattice calculations. We see that the PS and S screening

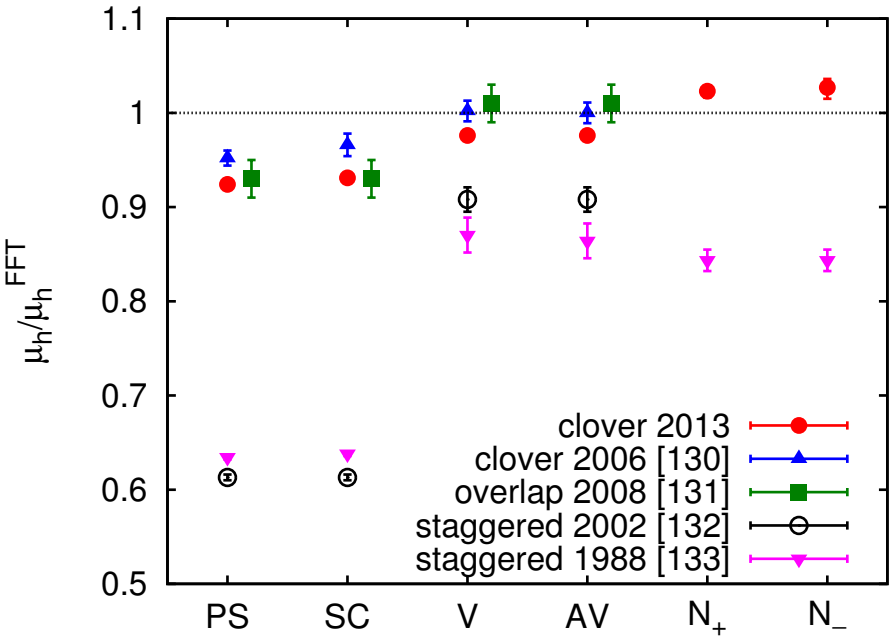

Figure 6.8: The ratio of screening masses measured at $T = 1.5T_c$ in quenched QCD with those in FFT. Along side we add the estimates for these ratios from earlier computations with clover [130], overlap [131] and staggered fermions[132, 133]. Unity on the y-axis indicates that the hadron propagates as freely propagating quarks in the absence of gluonic fields.

masses are only ∼8% away from the free theory estimates, while the V, AV and nucleonic channels already are consistent with a model of non-interacting quarks. We also observe that our estimates agree with previous work using clover quarks [130]. It also agrees with results of studies using overlap quarks at smaller lattice spacing [131]. However, it seems that studies with naïve staggered quarks always indicate stronger deviations from FFT than any of these above studies, indicating strong staggered artifacts in the estimates. Later studies using dynamical staggered fermions, with appropriate smearing to account for the staggered cut off artifacts, related to the taste-splitting, have shown that this is indeed the case and the estimates from this study were found to be much closer to the FFT [193].

6.6 Summary, conclusions and future prospects

In this work, we studied the hadronic screening correlators above and immediately below the deconfinement transition temperature, T_c, using non-perturbative lattice method in

the quenched approximation with lattice spacing $1/8T$ employing the clover improved Wilson quarks. We perform simulations at temperatures $T/T_c = 0, 0.95$ and 1.5. As seen in the other lattice calculations, we observed no statistically significant thermal effects in the mesonic correlations immediately below T_c. We also make the observation of the unphysical quenching artifacts in the scalar screening correlators immediately below T_c and make a first attempt to understand the thermal effects on the ghost coupling in these correlators. We found no statistically significant deviations with the available statistics in these studies also. Above T_c, clear evidence of the chiral symmetry restoration in terms of the pairwise degeneracy in the parity partner correlators and the weakly interacting nature of quarks was observed in the mesonic channels.

Above T_c, baryonic correlations also show clear evidence of the chiral symmetry restoration in terms of the pairwise degeneracy in the parity partner correlators and propagate as three weakly interacting quarks. Below T_c, we find interesting behavior in the nucleonic correlations, indicating precursor effects for the chiral symmetry restoration in the nucleonic channels immediately below T_c. While no such effects have been seen earlier either in the glue sector or with quarks, these observations are expected to have implications for the analysis of the heavy ion collision data. These implications clearly call for follow-up studies of nucleon below T_c.

Appendix

6.A Exceptional configurations

In our calculations we observe certain configurations with widely different behavior in the pseudoscalar correlator in comparison with the pseudoscalar correlators from the other majority of configurations. The pseudoscalar correlators in these configurations were found to be very much asymmetric about the center of the lattice with respect to the source and oscillating with unexpected features, which is different from the expected cosine hyperbolic behavior. A typical example of pseudoscalar correlator of a few of such configurations observed in this work is shown in Figure 6.9.

Configurations with such unexpected behavior have been observed in quenched calculations by various collaborations [130, 194, 195, 196, 197, 198] using the same fermion discretization as in this work. Pseudoscalar charge [196] in these configurations were found to show singular behavior below the critical hopping parameter value (κ_c) indicat-

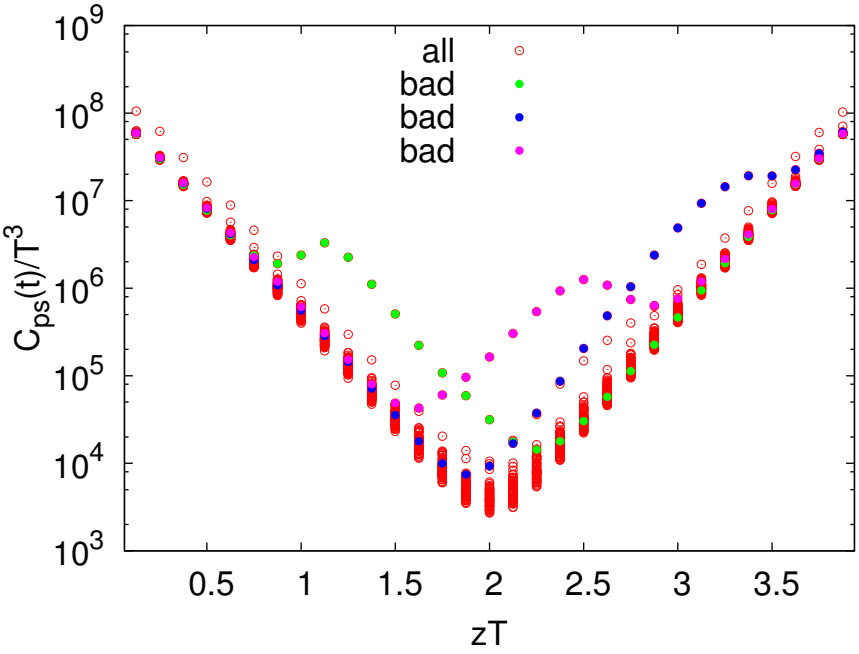

Figure 6.9: A typical case of appearance of exceptional configurations in pseudoscalar correlators. The filled circles are identified as correlators in exceptional configurations based on our analysis. These correlators are at $T = 1.5T_c$ at $m_{ps} = 250\ MeV$.

ing a shift in κ_c value corresponding to these configurations [195, 196]. In literature these configurations are called as exceptional configurations. An explanation for appearance of such configurations is as follows. The real part of all the eigenvalues of a discretized fermion operator (eg. clover improved Wilson fermions) with explicit chiral symmetry breaking term is not bound to have same signature. It can happen that a subset in the sampled set of configurations possess an eigenvalue near to $-m$ and hence $D + m$ is not invertible. In the dynamical simulations, these configurations will not be contributing as the fermion determinant will be zero. But in quenched calculations the non-zero measure of configurations having such unphysical zero modes causes unexpected behavior in the correlation functions and limits the quark mass to values much heavier than the physical quark mass, that can be studied using such operators[194].

There were attempts to ameliorate this problem in different ways in literature. ALPHA collaboration [199] used a twisted mass term in the lattice fermion operator to remove the singularities in the quark propagator due to the exceptional configurations. It was, however, shown that the twisted mass term doesn't solve the problem of exceptional configurations in the deconfined phase [200]. In the light hadron spectroscopic studies, [195] used fat-link improved clover fermions successfully to improve the chiral

properties of the operator and to suppress the unphysical configurations. However it was observed that the attractive short distance piece of the potential gets modified by the fattening. This results in serious systematic errors in the decay constant and quarkonium spectroscopic studies [201, 202]. Since one of the main objects of our study is the coupling of the scalar with the $\eta' - \pi$ ghost state in the finite temperature scalar screening correlators, we haven't used this technique to get rid of these unphysical configurations. Ref. [196] employs a modified quenched approximation in their work, in which they push the shifted κ_c in such configurations back to the average value of κ_c, which are determined from the chiral limit of the pseudoscalar masses in the well-behaved configurations. The method lacks a systematic way of labeling a configuration as exceptional, because even two 'well-behaved' configurations needn't have same κ_c always. Moreover, the overhead calculations needed to determine the zero mode in such configurations is also significantly large. Ref. [130] reported the observation of configurations with such unexpected behavior and to get rid of these issues, they handpicked and discarded such configurations during the analysis. In the present work, we follow a similar approach, but a systematic procedure developed based on phenomenology of such unphysical configurations. In comparison with most of the other techniques, our analysis requires very little overhead computation. Also this method could be supplemented in either of the methods in [196] or [130] to classify such configurations. Here we discuss the naive phenomenological approach we have employed to exclude the configurations with such unexpected behavior.

We used the pseudoscalar correlators to define two measures, the measure of symmetry(S) and the measure of oscillation(O). We defined cuts in these measures such that varying the measures slightly around the cut will not cause significant changes in the estimates. Those configurations which lie outside the defined cuts were excluded from the analysis. Below we discuss the details of the measures we defined and the details of the analysis done.

- **Measure of symmetry ($S^{(i)}$)**
  We expect the pseudoscalar correlator to be well-behaved and symmetric about the center in a periodic lattice. S, a measure of the symmetry in the pseudoscalar correlator, is defined as in eq. (6.18). The superscripts (i) are the configurations labels.

$$S^{(i)} = \sum_{t=2}^{N_\tau/2+1} {\alpha_t^{(i)}}^2 \tag{6.18}$$

$$\text{where} \quad \alpha_t^{(i)} = \frac{C^{(i)}(t) - C^{(i)}(N_\tau + 2 - t)}{\mathcal{C}(t)}$$

$$\text{and} \quad \mathcal{C}(t) = \frac{1}{2N}\sum_{i=1}^{N}(C^{(i)}(t) + C^{(i)}(N_\tau + 2 - t))$$

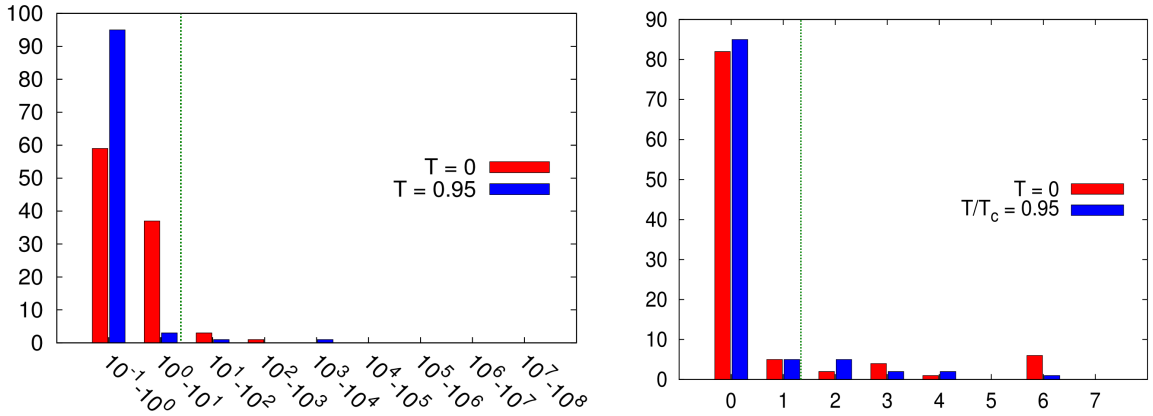

(a) (b)

Figure 6.10: Histograms of the quantity (a) S and (b) O. All the configurations on left hand side of the blue dotted line are considered as well-behaved configurations.

- **Measure of oscillation ($O^{(i)}$)**

  The pseudoscalar being the lightest, oscillations in the correlator is very unlikely and can occur only to the level of statistical fluctuations. We introduce a quantity, $O^{(i)}$, which is a measure of the oscillations observed in a correlator. It is defined as follows. Those configurations with the minima of the correlator lying outside the range $> \pm 3$ time slices from the center of the lattice with respect to the source point, are considered ill-behaved. Such configurations are removed before estimating the measure $O^{(i)}$. In each of the remaining configurations we count the no. of points $a(b)$ where the slope is positive(negative) in the first(second) half of the correlator excluding the middle band defined earlier. Then, $O^{(i)}$ is defined to be $a + b$.

The histograms of the measures for the lightest pseudoscalar mass at zero temperature and $T = 0.95T_c$ are shown in Figure 6.10. The blue dotted line is the cut used in the

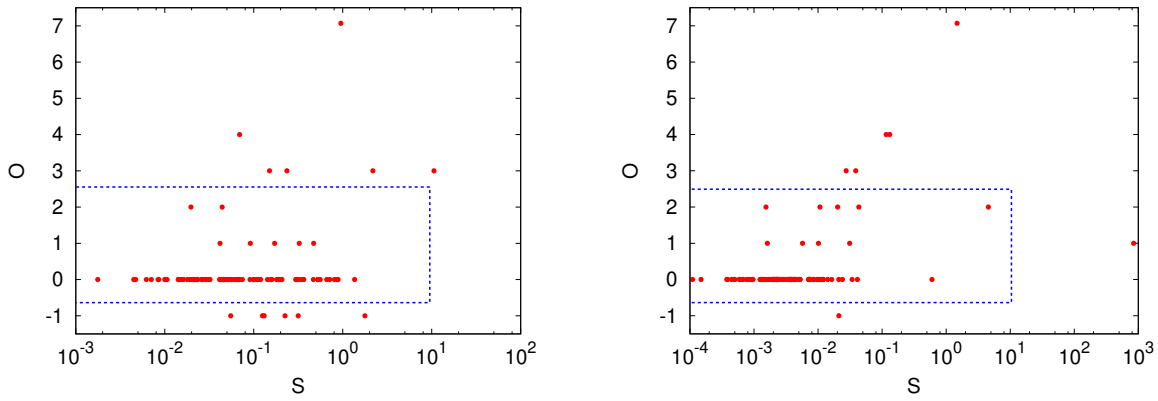

(a) (b)

Figure 6.11: Scatter plots of S and O. (a) at $T = 0$, (b) at $T = 0.95T_c$ for $m_{ps}/T_c 1.99$. The blue dotted line closed with the y-axis corresponds to the region of good behavior. For simplicity the superscript label for the configuration is omitted in the plots.

respective measures to exclude the unphysical configurations. The subplots in Figure 6.11 are the scatter plots of the configurations on these above defined measures, $S^{(i)}$ and $O^{(i)}$, for $m_\pi/T_c = 1.99$ studied at zero temperature and $T = 0.95T_c$. The blue dotted line is the cut used in our calculations.

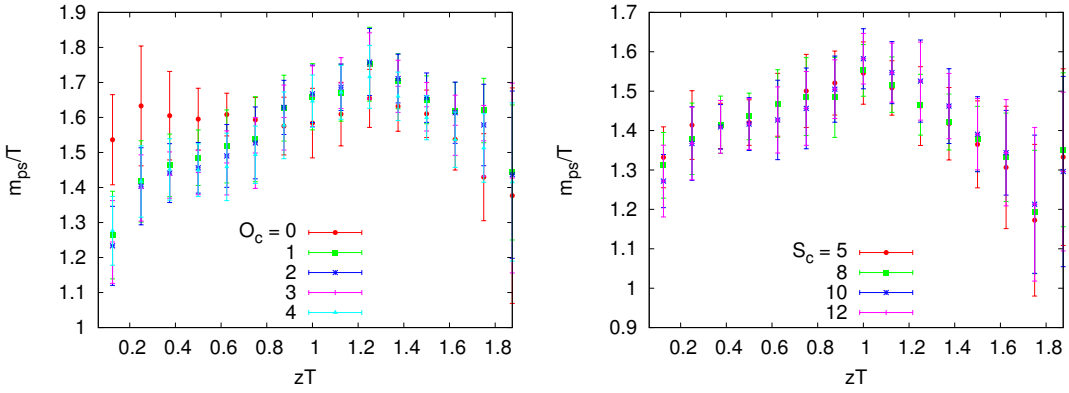

(a) (b)

Figure 6.12: Effective mass plots for pseudoscalar correlators with varying cuts on S and O. The effective mass is observed to be more sensitive to O than S.

The effective mass (see eq. (3.2)) plots for the pseudoscalar, estimated for various cuts attributed for the measures $S^{(i)}$ and $O^{(i)}$ are shown in Figure 6.12. It is evident from the plots that the cut doesn't affect the results much. In our calculations we took configurations, which are well-behaved as those with $((S^{(i)} \leq 10) \cap (O^{(i)} \leq 2))'$. The $(')$

T/T_c	κ	N	N_r
0	0.1347	100	71
0.95	0.1347	100	94
1.5	0.1355	70	67

Table 6.8: The total no. of configurations (N) generated and the no: of configurations (N_r) used for the analysis after discarding the configurations with strange behavior at different temperatures.

is to emphasize that the cuts are applied only in those configurations with well-behaved pseudoscalar correlator minima, as mentioned in the definition of the measure O. Table 6.8 contains the details regarding the no: of configurations generated and the no: of configurations used as well-behaved configurations for the analysis.

6.B Wall sources

In this section, we make a detailed comparison of the screening correlator with the corresponding correlators in the FFT. We used wall sources for FFT, and compared the effective masses, $m(z)$, obtained on $32^2 \times 8 \times N_z$ lattices (with $N_z = 80$), with those obtained in the interacting theory. Wall source at zero temperature is defined as the collection of point sources with equal magnitude in all the points on a given time slice. This is equivalent to a sum of the all the space indices at the source in a point-to-all quark propagator. This can be expressed algebraically in terms of the point-to-all quark propagator as

$$D_w^{-1}(t; x', y', z', t') = \sum_{x,y,z} D_p^{-1}(x, y, z, t; x', y', z', t'), \tag{6.19}$$

where $D^p(x, y, z, t; x', y', z', t')$ is the point-to-all quark propagator, with source at (x, y, z, t) and the sink at (x', y', z', t').

In Figure 6.13 we compare the PS and V screening masses for our lightest quarks (corresponding to $m_\pi/T = 1.52$ at $1.5T_c$) to screening masses in FFT with similar bare quark mass. In the free theory, the screening correlator for wall source in these two channels are equal. The results for the FFT were obtained on a lattice with $N_z = 80$ using the estimator $\ln C(z)/C(z+1)$ for the screening masses. The plateaus in the effective masses shown is due to the use of a wall source. When a point source is used, neither the free theory nor the interacting theory shows a plateau [130]. These checks give us confidence that we are able to extract the asymptotic behavior of the screening

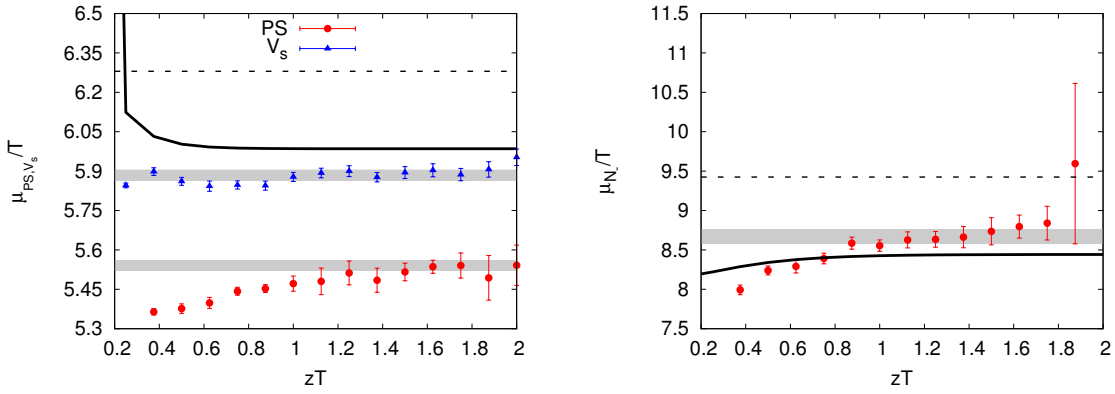

Figure 6.13: Effective masses, in units of temperature, for meson and nucleon sources, at $T = 1.5T_c$ and in FFT. The black continuous curve denotes the FFT screening masses for $N_t = 8$. The black dashed line shows the continuum value, $\mu = 2\pi T$ [129, 203]. The data points and the bands show the effective masses and the fitted estimate for the asymptotic value, respectively.

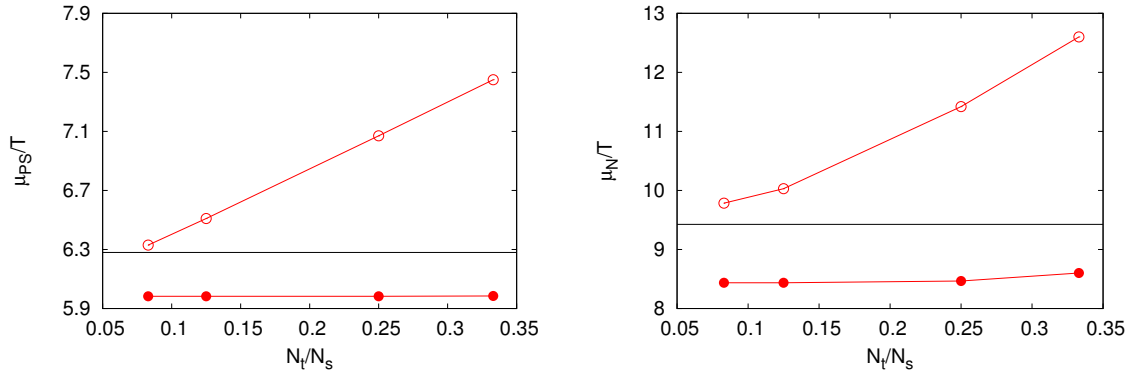

Figure 6.14: Mesonic and nucleonic screening masses in FFT as a function of $N_t/N_s = 1/LT$ for $N_t = 8$. The filled symbols are estimates from wall source quark propagators, while the unfilled symbols are estimated using point sources. In the latter case, since there is no plateau in the local mass, we use the prescription of [130] and use the local mass at distance $N_z/4$.

correlator.

The effective masses for the negative parity nucleon are also shown in Figure 6.13. In the interacting theory, a reasonable plateau is obtained in the effective mass, $C(z) \sim \exp(\mu(z) \times (N_z - z))$. The plateau is more pronounced in our data for heavier quarks. We see that the effective mass in the interacting theory is larger than that in the free

theory.

Since we use $N_s/N_t = LT = 4$ we also check finite volume effects in a theory of free quarks. In Figure 6.14 we show the screening masses for pseudoscalar meson and nucleon on lattices with $N_t = 8$ and varying N_s. With wall sources we find essentially no finite volume effect in either channels already for $LT = 4$. Since finite volume effects are larger in the free theory than in the interacting theory, therefore finite volume effects in our studies are expected to be small. In contrast, point sources give large finite volume effects [130].

Chapter 7

Summary and conclusions

This thesis is a combination of two major works on baryons from lattice QCD. The first part of it, involving charm baryon spectroscopy, is subdivided into two subparts : First one dealing with the excited state spectroscopy of charm baryons, while the second work is on charm hadron spectroscopy using overlap fermions. In the second part, we perform a finite temperature study of screening masses of hadrons, particularly for baryons, where we analyze the temperature dependence of the hadronic screening correlators above and immediately below the deconfinement transition temperature.

7.1 Excited state charm baryon spectroscopy

This work constituting first segment of the first work covers major part of the thesis. This work deals with the first non-perturbative calculation of the excited state spectra of charm baryons with one, two and three charm quarks. In these calculations, we extract highly excited states, which are very difficult to extract using the previously existing lattice QCD techniques, of charm baryons. Utilizing the advanced lattice QCD techniques like anisotropic lattice formalism, the derivative-based operator construction and the variational fitting techniques, we extract the spectrum of all the charm baryons having all possible flavor combinations with well-defined total spin up to $\frac{7}{2}$. We also perform several studies on various energy splittings between the charm hadrons. Being first of its kind in the excited charm baryon spectra calculation, this study serves as a foundation for several follow-up studies, which may help us to address many challenges in the baryon spectroscopy. A summary of the results from this work is as follows.

We extract approximately 20 states for each of the charm baryons, along with a

reliable identification of the spin-parity quantum numbers for each of these states. Beside identifying the spin of a state we are also able to decode the structure of operators leading to that state : whether constructed by relativistic, non-relativistic, hybrids, non-hybrid types or a mixture of them all. Similar to light and strange baryon spectra [102], we also find the number of extracted states of each spin in the three lowest-energy bands and the number of quantum numbers expected based on weakly broken $SU(6) \times O(3)$ symmetry agree perfectly, *i.e.,* all the charm baryon spectra remarkably resemble the expectations of quantum numbers from non-relativistic quark model [28, 29, 165]. Extracted spectra do not show the signature of diquark spectra and the chiral symmetry restoration as predicted by some models [204].

Since the spin dependent energy splittings can provide crucial information about interaction energy we study various energy splittings, including splittings due to hyperfine and spin-orbit coupling, for all the charm baryons. We find degeneracy between these spin-orbit split states is more or less satisfied both for bottom and charm quarks. While for the splittings, which mimics the binding energy of these states, comparison with the respective splittings at other quark masses suggest that these splittings can modeled with a form $a + b/m_{\rm ps}$ derived from heavy quark effective theory. From the fitted results involving both doubly and triply charm baryons, we are able to predict $B_c^* - B_c = 80 \pm 8$ MeV and $\Omega_{ccb}^*(3/2^+) = 8050 \pm 10$ MeV.

However, it is to be noted that pion mass used in this calculation is not physical and is 391 MeV. Furthermore, we have not used any multi-hadron operators in this calculation which will play a major role at lighter pion masses. Inclusion of those operators, particularly those involving light quarks, may affect some of the above conclusions, though to a lesser extent than their influence in the light hadron spectra. To get precise numbers for the excited spectra one needs to follow up this calculation with physical pion mass and multi-hadron operators.

The method used here to study charm baryons can also be employed for similar study for bottom baryons. Ground state bottom baryons have been studied by lattice QCD [80, 205, 206, 208, 207, 209]. However, so far excited state spectra from Lattice QCD is limited only to a few low lying states [210] and triply bottom baryons (Ω_{bbb}) [157] using NRQCD. Considering experimental importance and prospects a comprehensive study, using this method, is thus quite essential and an immediate extension of our work will be carried out for bottom baryons in future.

7.2 Charm hadron spectroscopy using overlap fermions

The second part of the spectroscopy work is precise non-perturbative calculation of the low lying charm hadrons at multiple lattice spacings with improved control over the cut off effects. Using a mixed action approach, we utilized the highly desirable features of small discretization errors and small taste breaking effects of the HISQ action and the small discretization effects and the low quark mass limit of the overlap fermion action. We are thus able to study a long range of pseudoscalar meson masses from $230 - 5000$ MeV. By tuning the charm quark mass using the kinetic mass, we made sure the discretization errors due to the uncertainty in the charm mass tuning is small. At this tuned charm quark mass, we extracted the meson and the baryon spectra containing one or more charm quarks. We made a comparative study between the results obtained in this method to out previous study on excited charm baryons. Both results are also compared with other lattice calculations and quark model calculations and experimental results, where available. The consistency within the lattice calculations and the agreement with the experimental values validates the credibility in both of our calculations. Thus, this calculation serves simultaneously as a complementary study to compare the results from our previous calculations and as an independent study with improved control over the systematics that gives predictions about the low lying charm hadron spectrum.

It is also worthwhile to consider excited state study using overlap fermions. However, the distillation method used for charm baryons will be prohibitively costly with extended baryons. One may consider excited state calculations using only local operators but using same flavor structures as those used in our study. The extension of overlap formulation to bottom sector in our current formulation is not possible. However, one may think about to use a full Fermilab type formulation to check whether it is at all possible to go to bottom quark mass with minimum discretization error.

7.3 Nucleons at finite temperature

In the second work, we investigate the nature of the strongly interacting matter at high temperatures using baryonic probes. In this work, we focused on the hadronic correlation lengths that exist in a pure $SU(3)$ gauge theory above and immediately below the deconfinement transition temperature, T_c. As seen in the other lattice calculations, we observed no statistically significant thermal effects in the mesonic correlations immediately below T_c. We also make the observation of the unphysical quenching artefacts in the

scalar screening correlators immediately below T_c and make a first attempt to understand the thermal effects on the ghost coupling in these correlators. We found no statistically significant deviations with the available statistics in these studies also. Above T_c, clear evidence of the chiral symmetry restoration in terms of the pairwise degeneracy in the parity partner correlators and the weakly interacting nature of quarks was observed in the mesonic channels.

Above T_c, baryonic correlations also show clear evidence of the chiral symmetry restoration in terms of the pairwise degeneracy in the parity partner correlators and propagate as three weakly interacting quarks. Below T_c, we find interesting behavior in the nucleonic correlations, indicating precursor effects for the chiral symmetry restoration in the nucleonic channels immediately below T_c. While no such effects have been seen earlier either in the glue sector or with quarks, these observations are expected to have implications for the analysis of the heavy ion collision data. These implications clearly call for follow-up studies of nucleon around T_c. In future we like to do a comprehensive calculation of baryonic correlations, including nucleonic, at various temperatures below T_c and just above T_c.

Bibliography

[1] S. Weinberg, Phys. Rev. Lett. **19**, 1264 (1967).

[2] A. Salam, Conf. Proc. C **680519**, 367 (1968).

[3] S. L. Glashow, Nucl. Phys. **22**, 579 (1961).

[4] P. W. Higgs, Phys. Lett. **12**, 132 (1964).

[5] S. Chatrchyan *et al.* [CMS Collaboration], Phys. Lett. B **716**, 30 (2012) [arXiv:1207.7235 [hep-ex]].

[6] G. Aad *et al.* [ATLAS Collaboration], Phys. Lett. B **716**, 1 (2012) [arXiv:1207.7214 [hep-ex]].

[7] D. J. Gross and F. Wilczek, Phys. Rev. Lett. **30**, 1343 (1973).

[8] H. D. Politzer, Phys. Rept. **14**, 129 (1974).

[9] E. Klempt and J. -M. Richard, Rev. Mod. Phys. **82**, 1095 (2010) and the references therein.

[10] M. F. M. Lutz *et al.* [PANDA Collaboration], arXiv:0903.3905 [hep-ex].

[11] K. T. Brinkmann, P. Gianotti and I. Lehmann, Nucl. Phys. News **16**, 15 (2006) [physics/0701090].

[12] F. Wick [CDF Collaboration], Int. J. Mod. Phys. Conf. Ser. **02**, 163 (2011) [arXiv:1105.0517 [hep-ex]].

[13] RAaij *et al.* [LHCb Collaboration], JHEP **1312**, 090 (2013) [arXiv:1310.2538 [hep-ex]].

[14] T. Abe *et al.* [Belle-II Collaboration], arXiv:1011.0352 [physics.ins-det].

[15] D. M. Asner, T. Barnes, J. M. Bian, I. I. Bigi, N. Brambilla, I. R. Boyko, V. Bytev and K. T. Chao *et al.*, Int. J. Mod. Phys. A **24**, S1 (2009) [arXiv:0809.1869 [hep-ex]].

[16] RPP : J. Beringer et al. (Particle Data Group), Phys. Rev. D **86**, 010001 (2012).

[17] M. Mattson *et al.* [SELEX Collaboration], Phys. Rev. Lett. **89**, 112001 (2002) [hep-ex/0208014].

[18] J. S. Russ [SELEX Collaboration], hep-ex/0209075.

[19] A. Ocherashvili *et al.* [SELEX Collaboration], Phys. Lett. B **628**, 18 (2005) [hep-ex/0406033].

[20] B. Aubert *et al.* [BABAR Collaboration], Phys. Rev. D **74**, 011103 (2006) [hep-ex/0605075].

[21] Y. Kato *et al.* [Belle Collaboration], arXiv:1312.1026 [hep-ex].

[22] R. Chistov *et al.* [BELLE Collaboration], Phys. Rev. Lett. **97**, 162001 (2006) [hep-ex/0606051].

[23] S. Capstick and W. Roberts, Prog. Part. Nucl. Phys. **45**, S241 (2000) and the references therein.

[24] V. Crede and W. Roberts, Rept. Prog. Phys. **76**, 076301 (2013) and the references therein.

[25] J. D. Bjorken, FERMILAB-CONF-85/69, Is the ccc a New Deal for Baryon Spectroscopy?, Int. Conf. on Hadron Spectroscopy, College Park, MD, Apr. 1985;

[26] A. Pineda and J. Soto, Nucl. Phys. Proc. Suppl. **64**, 428 (1998) [hep-ph/9707481].

[27] N. Brambilla, A. Pineda, J. Soto and A. Vairo, Nucl. Phys. B **566**, 275 (2000) [hep-ph/9907240].

[28] N. Isgur and G. Karl, Phys. Lett. B **72**, 109 (1977).

[29] N. Isgur and G. Karl, Phys. Rev. D **18**, 4187 (1978).

[30] P. Hasenfratz, R. R. Horgan, J. Kuti and J. M. Richard, Phys. Lett. B **94**, 401 (1980).

[31] Y. Jia, JHEP **0610**, 073 (2006) [hep-ph/0607290].

[32] J. Vijande, H. Garcilazo, A. Valcarce and F. Fernandez, Phys. Rev. D **70**, 054022 (2004) [hep-ph/0408274].

[33] H. Garcilazo, J. Vijande and A. Valcarce, J. Phys. G **34**, 961 (2007) [hep-ph/0703257].

[34] B. Silvestre-Brac, Few Body Syst. **20**, 1 (1996).

[35] J. G. Korner, M. Kramer and D. Pirjol, Prog. Part. Nucl. Phys. **33**, 787 (1994) [hep-ph/9406359].

[36] C. Albertus, J. E. Amaro, E. Hernandez and J. Nieves, Nucl. Phys. A **740**, 333 (2004) [nucl-th/0311100].

[37] C. Albertus, E. Hernandez, J. Nieves and J. M. Verde-Velasco, Eur. Phys. J. A **31**, 691 (2007) [hep-ph/0610131].

[38] J. M. Flynn, E. Hernandez and J. Nieves, Phys. Rev. D **85**, 014012 (2012) [arXiv:1110.2962 [hep-ph]].

[39] E. E. Jenkins, Phys. Rev. D **54** (1996) 4515 [hep-ph/9603449].

[40] W. Roberts and M. Pervin, Int. J. Mod. Phys. A **23**, 2817 (2008) [arXiv:0711.2492 [nucl-th]].

[41] N. Brambilla, A. Pineda, J. Soto and A. Vairo, Rev. Mod. Phys. **77**, 1423 (2005) [hep-ph/0410047].

[42] N. Brambilla, A. Vairo and T. Rosch, Phys. Rev. D **72**, 034021 (2005) [hep-ph/0506065].

[43] N. Brambilla, J. Ghiglieri and A. Vairo, Phys. Rev. D **81**, 054031 (2010) [arXiv:0911.3541 [hep-ph]].

[44] F. J. Llanes-Estrada, O. I. Pavlova and R. Williams, Eur. Phys. J. C **72**, 2019 (2012) [arXiv:1111.7087 [hep-ph]].

[45] B. A. Thacker and G. P. Lepage, Phys. Rev. D **43**, 196 (1991).

[46] G. P. Lepage, L. Magnea, C. Nakhleh, U. Magnea and K. Hornbostel, Phys. Rev. D **46**, 4052 (1992) [hep-lat/9205007].

[47] H. D. Trottier, Phys. Rev. D **55**, 6844 (1997) [hep-lat/9611026].

[48] C. T. H. Davies *et al.* [UKQCD Collaboration], Phys. Rev. D **58**, 054505 (1998) [hep-lat/9802024].

[49] S. Capstick and N. Isgur, Phys. Rev. D **34**, 2809 (1986).

[50] A. P. Martynenko, Phys. Lett. B **663**, 317 (2008) [arXiv:0708.2033 [hep-ph]].

[51] S. Migura, D. Merten, B. Metsch and H. -R. Petry, Eur. Phys. J. A **28**, 41 (2006) [hep-ph/0602153].

[52] S. M. Gerasyuta and E. E. Matskevich, Int. J. Mod. Phys. E **17**, 585 (2008) [arXiv:0709.0397 [hep-ph]].

[53] D. Ebert, R. N. Faustov and V. O. Galkin, Phys. Lett. B **659**, 612 (2008) [arXiv:0705.2957 [hep-ph]].

[54] J. -R. Zhang and M. -Q. Huang, Phys. Lett. B **674**, 28 (2009) [arXiv:0902.3297 [hep-ph]].

[55] Z. -G. Wang, Commun. Theor. Phys. **58**, 723 (2012) [arXiv:1112.2274 [hep-ph]].

[56] X. -H. Guo, K. -W. Wei and X. -H. Wu, Phys. Rev. D **78**, 056005 (2008) [arXiv:0809.1702 [hep-ph]].

[57] F. Butler, H. Chen, J. Sexton, A. Vaccarino and D. Weingarten, Nucl. Phys. B **430**, 179 (1994) [hep-lat/9405003].

[58] S. Aoki, *et al.* [CP-PACS Collaboration], Phys. Rev. Lett. **84**, 238 (2000) [hep-lat/9904012]

[59] C. W. Bernard, *et al.*, Phys. Rev. D **64**, 054506 (2001) [hep-lat/0104002].

[60] C. Aubin, *et al.*, Phys. Rev. D **70**, 094505 (2004) [hep-lat/0402030].

[61] S. Aoki *et al.* [PACS-CS Collaboration], Phys. Rev. D **79**, 034503 (2009) [arXiv:0807.1661 [hep-lat]].

[62] D. J. Antonio *et al.* [RBC and UKQCD Collaborations], Phys. Rev. D **75**, 114501 (2007) [hep-lat/0612005].

[63] A. Walker-Loud, *et al.*, Phys. Rev. D **79**, 054502 (2009) [arXiv:0806.4549 [hep-lat]].

[64] C. Alexandrou *et al.* [European Twisted Mass Collaboration], Phys. Rev. D **78**, 014509 (2008) [arXiv:0803.3190 [hep-lat]].

[65] S. Durr, *et al.*, Science **322**, 1224 (2008) [arXiv:0906.3599 [hep-lat]].

[66] C. T. H. Davies, K. Hornbostel, A. Langnau, G. P. Lepage, A. Lidsey, J. Shigemitsu and J. H. Sloan, Phys. Rev. D **50**, 6963 (1994) [hep-lat/9406017].

[67] C. T. H. Davies, K. Hornbostel, G. P. Lepage, A. J. Lidsey, J. Shigemitsu and J. H. Sloan, Phys. Rev. D **52**, 6519 (1995) [hep-lat/9506026].

[68] M. Okamoto *et al.* [CP-PACS Collaboration], Phys. Rev. D **65**, 094508 (2002) [hep-lat/0112020].

[69] A. Gray, I. Allison, C. T. H. Davies, E. Dalgic, G. P. Lepage, J. Shigemitsu and M. Wingate, Phys. Rev. D **72**, 094507 (2005) [hep-lat/0507013].

[70] C. Aubin, C. Bernard, C. E. DeTar, M. Di Pierro, E. D. Freeland, S. Gottlieb, U. M. Heller and J. E. Hetrick *et al.*, Phys. Rev. Lett. **95**, 122002 (2005) [hep-lat/0506030].

[71] A. Bazavov *et al.* [Fermilab Lattice and MILC Collaborations], Phys. Rev. D **85**, 114506 (2012) [arXiv:1112.3051 [hep-lat]].

[72] T. Burch, C. DeTar, M. Di Pierro, A. X. El-Khadra, E. D. Freeland, S. Gottlieb, A. S. Kronfeld and L. Levkova *et al.*, Phys. Rev. D **81**, 034508 (2010) [arXiv:0912.2701 [hep-lat]].

[73] G. C. Donald, C. T. H. Davies, R. J. Dowdall, E. Follana, K. Hornbostel, J. Koponen, G. P. Lepage and C. McNeile, Phys. Rev. D **86**, 094501 (2012) [arXiv:1208.2855 [hep-lat]].

[74] C. McNeile, *et al.*, Phys. Rev. D **86**, 074503 (2012) [arXiv:1207.0994 [hep-lat]].

[75] E. B. Gregory, *et al.*, Phys. Rev. D **83**, 014506 (2011) [arXiv:1010.3848 [hep-lat]].

[76] R. J. Dowdall *et al.* [HPQCD Collaboration], Phys. Rev. D **85**, 054509 (2012) [arXiv:1110.6887 [hep-lat]].

[77] R. J. Dowdall, C. T. H. Davies, T. C. Hammant and R. R. Horgan, Phys. Rev. D **86**, 094510 (2012) [arXiv:1207.5149 [hep-lat]].

[78] Y. Namekawa *et al.* [PACS-CS Collaboration], Phys. Rev. D **84**, 074505 (2011) [arXiv:1104.4600 [hep-lat]].

[79] D. Mohler and R. M. Woloshyn, Phys. Rev. D **84**, 054505 (2011) [arXiv:1103.5506 [hep-lat]];

[80] N. Mathur, R. Lewis and R. M. Woloshyn, Phys. Rev. D **66**, 014502 (2002) [hep-ph/0203253]

[81] R. Lewis, N. Mathur and R. M. Woloshyn, Phys. Rev. D **64**, 094509 (2001) [hep-ph/0107037].

[82] J. M. Flynn, *et al.*, [UKQCD Collaboration], JHEP **0307**, 066 (2003) [hep-lat/0307025].

[83] L. Liu, *et al.*, Phys. Rev. D **81**, 094505 (2010) [arXiv:0909.3294 [hep-lat]].

[84] R. A. Briceno, H. -W. Lin and D. R. Bolton, Phys. Rev. D **86**, 094504 (2012) [arXiv:1207.3536 [hep-lat]].

[85] C. Alexandrou, J. Carbonell, D. Christaras, V. Drach, M. Gravina and M. Papinutto, Phys. Rev. D **86**, 114501 (2012) [arXiv:1205.6856 [hep-lat]].

[86] G. Bali, *et al.*, J. Phys. Conf. Ser. **426**, 012017 (2013) [arXiv:1212.0565 [hep-lat]].

[87] S. Durr, G. Koutsou and T. Lippert, Phys. Rev. D **86**, 114514 (2012) [arXiv:1208.6270 [hep-lat]].

[88] Y. Namekawa *et al.* [PACS-CS Collaboration], Phys. Rev. D **87**, 094512 (2013) [arXiv:1301.4743 [hep-lat]].

[89] N. Mathur, Y. Chen, S. J. Dong, T. Draper, I. Horvath, F. X. Lee, K. F. Liu and J. B. Zhang, Phys. Lett. B **605**, 137 (2005) [hep-ph/0306199].

[90] D. B. Leinweber, W. Melnitchouk, D. G. Richards, A. G. Williams and J. M. Zanotti, Lect. Notes Phys. **663**, 71 (2005) [nucl-th/0406032].

[91] K. Sasaki, S. Sasaki and T. Hatsuda, Phys. Lett. B **623**, 208 (2005) [hep-lat/0504020].

[92] T. Burch, C. Gattringer, L. Y. .Glozman, C. Hagen, D. Hierl, C. B. Lang and A. Schafer, Phys. Rev. D **74**, 014504 (2006) [hep-lat/0604019].

[93] M. S. Mahbub *et al.* [CSSM Lattice Collaboration], Phys. Lett. B **707**, 389 (2012) [arXiv:1011.5724 [hep-lat]].

[94] M. S. Mahbub, A. O. Cais, W. Kamleh, D. B. Leinweber and A. G. Williams, Phys. Rev. D **82**, 094504 (2010) [arXiv:1004.5455 [hep-lat]].

[95] G. P. Engel, C. B. Lang and A. Schafer, Phys. Rev. D **87**, no. 3, 034502 (2013) [arXiv:1212.2032 [hep-lat]].

[96] M. Peardon, *et al.*, [Hadron Spectrum Collaboration], Phys. Rev. D **80**, 054506 (2009) [arXiv:0905.2160 [hep-lat]].

[97] C. Michael, Nucl. Phys. B **259**, 58 (1985);

[98] M. Luscher and U. Wolff, Nucl. Phys. B **339**, 222 (1990).

[99] J. J. Dudek, R. G. Edwards, N. Mathur and D. G. Richards, Phys. Rev. D **77**, 034501 (2008) [arXiv:0707.4162 [hep-lat]].

[100] S. Basak *et al.* [Lattice Hadron Physics (LHPC) Collaboration], Phys. Rev. D **72**, 074501 (2005) [hep-lat/0508018].

[101] R. G. Edwards, J. J. Dudek, D. G. Richards and S. J. Wallace, Phys. Rev. D **84**, 074508 (2011) [arXiv:1104.5152 [hep-ph]].

[102] R. G. Edwards, N. Mathur, D. G. Richards and S. J. Wallace, Phys. Rev. D **87**, 054506 (2013) arXiv:1212.5236 [hep-ph].

[103] J. J. Dudek, R. G. Edwards, M. J. Peardon, D. G. Richards and C. E. Thomas, Phys. Rev. Lett. **103**, 262001 (2009), [arXiv:0909.0200 [hep-ph]]

[104] J. J. Dudek, R. G. Edwards, M. J. Peardon, D. G. Richards and C. E. Thomas, Phys. Rev. D **82**, 034508 (2010) [arXiv:1004.4930 [hep-ph]].

[105] J. J. Dudek, R. G. Edwards, M. J. Peardon, D. G. Richards and C. E. Thomas, Phys. Rev. D **83**, 071504 (2011) [arXiv:1011.6352 [hep-ph]].

[106] L. Liu, *et al.*, [HSC], JHEP **1207**, 126 (2012) [arXiv:1204.5425 [hep-ph]].

[107] G. Moir, M. Peardon, S. M. Ryan, C. E. Thomas and L. Liu, JHEP **1305**, 021 (2013) [arXiv:1301.7670 [hep-ph]].

[108] J. J. Dudek and R. G. Edwards, Phys. Rev. D **85**, 054016 (2012) [arXiv:1201.2349 [hep-ph]].

[109] R. G. Edwards, B. Joo and H. -W. Lin, Phys. Rev. D **78**, 054501 (2008) [arXiv:0803.3960 [hep-lat]].

[110] H. -W. Lin *et al.* [HSC], Phys. Rev. D **79**, 034502 (2009) [arXiv:0810.3588 [hep-lat]].

[111] G. P. Lepage and P. B. Mackenzie, Phys. Rev. D **48**, 2250 (1993) [hep-lat/9209022].

[112] M. Padmanath, R. G. Edwards, N. Mathur and M. Peardon, arXiv:1307.7022 [hep-lat].

[113] M. Padmanath, R. G. Edwards, N. Mathur and M. Peardon, arXiv:1311.4806 [hep-lat].

[114] M. Padmanath, R. G. Edwards, N. Mathur and M. Peardon, arXiv:1311.4354 [hep-lat].

[115] D. B. Renner *et al.* [LHP Collaboration], Nucl. Phys. Proc. Suppl. **140**, 255 (2005) [hep-lat/0409130].

[116] R. G. Edwards *et al.* [LHPC Collaboration], Phys. Rev. Lett. **96**, 052001 (2006) [hep-lat/0510062].

[117] J. D. Bratt *et al.* [LHPC Collaboration], Phys. Rev. D **82**, 094502 (2010) [arXiv:1001.3620 [hep-lat]].

[118] C. Allton, C. Maynard, A. Trivini and R. Tweedie, PoS LAT **2006**, 202 (2006) [hep-lat/0610068].

[119] S. Durr, Z. Fodor, C. Hoelbling, S. D. Katz, S. Krieg, T. .Kurth, L. Lellouch and T. .Lippert *et al.*, PoS LAT **2007**, 113 (2007) [arXiv:0710.4866 [hep-lat]].

[120] K. Cichy, G. Herdoiza and K. Jansen, Acta Phys. Polon. Supp. **2**, 497 (2009) [arXiv:0910.0816 [hep-lat]].

[121] E. Follana *et al.* [HPQCD and UKQCD Collaborations], Phys. Rev. D **75**, 054502 (2007) [hep-lat/0610092].

[122] A. Bazavov *et al.* [MILC Collaboration], Phys. Rev. D **87**, no. 5, 054505 (2013) [arXiv:1212.4768 [hep-lat]].

[123] R. Narayanan and H. Neuberger, Phys. Rev. Lett. **71**, 3251 (1993) [hep-lat/9308011].

[124] H. Neuberger, Phys. Lett. B **417**, 141 (1998); ; *ibid.* B427 (1998) 353;

[125] R. G. Edwards, U. M. Heller and R. Narayanan, Phys. Rev. D **59**, 094510 (1999) [hep-lat/9811030].

[126] S. Basak, *et al.*, [ILGTI] PoS LATTICE **2012**, 141 (2012) [arXiv:1211.6277 [hep-lat]].

[127] S. Basak, S. Datta, M. Padmanath, P. Majumdar and N. Mathur, PoS LATTICE **2012**, 141 (2012) [arXiv:1211.6277 [hep-lat]].

[128] C. E. DeTar and J. B. Kogut, *Phys. Rev. Lett.* 59 (1987) 399, *Phys. Rev.* D 36 (1987) 2828.

[129] K. D. Born *et al.*(MT_c Collaboration), *Phys. Rev. Lett.* 67 (1991) 302.

[130] S. Wissel *et al.*, *PoS* LAT-2005, 164; S. Wissel, Ph. D *dissertation* (2006).

[131] R. V. Gavai, S. Gupta and R. Lacaze, *Phys. Rev.* D 78 (2008) 014502.

[132] R. V. Gavai, S. Gupta and P. Majumdar, *Phys. Rev.* D 65 (2002) 054506.

[133] A. Gocksch, P. Rossi and Urs M. Heller, *Phys. Lett.* B 205 (1988) 334.

[134] M. Cheng *et al.*, *Eur. Phys. J.* C 71 (2011) 1564;
D. Banerjee *et al.*, *Phys. Rev.* D 83 (2011) 074510.

[135] M. Cheng *et al.*, *Nucl. Phys.* A 862–863 (2011) 308.

[136] S. Datta, S. Gupta, M. Padmanath, J. Maiti and N. Mathur, JHEP **1302**, 145 (2013) [arXiv:1212.2927 [hep-lat]].

[137] K. G. Wilson, Phys. Rev. D **10**, 2445 (1974).

[138] T. DeGrand and C. E. Detar, New Jersey, USA: World Scientific (2006) 345 p

[139] C. Gattringer and C. B. Lang, Lect. Notes Phys. **788**, 1 (2010).

[140] I. Montvay and G. Munster, Cambridge, UK: Univ. Pr. (1994) 491 p. (Cambridge monographs on mathematical physics)

[141] P. T. Matthews and A. Salam, Nuovo Cim. **2**, 120 (1955).

[142] H. B. Nielsen and M. Ninomiya, Phys. Lett. B **105**, 219 (1981).

[143] B. Sheikholeslami and R. Wohlert, Nucl. Phys. B **259**, 572 (1985).

[144] M. Luscher, S. Sint, R. Sommer, P. Weisz and U. Wolff, Nucl. Phys. B **491**, 323 (1997) [hep-lat/9609035].

[145] J. B. Kogut and L. Susskind, Phys. Rev. D **11**, 395 (1975).

[146] S. R. Sharpe, PoS LAT **2006**, 022 (2006) [hep-lat/0610094].

[147] M. Luscher, Phys. Lett. B **428**, 342 (1998) [hep-lat/9802011].

[148] M. A. Clark and A. D. Kennedy, Nucl. Phys. Proc. Suppl. **129**, 850 (2004) [hep-lat/0309084].

[149] M. A. Clark, A. D. Kennedy and Z. Sroczynski, Nucl. Phys. Proc. Suppl. **140**, 835 (2005) [hep-lat/0409133].

[150] M. A. Clark and A. D. Kennedy, Phys. Rev. Lett. **98**, 051601 (2007) [hep-lat/0608015].

[151] G. P. Lepage, CLNS-89-971.

[152] F. Karsch, Nucl. Phys. B **205**, 285 (1982).

[153] G. Burgers, F. Karsch, A. Nakamura and I. O. Stamatescu, Nucl. Phys. B **304**, 587 (1988);

[154] T. R. Klassen, Nucl. Phys. B **533**, 557 (1998); [hep-lat/9803010].

[155] P. Chen, Phys. Rev. D **64**, 034509 (2001). [hep-lat/0006019].

[156] C. R. Allton *et al.* [UKQCD Collaboration], Phys. Rev. D **47**, 5128 (1993) [hep-lat/9303009].

[157] S. Meinel, Phys. Rev. D **85**, 114510 (2012).

[158] N. Brambilla, S. Eidelman, B. K. Heltsley, R. Vogt, G. T. Bodwin, E. Eichten, A. D. Frawley and A. B. Meyer *et al.*, Eur. Phys. J. C **71**, 1534 (2011) [arXiv:1010.5827 [hep-ph]].

[159] M. J. Savage and M. B. Wise, Phys. Lett. B **248**, 177 (1990).

[160] M. J. Savage and R. P. Springer, Int. J. Mod. Phys. A **6**, 1701 (1991).

[161] S. Fleming and T. Mehen, Phys. Rev. D **73**, 034502 (2006) [hep-ph/0509313].

[162] E. J. Eichten and C. Quigg, Phys. Rev. D **49**, 5845 (1994) [hep-ph/9402210].

[163] E. B. Gregory, C. T. H. Davies, E. Follana, E. Gamiz, I. D. Kendall, G. P. Lepage, H. Na and J. Shigemitsu *et al.*, Phys. Rev. Lett. **104**, 022001 (2010) [arXiv:0909.4462 [hep-lat]].

[164] Z. S. Brown, W. Detmold, S. Meinel and K. Orginos, PoS QNP **2012**, 107 (2012).

[165] O. W. Greenberg, Phys. Rev. Lett. **13**, 598 (1964).

[166] J. J. Dudek, R. G. Edwards and C. E. Thomas, Phys. Rev. D **87**, no. 3, 034505 (2013) [arXiv:1212.0830 [hep-ph]].

[167] H. Fukaya *et al.* [JLQCD Collaboration], Phys. Rev. Lett. **98**, 172001 (2007) [hep-lat/0702003].

[168] A. Li *et al.* [χQCD Collaboration], Phys. Rev. D **82**, 114501 (2010) [arXiv:1005.5424 [hep-lat]].

[169] O. Bar, G. Rupak and N. Shoresh, Phys. Rev. D **67**, 114505 (2003) [hep-lat/0210050].

[170] J. -W. Chen, D. O'Connell and A. Walker-Loud, Phys. Rev. D **75**, 054501 (2007) [hep-lat/0611003].

[171] K. Orginos and A. Walker-Loud, Phys. Rev. D **77**, 094505 (2008) [arXiv:0705.0572 [hep-lat]].

[172] N. Mathur *et al.* [xQCD Collaboration], PoS LATTICE **2010**, 114 (2010) [arXiv:1011.4378 [hep-lat]].

[173] S. Capitani, S. Durr and C. Hoelbling, JHEP **0611**, 028 (2006) [hep-lat/0607006].

[174] J. van den Eshof, A. Frommer, T. Lippert, K. Schilling and H. A. van der Vorst, Comput. Phys. Commun. **146**, 203 (2002) [hep-lat/0202025].

[175] Y. Chen, S. J. Dong, T. Draper, I. Horvath, F. X. Lee, K. F. Liu, N. Mathur and J. B. Zhang, Phys. Rev. D **70**, 034502 (2004) [hep-lat/0304005].

[176] C. T. H. Davies *et al.* [HPQCD Collaboration], Phys. Rev. D **81**, 034506 (2010) [arXiv:0910.1229 [hep-lat]].

[177] S. Tamhankar, A. Alexandru, Y. Chen, S. J. Dong, T. Draper, I. Horvath, F. X. Lee and K. F. Liu *et al.*, Phys. Lett. B **638**, 55 (2006) [hep-lat/0507027].

[178] A. X. El-Khadra, A. S. Kronfeld and P. B. Mackenzie, Phys. Rev. D **55**, 3933 (1997) [hep-lat/9604004].

[179] M. Benmerrouche, R. M. Davidson and N. C. Mukhopadhyay, Phys. Rev. C **39**, 2339 (1989).

[180] S. Gupta, *Phys. Rev.* D 64 (2001) 034507.

[181] G. Boyd *et al.*, *Nucl. Phys.* B 469 (1996) 419.

[182] D. Becirevic *et al.*, *Phys. Lett.* B 558 (2003) 69.

[183] W. Bardeen *et al.*, *Phys. Rev.* D 65 (2001) 014509.

[184] N. Mathur *et al.*, *Phys. Rev.* D 76 (2007) 114505.

[185] S. Prelovsek *et al.*, *Phys. Rev.* D 70 (2004) 094503.

[186] M. Lüscher *et al.*, *Nucl. Phys.* B 491 (1997) 344.

[187] G. P. Lepage and P. Mackenzie, *Phys. Rev.* D 48 (1993) 2250.

[188] M. Göckeler *et al.*, *Nucl. Phys.* B (*Proc. Suppl.*) 53 (1997) 896.

[189] S. Sint and P. Weisz, *Nucl. Phys.* B (*Proc. Suppl.*) 63 (1998) 856.

[190] S. Datta and S. Gupta, *Phys. Rev.* D 80 (2009) 114504.

[191] S. Gupta, *Phys. Rev.* D 60 (1999) 094505.

[192] R. Rapp and J. Wambach, *Adv. Nucl. Phys.* 25 (2000) 1.

[193] S. Gupta and N. Karthik, Phys. Rev. D **87**, 094001 (2013) [arXiv:1302.4917 [hep-lat]].

[194] M. Luscher, S. Sint, R. Sommer, P. Weisz, U. Wolff, *Nucl. Phys. B* **491** (1991), 323 – 343.

[195] T. DeGrand, A. Hasenfratz and T. G. Kovacs, *Nucl. Phys. B* **547** (1999) 259 – 280.

[196] W. Bardeen, A. Duncan, E. Eichten, G. Hockney and H. Thacker, *Phys. Rev. D* **57**, 1633 – 1641, (1998).

[197] M. Gockeler, A. Hoferichter, R. Horsley, D. Pleiter, P. Rakow, G. Schierholz and P. Stephenson, *Nucl. Phys. B (Proc. Suppl.)* **73** (1999) 889 – 891.

[198] A. Hoferichter, E. Laermann, V. K. Mitrjushkin, M. Muller-Preussker and P. Schmidt, *Nucl. Phys. B (Proc. Suppl.)* **63**A-C (1998) 164 – 166.

[199] R. Frezzotti, P. A. Grassi, S. Sint and P. Weisz, *Nucl. Phys. B (Proc. Suppl.)*, **83 – 84** (2000) 941 – 946.

[200] C. Gattringer and S. Solbrig, *PoS, LAT*2005:**127**.

[201] C. Bernard, T. DeGrand, C. DeTar, S. Gottlieb, Urs M. Heller, C. McNeile, K. Originos, R. Sugar and D. Toussaint, *Nucl.Phys. B (Proc.Suppl.)* **83** (2000) 289–291.

[202] C. Bernard, S. Datta, T. DeGrand, C. DeTar, S. Gottlieb, Urs M. Heller, C. McNeile, K. Originos, R. Sugar and D. Toussaint, *Phys. Rev. D* **66** (2002) 094501.

[203] V. I. Eletskii and B. L. Ioffe, *Sov. J. Nucl. Phys.* 48 (1988) 384;
W. Florkowski and B. L. Friman, *Z. Phys.* A 347 (1994) 271.

[204] L. Y. .Glozman, C. B. Lang and M. Schrock, Phys. Rev. D **86**, 014507 (2012) [arXiv:1205.4887 [hep-lat]].

[205] K. C. Bowler *et al.* [UKQCD Collaboration], Phys. Rev. D **54**, 3619 (1996) [hep-lat/9601022].

[206] A. Ali Khan, T. Bhattacharya, S. Collins, C. T. H. Davies, R. Gupta, C. Morningstar, J. Shigemitsu and J. H. Sloan, Phys. Rev. D **62**, 054505 (2000) [hep-lat/9912034].

[207] R. Lewis and R. M. Woloshyn, Phys. Rev. D **79**, 014502 (2009) [arXiv:0806.4783 [hep-lat]].

[208] W. Detmold, C. -J. D. Lin and M. Wingate, Nucl. Phys. B **818**, 17 (2009) [arXiv:0812.2583 [hep-lat]].

[209] H. -W. Lin, S. D. Cohen, N. Mathur and K. Orginos, Phys. Rev. D **80**, 054027 (2009) [arXiv:0905.4120 [hep-lat]].

[210] T. Burch, C. Hagen, C. B. Lang, M. Limmer and A. Schafer, Phys. Rev. D **79**, 014504 (2009) [arXiv:0809.1103 [hep-lat]].